Quantum transport studies for spintronics implementation : from supramolecular carbon nanotube systems to topological crystalline insulator

Joachim Schönle

Communauté
UNIVERSITÉ Grenoble Alpes

THÈSE

Pour obtenir le grade de

Docteur de la Communauté Université Grenoble Alpes

Spécialité: **Nanophysique**

Arrêté ministériel du 25 mai 2016

présentée par

Joachim Schönle

Thèse dirigée par
Wolfgang Wernsdorfer

et co-dirigée par
Franck Balestro

préparée au sein de l'**Institut Néel, CNRS**
et de l'**École Doctorale de Physique de Grenoble**

Quantum transport studies for spintronics implementation:

from supramolecular carbon nanotube systems to topological crystalline insulator

Thèse soutenue publiquement le **29 juin 2018** à Grenoble
devant le jury composé de:

Romain Danneau (Rapporteur)
Chargé de recherche, Karlsruhe Institute of Technology, Karlsruhe

Philippe Lafarge (Rapporteur)
Professeur, Université Paris Diderot, Paris

Christopher Bäuerle (Examinateur, Président du jury)
Directeur de recherche, Institut Néel-CNRS, Grenoble

Xavier Jehl (Examinateur)
Chargé de recherche, INAC-CEA, Grenoble

Acknowledgements

At this point, I would like to thank all those who have contributed to the successful completion of this dissertation through their guidance, assistance, and sometimes even just initial support.
First and foremost my thanks go to Wolfgang Wernsdorfer, who gave me the chance to work on this project in Grenoble. Thank you for honest criticism, helpful advice and always fair support of this work. The detail obsession and dedication with which you (still) pursue the lab work is absolutely impressive and makes every doctoral student look old in comparison. And if the work was ever very inconvenient on weekends, then the sight of your bike in the corridor is a great motivational aid.
A big thank you also goes to Franck Balestro, who after the change from Wolfgang to Karlsruhe suddenly had to deal with another doctoral student. Thank you for taking over this role, thank you for the effort you've done over and over again. Without your help, I would not have been able to finish this project successfully.
I would also like to thank the rest of the NanoSpin team, both the current members and those who have survived here. Thanks Oksana, Michael, Nard, Maria, Gheorghe, Pavel, Hugo, Stefano and Edgar. A special thank you, Christophe, for your advice on physics, about hiking routes to climbing moves. And also to Clement, who was a great help to me at the beginning and welcomed me well at a point in time when the non-permanents fraction of the group was still smaller.
Aussi à l'extérieur de l'équipe, beaucoup de gens à l'institut méritent mes remerciements. Tout d'abord, l'équipe NanoFab, dont la "maison" est pendant longtemps devenue la mienne. Merci Jeff, Bruno, Gwénaelle, Latifa et Seb. Même si les différentes pannes de matériel ont tordu le cou à plein d'échantillons, l'ouverture, la convivialité et, en général, l'atmosphère de travail dans et autour de l'équipe ont toujours été un plaisir. Un grand merci à Thierry Crozes, qui m'a soutenu dès le début. Also a thank you to Giorgos for your help with the PTA clean room.
L'atmosphère et la volonté de contribuer à la communauté de travail à l'Institut Néel est un point que j'ai perçu comme un grand plus. La liste de ceux qui m'ont aidé avec quelques coups et conseils est donc presque infinie, ce qui doit m'excuser de ne pas mentionner tout le monde par son nom. Merci à David Barral, Laurent Cagnon, Simon Le-Denmat, Valérie Reita et beaucoup d'autres. Merci également à Florence Pois et Elodie Bernard pour votre soutien dans l'arène de la bureaucratie française et à l'équipe Ingénierie Expérimentale, notamment en personne d'Eric Eyraud, dont l'aide a probablement permis d'éviter un désastre du cryostat ... ou deux.
Je voudrais aussi remercier Vincent Bouchiat et Laetitia Marty, dont la porte m'était toujours ouverte. Cela est particulièrement vrai de Richard Haettel, merci pour ton aide et ton expertise technique qui était précieuse pour un novice dans le secteur des CVD.

For the second of my projects I had the chance to work with some Bielefelders (No, that is not a sausage from Germany.). In particular a thank you to Robin and Denis for your participation, the visits and a very entertaining time, even if not always everything worked out as desired. In connection with this project a big thank you goes to Kiril from the KIT in Karlsruhe, who showed great helpfulness not only in terms of corrections of the manuscript, but was also open to discussion almost any time of day or night.
Finally, I would also like to thank the members of the jury for accepting the invitation and for making an official and essential contribution to completing this work.

Since such a job should not just be made entirely out of work, I would like to thank those who ensured this. In those almost 4 years I was able to make the acquaintance of some great people who made the time here at the institute an unforgettable one. Thanks Ovidiu, Ioan, Evan, Johanna, Anja, Sinem, Maria, Alvaro, Jorge, Kimon, Simone and many others.
Thanks also to the CAESUG ski team, especially (again) Jeff, Pierre and William, thanks to whom already the prospect of me on skis is not a danger to society anymore. Thank you for making some great moments possible.
And outside of the institute, I have also gained some friends here. Thanks in particular to you, JP, Claudio, Pierre and Katharina for a very great time.
Last but not least a big thank you to family and friends in Germany who (hopefully still) forgive me for making myself a bit scarce during the last years.

Preface

During my PhD at the Néel Institute, I engaged myself in two different projects. The first one, a work on carbon nanotubes and single-molecule magnets, is a consequential follow-up of the scientifical research focus of the NanoSpin group within the last years. The second one, based in the field of topological matter, started as a small side project of measurements of topological Heusler compounds, a sporadic but long-lasting collaboration of Wolfgang Wernsdorfer of Néel NanoSpin, the group of Günter Reiss in Bielefeld and the Max-Planck Institute in Dresden. In 2016, this project picked up more steam with a change to tin telluride topological crystalline insulator. This was also *enabled* by ongoing technical issues in the Néel cleanroom facilities, which repeatedly stalled the work on carbon nanotube samples for several months. As a result, similar amounts of time and effort was spent on the two respective projects which are thus equivalently included in this manuscript.

These two projects, while being vastly different on the first look, share several characteristics. Both are grounded in the field of fundamental research and based on the fabrication and study of hybrid quantum systems via transport measurements. Owing to the resulting characteristics, both systems are highly interesting for future spintronics applications. On the other hand, the underlying microscopic principles significantly differ in detail, which requires for the introduction of a broad context.

As a result, many aspects inevitably need to be presented separately. The four individual introduction chapters of part one, while being mostly self-contained, should therefore rather be seen pairwise in order to provide the context for the physics of supramolecular carbon nanotube systems and induced superconductivity in tin telluride topological crystalline insulator. In part two, the fabrication of devices and the measurement setup are presented and part three is finally dedicated to the performed experiments.

Abstract

The interconnected advance of nanofabrication techniques, rise of novel carbon-based materials and topological matter and understanding of coupled quantum effects in solid state physics has fueled a widespread scientifical interest in hybrid quantum systems, in which the interplay between gapped band structures and spin could be exploited for future implementation in revolutionizing spintroncis concepts, ranging from to data storage to quantum computation. Two different realizations, which are strongly researched as platforms in this context, are molecular systems and topological insulators. Owing to chemical tailoring and environmental decoupling of molecular spins, the former serve as well-controlled building blocks for spintronics applications, but the incorporation in circuitry and thus the upscaling remains problematic. In contrast, the most pressing issue of topological matter is the removal of trivial bulk influences to access the features arising from topology, which are particularly enticing when superconducting pairing is imposed. Two particular examples are studied in this work, namely supramolecular carbon nanotube systems and proximity-induced superconductivity in SnTe topological crystalline insulator.

In order to provide a naturally suited carrier for the localization, detection and manipulation of molecular spin systems, a fabrication technique for high-quality carbon nanotube devices, controllable by multiple local gate electrodes in order to enable local control of molecular hybrid systems, was developed. With these devices we demonstrated the required functionality by means of a double quantum dot configuration, tunable from p- to n-type characteristics. We can realize different coupling scenarios, from one strongly coupled large dot over weakly coupled double dots to almost total pinch-off, by inducing pn-barriers via the local gates. The segments created in this way can be stabily controlled over the entire device length and should hence provide a suitable backbone to study molecular physics.
So far, realization of such a supramolecular device is still lacking, which is explained by the very low yield of non-optimized molecule deposition techniques onto suspended carbon nanotube devices. The urgent requirement of in situ deposition is thus emphasized, which will presumably be realized with the continuation of this project at the KIT.

Thin film devices based on SnTe were fabricated and structurally and electrically characterized, indicating the presence of topological surface states in weak antilocalization measurements, but dominated by bulk shunting. To serve as platform for the investigation of possible unconventional Cooper pairing related to the non-trivial topology, fully functional Josephson junctions and SQUID devices were realized, for which superconducting pairing is induced by proximity to deposited superconducting layers. Strikingly, in-plane

magnetic field measurements give rise to the manifestation of φ_0-SQUIDs with tunable $0-\pi$-transitions. We discuss these features in the context of thin film characteristics, topology and spin-orbit physics.
While additional investigation and explanation of the coupling mechanisms at hand are required, the observed modulations provide first evidence for possible transitions from trivial superconductivity to unconventional coupling regimes in SnTe, which identifies the material class as a promising candidate for further research in the (highly interconnected) fields of topological superconductivity and spin-orbit physics.

Introduction and Summary

A crucial part of the microelectronic revolution of the 20th century is based on the integration of magnetism effects, or more fundamentally spins, which established the field of spintronics. Its concepts are already at the foundation of data storage applications of modern computer technology, like hard drives or MRAM.
With the interconnected advance of nanofabrication techniques, rise of novel materials like graphene and topological matter and understanding of (coupled) quantum effects in solid state physics, spintronics is still quickly emerging and many concepts just come into the range of conceivability. At this stage, there is thus a widespread scientifical interest in hybrid quantum systems, where the interplay between (gapped) band structures and spin could be exploited for future implementation in revolutionizing spintroncis concepts. In this context, the challenge of research is to create a fundamental knowledge of these systems and concepts and to filter and improve upon the existing basis in order to transition to a status of feasibility. Two of these concepts are investigated in the scope of this work.

One of the most intriguing subfields within this presented area of research is molecular spintronics, which could bring forth a modular and scalable building system for nanoscale spintronics applications, owing to perfect reproducibility and possible tailoring of electronic and magnetic properties via chemical synthesis. A particularly promising example are single-molecule magnets, which have already successfully shown to be suitable for spin valve or spin qubit operations.
One of the biggest challenges of the field is the integration of these nanometer-sized objects in complex circuits in order to allow for detection and manipulation of moleculear spin states, of both electronic and nuclear type. While several techniques have been proposed and investigated, ranging from conductive surface and scanning tunneling microscope tips over metallic break junctions to electromigrated metal junctions, a particularly compelling possibility is the coupling of molecules to sp^2-type carbon nanostructures to create predominantly organic supramolecular objects of low intrinsic disorder.
As shown in recent years by the NanoSpin group, carbon nanotubes (CNTs) can serve as such type of carrier for the single-molecule magnets, combining features of both constituents. By this means, the extraordinary transport characteristics of the CNT can be exploited, for instance high mobilities or stable and highly tunable charge states in quantum dot configurations, owing to inherent band gaps, without impairment or loss of the molecule's magnetic properties. The extension to multi-dot devices, with the controllable double dot as examplary embodiment, should then give way to possible investigation of coupling effects of these hybdrid systems and ultimately contribute to the exploration of possible upscaling.

A corner stone of this thesis project was hence the development of a dependable fabrication technique for high-quality CNT devices, controllable by multiple local gate electrodes in order to enable local control of molecular hybrid systems. Such approaches are usually very delicate by themselves, owing to the limited compatibility of CNT growth conditions and fabrication of complex nanoscale circuitry. Accordingly, the first six months were spent on a two-chip stamping approach, the nowadays predominant technique to counter these problematics, and the continuation of a process developed by a former group member. With no outlook of feasibility at sufficient yield in our facilities, this approach was put aside in 2015.
Subsequently, a process based on conventional one-chip fabrication was developed from scratch, for which optimization of sample design, lithography and deposition techniques as well as material choices had to be carefully incorporated, in order to accomodate the restrictions imposed by the CNT growth conditions on the prevention of leakage currents. Furthermore, the quality of the growth itself had to be maintained for the duration of this project, dictated by the circumstance of no other users or technical responsable of the CVD setup being present, by this creating the requirement of continuous balancing of technical integrity of the machine and outcome of the growth verified by characterization techniques.
As early tries, based on simplified designs of only 3 local gates and non-suspended devices, verified the feasibility of leakage-free gate control, the approach was subsequently refined to support a maximum of 5 gates and (at least partially) suspendend nanotubes. In 2017, we first succeeded in producing clean CNT devices, which could support a double dot configuration, tunable from p- to n-type characteristics. In these devices we can realize different coupling scenarios, from one strongly coupled large dot over weakly coupled double dots to almost total pinch-off, by inducing pn-barriers via the local gates. The segments created in this way can be stabily controlled over the entire device length and should hence provide a suitable backbone to study molecular physics.
So far, realization of such a supramolecular device is still lacking, which is explained by the very low yield of non-optimized molecule deposition techniques onto suspended carbon nanotube devices (and ongoing downtimes of the required facilities for nanotube samples). The urgent requirement of in situ deposition is thus emphasized, which will presumably be realized with the continuation of this project at the KIT.

Topological matter constitutes a second very enticing platform to investigate both fundamental principles as well as possible applications from spintronics to quantum computation. While often categorized by the colloquially denominated *topological insulator* as prime example, the class of topological matter actually comprises various different realizations, ranging from quasi-1D nanowires over 2D quantum spin Hall insulators to 3D material systems. Fundamentally, many of their properties derive from strong spin-orbit physics, ultimately leading to peculiar properties like highly transmittive edge and surface channels and locking of the charge carrier's spin to its momentum.
While topological matter is therefore also in the focus of research to realize more *conventional* concepts, for instance spin-orbit torques, a fundamental interest is based on the

interplay of topology and superconductivity. Soon after first experimental realizations, suggestions were made about the possibility of an unconventional type of superconductivity hosted at the interface between topological matter and conventional superconductors, by this circumventing the limitations of highly desired materials which intrinsically exhibit such coupling. Possible implications of such systems include Cooper pairing with finite momentum, a state closely related to the initially proposed FFLO phase, which allows for maintained superconducting properties beyond critical magnetic fields. Another intriguing proposal is the one of topological quantum computing, based on peculiar excitations, called Majorana bound states, which can naturally arise at these interfaces.

Material science of topological materials is still in its infancy and hence realization of such systems to date. This is why a multitude of possible candidates are actively investigated. Topological crystalline insulators, with tin telluride (SnTe) as a prime example, represent a new state of matter within this zoo of 3D topological materials, in which the electronic properties are governed by crystal rather than time-reversal symmetry.

This thesis project aimed to participate in the investigation of signs of unconventional superconductivity in SnTe. It was conducted in collaboration with the university of Bielefeld, Germany, with further support of the KIT, Germany. Sample preparation and characterization was done in Bielefeld, while low-temperature measurements were performed at the Néel Institute in Grenoble.

In the scope of this thesis, devices based on sputtered SnTe thin films were investigated. Transport experiments on bare films in Hall bar geometries revealed predominantly metallic behaviour. Nevertheless, weak anti-localization measurements indicated the presence of topological surface states, which are however strongly shunted by the bulk.

Superconducting hybrid devices, realized as both Josephson junctions and SQUIDs, were successfully established, based on the principle of proximity-induced coupling. A surprisingly strong coupling of SnTe to Ta superconductor was found and dependencies of superconductivity on sample geometries, temperature and magnetic field were investigated. The current-phase relation of SnTe/Ta was analyzed in the limit of strong kinetic effects. Electrostatic gating and rf exposure was explored, but predominant physics in such configurations turned out to be of purely conventional type, pointing out the importance of improvements on the material side.

Strikingly, in-plane magnetic field measurements gave rise to the manifestation of φ_0-SQUIDs with tunable $0 - \pi$-transitions, providing evidence for possible controlled transitions from trivial superconductivity to unconventional coupling regimes in SnTe, which identifies the material class as a promising candidate for further research in the field of topological superconductivity.

Introduction et Résumé

Une partie cruciale de la révolution microélectronique du XXe siècle repose sur l'intégration des effets de magnétisme, ou plus fondamentalement des spins, qui ont établi le champ de la spintronique. Ses concepts sont déjà à la base des applications de stockage de données de la technologie informatique moderne, comme les disques durs ou la MRAM.
Avec l'avancée interconnectée des techniques de nanofabrication, l'émergence de nouveaux matériaux comme le graphène et la matière topologique et la compréhension des effets quantiques (couplés) en physique du solide, la spintronique émerge rapidement et de nombreux concepts viennent à la portée d'imagination. À ce stade, il y a donc un intérêt scientifique répandu dans les systèmes quantiques hybrides, où l'interaction entre les structures de bande (gapped) et le spin pourrait être exploitée pour une mise en oeuvre future en révolutionnant les concepts spintroniques. Dans ce contexte, le défi de la recherche est de créer une connaissance fondamentale des systèmes et concepts et de filtrer et améliorer la base existante afin de passer à un état de faisabilité. Deux de ces concepts sont étudiés dans le cadre de ce travail.

L'électronique moléculaire est l'un des domaines les plus intrigants de la recherche moderne. Ce domaine pourrait produire un système de construction modulaire et évolutif pour des applications spintroniques à l'échelle nanométrique, grâce à une reproductibilité parfaite et une adaptation possible des propriétés électroniques et magnétiques. Un exemple particulièrement prometteur est celui des aimants à une seule molécule, qui se sont déjà avérés être appropriés pour la réalisation de spin valve et de qubit de spin. L'un des plus grands défis du domaine est l'intégration de ces objets de taille nanométrique dans des circuits complexes afin de permettre la détection et la manipulation d'états de spin moléculaires, de type électronique et nucléaire. Alors que plusieurs techniques ont été proposées et étudiées, s'étendant des surfaces conductrices à l'intégration au bout de de la pointe d'un microscope à effet tunnel, en passant par des jonctions à cassure métalliques ou de nano-gap métallique réalisé par électro-migration, une possibilité particulièrement intéressante est le couplage des molécules à des nanostructures de carbone de type sp^2 pour créer des objets supramoléculaires à prédominance organique de faible désordre intrinsèque.
Comme l'ont montré ces dernières années le groupe NanoSpin, les nanotubes de carbone (CNTs) peuvent servir de support pour les aimants à une seule molécule, en combinant les caractéristiques des deux constituants. Par ce moyen, les caractéristiques de transport extraordinaires du CNT peuvent être exploitées, par exemple des mobilités élevées ou des états de charge stables et hautement accordables dans des configurations de boites quantiques, sans dégradation ou perte des propriétés magnétiques de la molécule. L'extension à des dispositifs multi-boite quantique, avec la double boite contrôlable comme mode de

réalisation exemplaire, devrait alors laisser la place à une étude possible des effets de couplage de ces systèmes hybrides et contribuer finalement à l'exploration d'une mise à l'échelle possible.
Une pierre angulaire de ce projet de thèse a donc été le développement d'une technique de fabrication fiable pour des dispositifs de CNTs de haute qualité, contrôlables par de multiples électrodes de grille locales afin de permettre le contrôle local des systèmes hybrides moléculaires. De telles approches sont généralement très délicates en elles-mêmes, en raison de la compatibilité limitée des conditions de croissance des CNTs et de la fabrication de circuits nanométriques complexes. En conséquence, les six premiers mois ont été consacrés à une approche d'estampage à deux substrats, la technique prédominante de nos jours pour contrer ces problématiques, qui fut la poursuite d'un processus développé par un ancien membre du groupe. Sans perspective de faisabilité à rendement suffisant dans nos installations, cette approche a été mise de côté en 2015.
Par la suite, un procédé basé sur la fabrication conventionnelle à un substrat a été développé à partir de zéro, pour lequel l'optimisation de la conception des échantillons, les techniques de lithographie et de dépôt ainsi que les choix de matériaux ont dû être soigneusement incorporés afin de respecter les restrictions imposées par les conditions de croissance.
En outre, la qualité de la croissance des nanotubes elle-même a dû être maintenue pendant toute la durée de ce projet, dictée par le fait qu'aucun autre utilisateur ou technicien responsable de la configuration CVD n'était présent, ce qui a créé léxigence d'un équilibre continu de l'intégrité technique de la machine et le résultat de la croissance vérifiés par des techniques de caractérisation.
Comme les premiers essais, basés sur des conceptions simplifiées de seulement 3 grilles locales et CNTs non suspendus, ont vérifié la faisabilité d'un contrôle de grille sans fuite, l'approche a été affinée pour combiner un maximum de 5 grilles et des nanotubes (au moins partiellement) suspendus. En 2017, nous avons d'abord réussi à produire des échantillons CNT propres, permettant de mettre en évidence une configuration à double boite quantique, tout en ajustant des caractéristiques de type p à n. Pour ces échantillons, nous pouvons réaliser différents scénarios de couplage, d'une grande boite couplé fortement sur des doubles boites faiblement couplées à un étranglement presque total, en induisant des barrières pn via les grilles locales. Les segments créés de cette manière peuvent être contrôlés de manière stable sur toute la longueur du dispositif et devraient donc constituer une base appropriée pour l'étude de la physique moléculaire.
Jusqu'à présent, la réalisation d'un tel échantillon supramoléculaire fait encore défaut, ce qui s'explique par le très faible rendement des techniques de dépôt de molécules non optimisées sur des dispositifs à nanotubes de carbone en suspension. L'exigence urgente de dépôt in situ est ainsi soulignée, ce qui sera vraisemblablement réalisé avec la poursuite de ce projet au KIT.

La matière topologique non triviale constitue une deuxième plate-forme séduisante pour étudier à la fois les principes fondamentaux et les applications possibles de la spintronique au calcul quantique. Bien que souvent classé comme isolant topologique

familièrement dénommé comme exemple principal, la classe de la matière topologique comprend en fait différents systèmes, allant des nanofils quasi-1D aux isolateurs de Hall à spin quantique 2D aux matériaux 3D. Fondamentalement, beaucoup de leurs propriétés proviennent d'un fort couplage spin orbite, conduisant à des propriétés particulières comme des bords et surfaces hautement transmissibles et le verrouillage du spin du porteur de charge à son sens de mouvement.
Alors que la matière topologique est également au centre de la recherche pour réaliser des concepts plus conventionnels, par exemple des effets de torque spin orbite, un intérêt fondamental est basé sur l'interaction de la topologie et de la supraconductivité. Peu de temps après les premières réalisations expérimentales, des suggestions ont été faites sur la possibilité d'un type de supraconductivité non conventionnelle hébergé à l'interface entre la matière topologique et les supraconducteurs classiques, en contournant les limites des matériaux désirés qui présentent intrinsèquement un tel couplage.
Les implications possibles de ces systèmes comprennent l'appariement de Cooper avec une quantité de mouvement finie, un état étroitement lié à la phase FFLO initialement proposée, qui permet de maintenir les propriétés supraconductrices au-delè des champs magnétiques critiques. Une autre proposition intrigante est celle de l'ordinateur quantique topologique, basé sur des excitations particulières, appelé quasi-particule Majorana, qui peut naturellement se localiser à ces interfaces.
La science des matériaux topologiques, et donc la réalisation de tels systèmes, en est encore à ses débuts à ce jour. C'est pourquoi une multitude de candidats possibles est activement étudiée. Les isolants cristallins topologiques, avec tellurure d'étain (SnTe) comme exemple principal, représentent un nouvel état au sein de ce zoo des matériaux topologiques 3D, dans lequel les propriétés électroniques sont régies par des états de surface de Dirac protégés par une symétrie de miroir.
Ce projet de thèse visait à participer à l'enquête sur les signes de supraconductivité non conventionnelle dans SnTe. Il a été mené en collaboration avec l'université de Bielefeld, Allemagne, avec un soutien supplémentaire du KIT, Allemagne. La préparation des échantillons et la caractérisation a été faite à Bielefeld, tandis que les mesures à basse température ont été réalisée à l'Institut Néel à Grenoble.
Dans le cadre de cette thèse, des dispositifs basés sur des couches minces de SnTe, déposées par pulvérisation, ont été étudiés. Les expériences de transport sur des couches pures dans les géométries de la barre de Hall ont révélé principalement un comportement métallique. Néanmoins, des mesures d'anti-localisation faible ont indiqué la présence d'états de surface topologiques, qui sont cependant fortement shuntés par le bulk.
Des dispositifs hybrides supraconducteurs, réalisés à la fois comme jonctions Josephson et SQUID, ont été établis avec succès, basé sur le principe du couplage induit par proximité. Un couplage étonnamment fort de SnTe au supraconducteur Ta a été trouvé et dépendances de la supraconductivité sur les géométries des échantillons, la température et le champ magnétique ont été étudiées. La relation courant-phase de SnTe/Ta a été analysée dans la limite d'effets cinétiques forts. Le couplage électrostatique et l'exposition à des micro-ondes ont été explorés, mais la physique prédominante dans de telles configurations s'est avéré être de type purement conventionnel, soulignant l'importance des améliorations

sur le côté matériaux.
De manière frappante, les mesures de champ magnétique dans le plan ont donné lieu à la signature d'un φ_0-SQUID avec des transitions $0 - \pi$ accordables, fournissant des preuves de possibles de transitions contrôlées de la supraconductivité triviale aux régimes de couplage non conventionnels dans SnTe, qui identifie la classe matérielle comme un candidat prometteur pour d'autres recherches dans le domaine de la supraconductivité topologique.

Contents

Part I

Theoretical Introduction

1 Single-Molecule Magnets

1.1 Introduction to Molecular Spintronics

1.1.1 From Macroscopic to Molecular Spintronics

Two of the most significant discoveries in the field of condensed matter physics are the magnetoresistive effects of *tunnel magnetoresistance*[1] (TMR) and *giant magnetoresistance*[2] [3] (GMR), which gave rise to the control of spin currents and thus the development of the field of macroscopic spintronics, which originally shaped the modern computer industry. While the progress on the technological side has pushed the spatial dimensions into to the nanometer-scale and material science has enabled vast improvements of device performance, the underlying concepts are still close to the original ones.

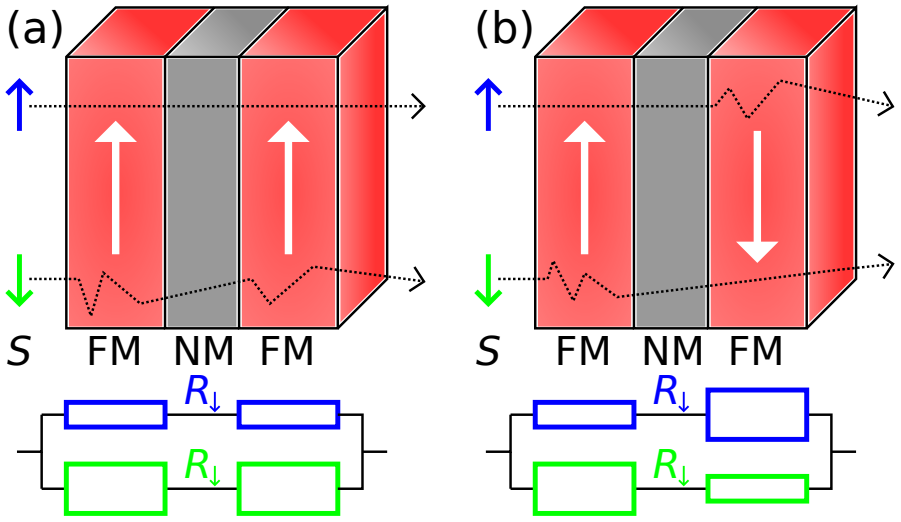

Figure 1.1: Giant magnetoresistance effect in ferromagnetic heterostructures, where two magnetic layers are spaced by a normal layer and independently switchable. The device is referred to as *spin valve* and resistances are represented by the size of the rectangles in the lower panels. a) For parallel magnetization of the layers only the transport of one spin type, here ($\downarrow$), is highly resistive due to scattering, while a low-resistive channel for ($\uparrow$) is created. The overall resistance is hence in the low configuration. b) For antiparallel alignment both spin types are repeatedly scattered, giving rise to an overall highly resistive configuration.

The GMR expresses itself as dependence of the resistance on the relative magnetization of ferromagnetic heterostructures, as illustratively explained in fig. 1.1 for a device of two such layers. For parallel alignment of the ferromagnetic layers, charge carriers of respective spin direction see a relatively small resistance due to reduced scattering events,

creating a transport channel with small resistance which also renders the total resistance of the device as small. Upon aligning the layers in an antiparallel configuration, both spin types are now subject to scattering and the total device resistance is large.
Akin to the GMR, the TMR gives rise to two states with different resistance, depending on the magnetization of the two ferromagnetic layers embedding the normal region. In contrast to the GMR, this normal region is a thin insulating barrier and transport is governed by tunneling.
Following the suggestion of Datta[4], spin currents provide the basis for many concepts. Means to efficiently polarize charge carriers have been established with the spin transfer torque[5] or spin-orbit torque[6], but intrinsic interactions in commonly used materials, for example hyperfine coupling to nuclear spins or spin-orbit coupling itself, usually still limit spin relaxations times.
A particularly interesting and new field to realize such kind of physics is the one of organic spintronics, where materials exhibit extraordinarily long spin relaxation times[7]. More specifically the field of (organic) molecular spintronics is on the rise, as it combines long spin relaxation times with very high reproducibility and possible engineering of magnetic properties[8] [9]. This is because the collective modes of macroscopic magnetization are replaced by the interactions of few spins at this scale, bringing quantum effects to the fore.

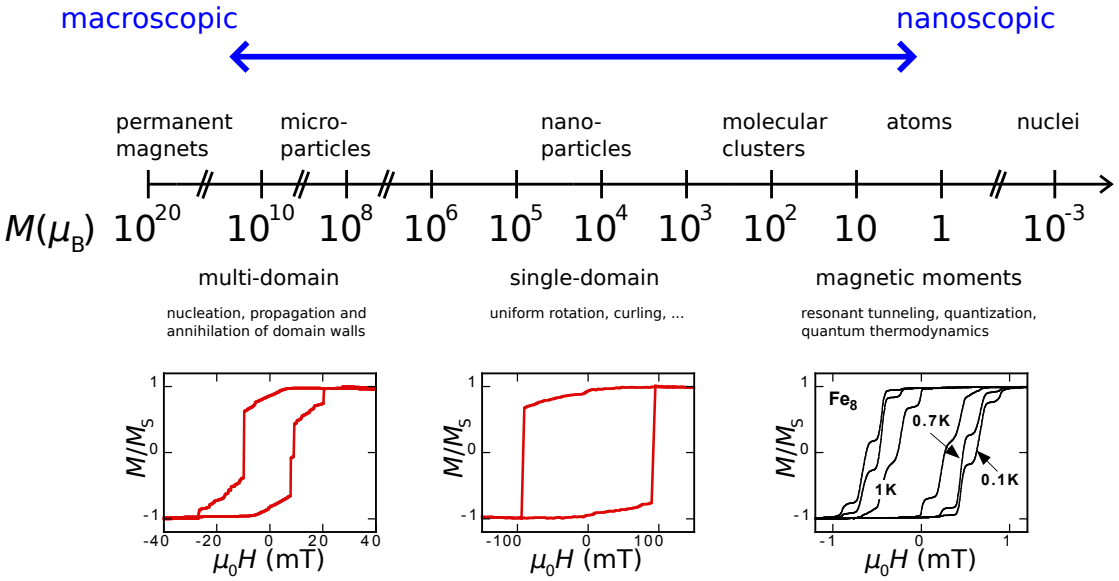

Figure 1.2: The transition from macroscopic to nanoscopic magnetism. At macroscopic scales magnetic domains separated by domain walls determine the behaviour via nucleation, propagation and annihilation. At mesoscopic scales the magnetization is in a single-domain state, reversing by uniform or non-uniform modes. At nanoscopic scales, for example molecular magnets, only few spins determine the reversal via quantum tunneling.
Adapted and modified from[9]

1.1.2 Single-Molecule Magnets

In 1980 Lis[10] reported on the synthesis of Mn_{12}-based molecules, suggesting interesting magnetic properties related to a strong *Jahn-Teller effect*. A few years later, Mn_{12}-acetate, a single-crystalline ensemble of identical molecular clusters, was investigated as first instance of single-domain magnets of a new class, the *single-molecule magnets* (SMM). Fabricated in a bottom-up approach via chemical synthesis, they ensure perfect reproducibility and possible tailoring of electronic and magnetic properties.
Typically consisting of a magnetic core of one or several metal ions and surrounding organic ligand shells, SMMs show a variety of magnetic effects[9], for example quantum tunneling of magnetization[11][12] and quantum coherence effects[13], making them extremely promising for applications in spintronics or as a possible spin qubit for quantum computing[8]. The interplay of the SMMs structural components results in *superparamagnetic* behavior and magnetic hysteresis arising from an anisotropy on the molecular scale[14][15][16]. The ligands promote a large single-spin ground state, for instance $S = 10$ in the case of Mn_{12}, which is only weakly coupled to the environment and therefore has very long spin relaxation times below the blocking temperature. It is thus possible to couple SMMs to quantum conductors like carbon nanotubes without losing their magnetic properties[1]. This coupling can be further optimized by modifications of the molecules' organic shells.

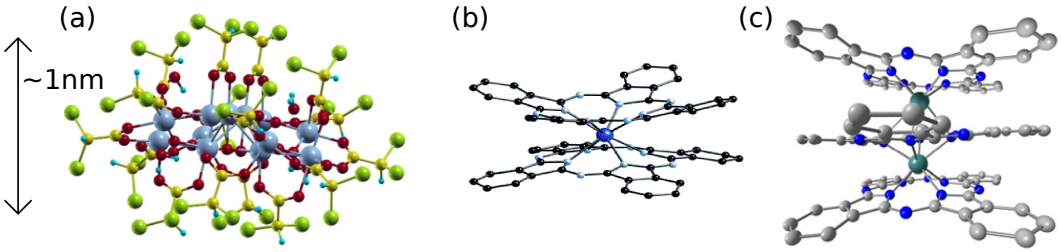

Figure 1.3: Examples of single-molecule magnets: a) $[Mn_{12}0_{12}COOR_{16}](H_2O)$ b) terbium double-decker $TbPc_2$ c) terbium triple-decker $(A_2B)_3\,PcTb_2$
Adapted from a)[17] b)[18] c)[19]

Ten years after the first experiments on Mn_{12}, single-nuclear SMMs came into the focus of research[20][21]. These molecules are typically based on a centered lanthanide ion surrounded by non-magnetic ligands like phthalocyanine groups (Pc). In contrast to the spin ensembles of Mn_{12}, the total angular momentum of these molecules consists of a spin S and an orbital momentum L of the single lanthanide ions, hence resulting in slightly different relaxation principles and eventually in higher blocking temperatures. One particular example within the group of single-nuclear SMMs is the terbium double-decker $TbPc_2$, which serves as a basic building block for this work and is therefore described in more detail in section 1.3. These molecules can also be synthesized as higher stacks, forming for instance triple-deckers with two magnetic cores.

1 However, a thorough treatment needs to take behaviour upon deformation into account, rendering Mn_{12} not very suitable for grafting on surfaces. This problem does not persist for other cases like the subsequently introduced single-nuclear SMMs.

But first the concepts of spin relaxation in SMMs are introduced. *Molecular Magnets*[12] by Bartolomé and coauthors is recommended to the interested reader for this topic.

1.2 Spin Relaxation in Single-Molecule Magnets

1.2.1 Mechanisms of Spin Relaxation

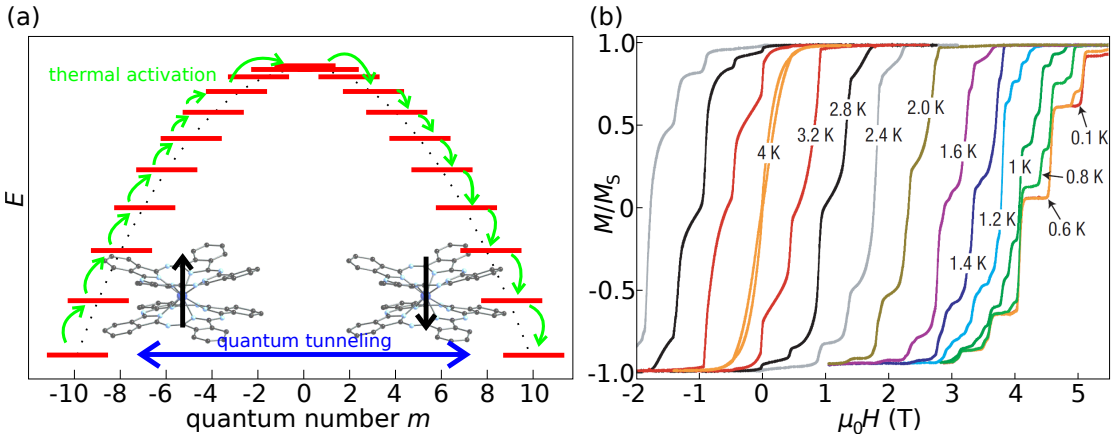

Figure 1.4: a) Schematic energy barrier of a $S = 10$ molecule (e.g. the Mn_{12}-acetate SMMs). Reversal of magnetization can occur either via quantum tunneling through the barrier or via thermal activation involving multiple phonon absorption and emission processes. b) Magnetization hysteresis loops of single crystals of $Mn_{12} - t$BuAc SMMs at different temperatures. At low temperatures thermally activated processes are reduced and steps, which can be assigned to quantum tunneling, become visible.
a) Based on[8], molecule from[18] b) Adapted from[22]

Single-domain magnetic particles like SMMs have two equivalent energy minima corresponding to opposite directions of the magnetic moment and separated by an energy barrier. This situation is referred to as magnetic bistability[14]. Generally the barrier is a result of anisotropy effects and its height depends on the particle size. Thermally activated reversals of magnetization over the barrier are typically phonon-assisted and follow an exponential Arrhenius law[12],

$$\Gamma_U \propto \exp\left(-\frac{U}{k_B T}\right), \tag{1.1}$$

with Γ_U being the thermal decay rate over the barrier of height U. At high temperatures spin flip processes occur fast and the overall magnetization averages to zero over long measuring times, leading to a superparamagnetic state. For low temperatures and small or zero magnetic fields phonon-assisted relaxation is very unlikely due to small lifetimes of excited states and vanishing phonon excitations in the system. As a result, relaxation times of SMMs are extraordinarily long, often reaching several years[16] below 2 K. For larger magnetic fields direct phonon processes can become an effective mechanism to reverse the magnetization.

However, it has been found that even for the conditions of low temperature and small field non-thermally activated changes of magnetization are possible, stemming from relaxation of the molecule's magnetic moment via tunneling through the anisotropy barrier [11] [23] [24]. This resonant process is called *quantum tunneling of magnetization* (QTM).
The spin relaxation process in SMMs is related to a large change of magnetic moment, which has to be absorbed by the system. However, angular momentum conservation is often taken for granted and therefore disregarded. This is a valid approach for the common case of macroscopic crystalline assemblies of molecules, which provide a bath of possible lattice excitations. On the molecular scale conservation laws cannot be neglected and a specific case has to be made for different types of systems, including the accessible bath. This is addressed in section 1.2.4 in a rather general way and ultimately results in practical restrictions for spin relaxation processes in SMM devices based on carbon nanotubes.

1.2.2 Quantum Tunneling of Magnetization

The easiest model to describe QTM in the presented double well system is a Hamiltonian containing a single *giant spin* **S** under an external magnetic field **H** which shifts the energy of the potential wells [12],

$$\mathcal{H} = -DS_z^2 - E\left(S_x^2 - S_y^2\right) - g\mu_\mathrm{B}\mu_0\mathbf{SH}, \tag{1.2}$$

with the spatial spin components S_i and the anisotropy constants D in z-direction and E in transversal direction. $D \gg E$ usually holds in SMMs, resulting in a magnetic *easy axis* in z-direction. The energy barrier or zero-field splitting $U = DS_z^2$ is hence given by the first term of eq. 1.2 and the Zeeman energy by the field-dependent one. Supposing spin quantization in z-direction with quantum number m and a field along the easy axis, $H = H_z$, $\mathcal{H}$ can be rewritten as:

$$\mathcal{H} = -Dm^2 - g\mu_\mathrm{B}\mu_0 m H_z. \tag{1.3}$$

In the case of Mn_{12} with its $S = 10$ ground state, the quantization leads to 21 energy levels. Tunneling between two levels m and m' is exclusively possible under resonance conditions, corresponding to discrete values of the applied magnetic field:

$$H_z = -\left(m + m'\right)\frac{D}{g\mu_\mathrm{B}\mu_0}. \tag{1.4}$$

A more in-depth analysis has to include level broadening, since quantum mechanics allows tunneling for finite overlap of the two corresponding wave functions. This overlap is created by the small transverse perturbation component in eq. 1.2. Under resonant field conditions this contribution leads to the formation of avoided level crossings, separated

by a *tunnel splitting* Δ, where resonant quantum tunneling can occur.
Tunneling rates Γ strongly depend on the levels under consideration, with transitions between m,$m' = \pm S$ being less likely due to small tunnel splittings. These rates can be examined at different levels of complexity. The easiest approach is to neglect dynamics and environmental effects and assume $\Gamma \propto \Delta^2/G$ with the homogeneous broadening G. Taking dynamics (the timescale of interaction) into account leads to the well-known and widely used *Landau-Zener* model[25] with a transition probability given by:

$$P_{\mathrm{LZ}}(m,m') = 1 - \exp\left(-\frac{\pi}{2\hbar g \mu_{\mathrm{B}} \mu_0 |m - m'|} \frac{\Delta_{m,m'}}{dH_{\parallel}/dt}\right). \tag{1.5}$$

Tunneling transitions can be induced by sweeping the magnetic field $H_{\parallel}$ over the avoided level crossing. Here, it has to be pointed out that the external magnetic field was introduced in eq. 1.2 under the assumption of the molecule's magnetic easy axis aligning with H_z of a cartesian coordinate system. In real devices the orientation of the molecules within this coordinate system is generally arbitrary, dependent on the deposition process or the installation of the measurement setup. It is therefore more convenient to use the notion of longitudinal fields $H_{\parallel}$, pointing in direction of the molecule's easy axis, and transversal fields $H_{\perp}$ perpendicular to this axis. The latter is commonly denoted as *hard axis*. The tunneling probability exponentially decreases with increasing sweep rate of the magnetic field or decreasing tunnel splitting.

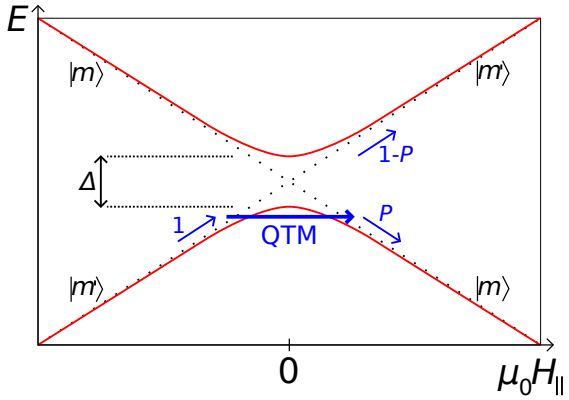

Figure 1.5: Schematic illustration of a magnetization tunneling event at an avoided level crossing Δ. The probability P of such an event can be calculated with the Landau-Zener model.

The environment adds homogeneous and inhomogeneous broadening arising from nuclear spins[26] [27], dipole fields[28] or phonons[29] with the latter generally having the smallest impact at low temperatures and small magnetic fields. As it has been mentioned before, a crucial contribution of the environment is the absorption of finite amounts of angular momentum and energy to enable tunneling after all.

1.2.3 Spin-Lattice Relaxation

Thermal activation involving subsequent phonon absorptions becomes unlikely at low temperatures. The most efficient mechanism for spin relaxation is therefore the *direct process*, a transition via the emission of a single phonon. For slightly higher temperatures two-phonon relaxation like the *Orbach process* or the *Raman process* can come to the fore.

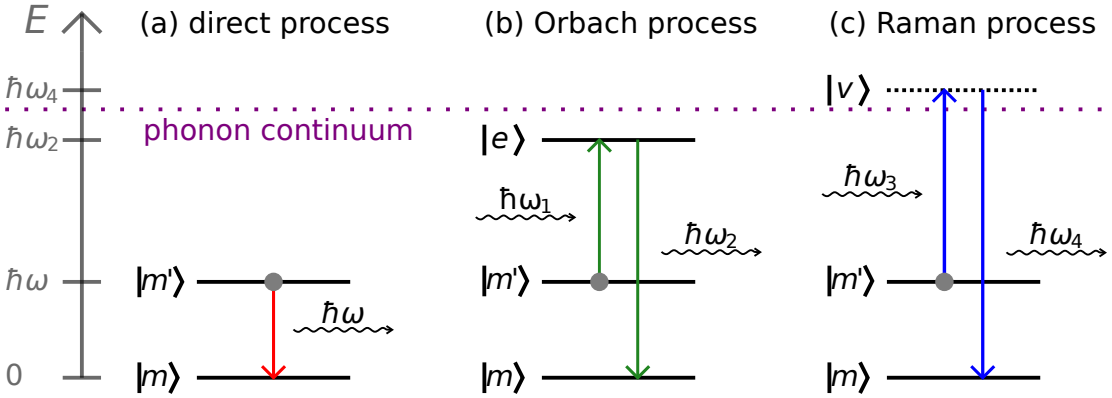

Figure 1.6: Three different phonon-assisted magnetization reversal processes. a) The direct process: A single phonon $\hbar\omega$ is emitted to enable the relaxation into the ground state. b) The Orbach process: Excitation via absorption of a phonon $\hbar\omega_1$ is followed by an emission $\hbar\omega_2$. c) The Raman process: Absorption of a phonon $\hbar\omega_3$ leads to the excitation into a virtual state. Subsequent relaxation is enabled by the emission of a phonon $\hbar\omega_2$.

The transition probabilities for the two-level system depicted in fig. 1.6a follow from Fermi's Golden Rule as[30]

$$w_{m\to m'} = \frac{2\pi}{\hbar} |\langle m|\,\mathcal{H}'\,|m'\rangle|^2 D(E) f_{BE}(E)\delta(E=\hbar\omega), \tag{1.6}$$

$$w_{m'\to m} = \frac{2\pi}{\hbar} |\langle m|\,\mathcal{H}'\,|m'\rangle|^2 D(E)\,(f_{BE}(E)+1)\,\delta(E=\hbar\omega), \tag{1.7}$$

with $w_{m\to m'}$ being the excitation via phonon absorption and $w_{m'\to m}$ the transition to the ground state due to phonon emission. The relaxation rate, defined as the inverse of the relaxation time τ, is given as the sum of the individual probabilities. Implying a Debye density of states $D(E) \propto E^2$ results in[30]:

$$\frac{1}{\tau} \propto |\langle m|\,\mathcal{H}'\,|m'\rangle|^2\,(\hbar\omega)^3 \coth\left(\frac{\hbar\omega}{2k_\mathrm{B}T}\right). \tag{1.8}$$

Early studies have shown that the underlying mechanism is a modulation of the crystal electric field or ligand field through ion motion under the action of lattice vibrations, leading to a fluctuating electric field. While the static field essentially splits the orbital

states of magnetic ions in a SMM (presented in a more detailed manner for the case of the terbium double-decker SMM in section 1.3), the dynamic contribution can excite transitions between those levels. This problem was initially tackled [31] with an expansion of the crystal (ligand) Hamiltonian $\mathcal{H}_{\mathrm{lf}}$ in powers of a mechanical strain ε,

$$\mathcal{H}_{\mathrm{lf}} = \mathcal{H}^0_{\mathrm{lf}} + \varepsilon\mathcal{H}^1_{\mathrm{lf}} + \varepsilon^2\mathcal{H}^2_{\mathrm{lf}} + ..., \tag{1.9}$$

where $\mathcal{H}^0_{\mathrm{lf}}$ represents the static contribution and $\mathcal{H}' = \varepsilon\mathcal{H}_{\mathrm{lf}}$ the first-order pertubation. Assuming degenerate levels at zero magnetic field[1] one can write $\hbar\omega = g\mu_{\mathrm{B}}H$ so that eq. 1.8 simplifies to

$$\frac{1}{\tau} \propto |\mathcal{H}^1_{\mathrm{lf}}|^2 H^3 \coth\left(\frac{g\mu_{\mathrm{B}}H}{2k_{\mathrm{B}}T}\right), \tag{1.10}$$

which explains the increasing impact of the direct process on relaxation at higher magnetic fields. Note the explicit dependence on the phonon density of states $D(E)$ in $\frac{1}{\tau}$, which is again a manifestation of the SMM's environment. Quantum systems, especially at lower dimensionality, can therefore have a substantially reduced transition probability.
This section is concluded by a brief description of the aforementioned two-phonon processes. In the Orbach process [32] the molecule is excited to a state $|e\rangle$ via the absorption of a phonon with energy $\hbar\omega_1$. Subsequently it can relax to the ground state via the emission of a second phonon $\hbar\omega_2$ as long as energy conservation $\omega = \omega_2 - \omega_1$ is granted. One can hence consider this process as an indirect relaxation from $|m'\rangle$ to $|m\rangle$ which may be faster than the direct transition, depending on the phonon density of states at higher energies. The relaxation rate follows as [30]:

$$\frac{1}{\tau} \propto |\mathcal{H}^1_{\mathrm{lf}}|^2 \left(\hbar\omega_2\right)^3 \frac{1}{\exp\left(\hbar\omega_2/k_{\mathrm{B}}T\right) - 1}. \tag{1.11}$$

The Raman process takes place via a virtual excited state $|v\rangle$ with an energy outside of the phonon continuum. Again energy conservation $\omega = \omega_4 - \omega_3$ is required and the relaxation rate can be written as [30]

$$\frac{1}{\tau} \propto |\mathcal{H}^2_{\mathrm{lf}}|^2 \left(\frac{k_{\mathrm{B}}T}{\hbar}\right)^7, \tag{1.12}$$

which depends on the second-order contribution $\mathcal{H}^2_{\mathrm{lf}}$.

1 Generally this does not hold, for example due to hyperfine effects.

1.2.4 Spin Relaxation and Conservation Laws

Transition to the molecular scale goes along with considerations concerning the involved mechanical degrees of freedom and how they are affected by the necessity of satisfying universally valid conservation laws. In this context one can distinguish the limiting cases of macroscopic magnetic objects on one side and single free molecules on the other side, in order to evaluate how the coupling of these single molecules to nanoscale carriers (for example carbon nanotubes) may affect relaxation processes. Eventually this problem results in a trade-off between decoupling of the molecule from its dissipative environment and the complete freezing of relaxation processes in the case of free molecules.
The classical macroscopic case of a magnetic rotator is described by the widely known *Einstein-de-Haas effect*[33]: A metallic rod is attached to a wire as a torsional rotator. Without an external magnetic field H the magnetic moments of the electrons are randomly orientated and the overall magnetization M is zero. Application of a magnetic field aligns the moments and momentum conservation requires a compensating mechanical angular momentum L directed opposite to M, leading to a rotation of the rod (see fig. 1.7a).

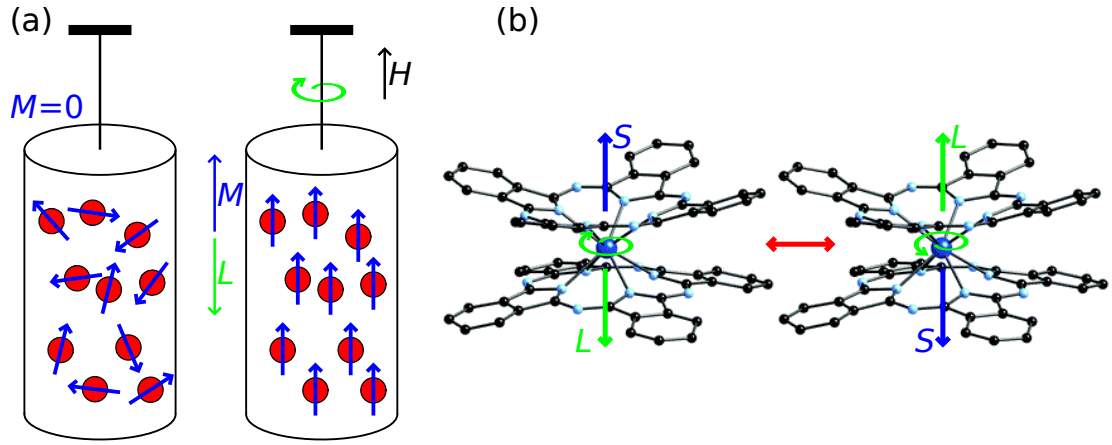

Figure 1.7: a) Einstein-de-Haas effect: the magnetic moments of electrons in a metallic rod are randomly orientated (left) and can be aligned with an external magnetic field. Angular momentum conservation creates a macroscopic rotation. b) A free magnetic molecule has to create a mechanical rotation L around its anisotropy axis in order to fulfill angular momentum conservation.
b) molecule from[18]

The same picture allows for a simple estimation of the requirements for spin tunneling processes in a free magnetic molecule[12]. Assuming the molecule as a rigid object one can define the rotational energy related to its moment of inertia I_z:

$$E_{\mathrm{rot}} = \frac{1}{2}\frac{L^2}{I_z}. \tag{1.13}$$

Tunneling at the anti-crossing between the spin states $\pm S$ lowers the energy of the system by $\Delta/2$ but in order to satisfy angular momentum conservation a mechanical rotation L

is created. This rotation comes at the cost of energy E_{rot}. It becomes directly clear that macroscopic bodies I_z are energetically not restricted, but molecules with tiny moments of inertia may be prevented totally from tunneling. The complete quantum mechanical treatment of this free particle problem is provided by O'Keeffe et al. [34].
An intensively studied case is the one introduced by Jaafar et al. [35] [36], a two-state macrospin, like a SMM, coupled to a torsional nano-resonator as depicted in fig. 1.8.

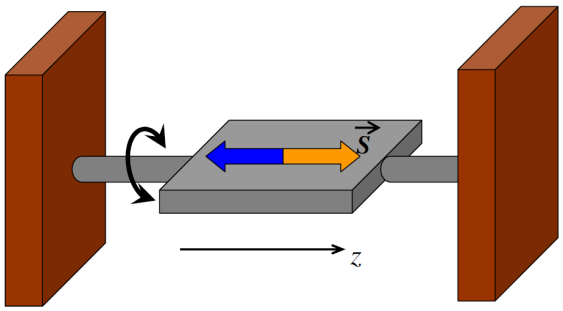

Figure 1.8: Two-state macrospin $\pm S$ coupled to a torsional resonator with spring constant k_{r}. Adapted from [37]

Calculations of this problem reveal that the coupling of the macrospin to the quantum state of the resonator leads to an interference of the spin tunneling paths which can completely suppress tunneling in the case of strong coupling. This coupling can be increased by lowering the moment of inertia I_z and the torsional stiffness of the resonator (or by increasing spin S) [38]. Hence a suppression of spin tunneling can be predicted for SMMs coupled to light mechanical resonators. Garanin et al. [37] calculated the renormalization of the two-state spin Hamiltonian[1] $\mathcal{H}_\sigma = \pm\Delta/2\sigma_x$ with $\sigma_x = |\Psi_{-S}\rangle\langle\Psi_S| + |\Psi_S\rangle\langle\Psi_{-S}|$. An effective tunnel splitting arises due to coupling of the macrospin to the torsional mechanical resonator:

$$\Delta \to \Delta_{\mathrm{eff}} = \Delta \exp\left(-\frac{\lambda^2}{2}\right) \quad \text{with} \quad \lambda^2 = \frac{2\hbar S^2}{\sqrt{k_{\mathrm{r}} I_z}}, \tag{1.14}$$

where k_{r} is the spring constant of the resonator. It follows that spin tunneling is suppressed for the case of coupling to a resonator with vanishingly small spring constant or coupling to a surface via a molecular leg, as it can be the case for SMMs attached to carbon nanotubes. Furthermore, decoherence effects [37] might occur for large parameters $\hbar\omega_r/\Delta$, but again the exact spectrum of the resonator $\hbar\omega_{\mathrm{r}}$ has to be taken into consideration.

1 $\mathcal{H}_\sigma$ explains the $\Delta/2$ energy argument made above [12]: A classical magnetic moment in the absence of spin tunneling is localied in the spin-up or spin-down state with an energy $\pm\Delta/2$. Delocalization of the spin due to tunneling therefore lowers the energy by $\Delta/2$.

1.3 Terbium Double-Decker Single-Molecule Magnet

This section is dedicated to the terbium double-decker SMM which has been primarily used for the preparation of this thesis. These molecules have been synthesized by Svetlana Klyatskaya and Mario Ruben at the Karlsruhe Institute of Technology in Germany.

1.3.1 Structural and Electronic Properties

The terbium double-decker molecule, for the sake of simplicity denoted as $TbPc_2$, consists of a single centered Tb^{3+} ion and two bisphthalocyaninato (Pc) ligands situated above and below the magnetic core[39]. These ligands preserve the magnetic properties of the SMM's magnetic core and enable the coupling to the environment which can be altered via modification of the ligand structure. Locally at the magnetic core, the ligand field interaction corresponds to a C_4 point group symmetry.

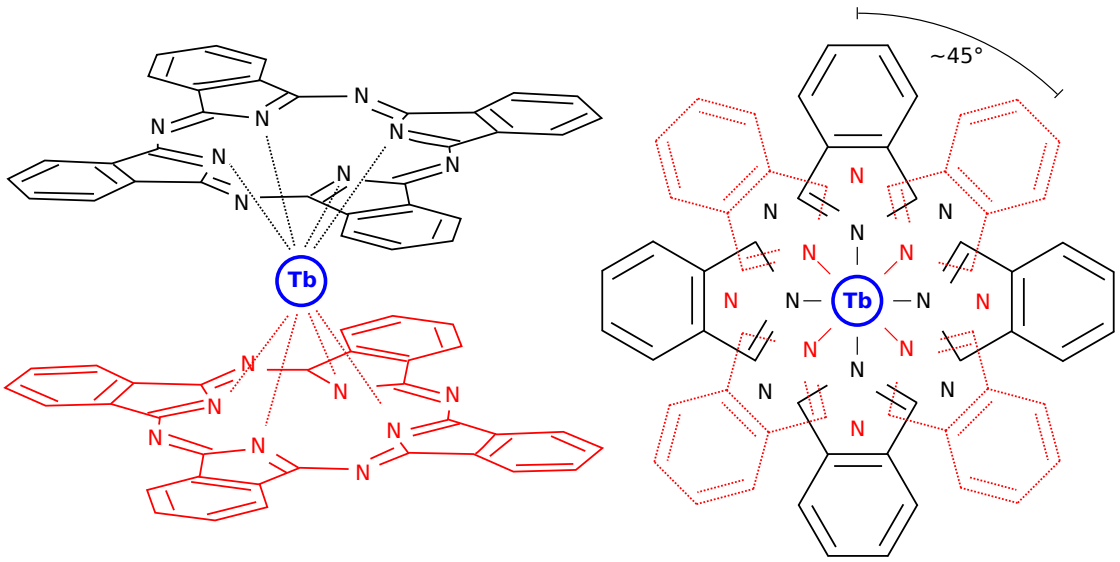

Figure 1.9: Left: The Tb^{3+} ion is embedded in two Pc ligands and coordinated by 8 nitrogen atoms. Right: Topview of the molecule and the xy-plane. The two ligands are mirror reflections of eachother, rotated around $\approx 45°$ in-plane.
a) Based on[20] b) Based on[39]

The electronic properties of $TbPc_2$ are mainly determined by the eight electrons in the 4f shells of the Tb^{3+} ion whose electronic configuration can be written as $[Xe]4f^8$. To derive the exact energy spectrum of Tb^{3+}, interactions have to be taken into account as well as the influence of the internal fields created by the ligands and externally applied magnetic fields.

Tb^{3+} Orbitals

The 4f shell filling of the Tb^{3+} follows from Hund's rules and their inherent assumptions for electron-electron interactions, giving rise to an orbital angular momentum $L = 3$ and a spin $S = 3$. The total angular momentum J hence couples to integer values in the range of $J = L - S = 0$ to $J = L + S = 6$. According to Hund's third rule for more-than-half shell filling, $J = 6$ is the ground state of this configuration, being $2J + 1 = 13$ times degenerated. Strong spin-orbit interactions, generally present in lanthanide ions, result in a large energy splitting in the order of $2900K$ between the $J = 6$ ground state and the first excited state $J = 5$, which has been stated both theoretically [40] and experimentally [41]. The orbital system can thus be strongly simplified for low temperatures, typically present in our experiments, and the discussion narrowed down to the degenerate ground state.

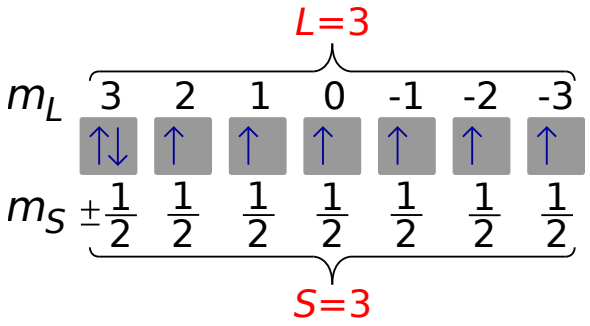

Figure 1.10: 4f shell filling of Tb^{3+}: the 8 electrons give rise to an orbital angular momentum $L = 3$ and a spin $S = 3$.

Ligand Field Splitting

Describing the ligand field contribution to the orbital energies has been a sustained challenge. In 1950 phenomenologic *Spin Hamiltonian* approaches were introduced, mainly based on the work of Abragam and Pryce [42]. Complexity arose from the coordinate system corresponding to the crystal symmetry. Later on it was found that the use of *operator equivalents* [43] can heavily simplify the calculation of crystal field matrix elements and thus the transformation of the Hamiltonian to a more suitable basis of the total angular momentum J [44] [45].

In more detail, these operator equivalents, linear combinations of the total angular momentum operators $\{J, J_z, J_\pm\}$ and commonly referred to as *Stevens operators* [43], make use of the well-documented transformation behaviour of tensor operators which can be expressed in spherical harmonics. Symmetry considerations can then be included rather easily for further simplification.

This is particularly interesting for lanthanide-based molecules because the placement of the 4f shells within the 5s and 5p orbitals leads to a decoupling from the environment that conserves J as a good quantum number. The effect of the crystal field can then be treated as pertubation of the spin-orbit coupling whose effect has been introduced already as the split-off of the $J = 6$ ground state.

The ligand field with symmetry of the C_4 point group[46] in $TbPc_2$ then contributes

$$\mathcal{H}_{\mathrm{lf}} = \alpha A_2^0 \langle r^2 \rangle \mathbf{O}_2^0 + \beta \left(A_4^0 \langle r^4 \rangle \mathbf{O}_4^0 + A_4^4 \langle r^4 \rangle \mathbf{O}_4^4 \right) + \gamma \left(A_6^0 \langle r^6 \rangle \mathbf{O}_6^0 + A_6^4 \langle r^6 \rangle \mathbf{O}_6^4 \right), \tag{1.15}$$

with Stevens operators $\mathbf{O}_k^q$ and constant coefficients α, β and γ, tabulated by Stevens[43]:

α	β	γ
- 1/99	2/16335	- 1/891891

The A_k^q are geometrical coordination coefficients which depend on the ligand charge distribution and can be obtained from measurements of NMR spectra[21] [46]:

$A_2^0\langle r^2\rangle$	$A_4^0\langle r^4\rangle$	$A_4^4\langle r^4\rangle$	$A_6^0\langle r^6\rangle$	$A_6^4\langle r^6\rangle$
595.7 K	−328.1 K	14.4 K	47.5 K	0 K

The bottom line of the impact of the Stevens operators, tabulated in the referenced publication, is the following: The diagonal $\mathbf{O}_k^0$ with $k = \{2, 4\}$ contain terms $\propto J_z^k$ which lift the degeneracy between states of different quantum numbers m_J, therefore introducing an energy gap of 600K between the ground state $m_J = \pm 6$ and the first excited state $m_J = \pm 6$.
Eventually this leads to a well-defined two-level quantum system of the electronic angular momentum at low temperatures. The off-diagonal term $\mathbf{O}_4^4$ (and also $\mathbf{O}_6^4$, however with negligible contribution) accounts for the C_4 point group symmetry, arising from a slight deviation from 45° orientation in the rotation angle of the ligand planes[1]. As a result, the degeneracy of the $\pm m_J$ energy spectrum is lifted by an induced splitting. This splitting is $\approx 1\,\mu\mathrm{K}$ for $\pm m_J = 6$ and can be identified as the corresponding tunnel splitting Δ at the avoided level crossings introduced in sec. 1.2.

Zeeman Effect

To complete the picture of the spectrum corresponding to the electronic problem, external magnetic fields have to be taken into account, acting by means of a Zeeman effect:

$$\mathcal{H}_{\mathrm{el}} = \mathcal{H}_{\mathrm{lf}} + \mathcal{H}_{\mathrm{Zeeman,J}}. \tag{1.16}$$

This Zeeman contribution to the Hamiltonian reads

$$\mathcal{H}_{\mathrm{Zeeman,J}} = g_{\mathrm{L}} \mu_{\mathrm{B}} J_z B_z \tag{1.17}$$

1 A perfect 45° orientation would lead to a higher symmetry of $D_{4\mathrm{d}}$.

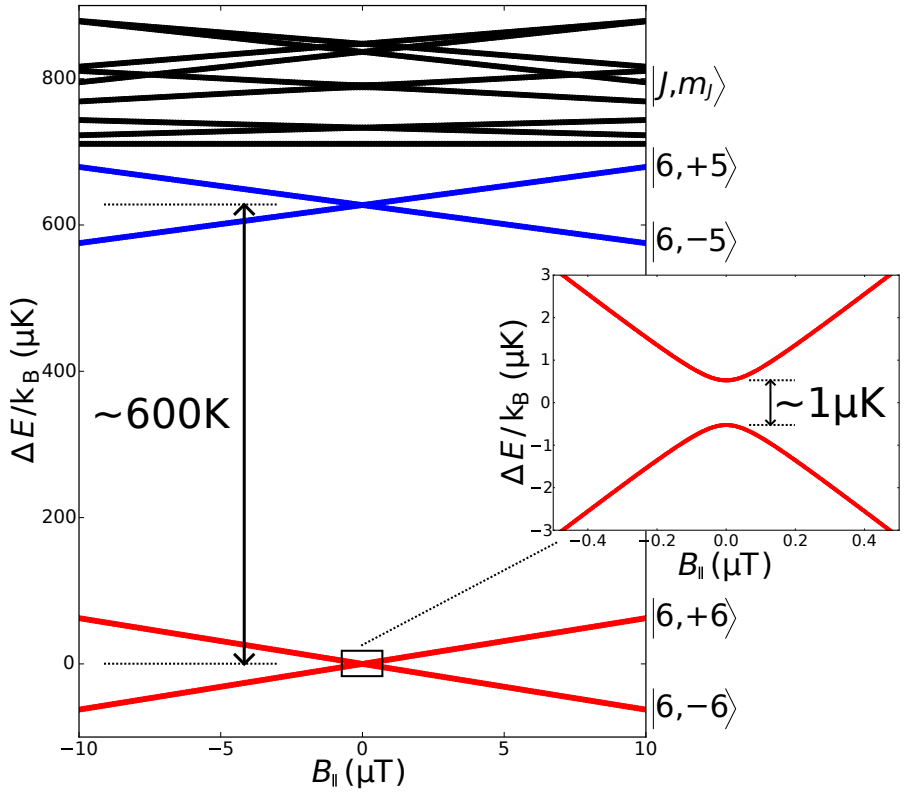

Figure 1.11: Energy spectrum of the 13 states of $J = 6$ in $TbPc_2$. Left side: No applied magnetic field, the splitting between ground state and first excited state is in the order of 600K. Right side: The magnetic field dependance of the levels. The inset shows the avoided level-crossing of the ground state at $B = 0$ with a tunnel splitting in the order of $1\mu K$.

in the used basis and for a magnetic field parallel to the molecules magnetic easy axis z. The Landé factor g_L of terbium can be accounted with 3/2 and μ_B is the Bohr magneton. Numerical diagonalization of the 13×13 matrix $\mathcal{H}_{el}$ leads to the energy spectrum presented in fig. 1.11 which contains all features that have been previously discussed.

Hyperfine Coupling

Further complexity arises from the inherent nuclear spin $I = 3/2$ of the terbium ion which splits all electronic states m_J into four sub-states $m_I = \pm 3/2, \pm 1/2$ each due to strong hyperfine coupling in $TbPc_2$. The hyperfine coupling Hamiltonian for this system consists of a dipolar and a quadrupole contribution. For the dipolar magnetic interaction the nuclear magnetic moment associated with I is considered to be interacting with a local magnetic field, created by the surrounding electrons and their inherent magnetic moment associated with J. For a free ion in LS-coupling the field precesses about J and only the component parallel to J has to be included:

$$\mathcal{H}_{\mathrm{hf}}^{\mathrm{dip}} = A_{\mathrm{hf}}\mathbf{IJ}. \tag{1.18}$$

The nuclear electric quadrupole interaction, which is usually so small that only diagonal elements of the electronics states created by the ligand field have to be included, has an axial symmetry and reads:

$$\mathcal{H}_{\mathrm{hf}}^{\mathrm{quad}} = P\left(I_z^2 - \frac{1}{3}I(I+1)\right). \tag{1.19}$$

The hyperfine interaction Hamiltonian can thus be written as

$$\begin{aligned}\mathcal{H}_{\mathrm{hf}} &= \mathcal{H}_{\mathrm{hf}}^{\mathrm{dip}} + \mathcal{H}_{\mathrm{hf}}^{\mathrm{quad}} \\ &= A_{\mathrm{hf}}\mathbf{IJ} + P\left(I_z^2 - \frac{1}{3}I(I+1)\right) \\ &= A_{\mathrm{hf}}\left(I_zJ_z + \frac{1}{2}\left(J_+I_- + J_-I_+\right)\right) + P\left(I_z^2 - \frac{1}{3}I(I+1)\right),\end{aligned} \tag{1.20}$$

with constants A_{hf}, P given by Ishikawa et al.[21]:

A_{hf}	P
24.89 mK	14.39 mK

The two hyperfine terms contribute in a different manner: The dipole interaction term splits the degeneracy of the four nuclear spin states m_I of each m_J, while the quadropolar term introduces unequal spacing via I_z^2. This turns out to be useful to individually address the different sub-states of $TbPc_2$.

Nuclear Zeeman Effect

Aditionally, the Zeeman effect of the nuclear spin I has to be taken into account with

$$\mathcal{H}_{\mathrm{Zeeman,I}} = g_{\mathrm{I}}\mu_{\mathrm{N}}I_zB_z, \tag{1.21}$$

where the g-factor of the nucleus g_{I} is 1.354[47] and μ_{B} the nuclear magneton. The complete Hamiltonian of $TbPc_2$ can then be written as:

$$\mathcal{H}_{\mathrm{TbPc_2}} = \mathcal{H}_{\mathrm{lf}} + \mathcal{H}_{\mathrm{Zeeman,J}} + \mathcal{H}_{\mathrm{hf}} + \mathcal{H}_{\mathrm{Zeeman,I}}. \tag{1.22}$$

Again, numerical diagonalization reveals the energy spectrum. Due to inclusion of the nuclear spin I the Hamiltonian $\mathcal{H}_{\mathrm{TbPc_2}}$ is now a 52×52 matrix. The results of this calculation are illustrated in fig. 1.12, again containing all previously mentioned features.

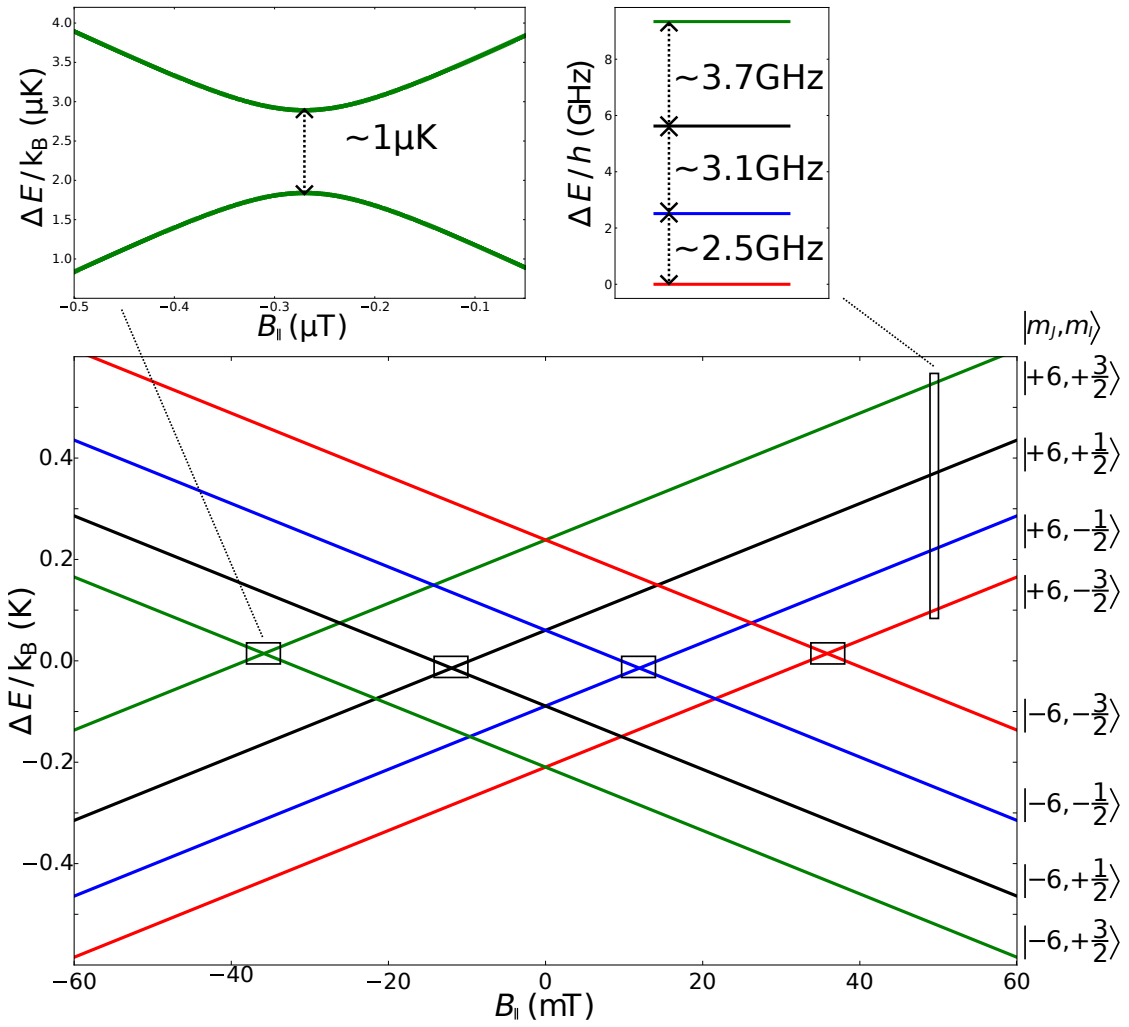

Figure 1.12: B-field dependent energy spectrum of the $m_J = \pm 6$ electronic ground state of $J = 6$, including the nuclear spin splitting. Four avoided level crossings are created (marked with the little boxes) with all tunnel splittings $\approx 1\,\mu\mathrm{K}$ as exemplarily illustrated for the leftmost one (the offsets are neglected in the inset). The right inset shows the unequal spacing between the four states in frequency units.

1.3.2 Spin Reversal in $TbPc_2$

Magnetization reversal of $TbPc_2$ is determined by the two processes discussed in sec. 1.2 and depicted in fig. 1.13. At small magnetic fields reversal occurs due to quantum tunneling of magnetization (QTM) at the positions corresponding to the four avoided level crossings. These processes are associated with sharp steps in magnetic hysteresis loops. At higher fields phonon-assisted direct transitions are the dominant mechanism. Experimental data showing microSQUID measurements of a crystal is provided in 1.14a. More than 4 jumps due to QTM are visible in such structures. The step-like behaviour

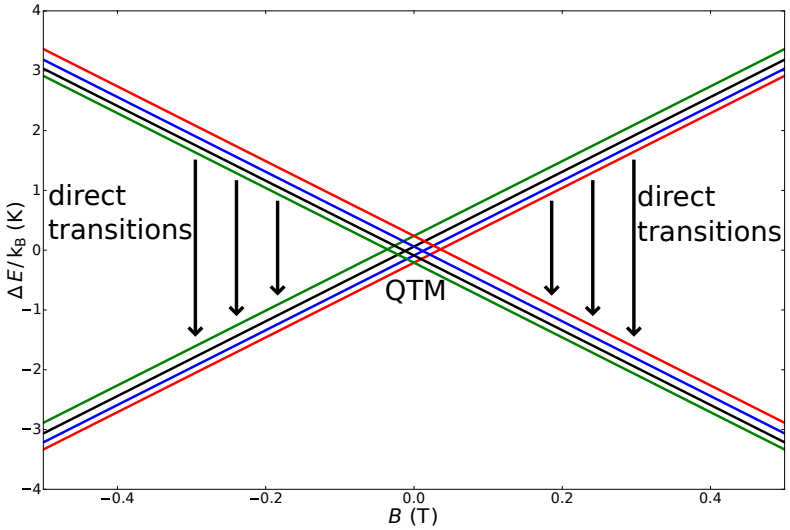

Figure 1.13: Magnetization reversal processes in a single $TbPc_2$ SMM. QTM occurs at the 4 anti-crossings at small magnetic fields. Direct processes cause reversal at larger fields.

vanishes for increasing sweep rates, making the direct phonon transition the more likely mechanism for reversal. In accordance with fig. 1.4, a similar effect could be observed for increasing temperature, demonstrating the transition of a quantum regime to classical thermal activation. In 1.14b, data on a single molecule is shown, for which 4 QTM jumps are observed. Coupling to the environment, for instance nearby quantum dots, can induce additional reversal processes via exchange coupling for individual molecules.

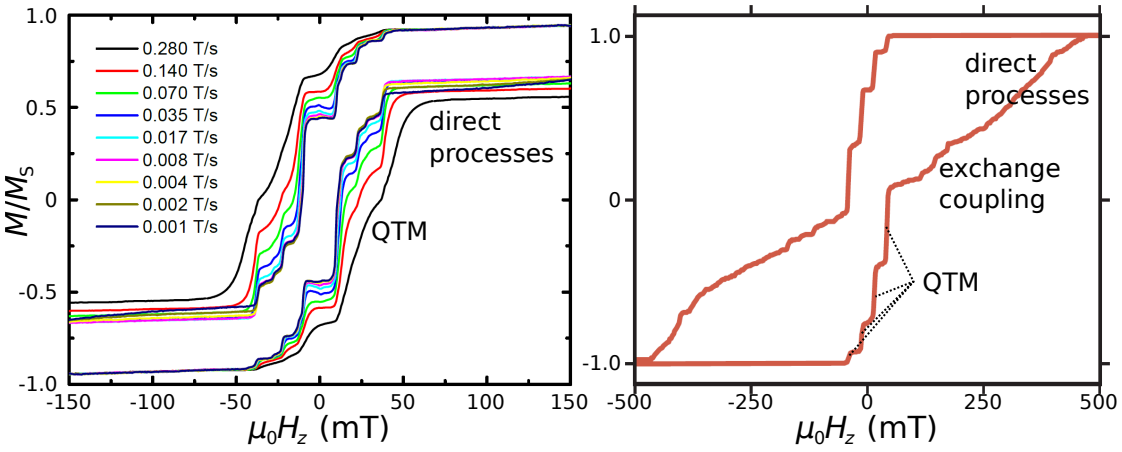

Figure 1.14: Magnetic hysteresis of $TbPc_2$. a) Assembly of 2% $TbPc_2$ diluted in a YPc_2 matrix and measured in a microSQUID setup. More than 4 QTM jumps can be observed as a result of the crystal. Phonon assisted direct processes are responsible for the reversal at larger fields (only a part is shown in this close-up). b) Single 2% $TbPc_2$ data integrated over 1000 field sweeps. 4 distinct QTM peaks are visible. Additional peaks occur due to exchange coupling to a nearby quantum dot.
a Adapted from [48], originally from [21] b) Adapted from [49]

2 Carbon Nanotube Double Quantum Dots

Tubular graphitic structures, referred to as *carbon nanotubes* (CNT), have been intensively researched from the beginning of the 1990s. As forerunner of then still elusive graphene and equipped with an array of intriguing properties, they first gave way to a perspective of organic carbon-based micro- and nanoelectronics. Building on the first report on *multi-wall carbon nanotubes* (MWCNT) in 1991 by Iijima[50] from the NEC laboratories, progress was made quickly on the theoretical[51] description and fabrication[52][53] of *single-wall* specimen (SWCNT), too. The latter provide a more controlled environment for the investigation and exploitation of transport phenomena on the nanoscale[1].
First single-electron transistor applications[54][55] were realized soon after, followed by field-effect transistors[54][56]. Showing extraordinarily high conductivity and charge carrier mobilities, nanotubes became one of the most coveted model materials for potential future computer technology, for example memory applications[57].
While the transition to the mass market of electronics did not happen to date, nanotubes remain in the focus of research for quantum-based transport phenomena[2], constituting systems for the realization of physics at the heart of electronics and spintronics. Here, advantage can be taken of the well-conserved transport properties of CNTs giving rise to stable but adjustable charge states at low temperatures, a regime very generally referred to as *quantum dot* (QD). With the possibility of having band gaps one can principally tune multidot regimes in CNTs with induced pn-barriers, creating a platform for the investigation of spin-valley physics[60] or electron-phonon coupling[61] in *nanoelectromechanical systems* (NEMS).
A particularly interesting case arises for the use of nanotubes as carriers for the single-molecule magnets presented in the previous chapter. The possibility to graft these molecules onto CNTs[39] opens up a route to novel molecular spintronics concepts[62], with practical realizations such as molecular spin valves[63] or spin-based molecular *nanoelectromechanical systems*[64] (NEMS), studied in the NanoSpin group in recent years. In these hybdrid devices spin-polarized quantum dots are created, combining features of both constituents.
Before approaching hybrid systems of CNTs and SMMs, an introduction to the electronic properties and transport in CNT (double) quantum dots is provided in the following.

1 The high potential of CNTs for (macroscopic) mechanical applications is not discussed in this chapter, nor are electro-optical, electro-thermal or biomedical implementations.

2 The case of (induced) superconductivity in CNTs is not treated either, but in anticipation of the second part of this PhD, which covers induced superconductivity in another novel material, it should be pointed out that CNTs can constitute interesting systems for such physics as well, ranging from nano-SQUIDs[58] to unconventional coupling[59].

2.1 Properties of Carbon Nanotubes

2.1.1 Structural Properties

Carbon nanotubes can be considered as quasi-one-dimensional objects due to their small diameter of a few nanometers and typical lengths which easily exceed the µm range with modern synthesis principles[65]. They are most easily described in terms of rolled-up two-dimensional graphene sheets (see fig. 2.1) for the case of single-wall (SWCNT) tubes, inheriting many properties of the underlying honeycomb lattice. The following description is restricted to this case, as CNTs used for the preparation of this thesis are exclusively of this type.
With the two honeycomb lattice vectors $\mathbf{a}_i$ and discrete numbers n,m counting the lattice sites one can define the chiral vector $\mathbf{C}$,

$$\mathbf{C} = n\mathbf{a}_1 + m\mathbf{a}_2, \tag{2.1}$$

which handily covers CNT symmetries: The two symmetry directions *zigzag* and *armchair* follow as special cases of $\mathbf{C}$ with $\varphi = 0°$ and $\varphi = 30°$ respectively, while SWCNTs are labeled *chiral* for angles in between. The angle φ is also called *helicity* of the nanotube and $\mathbf{C}$ defines the diameter d via

$$d = \frac{1}{\pi}|\mathbf{C}| = \frac{a}{\pi}\sqrt{n^2 + m^2 + nm}, \tag{2.2}$$

where the honeycomb lattice constant is given by $a = 1{,}42\,\text{Å}$.

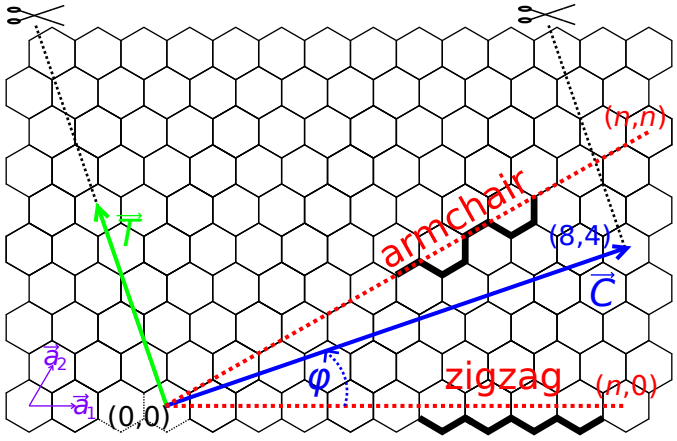

Figure 2.1: Illustrative construction of a SWCNT from 2D graphene is done by cutting the graphene sheet along the chiral vector $\mathbf{C}$ (blue line) and the perpendicular dashed black lines, then rolling up the sheet along $\mathbf{C}$. The armchair and zigzag SWCNTs (red dashed lines) are special symmetry directions of $\mathbf{C}$. The vector $\mathbf{T}$ is constructed perpendicular to $\mathbf{C}$ by using the nearest lattice point. The unit cell is defined by $|\mathbf{T} \times \mathbf{C}|$.

2.1.2 Electronic Properties

Due to the close structural relation the electronic properties of SWCNTs follow straight from the underlying graphene and thus even more fundamentally from the electronic configuration of carbon, which reads $1s^2 2s^2 2p^2$. In graphene this configuration gives rise to three sp^2-type hybrid orbitals, enabling σ-bonds, and remaining $2p_z$-orbitals, which form delocalized π-bonds. Neglecting spin-orbit coupling the $2p_z$ do not hybdridize further with lower energetic states and the resulting band structure $E(\mathbf{k})$ of graphene can be determined in tight-binding calculations [66]. Transport properties are exclusively determined by the two-band structure of conduction band π and valence band π^* whose energy dispersion can be found as

$$E(\mathbf{k}) = \pm t\sqrt{3 + f(\mathbf{k})} - t' f(\mathbf{k}), \tag{2.3}$$

with t and t' being the hopping parameters between nearest and next-nearest lattice sites respectively. Both parameters can be calculated with *ab initio* methods [67] and the impact next-nearest neighbour coupling t' is broken electron-hole symmetry. The function $f(\mathbf{k})$ in this expression is given by

$$f(\mathbf{k}) = 2\cos\left(\sqrt{3}k_y a\right) + 4\cos\left(\frac{\sqrt{3}}{2}k_y a\right)\cos\left(\frac{3}{2}k_x a\right), \tag{2.4}$$

which results in six pairs of cones positioned at the *Dirac points*, the lattice points of the still hexagonal lattice in $\mathbf{k}$-space (see fig. 2.2). Only K and K' are inequivalent - the other points are shifted by reciprocal lattice vectors - and hence they form two electronic states distinguished by the notion of *valleys*.

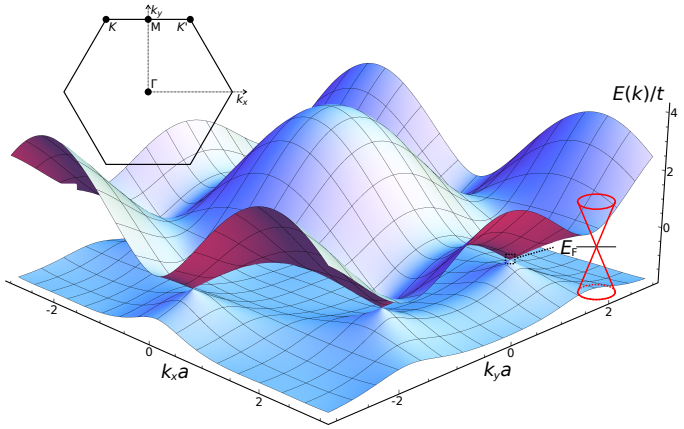

Figure 2.2: Tight binding dispersion of graphene in next-nearest neighbour approximation with $t = 2.7\,\mathrm{eV}$, $t' = 0.2t$ [67] and in units of t. The upper left inset represents the first Brillouin zone of graphene with the two inequivalent Dirac points K and K', while the right inset shows the linear dispersion for k-values around the Dirac point(s).

There is no band gap in pristine graphene, as the pairs of cones align perfectly at the Fermi energy E_F. Expansion around these points with $\mathbf{k} = \mathbf{K} + \mathbf{q}$ for $|\mathbf{q} \gg \mathbf{K}|$ and neglection of t' reveals the famous linear dispersion of graphene,

$$E(\mathbf{q}) = \pm\hbar v_\mathrm{F}|\mathbf{q}| + \mathcal{O}((q/K)^2), \tag{2.5}$$

corresponding to the case of massless relativistic particles with Fermi velocity[1], in the tight-binding model given by [66] $v_\mathrm{F} = 3ta/2 \approx 10^6\,\mathrm{ms}^{-1}$.
Generated by periodic boundary conditions and Bloch functions, a graphene sheet can be considered as infinite. Then the crossover to CNTs is done in the *zone-folding* approximation via quantization of the graphene dispersion in the spatially restricted circumferential direction. The wave vector $k_\perp$ perpendicular to the longitudinal tube axis is then a set of discrete values

$$\mathbf{kC} = \pi d k_\perp = 2\pi l, \tag{2.6}$$

with the chiral vector $\mathbf{C}$ and and integer l, while the longitudinal wave vector $k_\parallel$ remains approximately continuous. The Dirac cones can then be described with the dispersion

$$E_\mathrm{D}\left(k_\perp, k_\parallel\right) = \pm\hbar v_\mathrm{F}\sqrt{k_\perp^2 + k_\parallel^2} \tag{2.7}$$

and the missalignment $\Delta k_\perp$ of the cones with respect to the $k_\perp, k_\parallel$ sub-bands determines 1D trajectories via their intersection, corresponding to the nanotubes' allowed $\mathbf{k}$-values (see fig. 2.3). According to this model, CNTs can only be metallic if the allowed k-values cut the cones directly at the Dirac point. Saito et al. [69] found the following condition for metallic SWCNTs and an integer p:

$$2n + m = 3p. \tag{2.8}$$

This condition renders armchair SWCNTs always metallic since those are defined by the chiral indices n,n. Zigzag SWCNTs can be either metallic, $n = 3p$, or have a gap in all other cases. However, curvature effects, which shift the Dirac points with respect to the Brillouin zone of flat graphene and induce an additional missmatch $\Delta k_\perp^\mathrm{CV}$, were not included in the picture above. By taking curvature into account, Hamada et al. [51] found a more strict condition for metallic nanotubes:

$$n = m. \tag{2.9}$$

1 Substrate engineering in real devices [68] nowadays allows for much higher Fermi velocities $\geq 3{\cdot}10^6\,\mathrm{ms}^{-1}$.

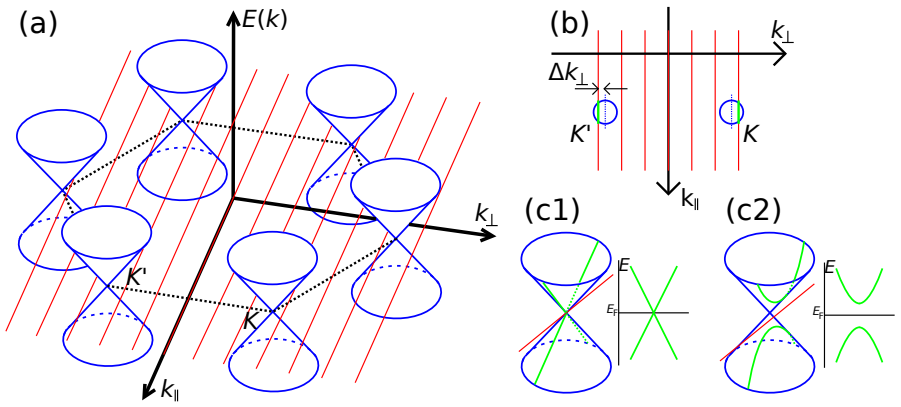

Figure 2.3: a) Quantization of the wave vector $k_\perp$ perpendicular to the CNT axis (red lines) gives rise to sub-bands. The alignment of these sub-bands with the Dirac cones determines the CNT dispersion near the Fermi energy E_F. Here, the sub-bands do not intersect the Dirac points, leading to a band gap. b) Topview of the situation in (a) and the quantization-induced missmatch $\Delta k_\perp$ of the Dirac cones at K and K'. c) Two different alignments and the resulting dispersion relation, a metallic CNT (c1) and a semiconducting CNT (c2).
Based on [70]

This applies only for armchair CNTs, while zigzag CNTs have a small gap for

$$n - m = 3p, \tag{2.10}$$

with $p = 1,2,...$ or a larger gap in the remaining cases. The scaling of the band gap with the CNT diameter was determined by Kane et al. [71] to be $1/d$ for larger gaps and $1/d^2$ in the case of small gaps.
However, the presented classification of nanotubes requires a reasonable resemblance of the 2D graphene structure, which holds true for sufficiently large CNT diameters. For small diameters the problem cannot be treated within a tight binding approach anymore. Strong curvature effects, for example a π-σ-hybridization, can be taken into account in ab initio calculations, showing that zigzag CNT (4,0) and (5,0) band gaps are actually much smaller [72] than calculated before or that a (6,0) CNT is metallic [73]. Also, additional effects like mechanical strain can influence the electronic properties and induce gaps in otherwise metallic CNTs or modify the gap of semiconducting ones [74] [75].
This curvature-induced gap in carbon nanotubes is an integral ingredient for promising electronic applications: it allows for the electrostatical confinement of charge carriers as it is commonly used in other semiconductor applications. In contrast, the lack of a band gap in pristine monolayer graphene is an obstacle for charge confinement due to the presence of Klein tunneling. [76] [77].
As it is the case in graphene, the Dirac points K and K' form two valleys with a relatively robust degeneracy. How this degeneracy affects transport properties and how it is ultimately lifted by spin-orbit interactions will be explained in sec. 2.2 and 2.3.

2.2 Transport in Carbon Nanotube Quantum Dots

Transport in quantum objects like CNTs can be discussed in a huge variety of different theoretical approaches, exceeding by far the framework of this thesis. Thus emphasis is set on the explanation of properties and effects arising in the regimes our samples are driven in: the case of low temperatures and moderate to high resistances. In order to point out this regime, transitions from quasi-one-dimensional nanotubes to quasi-zero-dimensional quantum dots and from room temperature behaviour to low temperature measurements are shortly reviewed beforehand.

2.2.1 General Perspective

Landauer Formula

Charge transport through one-dimensional conductors can be treated within Landauer's formalism. It states that the conductance is a multiple of the conductance quantum $G_0 = e^2/h \approx 38.8\,\mu\mathrm{S}$ [78], depending on the number of available transport channels i and their respective transmission coefficiants t_i at the Fermi energy E_F,

$$G \propto \frac{e^2}{h} \sum_i t_i \left(E_\mathrm{F}\right), \tag{2.11}$$

which also carries a distribution function dependence in its complete form [79]. When E_F is situated well within an electron or hole sub-band then transport is governed by the properties of both the 1D conductor and the contact interface. In the ideal case of *ballistic* transport, valid for a conductor length smaller than the mean free path, $L < l_\mathrm{m}$, and perfect contacts, the individual transmission is $t_i = 1$. For carbon nanotubes with their fourfold degenerated sub-bands $\sum_{K,\sigma} 1 = 4$ due to valleys K and spin σ, this results in a minimum intrinsic resistance of $R = R_0/4 \approx 6.5\,\mathrm{k\Omega}$. When E_F lies inside of the band gap of the conductor, transport is thermally activated, leading to only small differences at room temperature between metallic CNTs and CNTs with small band gap, while semiconducting CNTs show generally a lower conductance [80].
Scattering in the nanotube for $L > l_\mathrm{m}$ contributes to the total device resistance, just as additional contact resistances R_c do, leading to [81]:

$$R \approx 4\frac{e^2}{h} + \frac{h}{4e^2}\frac{L}{l_\mathrm{m}} + R_c. \tag{2.12}$$

Contact resistances of metallic CNTs can be relatively easily reduced and together with usually large mean free paths l_m and high current densities this makes for use as interconnects [82]. On the other hand, the weak dependence on applied electric fields excludes them from transistor-type applications. In contrast, the high transconductance in semiconducting CNTs, together with large carrier mobilities [57] [83], makes these devices

promising candidates not only for FETs but also for controllable molecular spintronics applications. However, the interface of semiconducting CNTs with metal contacts typically has to be treated with more diligence due to the prevalent formation of often highly resitive *Schottky barriers*.

Schottky Barriers at Metal-Nanotube Interfaces

The most basic resistance occurring at interfaces between metals and carbon nanotubes arises from imperfect adherence due to lacking cleanliness. The first transistor-type devices were fabricated by deposition of laser-ablated CNTs dispersed in solution on top of pre-patterned electrodes of noble metals with high *work functions* such as gold or platinum. These devices typically had low yield, high contact resistances exceeding $1\,\mathrm{M\Omega}$ as well as strongly unipolar p-type conductance [84] [85]. Later on, more advanced patterning principles were developed and metals with good *wetting* abilities as well as high work functions, such as palladium, were ascribed to be good contact materials, with resistances well below $100\,\mathrm{k\Omega}$ for CNT diameters exceeding $2\,\mathrm{nm}$ [86]. The diameter of the nanotube influences not only the overlap of the electronic wave functions but also (inversely) determines the CNT gap size and hence the likelihood of an energy barrier formation at the interface, which is the Schottky barrier Φ_B. This barrier generally stems from bending of the semiconductor's sub-bands in order to match its work function with the one of the metal at the interface, which often leads to the Fermi level E_F being situated in the band gap in order to establish equilibrium. In the case of vanishing or negative barrier height the contact is called *ohmic*. Hence, the interface should be tunable via the metal's specific work functions according to the *Schottky-Mott rule*.

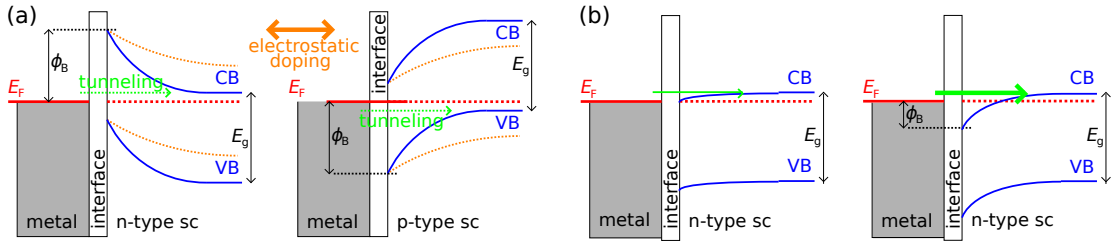

Figure 2.4: Schematic of a metal-semiconductor-interface for different Schottky barrier types. a) Positive Schottky barrier of height Φ_B for n-type semiconductor (left) and p-type semiconductor (right). Transport takes place via tunneling through the barrier or thermal activation over the barrier in the case of high temperatures. The resistance is generally high. Ambipolar devices can be tuned between n- and p-type conductance by applying static electric fields. b) Zero-barrier (left) and fully ohmic case with negative barrier (right) for n-type semiconductor. The resistance is strongly reduced.

However, this picture is not complete. For conventional metal-semiconductor contacts the interface rarely shows dependance on the work function, but an effect called *Fermi level pinning* determines the behaviour. Surface states within the band gap get strongly occupied and pin E_F deep within the band gap, resulting in large barriers and high resistances. For carbon nanotubes, Fermi level pinning isn't as dominant as for conven-

tional semiconductors since its effect is limited to the length scale of the CNT diameter. The resulting barriers are so thin that the tunnel current penetrating them is relatively high [87] [88].
The exact type of the metal surface and its chemical composure thus strongly affects the contact properties to carbon nanotubes. In this regard different materials lead to specific doping of the CNT, for instance p-type conductance for noble metals like Pd or Pt. But chemical modifications, such as exposure of palladium to hydrogen [86], gold to oxygen [89], or the use of thermally annealed TiC-contacts [90] not only strongly alter the contact resistance, but also ambipolar transport behaviour with typically strong electrostatic modulation becomes possible. This is realized by tuning of the electrochemical potential (in equilibrium corresponding to the Fermi level) via gate electrodes and will be explained in more detail in the following sections.
In the last years the use of clean carbon nanotubes fabricated by *chemical vapour deposition* (CVD) became more and more common. The direct growth on-chip not only allowed for omission of contamination created by chemical solutions, but also enabled the possibility of *ultra-clean* suspended CNT devices. Deviating from early results with less developed fabrication techniques, these CNTs grown on molybdenum [91] or platinum [92] electrodes had low contact resistances and total device resistances of several $10\,\mathrm{k}\Omega$ attributed to the formation of carbide structures at the elevated growth temperatures of typically $800 - 1000\,\mathrm{C}^\circ$.
While the optimization of contact resistances remains a challenge for the application of advanced FET devices, their presence provides an intrinsic mechanism for the formation of quantum dots, quasi-zero-dimensional quantum objects with strongly controlled charge states at sufficiently low temperatures.

Carbon Nanotube Quantum Dot Devices

As previously explained, carbon nanotubes can be considered as quasi-one-dimensional objects due to spatial restriction in the lateral direction. To fully constrict electrons on a quai-zero-dimensional island efficient barriers have to be created in the longitudinal direction as well. An intrinsic mechanism are the aforementioned Schottky barriers, but another possibility arises from pn-junction barriers which can be created in nanotubes by applying static electric fields [93] [94]. The field shifts the chemical potential in the CNT locally and creates regions around the transition depleted of charge carriers which can act as a tunnel barrier.
Additional barriers at random positions can arise from disorder, for example due to contact defects or adsorbates on surfaces like the gate oxid [95]. Their occurrence is strongly reduced in suspended devices. This allows for controlled creation of series of quantum dots (see fig. 2.5) or spatial shifts of individual quantum dots [96]. Finally it should be anticipated here that also the interaction of single molecule magnets with carbon nanotubes leads to the formation of barriers or local dots respectively.
The energy quantization in longitudinal direction is strongly influenced by the exact type of boundary condition and the size of the dot. Boundaries can be atomically sharp or smooth and the latter further subdivided into hard-wall and soft-wall conditions [97].

Either way resulting spectra are quite unique for real devices with energy level splittings ΔE increasing for smaller quantum dots. For metallic nanotube quantum dots of length L the confinement is often relatively well described with [54]

$$\Delta E = \frac{h v_\mathrm{F}}{2L}. \tag{2.13}$$

Shells consisting of electron states with equivalent energy can be defined via a longitudinal quantum number ν. Usually the two valleys K and K', together with the twofold spin degeneracy, result in a fourfold degeneracy of the quantum dot's electron shells. However, this is only approximately true since coupling of spin and orbit, even in very clean nanotubes, gives rise to a fine structure with lifted degeneracy [98]. This will be treated in more detail in section 2.3.2 but neglected for the time being.

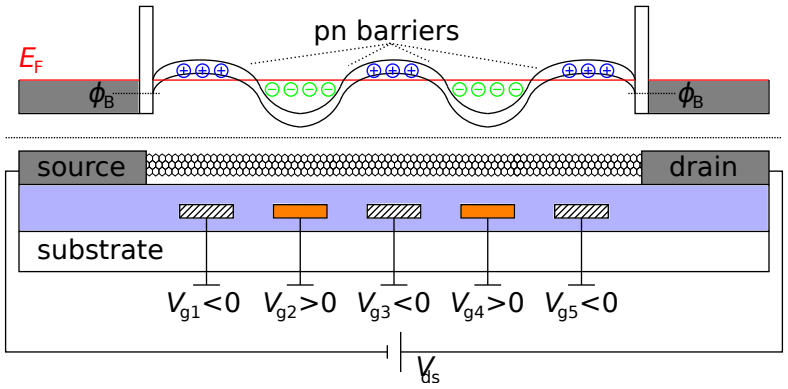

Figure 2.5: Schematic of a multi-terminal CNT device and its respective band diagram, consisting of a CNT quantum dot connected by metallic source and drain electrodes and driven by a voltage V_ds. The nanotube is typically p-doped by the contact metal and separated from the reservoirs via Schottky barriers. Several local gates are capacitively coupled to the dot and can induce n-type segments which are thus separated via pn-barriers, here arbitrarily positioned above gates 2 and 4.

Typical devices consist of (at least) one quantum dot directly connected to metallic source and drain electrodes via tunnel junctions and are controlled by (at least) one gate electrode, as it is schematically represented in fig. 2.5. The gate is capacitively coupled to the dot without direct charge flow. Practically this is realized with sufficient spacial distance for suspended devices and/or the use of dielectrics in between. These insulating layers are typically *high-*κ dielectrics like Al_2O_3 or HfO_2 because efficient coupling, described by

$$C = \frac{\varepsilon_0 \kappa A}{d} \tag{2.14}$$

for a capacitor of area A and distance d, is possible without the necessity of a layer thickness so small to induce tunneling leakage.

Gate electrodes can be realized as top gates, side gates or bottom gates, with each type having particular advantages and drawbacks. Top gates are easy to fabricate but they limit the cleanliness of the CNT device due to the necessary contact of the CNT with the gate oxide. Side gates do not induce disorder but their minimal distance to the device and therefore their efficiency is limited by common fabrication techniques. Bottom gates, typically used for clean and (at least partially) suspended devices, have none of these limitations. However, global gates (implemented via doped substrates) lack local control and the fabrication of complex nano-scale electronic circuits is not straightforward due to the high temperatures required for CVD growth. This severely limits the number of suitable materials and layouts and will be discussed in more detail in chapter 5.
As it has been mentioned before, quantum dots can be considered as systems with high controllability of charge states. In order to achieve this regime, a transition to low temperatures is required, where quantum effects are no longer smeared out by thermal fluctuations.

Transport Regimes at Low Temperatures

Reducing the scale to small electron islands like quantum dots gives rise to physics based on discrete charge effects for tunnel barriers sufficiently opaque to confine charge carriers on the island. This effect was first reported by Giaever et al.[99] for small metallic grains in 1968. Fulton et al.[100] subsequently related the occurring IV oscillations to single electrons tunneling through the barriers of small junctions. The energy scale of these effects is given by the so-called *charging energy* E_C,

$$E_\mathrm{C} = \frac{e^2}{C}. \tag{2.15}$$

E_C is the amount of energy necessary to transfer an electron of charge e onto a small island of capacitance C, a process which is impeded by Coulomb repulsion. The island can be either metallic with a dense distribution of accessible energy levels or it can have discrete levels spaced with ΔE, as it is the case for quantum dots. Generally the temperature has to be low in comparison to the involved energy scales in order to avoid masking of quantum effects due to thermal fluctuations over the barriers:

$$k_\mathrm{B}T \ll E_\mathrm{C}, \Delta E. \tag{2.16}$$

Furthermore, occurring transport phenomena are strongly dependend on the character of the tunnel barriers and their opaqueness, expressed with either resistance R_t or *coupling* Γ. Mathematically Γ is given by the tunneling rate and, given that the current is $I = e\Gamma$, it is clear that Γ directly depends on R_t. On the other hand, $\hbar\Gamma$ corresponds to a line broadening of the dot, caused by the coupling of its discrete spectrum to the continuous density of states in the reservoirs. Using Γ one can distinguish three (usually overlapping) regimes:

- **open quantum dot regime**: $\hbar\Gamma \gg E_C$
  transport dominated by quantum interference
  (classical analogon: Fabry-Perot interference)
- **intermediate quantum dot regime**: $\hbar\Gamma \leq E_C$
  charging effects and quantum interference
  (Kondo physics, higher order tunneling processes)
- **closed quantum dot regime**: $\hbar\Gamma \ll E_C$
  charging effects dominate transport
  (single electron tunneling, Coulomb blockade)

In ambipolar CNT devices all three regimes can principally be realized by varying the chemical potential over a large range [101]. Usually at least a transition of more strongly coupled p-type transport to (partially blocked) n-type transport is observed (see fig. 2.6). Since the robust charge states of the closed quantum dot are beneficial to a controlled operation of CNT-SMM spintronics devices, mainly this regime is stressed in the following. It features the so-called *single electron tunneling*, where electrons pass the island one by one and the (three-terminal) quantum dot device is referred to as *single electron transistor* (SET).

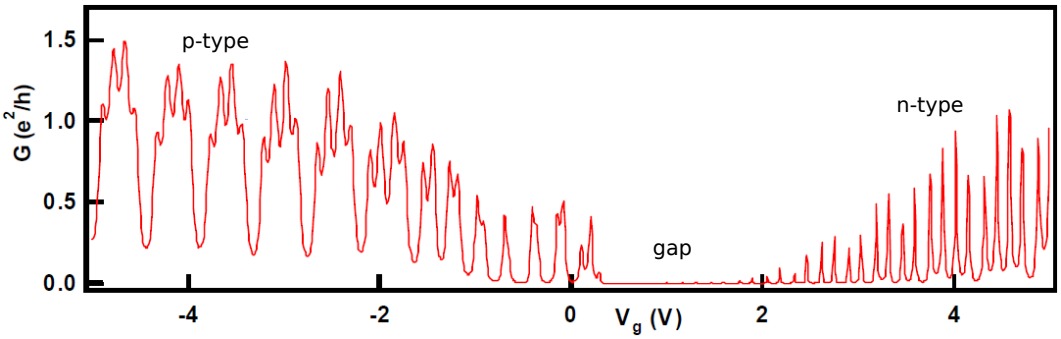

Figure 2.6: The gate-induced transition between p-type and n-type transport regimes in a CNT, measured at 300 mK and $V_{ds} = 1$ mV. The first shows clear evidence of Fabry-Perot interference while Coulomb blockade dominates for the latter. The fourfold symmetry of the CNT can be observed as fine structure in the Fabry-Perot peaks. The conductance is typically higher in the p-type region since commonly used contact metals dope the CNT p-type, thus a smaller Schottky barrier is created at the interface.
Adapted from [92]

2.2.2 The Closed Quantum Dot Regime

In the closed quantum dot regime coupling of the reservoirs to the dot is weak, corresponding to barrier resistances exceeding the resistance quantum, $R_t \geq 25.8\,\mathrm{k\Omega}$. As a result, electrons tunnel one by one and a phenomenon called Coulomb blockade dominates the transport, which can be theoretically described within the so-called *orthodox theory*.

Single Electron Tunneling and Coulomb Blockade

The origin of the Coulomb blockade can already be deduced from a single tunnel barrier of capacitance C. A tunneling process of a discrete charge e through the barrier is only possible when the difference of the charging energies before and after the event is positive:

$$\frac{Q^2}{C} - \frac{(Q-e)^2}{C} > 0. \tag{2.17}$$

Q is the charge brought to the junction from the reservoir, which is continuous due to possible infinitesimal shifts of the metallic charge distribution. It is clear that this condition is only fulfilled for $Q > Q_c = e$ or equivalently a driving voltage $V > V_c = e/C$. Otherwise transport is prohibited, which is referred to as Coulomb blockade. Therefore at V_c the junction undergoes periodic charging, provided by a voltage source, and discharging via discrete changes e corresponding to tunneling events.

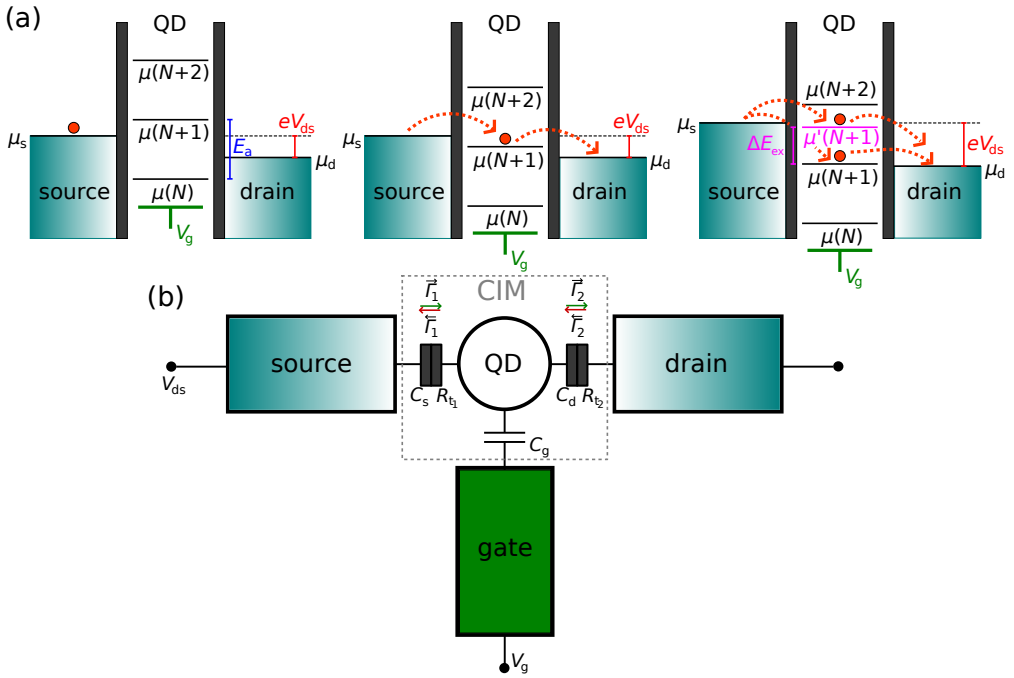

Figure 2.7: a) Transport over a quantum dot defined between two tunnel junctions. The bias V_{ds} opens a transport window and V_g shifts the chemical potential of the dot. When no quantum dot level lies inside of the transport window the system is situated in the regime of Coulomb blockade and the electron number is fixed to N (left). When $\mu(N+1)$ aligns with the window sequential tunneling is activated, alternatingly shifting the occupation between N and $N+1$ (middle). For sufficiently large bias voltage a second level can be accessible, for example an excited state $\mu'(N+1)$, opening another transport channel for sequential tunneling (right). The levels are not infinitesimally small but broadened due to thermal and lifetime effects. b) Circuit in the constant interaction model picture. The tunnel junctions are described by resistors R_{t_i} and capacitors C_s, C_d in parallel and the gate coupling by C_g.
Based on [102]

This principle can be generalised for quantum dots between two reservoirs and a gate. To do so the chemical potentials of the system have to be introduced. A current over the dot is driven by a difference in the chemical potentials of source and drain reservoirs, μ_s and μ_d, which is established by a bias voltage V_ds, resulting in a *transport window* of size eV_ds. The gate shifts the chemical potential of the dot $\mu(N)$, given by the difference in total energy U of the system with N and $N-1$ electrons:

$$\mu(N) = U(N) - U(N-1). \tag{2.18}$$

In this simple semi-classical picture U contains both the electrostatic interaction and the single particle energies E_i,

$$U(N) = \frac{(-Ne + \kappa_\mathrm{s} C_\mathrm{s} V_\mathrm{ds} - \kappa_\mathrm{d} C_\mathrm{d} V_\mathrm{ds} - C_\mathrm{g} V_\mathrm{g})^2}{2C_\Sigma} + \sum_{i=1}^{N} E_i, \tag{2.19}$$

where $\kappa_\mathrm{s/d}$ defines the bias voltage drop at the individual junctions. The system is characterized by a capacitance C_Σ which is explained within the framework of the *constant interaction model* (CIM) in the next section (see also fig. 2.7b). One can also define an *addition energy* E_a as the difference in chemical potentials,

$$E_\mathrm{a}(N) = \mu(N) - \mu(N-1) = E_\mathrm{C} + \Delta E(N), \tag{2.20}$$

as well as a chemical potential for the excited states of the quantum dot:

$$\mu'(N) = \mu(N) + \Delta E(N+1). \tag{2.21}$$

When a discrete level of the dot moves into the transport window due to the interplay of gate V_g and bias V_ds, Coulomb blockade gets lifted and electrons tunnel resonantly one by one through the dot, leading to a dot charge oscillating with $1e$. In the other case the current is blocked and the electron configuration stays constant (see figure 2.7a). The weak coupling results in tunneling events clearly separated in time and therefore independent as well as a long duration of stay of the charge carriers on the dot. These incoherent processes are referred to as *sequential tunneling*.
The dependence on both V_ds and V_g is often brought out *stability plots* of the differential conductance $G = dI/dV$. In this case rhombic regions of fixed charge states, called *Coulomb diamonds*, arise. These transport measurements make spectroscopic information of the dot, like E_C, ΔE or excitations, directly accessible (see fig. 2.8). Excitations can be vibrational modes of the nanotube [103] [104] for instance, usually treated within the Frank-Condon model [103]. As it has been already explained in sec. 1.2.4, these modes can be important for the working principle of suspended spintronique devices, which will be addressed again in sec. 2.5.2. Other possible excitations are of electronic origin, for

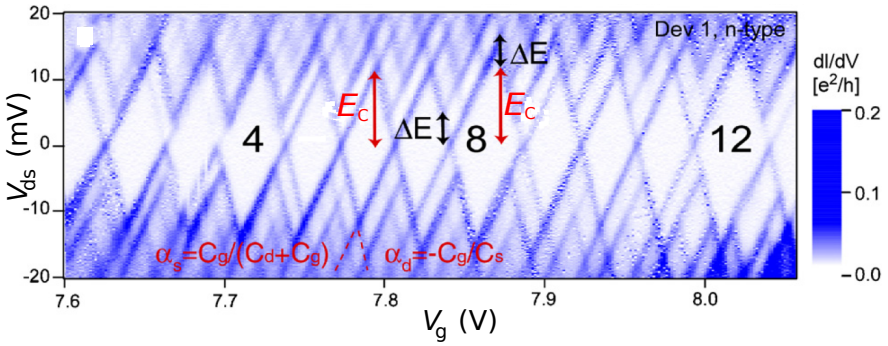

Figure 2.8: Stability plot of a SWCNT with small band gap, contacted by Au/Pd electrodes and measured at 4 K in the n-type region. Coulomb diamonds can be observed and every fourth diamond is larger, indicating the filling of a new shell with fourfold degeneracy. The diamond's height gives access to E_C and ΔE and the slopes α can be used to deduce the capacitances of the CIM.
Adapted from [101]

example resulting from spin polarizations [105] due to magnetic fields. In contrast, some devices show lifted valley degeneracy [106] [104]. To describe excitations in a more complete manner Oreg et al. [107] implemented additional terms to the CIM, which is subsequently presented in its basic form.

The Orthodox Theory and the Constant Interaction Model

The theoretical model for single-particle effects on small islands was mainly developed by Averin and Likharev [108] as well as Ingold and Nazarov [109]. While initially introduced for metallic islands, generalization to quantum dot systems was soon added [110] [111]. Tunneling processes can be classified by the number of involved particles, corresponding to the mathematical order of terms in pertubation calculations. For sequential tunneling the order is one, resulting in a linear response approach which is exactly the framework of the orthodox theory, while higher-order *cotunneling* processes are neglected. Quantum mechanically the physics of such a system is given by the Hamiltonian

$$\mathcal{H} = \mathcal{H}_\mathrm{s} + \mathcal{H}_\mathrm{d} + \mathcal{H}_\mathrm{QD} + \mathcal{H}_\mathrm{el} + \mathcal{H}_\mathrm{t1} + \mathcal{H}_\mathrm{t2}, \tag{2.22}$$

which contains contributions of the two reservoirs $\mathcal{H}_{\mathrm{s/d}}$, the dot $\mathcal{H}_\mathrm{QD}$, the electrostatic energy $\mathcal{H}_\mathrm{el}$ and the tunneling through the two barriers $\mathcal{H}_{\mathrm{t1/t2}}$. The electrostatic contribution is often treated within the constant interaction model (see figure 2.7b), which introduces both the tunnel junctions and the gate coupling as capacitances[1] and makes the following assumptions: The Coulomb interaction of the electrons on the dot can be described by a single constant capacitance $C_\Sigma = C_\mathrm{s} + C_\mathrm{d} + C_\mathrm{g}$ and the single particle energies E_i remain unaffected by these Coulomb interactions. The gate then induces

1 Several capacitances in the case of multiple gates.

an effective charge state of the dot $q_{\mathrm{eff}} = -Ne - C_{\mathrm{g}}V_{\mathrm{g}}$ which defines the electrostatic contribution:

$$\mathcal{H}_{\mathrm{el}} = \frac{(ne - C_{\mathrm{g}}V_{\mathrm{g}})^2}{2C_{\Sigma}}. \tag{2.23}$$

Subsequently, the four tunneling rates Γ, corresponding to two barriers and two possible directions, can be calculated in time-dependent pertubation theory, dependent on charge state n whose occupation probability p_n is given by a master equations [109]:

$$\frac{d}{dt}p_n = -\left(\Gamma_{n-1,n} + \Gamma_{n+1,n}\right) \cdot p_n + \Gamma_{n,n+1} \cdot p_{n+1} + \Gamma_{n,n-1} \cdot p_{n-1}. \tag{2.24}$$

The overall current is then given as

$$I = e \cdot \sum_{n=-\infty}^{+\infty} p_n \cdot \left(\overrightarrow{\Gamma_1}(n) - \overleftarrow{\Gamma_1}(n)\right), \tag{2.25}$$

which recovers the physics of sequential processes where tunneling over one barrier determines the behaviour, leading to $I \propto 1/R_{\mathrm{t}}$.

2.2.3 The Intermediate and Open Quantum Dot Regimes

Although the two more strongly coupled regimes are from smaller importance for the used devices in this work, their presence is hardly completely separable. Especially the occurrence of higher-order tunneling effects usually depends on specific device resistances which uncontrollably vary with common fabrication techniques. These features can complicate the spectra in a regime still resembling the closed quantum dot.

The Intermediate Quantum Dot Regime

For moderate coupling of the dot to the leads second-order processes come to the fore which involve simultaneous tunneling over both junctions and therefore scale with $I \propto 1/R_{\mathrm{t}}^2$. In this context *simultaneous* refers to a time scale $\hbar/\Delta E$ given by the Heisenberg uncertainty, where ΔE is the energy of the state relative to the Fermi energy. This principle allows for the occupation of classically forbidden states with energies outside of the transport window. Different processes are possible within these restrictions, either giving rise to transport channels within the Coulomb diamonds or adding to the tunnel rates of the sequential events. The most commonly occurring effects are *elastic cotunneling*, *Kondo effect* and *inelastic cotunneling* which are thus briefly introduced.
Elastic cotunneling (see fig. 2.9) leads to conduction in the tails of lifetime broadened peaks and can be observed already for small bias, corresponding to a situation close to

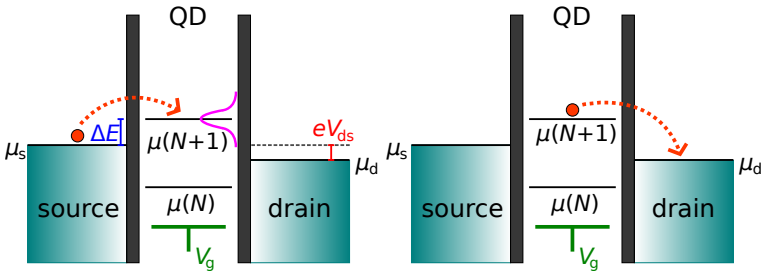

Figure 2.9: In an elastic cotunneling process a classically forbidden level $\mu(N+1)$ can be briefly occupied within the Heisenberg uncertainty (schematically represented by the purple line shape). A similar process exists for the occupied level $\mu(N)$ and reversed chronology of the partial tunneling processes.
Based on [102]

equilibrium [112]. It is always present, even though its contribution may be vanishingly small, and adds to the sequential tunneling as a background in the blocked regions.

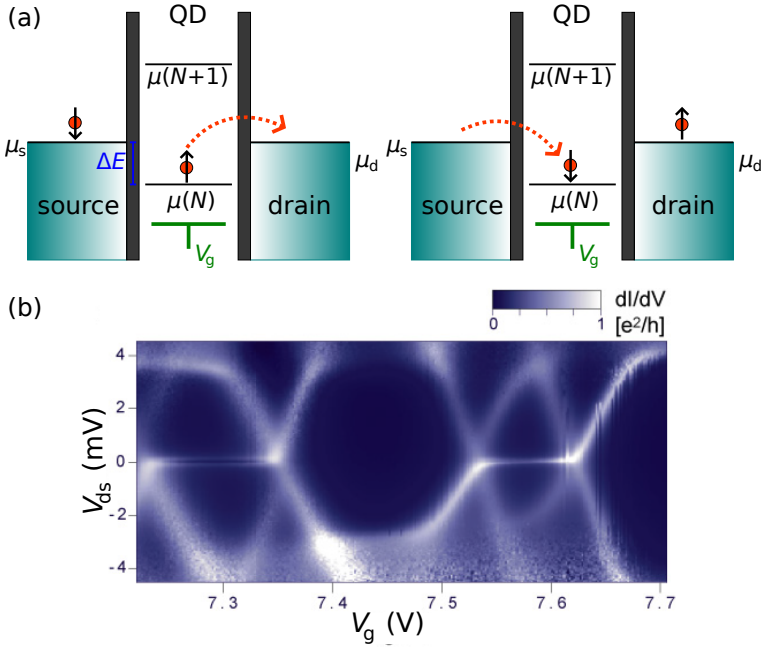

Figure 2.10: a) Within the limits of the Heisenberg uncertainty the electron can tunnel out of the dot to create the intermediate virtual state of an unoccupied $\mu(N)$ level. Then another electron, with high probability of opposite spin due to exchange coupling, can occupy the dot. The energy is conserved in this process. b) Measurement of a CVD grown CNT at $30\,\mathrm{mK}$ reveals conductance ridges at zero bias for odd electron occupation, corresponding to a $S = 1/2$ Kondo effect. The spin states are split due to a small magnetic field.
a) Based on [102] b) Adapted from [113]

The Kondo effect in quantum dots can be considered as an elastic co-tunneling process. It was discovered as a resistance increase in metals with magnetic impurities at low temperatures and explained by Jun Kondo [114]: anti-ferromagnetic exchange coupling of

the conduction electrons to the magnetic impurity creates a locally non-magnetic state and increases the effective mass of electrons. The same effect has been discovered in carbon nanotube quantum dots as well [115]. A quantum dot occupied by an odd number of electrons has an unpaired effective spin of $S = 1/2$ and can thus be seen as a magnetic impurity between the leads. Due to exchange coupling electrons from the leads tunnel through the barriers to screen the spin which creates a transport channel at zero bias. These effects are only visible at temperatures below the Kondo temperature T_K which is dependent on the size of the quantum dot and the applied gate voltage.
There is another possibility for a Kondo transport channel, namely for even electron occupation with two electrons forming a $S = 1$ triplet state. For the $S = 0$ singlet state no Kondo effect is observed. The situation is more complicated in carbon nanotubes where a orbital Kondo effect can flip the orbital quantum number [116]. An entanglement of $S = 1/2$ and orbital Kondo is possible, leading to Kondo physics which obeys SU(4) symmetry [116] [117].

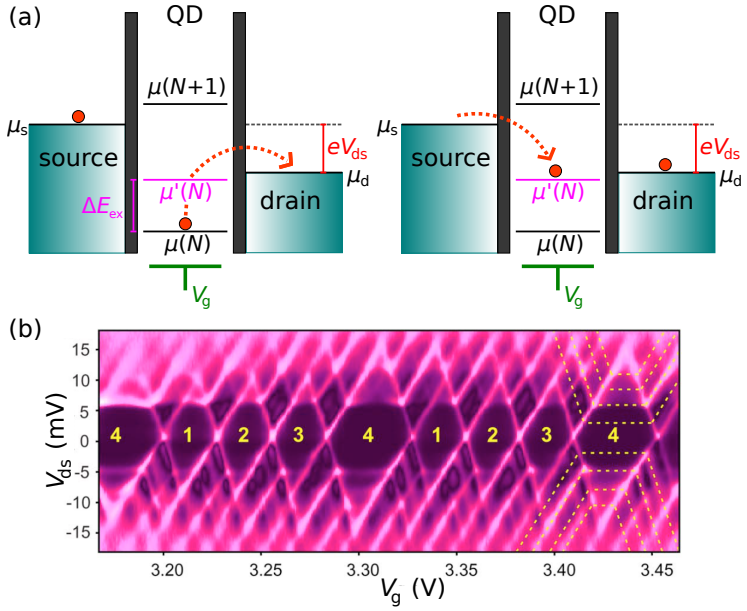

Figure 2.11: a) Inelastic cotunneling process. An electron tunnels from the ground state to the drain and the excited state gets occupied via another tunneling process within Heisenberg's uncertainty. b) A CVD grown CNT of 750 nm measured at 300 mK. Several conduction channels inside of a Coulomb diamond are visible which correspond to inelastic cotunneling.
a) Based on [102] b) Adapted from [106]

Inelastic cotunneling gains importance for higher bias voltages where the dot is noticeably driven out of equilibrium. At $V > \Delta E_{ex}$, the splitting of the first excited state, an electron can tunnel out of the ground state of the dot $\mu(N)$ which shortly creates a classically forbidden intermediate virtual state. Subsequently another electron occupies the excited state. This process opens a transport channel inside the Coulomb diamond in parallel to the zero-bias axis and due to a second equivalent process it appears symmetrically. The excited state of the dot can further relax via phonon or photon emission or in a

cotunneling process involving a single barrier. Excitations involved in this process can be of electronic or vibrational origin.

The Open Quantum Dot Regime

In the open quantum dot regime transport is governed by highly transparent barriers where $\hbar\Gamma \gg E_C$. In carbon nanotubes this regime is typically realized for p-type carrier transport with good contact metals. Transport cannot be broken down to single particle level anymore and interference plays an important role, especially for decreasingly small devices approaching the charge carriers' coherence length. When transport over the nanotube is quasi-ballistic and the contacts give rise to conductance close to the quantum limit, the nanotube can act as a coherent electron waveguide and a resonant cavity is formed between the nanotube-metal interfaces. As a result, an interference pattern with origin closely related to the classical optical Fabry-Perot phenomenon can be observed [118] [101].

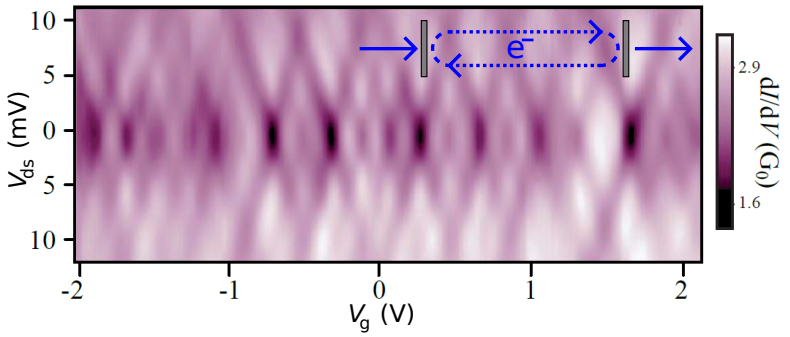

Figure 2.12: Interference pattern of a 530 nm CNT measured at 4 K. The inset illustrates the principle of multiple reflections in the cavity created between the CNT-contact interfaces which create the interference.
Adapted from [118]

However, these interference patterns are not a given. Many devices show single particle tunneling effects on the p-side as well, often with increased conductance level and hence deformed Coulomb diamonds.

2.3 The Effect of Spin and Orbit in Carbon Nanotubes

The influence of a magnetic field on the band gap of carbon nanotubes was first described by Ajiki et al. [119] within a *kp*-pertubation approach and subsequently generalized by Lu [120], who found a metal-insulator transition, a band gap opening for certain metallic nanotubes. Consequently a magnetic moment can be assigned to carbon nanotubes, corresponding to circumferential motion of the electrons. On the other hand, spin-orbit coupling was overlooked for a long time, despite being theoretically predicted [121]. Its presence lifts the fourfold degeneracy and leads to several interesting effects that have to be taken into account for applications involving spin and valley.

This section intends to provide an overview of occurring effects following the review paper of Laird et al. as guideline. More details can be found in aforesaid work.

2.3.1 Orbital Magnetic Moment

For a field parallel to the nanotube axis, described by the vector $\mathbf{T}$, the dispersion relation is given by the transformation [119] [120] $E_B(\mathbf{k}) = E_{B=0}\left(\mathbf{k} + \mathbf{\Delta k}_\perp^B\right)$ with a magnetic field induced displacement

$$\mathbf{\Delta k}_\perp^B = \Delta k_\perp^B \hat{\mathbf{C}} = \frac{edB_\parallel}{4\hbar}, \tag{2.26}$$

where $\hat{\mathbf{C}}$ is the unit vector of chirality formerly introduced. This displacement of the Dirac cones with respect to the quantization lines opens a band gap for metallic nanotubes, given as

$$E_g\left(B_\parallel\right) = \frac{edB_\parallel}{2}. \tag{2.27}$$

due to the linear dispersion. For nanotubes with a band gap at zero field the behaviour is slightly different, since the quantization axes for the valleys K and K' have opposite $k_\perp$-values with respect to the Dirac cone center. Therefore the sub-band gaps for K and K' evolve conversely with the value given in eq. 2.27, leading to a band gap closing at a critical magnetic field. For further increasing fields the band gap reopens again [122]. This effect usually requires large fields but was nevertheless experimentally demonstrated Jhang et al. [123] in 2011.
The change of energy in an applied magnetic field allows for the assignment of a magnetic moment μ in line with the general concept $E = -\mu B$. In this particular case one can define

$$\mu_{\mathrm{orb}} = \frac{\partial E}{\partial B_\parallel} = \frac{ed}{4\hbar}\frac{\partial E_{\mathrm{D}}\left(k_\perp, k_\parallel\right)}{\partial k_\perp}, \tag{2.28}$$

with the dispersion of the cones given in eq. 2.7. For low-energy electrons close to the band gap this reduces to

$$\mu_{\mathrm{orb}} \equiv \frac{edv_{\mathrm{F}}}{4}, \tag{2.29}$$

directed along the nanotube axis. The orbital magnetic moment can be illustratively explained with circumferential movement of the electrons around the nanotube, depending on the esign of μ_{orb} of the sub-bands at the Dirac points K and K' in particular nanotubes.

This leads, for example, to clockwise motion in the valence band and anti-clockwise motion in the conduction band for the cone at K, while the situation is exactly reversed at K' due to symmetry considerations. The opposite magnetic moment was experimentally demonstrated by means of the resulting energy splitting in an applied B-field by Jarillo-Herrero et al.[124].

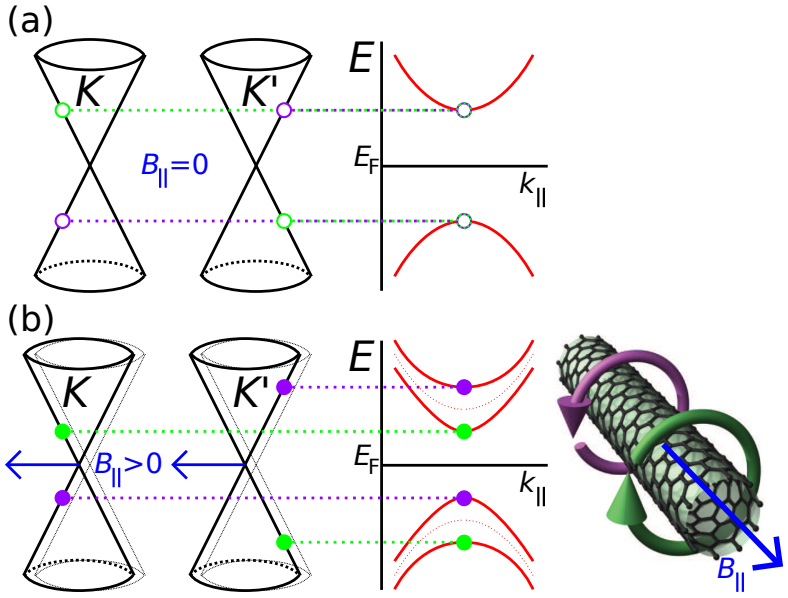

Figure 2.13: A nanotube with a band gap at zero field $B_{||} = 0$ is valley-degenerat (upper panel). When a field is applied the Dirac cones shift with respect to the quantization lines and the valley degeneracy is lifted (lower panel). This can be assigned to a circumferential motion of the electrons in a direction corresponding to the presign of the orbital magnetic moment.
Based on[125]

Along the lines of the *g-factor* $g_s \equiv \mu_s/\mu_B \approx 2$ for the Zeeman effect one can define $g_{orb} \equiv \mu_{orb}/\mu_B$ and express the interplay of both effects in a B-field[126],

$$\Delta E_B = \left(\frac{1}{2} g_s s + g_{orb} \tau \cos(\theta)\right) \mu_B B, \tag{2.30}$$

with $s = \pm 1$ representing both spin directions $\{\uparrow, \downarrow\}$, the index $\tau = \pm 1$ for the two valleys $\{K,K'\}$ and the angle of B-field and nanotube axis θ. Jespersen et al.[126] also found a dependence of g_{orb} on the confinement energy and the shell filling of the quantum dot. Usually g_{orb} is many times higher than g_s[122][124][126].

2.3.2 Spin-Orbit Coupling

Spin-orbit coupling $\mathcal{H}_{LS} = \Delta_{SO}\mathbf{LS}$ in carbon structures was generally believed to be small due to the low atomic mass number $Z = 6$. The resulting intrinsic spin-orbit coupling of flat graphene was reported[127] to be in the order of $\Delta_{SO} \propto 10\,\text{mK} \approx 1\,\mu\text{eV}$. However, in 2000 Ando[121] predicted the existence of a significant spin-orbit coupling in

carbon nanotubes, related to curvature effects breaking the spatial inversion symmetry of graphene. Therefore hopping processes between neighbouring atoms in different orbitals σ and π should be allowed which strongly enhance the effect of spin-orbit interaction on the inter-atomic scale. Indeed, in 2008 Kümmeth et al.[98] provided first experimental proof of significant spin-orbit coupling in carbon nanotubes of $\Delta_{SO} \approx 370\,\mu eV$. This discovery was enabled by improved fabrication techniques to yield clean CNT devices. Prior to this the influence of spin-orbit coupling was masked by larger intervalley scattering effects $\Delta_{KK'}$[1] due to disorder.

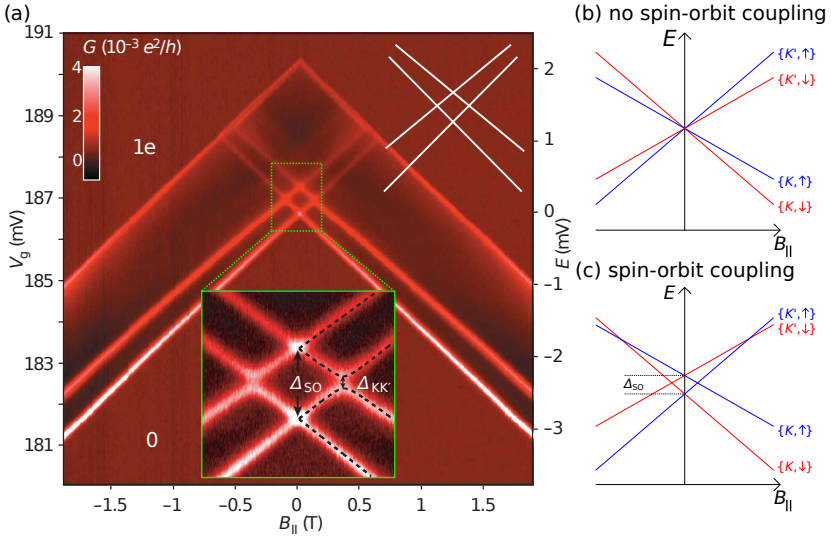

Figure 2.14: a) Measurement of the energy splitting in a longitudinal magnetic field at the transition of the zero- and one-electron state in a CNT quantum dot. The close-up clarifies the presence of spin-orbit coupling Δ_{SO} and intervalley scattering $\Delta_{KK'}$. Spin-orbit coupling lifts the fourfold degeneracy in a way schematically presented in (c). b) The energy levels in a longitudinal field without spin-orbit coupling but with the combined effect of coupling to an orbital moment and a spin, as introduced in sec. 2.3.1. c) The splitting in a longitudinal field with spin-orbit coupling.
a) Adapted from[98] b,c) Based on[125]

The special character of the spin-orbit coupling is governed by its preservation of time-reversal symmetry, whereas external magnetic fields break this symmetry by means of a Zeeman contribution. As a result, the zero-field states obey Kramers theorem and are thus twofold degenerate in contrast to the formerly assumed fourfold degeneracy of spin and valley. The sign of Δ_{SO} then determines the composure of these doublets with parallel alignment of the magnetic moments corresponding to spin and valley preferred for $\Delta_{SO} > 0$. This leads to the results measured by Kümmeth et al. and depicted in fig. 2.14c.

Theoretical in-depth studies showed that there are two different types of spin-orbit coupling present in carbon nanotubes[125]. The one predicted by Ando can be considered as

1 The physical meaning of this parameter is the one of an avoided level crossing between the states K and K', as introduced for quantum tunneling of magnetization in chapter 1.

orbital-type, corresponding to a horizontal shift of the Dirac cones. It is the manifestation of a Rashba effect in carbon nanotubes, where the curvature induces a radial electric field which couples to the azimuthal momentum component of the electrons as an effective magnetic field, also breaking the electron-hole symmetry. Next-order terms in pertubation theory give rise to a Zeeman-type effect, corresponding to a vertical shift of the cones dependent on the spin direction [128], which leaves the electron-hole symmetry unaffected. Generally spin and orbit remain good quantum numbers for the presence of longitudinal fields. Jespersen et al. [129] found the coupling to be dependent on the shell filling,

$$\Delta_{\mathrm{SO}} = 2\left(\Delta_{\mathrm{SO}}^{\mathrm{Zee}} \mp \frac{\Delta_{\mathrm{SO}}^{\mathrm{orb}}}{\sqrt{1+\left(\frac{E_\nu}{E_\mathrm{g}}\right)^2}}\right), \tag{2.31}$$

with E_ν denoting the single-particle energy of the ν-th longitudinal mode, E_g the CNT band gap arising from curvature and $\Delta_{\mathrm{SO}}^{\mathrm{Zee}}$ and $\Delta_{\mathrm{SO}}^{\mathrm{orb}}$ the two contributions of spin-orbit coupling. Δ_{SO} generally depends on the CNT diameter as well as the chirality but experimentally measured values vary in a large range [98] [130] and often deviate strongly from theoretical predictions. Furthermore, the situation in nanotubes can be more complicated due to the interplay of spin-orbit and Kondo physics [131].

2.4 Carbon Nanotube Double Quantum Dots

Coupling between quantum dots with their precisely controlled charge states allows for strikingly new effects arising from tunneling processes between individual dots and their quantized states. These interdot transitions depend on the coupling strength as well as the character of the involved states. The inclusion of spin and its selection rules leads to the so-called *Pauli blockade* which enables measurement and manipulation of spin states in such systems [132]. Generally the energy levels and possible transitions are modified by electron-electron interactions, hyperfine coupling effects or disorder (see fig. 2.15a). For carbon nanotubes the spectrum is more complicated due to the presence of the two valleys and spin-orbit coupling, leading to combined spin-valley effects observable in transport measurements.

2.4.1 Charge Diagrams in Double Quantum Dots

As a first steps towards a description of CNT double quantum dots, one can study charge diagrams of a generic double quantum dot, neglecting spin and valley effects. This generalization of the concept introduced in sec. 2.2.2 was derived by van der Wiel et al. [133]. Similar to the single quantum dot (see fig. 2.7b) the double dot can be represented by a system of tunnel junctions and capacitances, as shown in fig. 2.15b. It is important to state the role of several gates present in this system: While it is generally possible to realize double quantum dots with just two gates, each controlling

an individual dot, full control of the system can only be achieved for five gates or more. Then the additional three gates are used to tune the coupling of each respective barrier. Nevertheless, the gates controlling the dots are labelled with *g1* and *g2* in this theoretical section.

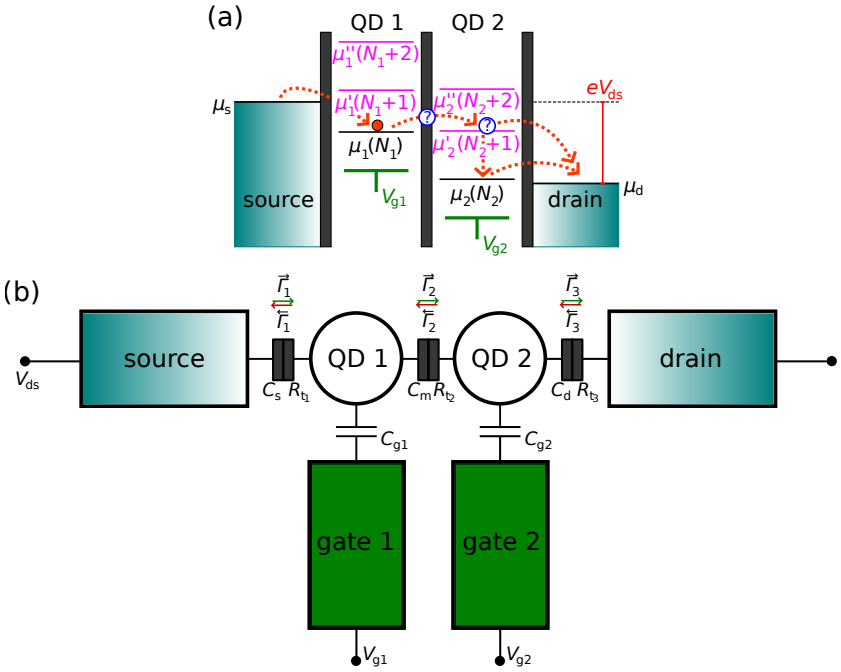

Figure 2.15: The double dot as an expansion of the single dot scheme of fig. 2.7. a) Transport over the double dot system depends on the alignment of the potentials of both dots. Excitation levels and selection rules can play an important role in these coupled quntum systems. b) The interdot barrier C_m determines the coupling of the two individual dots. The dots are tuned by individual local gates.

Similar to the simple semi-classical treatment in sec. 2.2.2, one can define the chemical potentials of the two dots as

$$\begin{aligned}\mu_1 &= U\left(N_1, N_2\right) - U\left(N_1 - 1, N_2\right) \\ &= \left(N_1 - \frac{1}{2}\right) E_{\mathrm{C}_1} + N_2 E_{\mathrm{C}_\mathrm{m}} - \frac{1}{e}\left(C_{\mathrm{g}1} V_{\mathrm{g}1} E_{\mathrm{C}_1} + C_{\mathrm{g}2} V_{\mathrm{g}2} E_{\mathrm{C}_\mathrm{m}}\right), \end{aligned} \tag{2.32}$$

$$\begin{aligned}\mu_2 &= U\left(N_1, N_2\right) - U\left(N_1, N_2 - 1\right) \\ &= \left(N_2 - \frac{1}{2}\right) E_{\mathrm{C}_2} + N_1 E_{\mathrm{C}_\mathrm{m}} - \frac{1}{e}\left(C_{\mathrm{g}1} V_{\mathrm{g}1} E_{\mathrm{C}_\mathrm{m}} + C_{\mathrm{g}2} V_{\mathrm{g}2} E_{\mathrm{C}_2}\right), \end{aligned} \tag{2.33}$$

for neglected energy level splitting and cross-capacitances C_{ij}. The appearing charging energies are given by

$$E_{\mathrm{C}_{1/2}} = \frac{e^2}{C_{1/2}} \left(\frac{1}{1 - \frac{C_\mathrm{m}^2}{C_1 C_2}} \right), \tag{2.34}$$

$$E_{\mathrm{C_m}} = \frac{e^2}{C_\mathrm{m}} \left(\frac{1}{\frac{C_1 C_2}{C_\mathrm{m}^2} - 1} \right), \tag{2.35}$$

where $E_{\mathrm{C}_{1/2}}$ describe the individual dots with capacitances $C_{1/2} = C_{\mathrm{s/d}} + C_\mathrm{m} + C_{\mathrm{g1/g2}}$. $E_{\mathrm{C_m}}$ is the energy change in one dot when an electron is added to the other, hence can be considered as a coupling. One can distinguish the limiting cases of no coupling, $C_\mathrm{m} = 0$, where the dots are charged individually, and the one where $C_\mathrm{m}/C_{1/2} \to 1$ becomes the dominant capacitance. In the latter case one effective large dot is created.

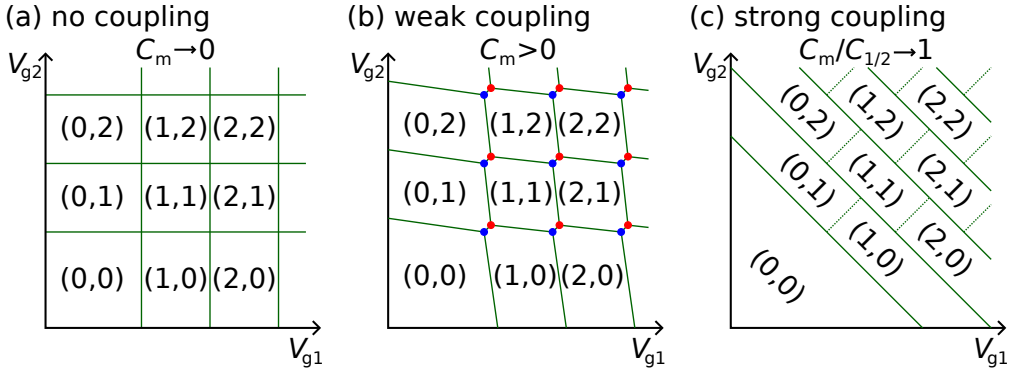

Figure 2.16: The double dot system for the cases of a) no interdot coupling b) weak interdot coupling and c) strong interdot coupling. Charge states are now based both dots with notation (i,j). The case of weak coupling exhibits pairs of triple points which correspond to an electron transport process (blue dot) and a hole transport process (red dot) over the double dot.
Based on [133]

It is beneficial to look more closely at the case of weak coupling (see fig. 2.16b) to study excitations and selection rules of a double dot system. For low bias voltages the charging diagrams now shape pairs of *triple points* where three charge states of the double dot coincide. Ideally transport is only possible at these points. The pairwise occurrence can be explained by the presence of an electron process,

$$(N_1, N_2) \to (N_1 + 1, N_2) \to (N_1, N_2 + 1) \to (N_1, N_2)\,, \tag{2.36}$$

and a hole process

$$(N_1 + 1, N_2 + 1) \to (N_1 + 1, N_2) \to (N_1, N_2 + 1) \to (N_1 + 1, N_2 + 1)\,, \tag{2.37}$$

whose energy differences $E_{\mathrm{C_m}}$ determine the spacing of the triple point pair.

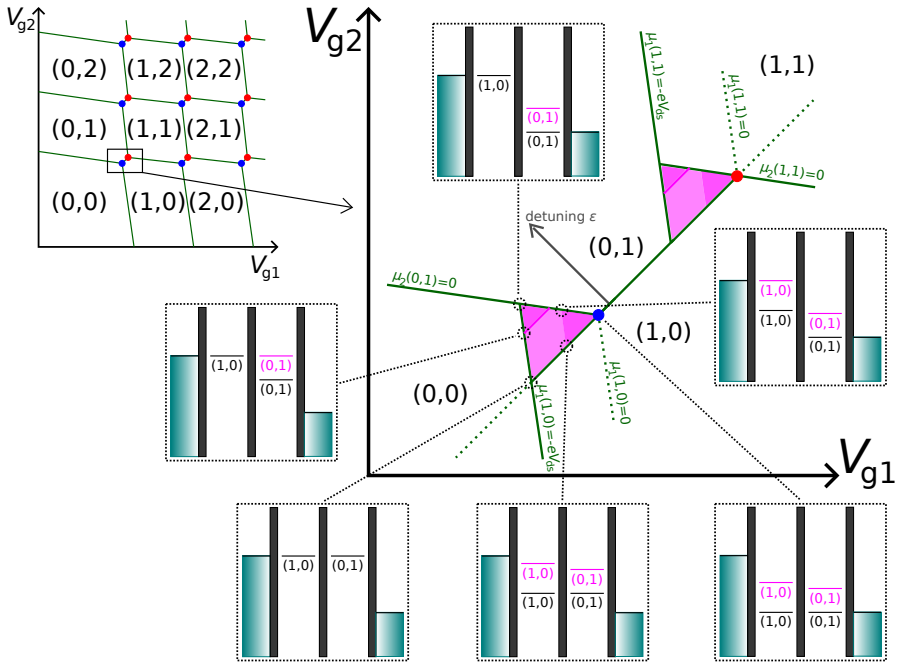

Figure 2.17: Extension of a pair of triple points to bias triangles for large voltages V_{ds}. Excited states of the quantum dots appear as elastic tunneling channels (solid purple line) parallel to the triangle base. For further increased bias the triangles merge and can contain several excited states.
Based on [132]

Taking a level splitting of the quantum dots into account, one can probe the excited states by applying a larger bias voltage. For non-zero current the triple points then extend to *bias triangles* which merge for increasing V_{ds} and exhibit conductance channels parallel to the triangle base [133] [132] [134], corresponding to excited states of the quantum dot system. Fig. 2.17 depicts the principle of these triangles for the case of a source connected to voltage V_{ds} and a drain connected to ground. Along the triangle base (and every line parallel to it) the potentials of both dots are only changed equally with respect to source and drain. The axis perpendicular to the base corresponds to a change of the potentials with respect to eachother but constant average. It is usually referred to as *detuning* ε. Along the two legs of the triangle either the potential in the left dot (left leg) or right dot (right leg) are fixed with respect to the voltage source. Moving from the lower left corner along the left leg, inelastic tunneling determines transport until an excited state in the right dots opens another elastic tunneling channel parallel to the base. This allows for spectroscopic analysis of the quantum dot levels.
The presence of a small band gap in CNTs allows for the tuning between p-type and n-type conductance. In samples where the interdot barrier is created by a gate-induced pn-barrier, this leads to four different regimes of the double dot system: a (n,p)-region, a (p,n)-region and two regions with vanishing interdot barrier, (n,n) and (p,p), where the system is made of one effective large dot (see fig. 2.18).

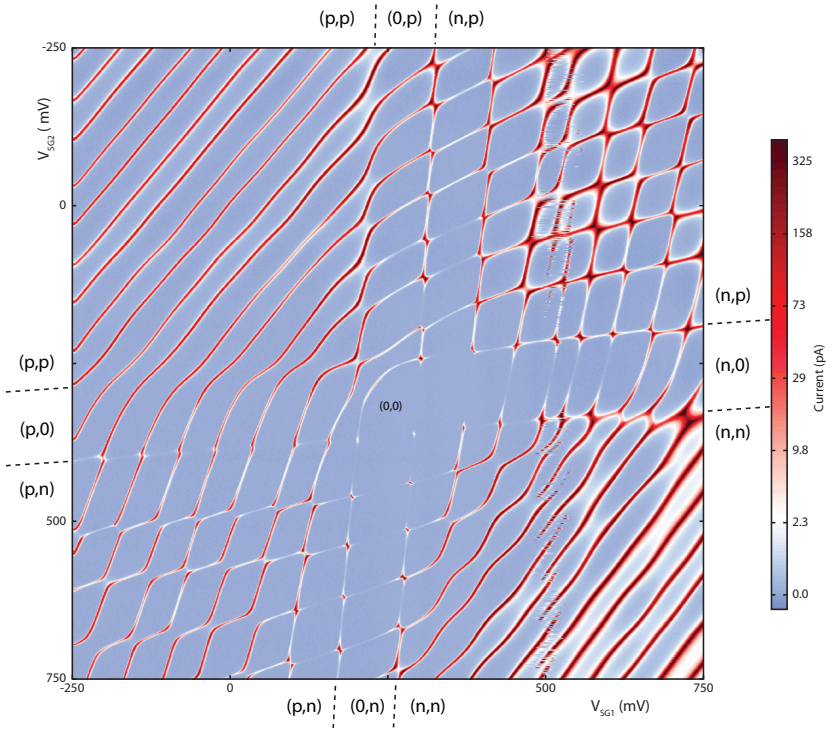

Figure 2.18: Charge diagram for a CNT double quantum dot. The inherent band gap allows for the tuning between weakly coupled (n,p),(pn) and strongly coupled (n,n),(p,p) regimes. Adapted from [135]

2.4.2 The Principle of Pauli Blockade in Conventional Double Dots

Pauli Blockade is a phenomenon generally found in double quantum dots and it stems from selection rules for transitions between multi-electron states when a spin degree of freedom is included. In this case physics is governed by Pauli statistics for fermions or the so called *Pauli exclusion principle* which forbids electrons of parallel spin the occupation of the same spatial orbital. In CNTs the presence of a valley degree of freedom and spin-orbit coupling gives rise to a richer energy spectrum and more complex selection rules in comparison to conventional semiconductors. Therefore the concept is first explained for the latter.

A single quantum dot can enter a one-electron state by tunneling of either a spin-up $|\uparrow\rangle$ or a spin-down $|\downarrow\rangle$ electron. Without an external magnetic field these states are degenerate. The ground state is given by the occupation of the lowest shell of the dot[1]. When a second electron enters the dot, quantum statistics enforces the formation of either singlet states S,S' with spin $S_z = 0$ or a triplet state T with $S_z = 1$. The singlet ground state S is given by the antisymmetric spin state $|S\rangle = (|\uparrow\downarrow\rangle - |\downarrow\uparrow\rangle)/\sqrt{2}$ where two electrons fill the lowest shell to create a antisymmetric total wavefunction obeying the

1 In a CNT this corresponds to the shells created by the longitudinal confinement.

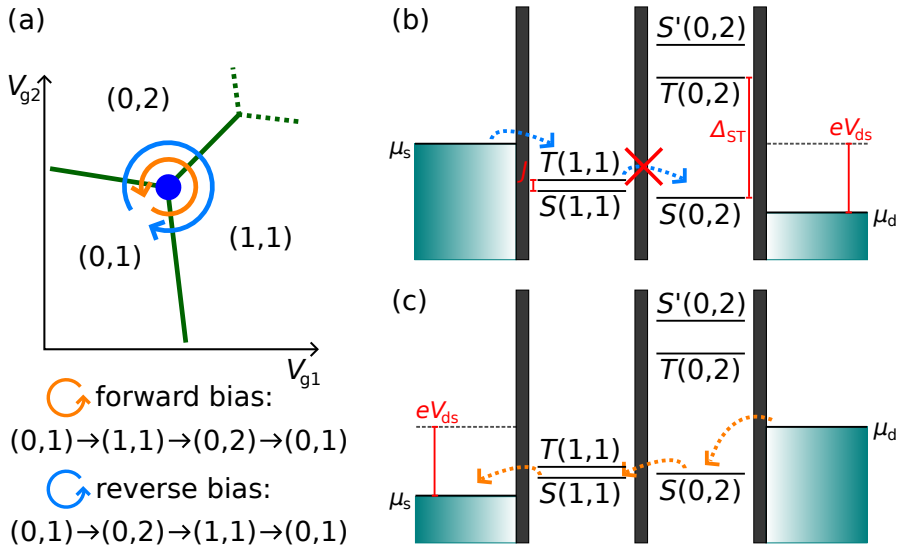

Figure 2.19: Pauli blockade and current rectification in conventional semiconductor double dots. a) The system is generally driven in a two-electron regime. There are two transport processes depending on the direction of the bias voltage. b) For an applied forward bias transport over the double dot is hindered by Pauli blockade. A transition from the $T(1,1)$ to $S(0,2)$ charge state is forbidden due to the Pauli principle while $T(0,2)$ is energetically out of reach. c) For an applied reverse bias the blockade is lifted.
b,c) Based on [125]

Pauli principle for fermions. The triplet state with its symmetric spin state requires the occupation of a higher shell to create an antisymmetric total wavefunction. It is threefold degenerate and includes the states $|T_+\rangle = |\uparrow\uparrow\rangle$, $|T_0\rangle = (|\uparrow\downarrow\rangle + |\downarrow\uparrow\rangle)/\sqrt{2}$ and $|T_-\rangle = |\downarrow\downarrow\rangle$ which are separated from S by the usually significant singlet-triplet splitting Δ_{ST}. The two electrons in different orbitals can also have a symmetric spatial wavefunction to create the excited and non-degenerate singlet state S'.
In the most simple case Coulomb interaction is treated within the constant interaction model and the two-electron states are further separated from the one-electron state by one charging energy E_{C}. In more detail, Coulomb and exchange interactions have to be taken into account [136] which lowers the energy of the triplet with respect to the singlet ground state and therefore create a splitting $\Delta_{\mathrm{TS'}}$ between the triplet T and the excited singlet S'. The energy spectrum of the two-electron dot is schematically shown in fig. 2.19b and 2.19c.
The double dot system is typically driven with two electrons which allows for the investigation of multiple-particle physics and selection rules but keeps the number and complexicty of involved states simple enough. This regime is represented by the triple point in fig. 2.19a where the occupation alters between (0,1), (1,1) and (0,2) with a sequence depending on the polarity of the applied bias voltage. In both cases the right dot remains always occupied by at least one electron, (0,1), with either $|\uparrow\rangle$ or $|\downarrow\rangle$, leading to a broken inversion symmetry that impacts the transition rates in different directions and thus leads to a current rectification [137].

A non-vanishing tunnel coupling between the dots hybridizes the charge states (0,2) and (1,1), leading to a tunnel splitting. However, interdot transitions conserve the spin and tunnel splittings are only created for the same spin states. The transition from $S(1,1)$ to $T(0,2)$ is hence forbidden due to the Pauli principle. In the case of an applied reverse bias (fig. 2.19c), a second electron in the drain can easily tunnel onto the right dot to fill the singlet state $S(0,2)$. Then an electron of the right dot tunnels onto the left dot to create the $S(1,1)$ singlet state and subsequently to the source.
In the other case of an applied forward bias (fig. 2.19b), the left dot is populated with an electron to create a (1,1) state. However, the singlet $S(1,1)$ and triplet $T(1,1)$ are only slightly degenerate in the case of weak tunnel coupling between the two dots, expressed via an effective exchange coupling J. Hence, the occupation probability of both states has the same magnitude[1]. A electron tunneling onto $S(1,1)$ has the possibility to exit via $S(0,2)$, but as soon as $T(1,1)$ is occupied the current over the dot is blocked. On the other hand, the triplet state $T(0,2)$ is too high in energy and cannot be populated. The occupied $T(1,1)$ state therefore has a long lifetime and leads to a blocked transport with is referred to as *Pauli blockade*. The transport is determined by the usually low spin relaxation rate into the singlet state.

2.4.3 Pauli Blockade and Spin-Valley Blockade in CNT Double Quantum Dots

In CNT double dots the principle presented above has to be extended by valley degree of freedom and spin-orbit coupling. An in-depth theoretical treatment of this issue including the effect of Coulomb correlations is provided by Wunsch [138] who calculated the two-electron spectrum of a single dot, subsequently extended by von Stecher et al. [139] to double dots. Weiss et al. [140] also gave insight on this topic with stronger focus on the spin-orbit spectra for suppressed correlations.
Single-particle states describe the correlated two-electron problem sufficiently well for small quantum dots. When intervalley scattering as well as the weak dependence of the wave vectors on spin-valley degrees is neglected, one can separate the orbital from the spin-valley part of the single-particle states localized in the two dots [138]:

$$E_{n,\tau,s}^{QD1/QD2} \approx E_n \pm \frac{\varepsilon}{2} + E_{\tau,s}. \tag{2.38}$$

Here E_n are the orbitals resulting from the longitudinal confinement[2], $\pm\varepsilon/2$ is a symmetric detuning in the dots and $E_{s,\tau}$ the contribution of the spin-valley degrees of freedom, with again $s = \pm 1$ for spins $\{\uparrow, \downarrow\}$ and $\tau = \pm 1$ for the two valleys $\{K,K'\}$.
Since interactions, described by a long-range Coulomb potential, are diagonal in the spin-valley space [138], both the orbital and the spin-valley part contribute separately to the energy and the wave functions of the two-particle problem. The wave overall

1 However, J can be electrically changed via the detuning ε.
2 Again only the two lowest levels are included.

	spin-orbit energy		
	$-\Delta_{\mathrm{SO}}$	0	Δ_{SO}
$S(0,2)$	$(K\downarrow, K'\uparrow)$	$(K\downarrow, K\uparrow)$	$(K\uparrow, K'\downarrow)$
		$(K\downarrow, K'\downarrow)$	
		$(K\uparrow, K'\uparrow)$	
		$(K'\uparrow, K'\downarrow)$	
	spin-orbit energy		
	$-\Delta_{\mathrm{SO}}$	0	Δ_{SO}
$AS(0,2)$	$(K\downarrow, K\downarrow)$	$(K\downarrow, K\uparrow)$	$(K\uparrow, K\uparrow)$
	$(K\downarrow, K'\uparrow)$	$(K\downarrow, K'\downarrow)$	$(K\uparrow, K'\downarrow)$
	$(K'\uparrow, K'\uparrow)$	$(K\uparrow, K'\uparrow)$	$(K'\downarrow, K'\downarrow)$
		$(K'\uparrow, K'\downarrow)$	
	spin-orbit energy		
	$-\Delta_{\mathrm{SO}}$	0	Δ_{SO}
$S'(0,2)$	$(K\downarrow, K'\uparrow)$	$(K\downarrow, K\uparrow)$	$(K\uparrow, K'\downarrow)$
		$(K\downarrow, K'\downarrow)$	
		$(K\uparrow, K'\uparrow)$	
		$(K'\uparrow, K'\downarrow)$	

Table 2.1: The three lowest multiplets in a CNT quantum dot occupied by two electrons. The multiplets are named according to their longitudinal symmetry under electron exchange and subdivided with respect to their spin-orbit energy.

antisymmetric functions can then be classified according to their orbital symmetry under particle exchange[139]. This leads to a ground state multiplet of six states with symmetric orbital part or parity $P = 1$ and a higher multiplet of ten states with antisymmetric orbital part or $P = -1$. These multiplets are the carbon nanotube's analogons to the formerly presented singlet state $S(0,2)$ and triplet state $T(0,2)$ in conventional semiconductors. With respect to their longitudinal symmetry they are labelled with $S(0,2)$ and $AS(0,2)$ and tabulated in table 2.1, together with the higher symmetric multiplet $S'(0,2)$.
In this approximation the energy difference between the multiplets is solely created by the orbital part which includes the Coulomb correlations. The splitting within the multiplets is due to spin Zeeman and orbital Zeeman effect as well as spin-orbit coupling (see sec. 2.3). The eigenstates to these tabulated indices $\tau s, \tau' s'$ read

$$S_{n\tau s,n'\tau' s'}(0,2) = |1\tau s\rangle_1 |1\tau' s'\rangle_2 - |1\tau s\rangle_1 |1\tau' s'\rangle_2 , \tag{2.39}$$

$$\begin{aligned} AS_{n\tau s,n'\tau' s'}(0,2) = {} & |1\tau s\rangle_1 |2\tau' s'\rangle_2 - |2\tau s\rangle_1 |2\tau' s'\rangle_2 \\ & + |1\tau' s'\rangle_1 |2\tau s\rangle_2 - |2\tau' s'\rangle_1 |2\tau s\rangle_2 , \end{aligned} \tag{2.40}$$

$$\begin{aligned} S'_{n\tau s,n'\tau' s'}(0,2) = {} & |1\tau s\rangle_1 |2\tau' s'\rangle_2 + |2\tau s\rangle_1 |2\tau' s'\rangle_2 \\ & - |1\tau' s'\rangle_1 |2\tau s\rangle_2 - |2\tau' s'\rangle_1 |2\tau s\rangle_2 \end{aligned} \tag{2.41}$$

and the (1,1) configurations can be obtained by identifying $S'(0,2) \rightarrow S(1,1)$, $AS(0,2) \rightarrow AS(1,1)$ and assigning $n = 1(2)$ to the lower orbital in the right (left) dot. For $n = n' = 1$ the states $AS(1,1)$ then vanish. Therefore a transformation from $AS(1,1)$ to (0,2) is only possible for certain conditions: a change in spin s and/or valley τ for $AS(1,1) \rightarrow S(0,2)$ or the involvement of higher orbitals in the right dot for $AS(1,1) \rightarrow AS(0,2)$. The $AS(1,1)$ states are thus referred to as *blocked*, similar to the case of conventional semiconductors [125]. Due to the interplay of spin and valley the effect is called *spin-valley blockade*.

However, the energy difference $\Delta_{S,AS}$ between $S(0,2)$ and $AS(0,2)$ in clean carbon nanotubes is smaller than in typical conventional semiconductors due to Coulomb correlations and valley degeneracies [135] [138]. A workaround is provided by disorder or smaller dot sizes, which are experimentally either not desirable or feasible. Alternatively, $\Delta_{S,AS}$ can be enhanced by using the band gap as an effective additional splitting for certain transitions, as demonstrated by Pei et al. [60] for the triple point $(3h,0) \rightarrow (2h,0) \rightarrow (3h,1e) \rightarrow (3h,0)$. On the other hand, relaxation or dephasing of spin and valley states, mediated by hyperfine coupling, can lift spin-valley blockade in CNTs [60] [141] [142].

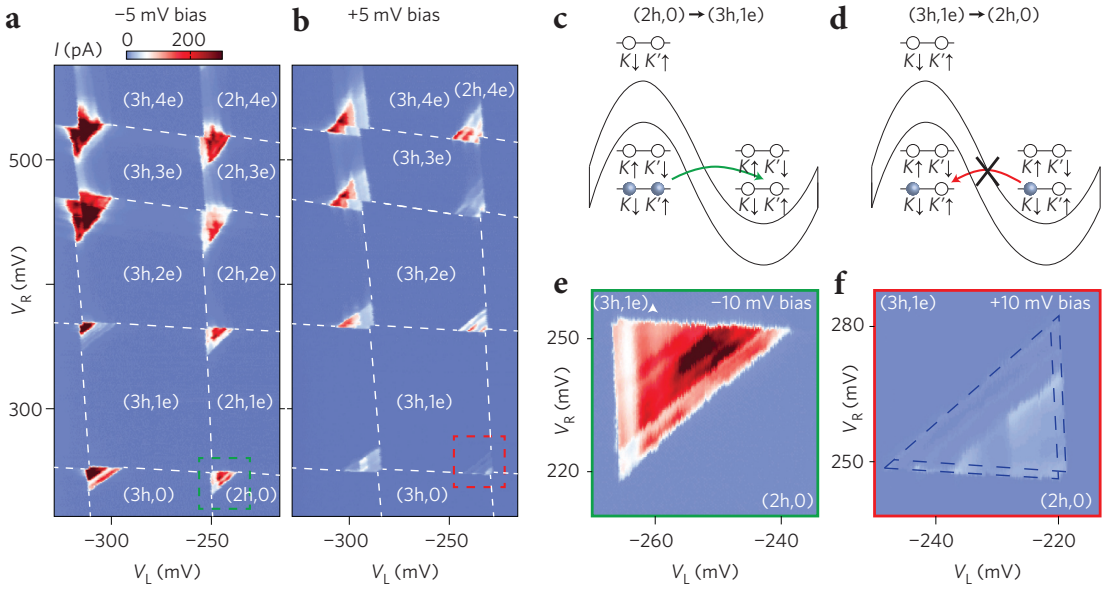

Figure 2.20: Charge diagram and bias triangles for a CNT double dot in a (p,n) regime for a) reverse bias with increased conductance and b) forward bias, where spin-valley blockade is enhanced due to the effect of the CNT band gap. d/f) The double dot bands and the detailed bias triangle marked in fig. 2.20a, where the transport is not blocked. e/g) The situation of spin-valley blockade depicted in 2.20b.
Adapted from [60]

2.5 Molecular Spintronics with SMMs and CNTs

In order to integrate single-molecule magnets in electronics and spintronics, techniques for contacting these tiny objects in a controlled way have to be developed. Differing in type of the contact, coupling strength or number of the molecules, several possible implementations were proposed [8], of whom many have been already investigated.
A crucial component of such applications is usually the possibility to readout (or sometimes manipulate) the SMM's spin states with a current flow. Broadly speaking one can hence classify devices by means of their current path, based on the notion if current passes the molecule directly[1] or adjacently through a coupled carrier substrate. Fig. 2.21 illustrates three possible concepts in this mold.
For the case of one directly coupled SMM, spin transistor devices can be fabricated, where the two connections are made up of a conductive surface and a scanning tunneling microscope tip, metallic break junctions or electromigrated metallic junctions. Particularly the latter case has been extensively studied in the NanoSpin group in recent years [49] [143].

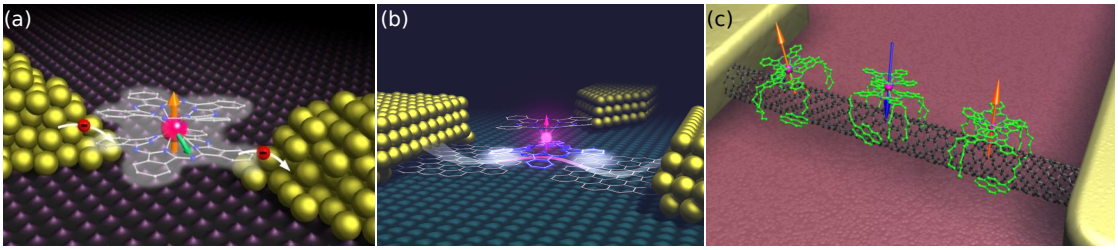

Figure 2.21: Three different realizations of SMMs integrated in an electronic circuit. a) A molecular spin transistor with a single SMM connected with an electromigrated gold junction. b) A similar device based on a graphene junction. c) A spin valve with SMMs grafted onto a carbon nanotube.
Adapted from a) [143] b) [144]

Another enticing concept uses the favorable coupling, presented in more detail in sec. 5.3, of carbon nanostructures and SMMs to create supramolecular hybrid structures [62]. While graphene has been investigated as a possible carrier [145] [144], carbon nanotubes have shown particular promise. In those devices the current flows through the nanotube, weakly coupled to the SMM, which enables non-invasive readout, leaving the molecular magnetic properties basically unchanged. In case of two or more coupled SMMs this gives rise to the model of supramolecular spin valves, but one could also envision an extension of the circuit to obtain a nano-SQUID [58] of extraordinarily high magnetic sensitivity.
It should be added that CNTs have been used in similar fashion by other groups, for instance as detector for Mn_4 molecules [146], lysozyme proteine dynamics [147] or charge blinking effects of semiconductor nanocrystals [148], usually realized with noise measurements. The following synopsis is, however, limited to the results obtained by the NanoSpin group for supramolecular devices based on CNTs and SMMs.

1 In the case of $TbPc_2$ this notion addresses nevertheless the surrounding ligands and not the magnetic core.

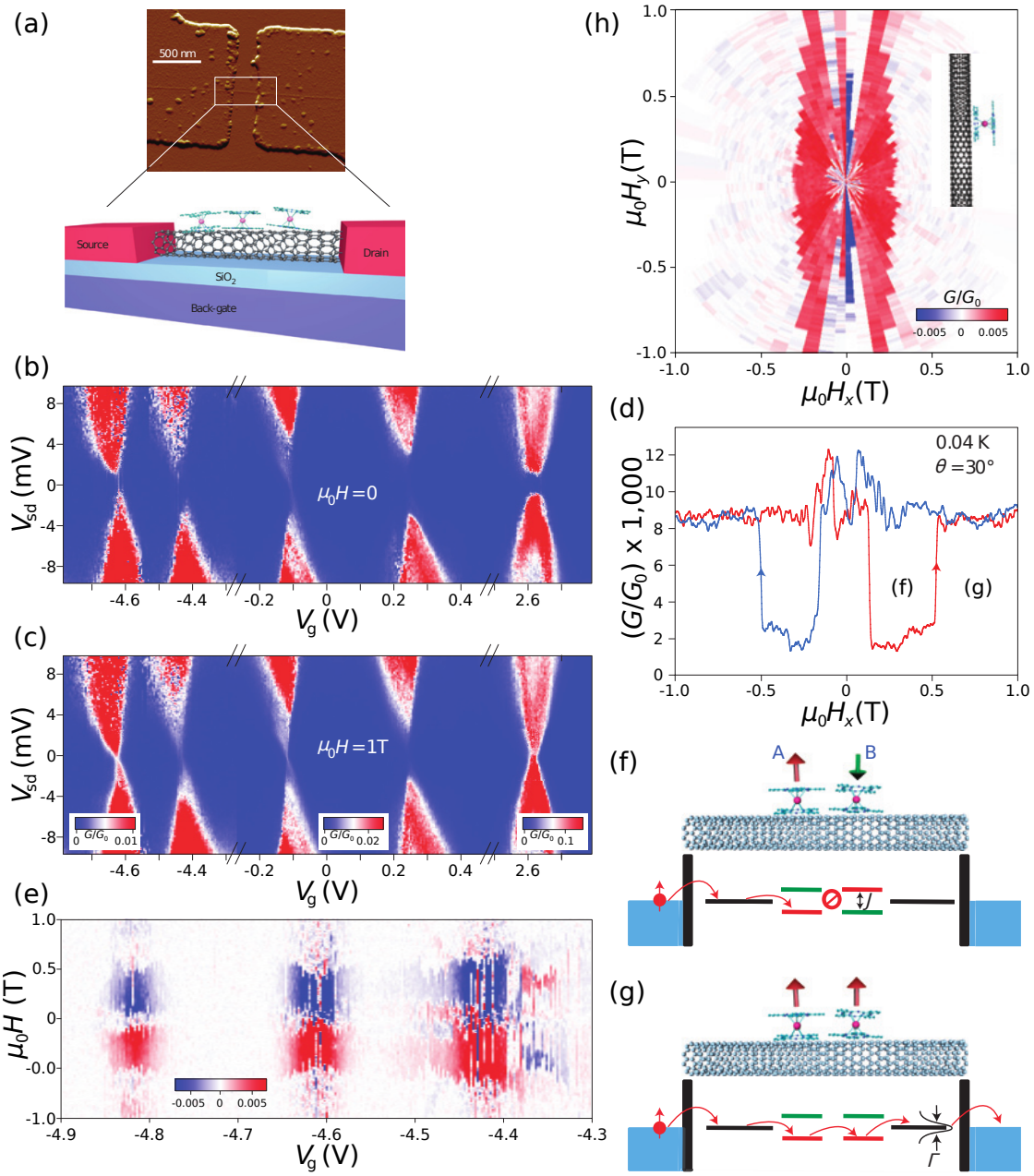

Figure 2.22: a) AFM image and schematic of the device. b) Coulomb map without applied magnetic field, where random orientation of the molecules blocks transport at the degeneracy points. c) Application of a field aligns the molecules and enables transport. d) Zero-bias magnetoconductance curve, characteristic for all Coulomb peaks. The jumps at small fields are attributed to QTM, the ones at large fields to direct phonon processes. e) Gate dependence of the conductance measurement, plotted as difference of trace and retrace to measure magnetic hysteresis. f,g) Schematic transport in the hybrid system. Molecules induce local spin-polarized dots which explain the different conductance levels in (d). h) Conductance measurement in the $H_x - H_y$-plane, indicating the magnetic easy axis along x.
Adapted and reconstructed from [63]

2.5.1 CNT Spin Valve

In 2011 Urdampilleta et al.[63] from the NanoSpin group reported on the realization of a supramolecular spin valve, using CNTs and SMMs, with the results compiled in fig. 2.22. The CNTs were deposited from solution onto Si/SiO_2 with back gate functionality, contacted from the top and subsequently functionalized with $TbPc_2$.
Coulomb maps with and without applied magnetic field indicate the influence of the attached molecules, as transport at the charge degeneracy points is blocked for random alignment of the molecules' magnetic moments . Aligning the moments with an external field lifts the blockade.
This gives rise to a spin valve effect (fig. 2.22d), which manifests itself as two different conductance levels, alternating via sharp jumps. These jumps can be attributed to the magnetization reversal in individual SMMs, creating states of parallel alignment with high conductance and antiparallel alignment with low conductance. The reversal processes can be assigned to the discussed concepts of quantum tunneling (at small fields) and phonon-assisted reversal (at large fields). In this case, the presence of four separate jumps indicates the coupling of two SMMs to the CNT[1].
The working point in the applied gate needs to be adjusted to find such behaviour, as there are usually only small windows in which the coupling of SMM CNT is sensitive to the spin valve effect. This is particularly true for devices with only one back gate electrode, allowing for only the manipulation of one *global* parameter, possibly affecting an ensemble of molecules. The effect is also very sensitive to the direction of the applied magnetic field, as $TbPc_2$ has strong anisotropy and the molecules generally attach randomly aligned to the CNT. The hysteresis signal thus allows for identification of the molecules easy axis (fig. 2.22h), in this case along x. As different molecules practically never align the same way, this anisotropy can be exploited to detune different molecular contributions.
The transport via such an coupled system can be intuitively explained with the creation of local spin-polarized quantum dots due to exchange interaction J. The spin splitting creates effective tunnel barriers for one (parallel configuration) or both spin types (antiparallel configuration), giving rise to the two observed conductance levels. This effect is hence very similar to the GMR explained in sec. 1.1.1, but arises on the molecular scale.
Measurements for a similar device, presented in fig. 2.23, later revealed the nuclear spin states of terbium[149], manifesting themselves as four separate and reproducible jumps in conductance at magnetic field values corresponding to the positions of the avoided level crossings (fig. 2.23a,b). Here, the applied field H is aligned with the easy axis of molecule B, rendering QTM processes symmetric around $H = 0$. The probability of these QTM processes shows good agreement with the theoretical Landau-Zener model.
It is important to point out the particular nature of these samples, for which the nanotubes are non-suspendedly placed directly on the substrate surface. This coupling to a bulk bath enables QTM transitions in the first place, even though the linear increase in tunnel

1 Generally, there can be more molecules grafted to the CNT, which do not respond to applied magnetic fields in the chosen range due to either very weak coupling or strongly deviating magnetic easy axis.

splitting Δ with transverse magnetic field, shown in the inset of fig. 2.23c, could be a signal for the importance of conservation laws even for this case.

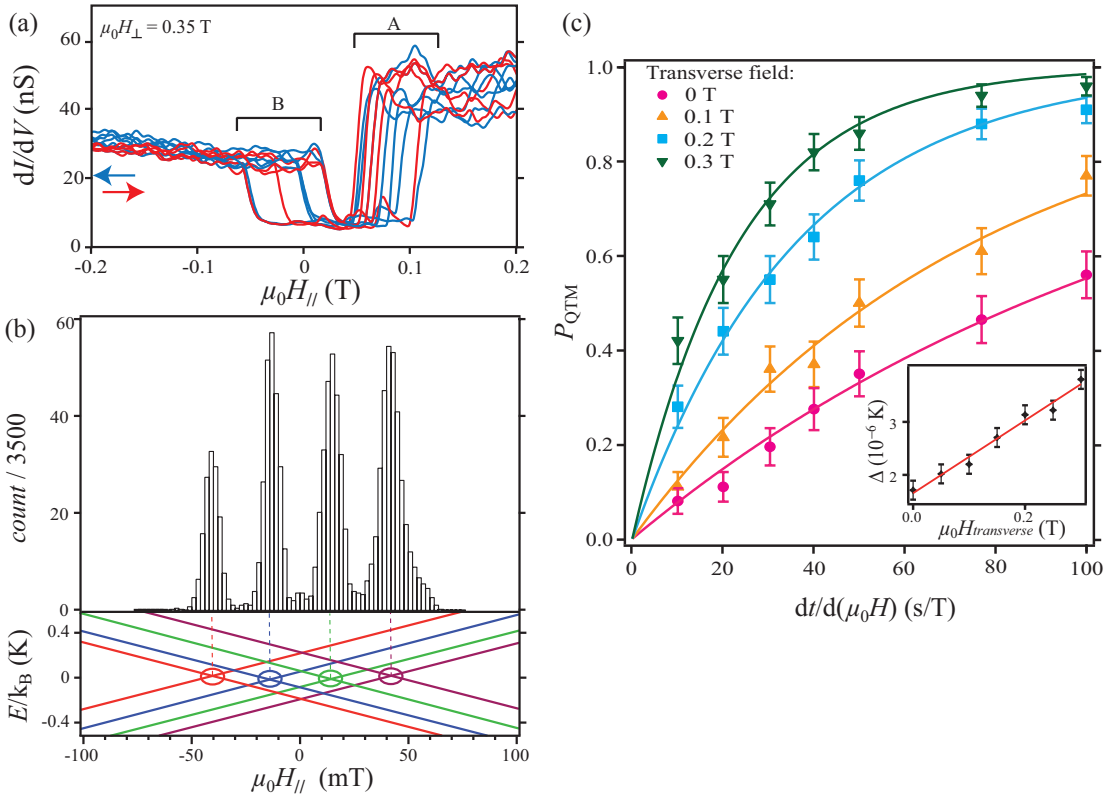

Figure 2.23: a) Magnetoconductance curves of a spin valve device. The QTM field values for molecules A and B are clearly split. Four peaks can be distinguished for molecule B, corresponding to the fourfold nuclear splin splitting. b) Histogram of the QTM positions of molecule B for 3500 consecutive traces. The avoided level crossings of the Zeeman diagram can be identified as origin of the effect. c) QTM probability as a function of the inverse of the field sweep rate and different transverse fields. The experimental data is fitted with the Landau-Zener model, yielding the tunnel splitting Δ (inset).
Adapted from [149]

Recently, a more detailed theoretical description for transport in a CNT with coupled SMMS was developed [150]. In this model the conduction electrons hybdridize with delocalized electronic states on the $TbPc_2$ ligands, which induces a Fano resonance that gives rise to strong backscattering for certain configurations of electron and molecule spins. This breaks up the CNT quantum dot in, for instance, a series of $n_\uparrow = 1, n_\downarrow = 3$ dots for parallel ($\uparrow\uparrow$) and $n_\uparrow = 2, n_\downarrow = 2$ dots for antiparallel ($\uparrow\downarrow$) molecule spins. The GMR effect can be explained by means of an effective antiferromagnetic coupling between the molecule spins, which may depend on the molecules' positions and be tunable with a gate. Spins are aligned when the Zeeman energy overcomes this coupling. With this model both the Coulomb maps and the magnetoconductance curves can be derived.

2.5.2 CNT NEMS

In 2013 Ganzhorn et al. probed the $TbPc_2$ spin with the nonlinear mechanical properties of a suspended carbon nanotube, where the magnetization reversal induces a detectable change in resonance frequency, proving that CNT NEMS can be used as highly sensitive magnetometers[151]. Later on, the spin reversal in the SMM grafted to such a device was measured and assigned to particular phonon modes, again resolving the fourfold nuclear spin splitting[64]. The results of this experiment are illustrated in fig. 2.24.

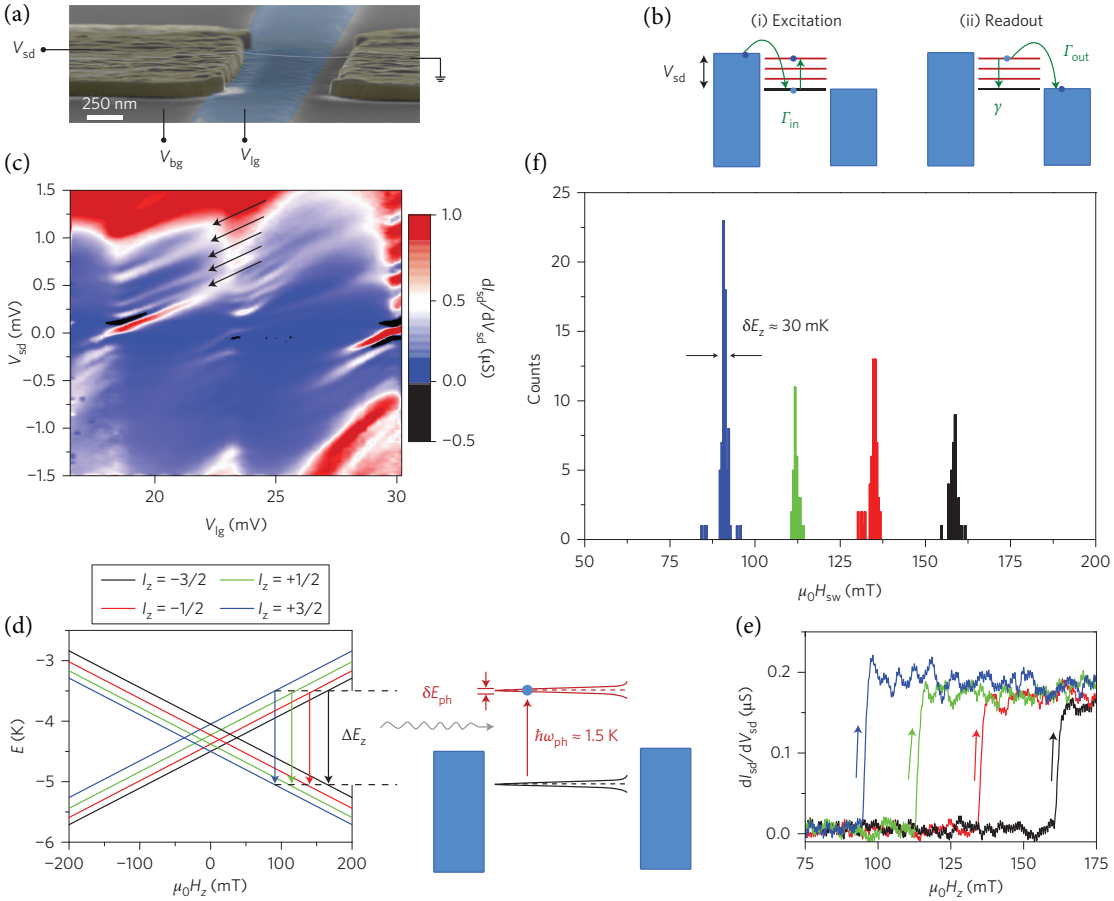

Figure 2.24: a) False color SEM image of the suspended CNT device. b) Excitation and readout of LSM of a CNT NEMS: i) Tunneling onto the CNT shifts the equilibrium position of the CNT along its axis, leaving the electron in an excited vibrational state (red). ii) For $\Gamma_{\text{out}} > \gamma$, the electron tunnels out of the excited state and equidistant lines are observable in transport spectroscopy. c) Coulomb map at $20\,\text{mK}$ and $1.4\,\text{T}$. The black arrows indicate excited LSM. d,e) Tuning to such a state ($V_{\text{lg}} = 16.5\,\text{mV}, V_{\text{lg}} = 0$) allows for the detection of magnetization reversal, observable again as 4 distinct swiching fields in conductance. The derived Zeeman energy yields the phonon energy, $\Delta E_{\text{Z}} = \hbar\omega_{\text{ph}} = 1.5\,\text{K}$. f) Histogram of the switching for 200 field sweeps, where 4 dominant events are observed, corresponding to the $TbPc_2$ nuclear spin states.
Adapted from[64]

Due to the available phonon modes in such a suspended CNT being quantized in energy,

relaxation could be assigned to the coupling to one particular longitudinal stretching mode (LSM) at energy $\hbar\omega_{\mathrm{ph}} = 1.5\,\mathrm{K}$.
More extensive studies of the spin reversal characteristics revealed that these processes can indeed be exclusively assigned to relaxation via phonon modes of the suspended CNT, while QTM was absent for the entire studied parameter range [152] (see fig. 2.25). This blockade of QTM is in agreement with the concepts presented in sec. 1.2.4, where the importance of the spin and phonon baths was stressed. Here, the QTM process is prohibited by conservation laws, as the suspended CNT constitutes a very finite bath, unable to match the change of angular momentum for $J = 6 \rightarrow J = -6$ in the corresponding energy range of $\Delta \approx 1\,\mu\mathrm{K}$ that needs to be transferred for such a reversal.

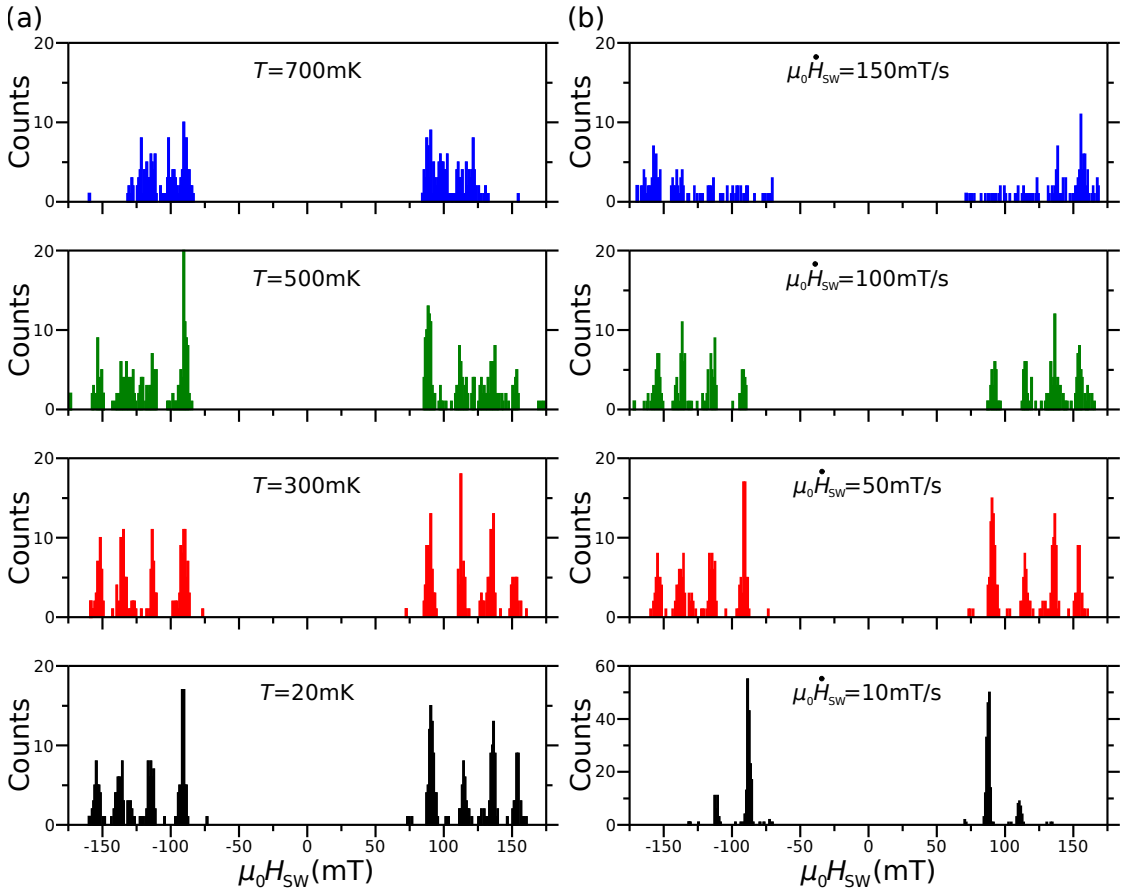

Figure 2.25: a) Histograms of the switching fields $\mu_0 H_{\mathrm{SW}}$ for 200 sweeps at a rate of $50\,\mathrm{mTs}^{-1}$ at different temperatures. Switching events at positive fields correspond to trace, events at negative field to retrace. No QTM is observed around zero magnetic field at any temperature, relaxation can hence be exclusively assigned to direct processes. b) Similar measurements for constant temperature $20\,\mathrm{mK}$ and varying sweep rates. The same observation is made for the absence of QTM.
Adapted from [152]

3 Tin Telluride within the Topological Class of Matter

3.1 Classification of Matter and Topology

3.1.1 Landau Phases and the Concept of Symmetry Breaking

Our understanding of different phases in solid state physics has been strongly influenced by Landau's phenomenological theory of phase transitions [153] for the bigger part of the 20th century, which has seen such important discoveries as superconductivity or the emergence of semiconductor applications. The classification of ordered phases follows from the system's inherent symmetries - the ones that are conserved and the ones that are spontaneously broken at transitions. To describe phases and their transitions Landau introduced a free energy expansion with a local order parameter characteristic for the system under consideration. It is nonzero in an ordered phase, vanishes beyond the transition and the way this order parameter transforms under certain symmetry operations of the underlying system characterizes the phase. In a mathematically more general way such systems are usually treated with group theory.
Closely related to the concept of broken symmetries is the appearance of gapless excitations, called *Goldstone bosons*, which correspond to fluctuations of the order parameter and define the low-energy properties of these systems. This mathematical abstraction manifests itself in many condensed matter systems. The three-dimensional space group for instance is broken down to certain symmetry groups in crystal structures which are not invariant under translational operations. The resulting excitations are the phonons of the crystal lattice. In magnetically ordered phases the rotational symmetry of the spins is broken and spin waves arise as the excitation spectrum. Superconductivity is another phenomenon that is generally treated with a symmetry breaking approach. As a matter of fact the famous Ginzburg-Landau theory [154] was deliberately developed to describe superconductors macroscopically. In its original form it is defined such that $U(1)$ gauge symmetry is broken, a mechanism that also holds for the microscopic BCS theory [155] by Bardeen, Cooper and Schrieffer from 1957. This is, however, a somewhat incomplete picture since dynamical fields are neglected. Newer theoretical studies show that common 3D *s*-wave superconductors actually obey an order that is referred to as *topological* in its most general sense [156]. This will be briefly touched upon later in a broader context. Chronologically it should be pointed out first how experimental discoveries of the 1980s opened up a different view on condensed matter physics beyond Landau's approach of broken symmetries.

3.1.2 First Evidence of Topology in Solid State Physics

The discovery of the quantum Hall effect in its integer form (QHE) 1980 by von Klitzing et al.[157] and its fractional form (FQHE) by Tsui et al.[158] in 1982 paved the way for important developments in the understanding of condensed matter physics that led to the recent boost in the field of topological matter.
The effect appears in electron gases confined to two dimensions and subject to strong magnetic fields perpendicular to the 2DEG. A perpendicular magnetic field causes the electrons to follow cyclotron orbits that close for sufficiently large fields. This motion can be described as a harmonic oscillator whose levels' quantization, called Landau levels, becomes apparent at low temperatures. The orbits then separate and the 2DEG becomes insulating. This is, however, only true for the bulk of the system. At the edges of the 2DEG the orbits do not close but the electrons can skip along conductive 1D channels that have quantized conductance $e^2/h \approx 7.75 \cdot 10^{-5}\,\mathrm{S}$. These edge states are considered as *chiral* since the movement is only allowed along one direction, which results in those channels being non-sensitive to backscattering processes. Furthermore, the transverse Hall conductance shows very robust plateaus given by Ne^2/h with N being an integer in the QHE and a fraction in the FQHE.

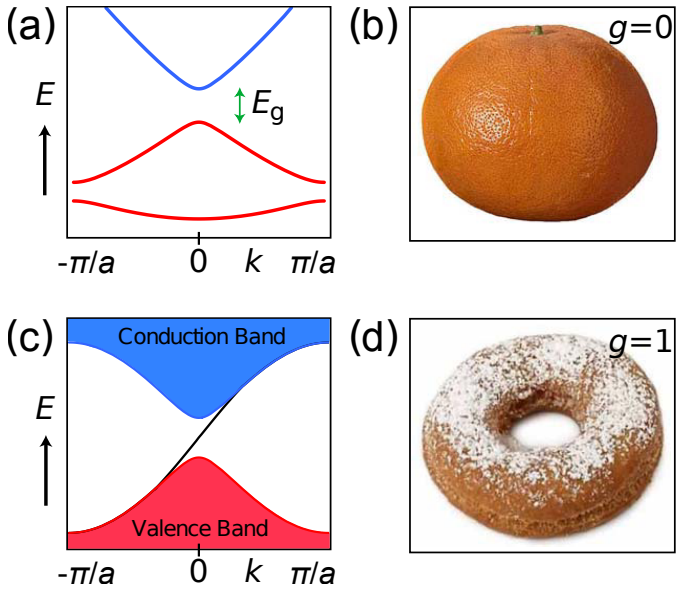

Figure 3.1: Topology from the band structure perspective, illustrating the difference of a,b) topologically trivial band insulators and c,d) topologically non-trivial QH structures with their corresponding topological objects of genus $g = [0,1]$. The bulk topology of the QH state gives rise to a gapless chiral edge state within the bulk band gap.
Adapted from[159]

The quantum Hall state does not break any symmetry other than time-reversal symmetry and can thus not be described by local order parameter according to Landau's theory. In order to distinguish it from ordinary insulator states a totally different perception was required. This was provided by Thouless et al.[160] who classified gapped band structures

by grouping them such that continuous transformations do not close the bulk energy gap within one class. These classes are then described by a topological invariant n called *TKKN number* or *Chern number* which is related to the number of stable gapless edge states or a Brillouin zone Berry flux F_{m} of occupied bands m via [159]

$$n = \sum_{\mathrm{m}} \left(\frac{1}{2\pi} \int \mathrm{d}^2\mathbf{k}\, F_{\mathrm{m}} \right) \tag{3.1}$$

and corresponds exactly to the integer N in the conductance of the QHE. The gapless edge channels thus arise from a non-trivial bulk band structure in terms of topology when this system is extended by a trivial structure as an ordinary insulator or even the vacuum. This relation was later generalized by Qi et al. [161] for non-trivial 2D insulators and is usually discussed as *bulk-boundary correspondence*.
It particularly holds for charge carriers with spin degree of freedom as it can be found in the quantum spin Hall effect (QSHE), which was experimentally discovered as recently as 2007 by the group of Molenkamp [162]. The QSHE is at the heart of *topological insulators* (TI) which are described by a new topological invariant ν. Each edge has now two conductive channels with fixed spin orientation which is referred to as *spin-momentum locking*. Similar to the QHE these channels are protected against elastic backscattering for non-magnetic impurities which do not enable spin flip processes. In contrast to the QHE, the QSH state does not break time-reversal symmetry. Its surface states are considered to be protected by this symmetry and its appearance is promoted by spin-orbit coupling, which acts as an internal field and will be discussed in sec. 3.2 in more detail.

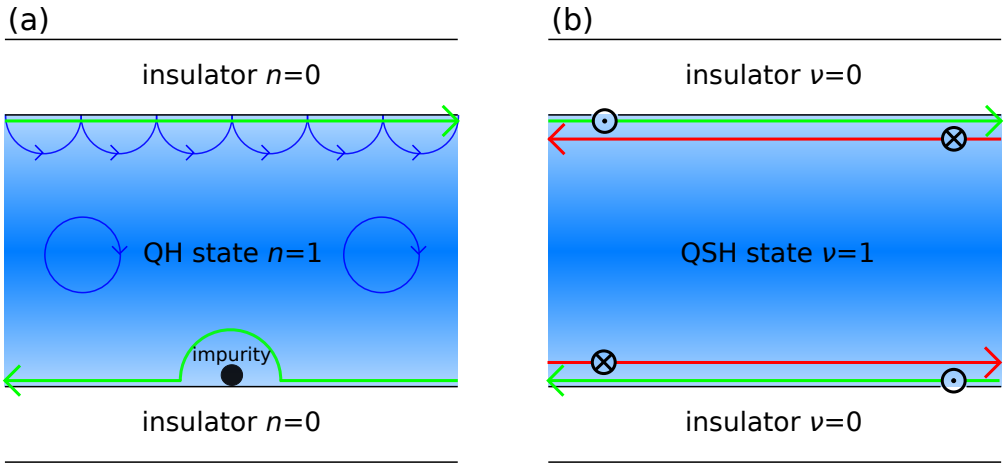

Figure 3.2: The principle of edge channel charge transport for a) the QHE and b) the QSHE and their underlying topological invariants, the Chern number n and the Z_2 invariant ν. The orbits of the QHE, caused by an external magnetic field, are schematically represented as localized in the bulk and skipping at the edges. The chiral transport channels at the edges are robust to disorder since backscattering is not allowed. The QSHE has an additional spin degree of freedom perpendicular to the plane with their direction indicated by the dots and crosses. The edge channels are termed as *helical* due to the charge carrier momentum locked to their spin polarization. These channels are robust to scattering at non-magnetic impurities.
Based on [163]

3.1.3 The Concept of Topology and its Implications on Quantum States of Matter

In order to understand the concept of topology in a more general context it is inevitable to realize that there are two slightly different mindsets using this term and basically the difference arises from the perspective of a band theory and the perspective of a quantum field theory. This is of importance since approvable physics emerges from a proper understanding of these systems and the underlying (quantum-statistical) description. The subsequent chapters of topological insulators and superconducting applications will then, however, be treated within the more classical approach in order to not go beyond the scope of this work.
First descriptions of the QHE were derived from the perspective of a band structure of non-interacting particles, as done by Thouless et al. or Haldane [164] for an equivalent graphene model system. The appearing Chern number can be visualized by the mathematical concept of closed 2D surface integrals which give rise to a topological invariant that is related to the genus of the surface. This genus has the value $g = 0$ for a trivial sphere and $g = 1$ for a torus, two objects that are topologically distinct [159]. On the other hand, it was shown early that the FQHE is definitely a correlated state that contains some sort of long-range order which needs to be described with a quantum field theory [165]. This effective topological field theory is referred to as Chern-Simons theory in its original form [166] [167]. The progress of these two different schools of thinking led to a rather confusing definition of topology today with the first one being more classical rather than embodied in a fully quantum-mechanical treatment.
A general and fully quantum-mechanical classification of topological systems has been developed mainly by Wen [168] [169] [170]. It introduces the concept of *entanglement*, which can be long-ranged (LRE) and short-ranged (SRE), depending on the decomposition of the underlying quantum system. A system, whose state can be decomposed in a tensor product of each site,

$$|\Psi\rangle = \otimes_i |\Psi_i\rangle \,, \tag{3.2}$$

is considered local or SRE, while topological order or LRE is the property of a gapped quantum system that cannot be transformed into such a product state without a gap-closing quantum phase transition. This most general definition classifies topological superconductors and insulators as SRE, while common s-wave superconductors with dynamic electromagnetism or the FQHE are LRE.
In this sense topological insulators are also referred to as symmetry-protected topological/trivial states (SPT). The gapless boundary states of a QSHE-based topological insulator, for instance, are protected by time-reversal symmetry. The importance of this classification becomes clearer in the context of topological quantum computing (TQC), a still theoretical concept which is based on excitations called *anyons*.
Anyons are quasiparticles which obey neither fermionic nor bosonic statistics, they are described by representations of the Artin braid group and can be abelian or non-abelian. Non-abelian anyons are the foundation for topological quantum computing as suggested

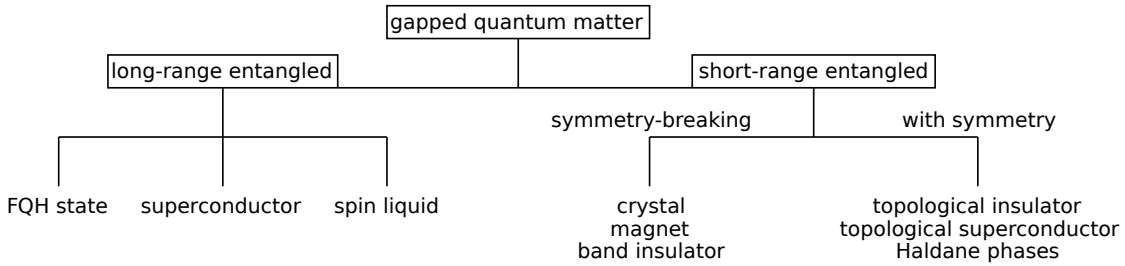

Figure 3.3: Quantum topology classification of matter according to Wen. Topology is defined as property of sytems with long-range entanglement.
Based on [170]

by Kitaev [171]. They form topologically degenerate multi-level systems which are hence robust to local pertubations, the cause for decoherence in common quantum computer concepts based on the local trapping of multi-level quantum systems. Different systems have come into the focus of research to realize such physics.
Possible candidates are local excitations of systems with a topology defined as above (in the sense of LRE), for example in the 5/2 Laughlin state excitations of the FQHE [172] [173]. However, there is also the possibility for non-abelian physics to appear as defects in SRE states. Examples for the latter are the the prominent Majorana zero modes that can couple to vortices at the endpoints of p-wave (topological) superconductors [174], vortices at interfaces in hybrid systems of s-wave superconductors and topological insulators [175] or even hybrid-systems of superconductors and semiconductor nanowires with strong Rashba spin-orbit coupling [176].

3.2 Topological Insulators

The following two chapters are dedicated to the introduction of some of the most significant examples of symmetry-protected topological matter, namely the topological insulators (TI) in two and three dimensions and the topological crystalline insulator (TCI). While time-reversal symmetry governs the robustness of the TI states, TCIs are subject to a wider range of possible crystal symmetries. Further semantic differences concerning the definitions of topology introduced before are widely ignored within this chapter. The interested reader is referred to the review paper of Hasan et al. [159] which served as guideline for parts of this overview.

3.2.1 2D Topological Insulators

The quest for topological phases other than the QHE was at first only of theoretical nature. In 2005 Kane and Mele [177] suggested graphene as a system that could promote a quantum spin Hall effect. The idea is related to Haldane's model system of a QHE in graphene which introduced a relativistic mass m or equivalently a (bulk) band gap to the Dirac points of graphene by breaking time-reversal symmetry artificially. The Dirac energy dispersion of graphene presented already in sec. 2.1.2 then transforms to

$$E(\mathbf{q}) = \pm\hbar v_{\mathrm{F}}|\mathbf{q}| \rightarrow \pm\sqrt{(\hbar v_{\mathrm{F}}|\mathbf{q}|)^2 + m^2}, \tag{3.3}$$

which corresponds to a QH state and not an ordinary insulator. However, this ignores the spin of the electrons. By introducing a spin-orbit coupling with full lattice symmetry, spin s_z conservation is sustained and the above relation holds for $m \rightarrow \Delta_{\mathrm{SO}}$, which produces basically two copies of Haldanes model for $s_z = \pm 1$ in graphene. Kane and Mele showed that this gives rise to a spin Hall conductivity in an applied electric field whereas the Hall conductivity is net zero due to the two spin types. In real systems s_z conservation does not hold due to contributions from inter-band couplings, disorder or interactions like Rasha spin-orbit coupling. But even for the presence of perturbations time-reversal symmetry protects Kramers degeneracy at special points, with their exact properties depending on the crystal termination. This degeneracy ensures the gapless character of the edge states which promotes helical transport - there are two channels in opposite directions for opposite spins $s_z = \pm 1$ as it was schematically shown in fig. 3.2. In a second work Kane and Mele[178] classified the QSH state by means of a topological invariant similar to the Chern number of the QH state. They argued that the Chern number n vanishes due to time-reversal invariance of the QSH state, but there is a Z_2 invariant ν that can take on the values $\nu = 0$ for trivial and $\nu = 1$ for non-trivial states under the QSH classification. ν depends on the way how points with time-reversal invariant momenta are connected, which can be with an even or odd number of edge states intersecting the Fermi energy. Pairwise annihilation renders systems with even numbers of these states trivial, whereas an odd number always maintains at least one gapless edge state situated in the bulk band gap that is robust to smooth distortions of the system.

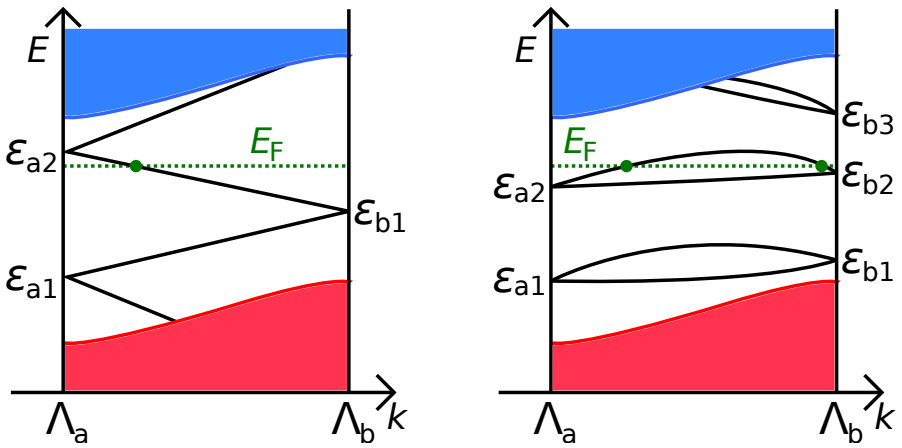

Figure 3.4: Surface spectrum with twofold degenerate states at time-reversal invariant momenta λ_{a} and λ_{b}, referred to as *Kramers pairs*. The case of non-trivial $\nu = 1$ (left) and trivial $\nu = 0$ (right) are distinguished. For $\nu = 1$ only one level crosses E_{F} and Kramers pairs "switch partners" between invariant momenta, while two levels cross E_{F} for $\nu = 0$.
Based on[179]

Graphene is practically not suitable for the creation of QSH states mainly due to its very small spin-orbit coupling [180]. The model nevertheless paved the way for quick success in the research of QSH states. Looking at systems with much larger spin-orbit coupling, Bernevig et al. [181] predicted a QSHE in sandwiched CdTe/HgTe/CdTe quantum well structures which was then experimentally confirmed by the group of Molenkamp [162] in 2007.

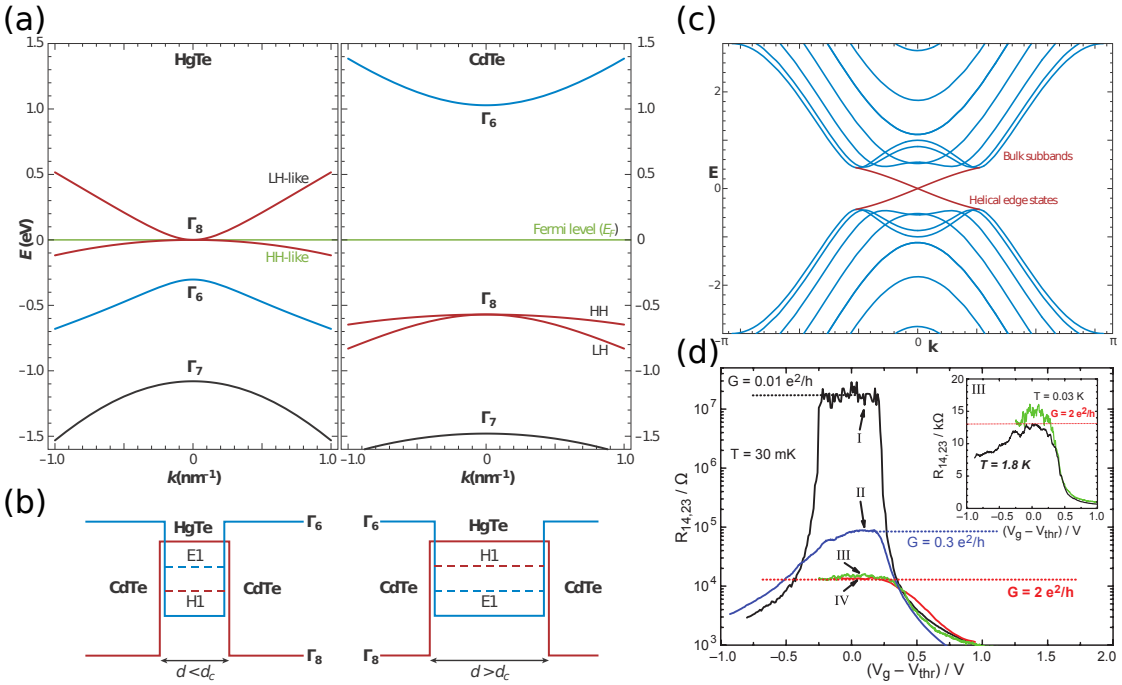

Figure 3.5: A QSHE can be realized in HgTe quantum wells. a) The bulk bandstructure of HgTe is inverted with respect to CdTe. b) Above a critical thickness d_c CdTe/HgTe/CdTe layers undergo a quantum phase transition to the inverted regime which is topologically non-trivial and has spin-locked edge states. c) Analytical calculation of the band structure reveals gapless edge states. d) Measured 4-terminal resistance of different quantum wells below (I) and above (II,III,IV) d_c. Sufficiently short samples (III,IV) show a width-independent quantized resistance due to edge channel transport. This also holds for higher temperatures (inset).
a,b,c) Adapted from [163], originally from [181] d) Adapted from [162]

The occurrence of the QSHE in these stacked layers is closely related to the underlying bulk band structures. CdTe has a conventional band structure of a Γ_8-symmetric valence band and a Γ_6-symmetric conduction band. In HgTe, however, these bands are inverted due to the influence of spin-orbit coupling: the Γ_8 band is energetically pushed above the Γ_6 band. This band inversion is the fundamental principle of topological insulator realizations. Bernevig et al. [181] found a critical thickness d_c of HgTe above which the layered system undergoes a quantum phase transition into the inverted regime, represented by a change of the sign of the Dirac mass term and consequently a different topological Z_2 invariant at both sides of the transition.
The QSHE in this particular system was soon experimentally confirmed with gate-tunable quantum wells grown from molecular beam epitaxy and patterned into Hall bar

structures. By tuning the Fermi energy into the gap, samples of different thickness show fundamentally different behaviour which is indicated by their resistance as presented in fig. 3.5d. For samples below the critical thickness $d_c = 6.3\,\mathrm{nm}$ the gap resistance diverges while samples in the inverted regime have quantized resistance plateaus exactly corresponding to the expected value of $G = 2e^2/h$ for biased terminals. These plateaus are reproduced for different widths and therefore transport is governed by ballistic edge states, which holds for channels shorter than the inelastic mean free path l_{inel}. Later on spin-momentum locking of the edge channels was also demonstrated by the Molenkamp group [182].

3.2.2 3D Topological Insulators

Soon after the description of the QSHE the theory was generalized for 3D systems [183] [184] in slightly different manners. For both cases the Z_2 topology was found to be described by four invariants: $\nu_0;(\nu_1\nu_2\nu_3)$. The first invariant ν_0 defines the cases of trivial or *weak topological insulators* ($\nu_0 = 0$) and *strong topological insulators* ($\nu_0 = 1$), depending if an even oder odd number of Kramers degenerated points is enclosed by the surface Fermi arc. In contrast to the 2D QSH bulk state, the degenerated points representing the surface states now shape Dirac cones for massless fermions in the case of a 3D bulk.
Weak topological insulators can be seen as stacked QSH layers. However, surface states, if present, are not symmetry-protected. Therefore disorder can eliminate the topological distinction[1] of these phases and trivial band insulators [183]. The second set of invariants $(\nu_1\nu_2\nu_3)$ can be interpreted as Miller indices for the reciprocal lattice describing the Kramers invariant momenta.
The strong topological insulator has surface states which are robust to disorder due to time-reversal symmetry protection. For a Fermi energy in the bulk band gap, the surface Fermi arc of 3D TIs encloses an odd number of Dirac point while the partner Dirac points reside on the opposite surface. The surface states then define a 2D *topological metal* [183] which can be described by [186]

$$\mathcal{H}_{\mathrm{surface}} = \hbar v_{\mathrm{F}} \boldsymbol{\sigma} \mathbf{z} \times \mathbf{k} \tag{3.4}$$

for a single Dirac surface point. Here, $\mathbf{z}$ is the unit vector perpendicular to the TI surface. Calculation of the spin states reveals that the spin must be perpendicular to the momentum $\mathbf{k}$, which is a direct consequence of time-reversal symmetry conservation. As a result, electrons circling the Fermi arc aquire a Berry phase which has to be either 0 or π. This corresponds again to a Z_2-type classification with the value 0 being the trivial and π the non-trivial case and provides the link to quantum field theoretical descriptions [187] where this phase is an universally quantized parameter. The non-trivial phase leads to *weak anti-localization* effects (WAL) in an applied magnetic field, opposed

1 It was later found that there are systems which are protected by ensemble-averaged translational symmetries, creating the notion of *statistical topological insulators* [185].

to *weak localization* or *Anderson localization* in the trivial case. It can be shown that, in the non-trivial case, a conductance of half a QH plateau, $G = 1/2\ e^2/h$, can be associated with a single surface Dirac cone. This conductance cannot be reduced to zero by disorder [188]. Practically, the 3D TI surface governs ballistic transport channels for $L < l_{\text{inel}}$, similar to the case of 2D QSHI, but in real systems the overall transport is often dominated by diffusive channels due to not depleted bulk states, which are inevitably excited and measured in parallel to the the surface channels.

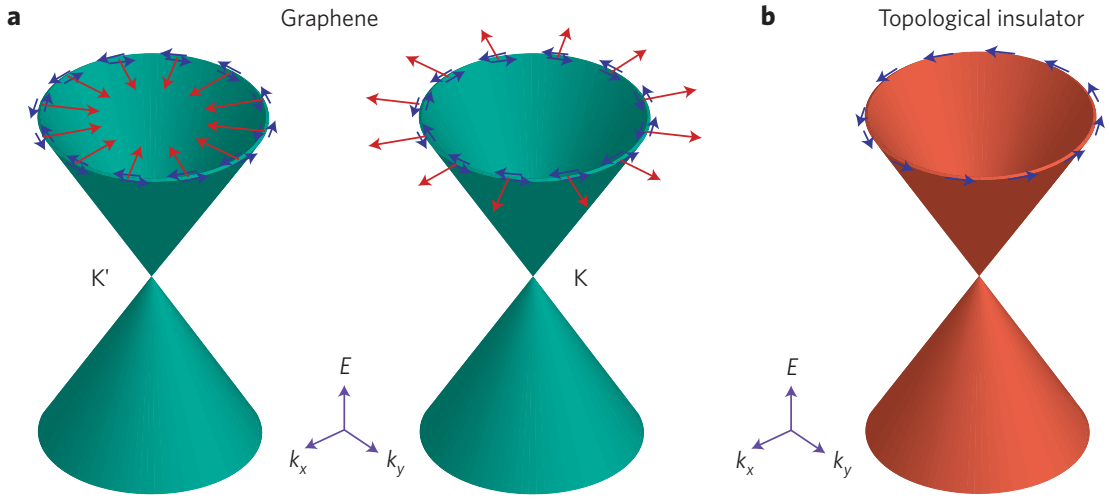

Figure 3.6: The Dirac cones of graphene and a 3D TI in comparison. a) Graphene has four Dirac cones arising from valley and spin. The individual cones, described by a pseudo-spin, intersect at the K and K' points and spin degeneracy (blue arrows) for negligible spin-orbit coupling doubles each cone. b) A 3D TI has a single Dirac cone which intersects at a Kramers-point. The spin is locked to the momentum and circles in the surface plane. The case of negative velocity is shown, while many real 3D TIs exhibit positive direction of rotation.
Adapted from [189]

It is also of importance to study the *spin chirality* arising from eq. 3.4. Depending on the sign of v the spin circles clockwise or counter-clockwise. In real systems with present mirror symmetries there is only one possible direction, described by the *mirror Chern number* [190]. This will be discussed for topological crystalline insulators in more detail, where the classification by mirror symmetries becomes crucial. In general, symmetries of the lattice play an important role for 3D TIs. When carefully incorporated into the theoretical description, they allow for an easier identification of TI states from band structure calculations [179].

Semiconducting alloy $Bi_{1-x}Sb_x$ was the first 3D TI to be experimentally confirmed [191]. Both pure bismuth and pure antimony are semimetals with strong spin-orbit coupling and an inverted direct band gap that allows for a topological classification according to Fu and Kane [179] with antimony being the topologically non-trivial component 1; (1,1,1). At a ratio of $x = 0.04$ the alloy's band gap closes, giving rise to 3D Dirac point. In the following, surface spin textures including a π Berry phase [192] and the absence of elastic backscattering despite strong disorder [193] were demonstrated. However, the complicated

surface structure of $Bi_{1-x}Sb_x$ with three L-points showing band inversion makes this material difficult to use.
Subsequently, other materials as Bi_2Se_3 [194] [191] [195], Bi_2Te_3 [196] [197] or Sb_2Te_3 [197] were found and investigated. Those materials mainly differ in size of the band gap, stoichiometry of the compound and presence of surface-warping potentials. A promising candidate for spintronics applications is Bi_2Se_3, which exhibits a simple surface structure of a very pronounced single Dirac cone at the Γ-point and a large band gap [198] of $\approx 0.35\,\mathrm{eV}$.

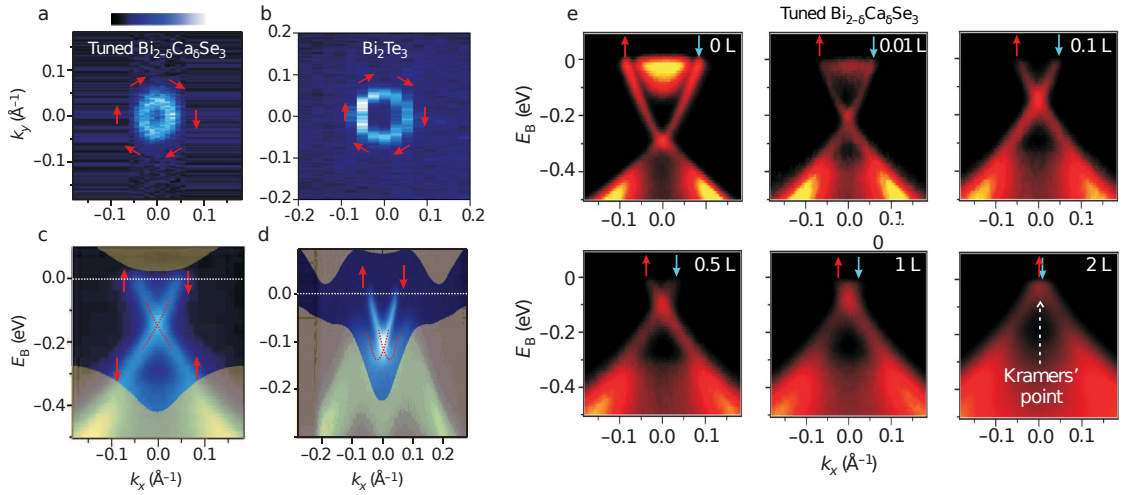

Figure 3.7: a,b) Detection of spin-momentum locking in 3D TIs Bi_2Se_3 with Ca-counter-doping and Bi_2Te_3 via spin-resolved ARPES. Red arrows indicate the circling spin direction on the Fermi surface (1,1,1). c,d) ARPES dispersion along k_x. Shaded regions represent the bulk bands projected onto the aforementioned surface. e) High-resolution ARPES mapping of the Fermi surface of Ca-doped Bi_2Se_3 near the Kramers-point Γ. The sample surface is exposed to NO_2 for surface p-doping. The Dirac point is gradually shifted from the n-band (0L) into the bulk gap to align with E_F (2L).
Adapted from [191]

An important tool for the investigation of surfaces and their properties in 3D TIs is angle-resolved photoemission spectroscopy (ARPES) because of the possibility to only probe surface states. ARPES can also be conducted in a spin-resolved mode to measure surface spin polarizations and deduce the Berry phase. Conventional transport measurements, on the other hand, always include bulk contributions when the surface Fermi energy does not align perfectly with only the surface states or the bulk Fermi energy is not situated in the bulk band gap. Technically this is almost impossible since stoichiometric defects normally tune the bulk Fermi energy into either the valence or conductance bands and the band gaps are usually relatively small. Electrostatic gating of such quasi-metallic systems is limited. Concepts of counter-doping have been developed to reduce these contributions but bulk conductivity remains an issue in approaches based on the introduced compounds. However, it has been demonstrated that the Fermi energy and Dirac point structure can be engineered to a more ideal case by combining different compounds, for example ternary $(Bi_{1-x}Sb_x)_2Te_3$ by Zhang et al. [199] or $Bi_{2-x}Sb_xTe_{3-y}Se_y$ by Arakane et al. [200]

3.3 Tin Telluride Topological Crystalline Insulator

3.3.1 Introduction to Topological Crystalline Insulators

In the context of band structure investigations of TIs, crystallographic properties served as means allowing for simplification and hence classification of topological matter [179]. It was soon recognized that crystal symmetries can give rise to new topologically distinct classes as well. One of these classes is the topological crystalline insulator (TCI), first described by Fu [201] in 2011. In TCIs symmetries of the crystal lattice take on the role of time-reversal symmetry in TIs which had led to robust surface states for systems with strong spin-orbit coupling and band inversion. Likewise, TCIs show robust surface states that exhibit promising properties for applications based on materials which do not necessarily require strong spin-orbit interactions. Different to the case of time-reversal symmetry (TRS) in TIs, crystal surfaces can be governed by or break a wide range of different (bulk) crystal symmetries. Hence a careful treatment of the symmetry groups is necessary, leading to a rich class of new materials and systems. One of the most common concepts within the TCI group are systems where surface states are protected by mirror symmetries of the crystal, as it it the case for tin telluride (SnTe) described in this chapter.

Mirror-symmetric topology is described by the aforementioned mirror Chern number $n_{\mathcal{M}}$ which was originally introduced by Teo et al. [190] to describe the 3D TI BiSb. A mirror-symmetric operation $\mathcal{M}$ for spinful electrons, which transforms e.g. $x \to -x$, can be decomposed into a product $\mathcal{M}(x) = PC_2(x)$ of spatial inversion P and two-fold rotation C_2 around the axis perpendicular to the mirror plane at $x = 0$. This results in eigenvalues $\eta = \pm i$ for $\mathcal{M}$ and electrons with wavevectors $\mathbf{k}$ within the planes $k_x = 0$ (or equivalently $k_x = \pi/a$) of the 3D Brillouin zone are then invariant under the given mirror operation. Bloch eigenstates $\Psi_{\eta,\mathbf{k}}$ for these electrons can be built as eigenstates of $\mathcal{M}$ and occupied bands within the 2D plane are classified with a *mirror invariant* n_η for both types of eigenstates. For the given mirror operation the topological character is defined by two combinations of the individual mirror invariants,

$$n = (n_{+i} + n_{-i}) \text{ and } n_{\mathcal{M}} = \frac{1}{2}(n_{+i} - n_{-i}), \tag{3.5}$$

where n is the total Chern invariant which describes a Hall conductance and $n_{\mathcal{M}}$ the mirror Chern number. In the presence of time-reversal symmetry n is zero, but non-trivial topological states are nevertheless possible for non-vanishing $n_{\mathcal{M}}$. In a crystal there can be several of such planes with invariant mirror-symmetry and crystal surfaces may or may not obey the bulk symmetry and form protected surface states, depending on the symmetry of the termination.

One important consequence of crystal-symmetry-protected surface states is that there can be an even number of surface Dirac cones, in contrast to TRS TI within the Z_2 classification. Thanks to the broad class of possible crystal symmetries of bulk and surface, perturbations can arise in many different ways and produce intriguing effects,

often related to the opening of a small gap in the surface Dirac states. Ando and Fu listed some of the important examples (which do not necessarily only hold for TCIs) and their ramifications in their review [202]:

- **ferroelectric structural distortion**
  Relative displacements of the ionic sublattices in IV-VI-semiconductor compounds can break mirror symmetry and give a mass to the Dirac fermions [203] [204].

- **magnetic dopants**
  Out-of-plane magnetic fields break TRS and can gap out Dirac surface states, induced e.g. via exchange coupling to magnetic impurities. This can create unusual discrete Landau levels and cause quantum (anomalous) Hall states [204] [205]. On the other hand, it is still possible to have gapless surface states in magnetic TCIs as long as the field direction is perpendicular to the mirror plane.

- **mechanical strain**
  Non-uniform strain fields can shift the surface Dirac points, which are not pinned to time-reversal invariant momenta in TCIs, within the Brillouin zone. The resulting bands could explain unconventional interface superconductivity [204] [206].

- **layer thickness**
  The principle of separated surfaces is altered when the layer thickness of 3D TIs and TCIs becomes small. In thin films surface states can hybridize, giving rise to 2D-type edge channels in SnTe TCI, which gap out with perpendicular electric fields [207]. Reducing the layer thickness below a critical value destroys the bulk topology [208] [209].

- **disorder**
  Symmetry-breaking of the surface states creates phases which are locally gapped. However, there are two types of phases which are still connected by mirror symmetry and hence can build out conducting channels at their domain walls, protected from elastic backscattering, as long as time-reversal symmetry is preserved [203]. Since disorder breaks mirror symmetry randomly, the surface is made up by and equal weight of these phases whose domain walls percolate throughout the surface. This corresponds to the principle of averaged mirror symmetry which is the base of the broader class of statistical topological insulators [185] mentioned before.

3.3.2 Tin Telluride Topological Crystalline Insulator

The alloy $Pb_{1-x}Sn_xTe$ has early been known to undergo a band inversion [210] at $x = 0.35$ and thus to exhibit gapless surface states at the interface [211]. What was originally thought about as an exotic phase turned out to be the first description of a topological insulator class. However, it took the full understanding ot the emerging field to realize the topological state of this material within the TCI class [203] because the primal Z_2 classification branded $Pb_{1-x}Sn_xTe$ as topologically trivial. This is because band inversion

occurs at an even number of four equivalent points and gapless surface states were hence predicted to be destroyed by disorder rather than topologically protected.
More precisely, Hsieh et al.[203] showed that it is the compound SnTe which can be classified as a TCI while PbTe is topologically trivial. It is hence the former that exhibits gapless surface states that can occur in the pure case and at the alloy's $Pb_{1-x}Sn_xTe$ interface. While SnTe at low temperatures also has the larger band gap[212] of $E_g \approx 0.3\,\mathrm{eV}$ compared to PbTe with $E_g \approx 0.18\,\mathrm{eV}$ and is therefore interesting for applications in its pure form, the alloy in the Pb-rich inverted regime can practically nevertheless be the more promising candidate. This is due to the fact that Sn-vacancies in SnTe are a common and thermally stable configuration that normally drives SnTe deep into the p-doped regime, making it very hard to tune E_F into the gap[213]. This problem can be mitigated by using nanostructures or counter doping[214], but bulk conductivity remains an obstacle for this particular material class.

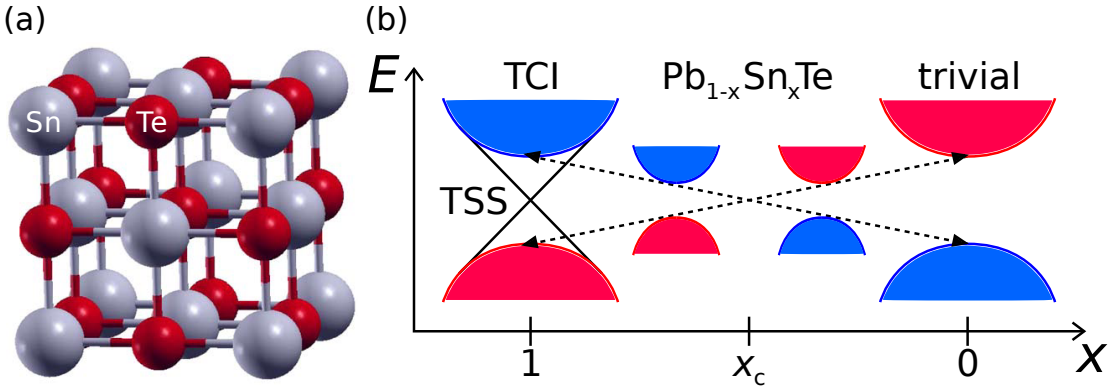

Figure 3.8: a) Cubic rock salt lattice of SnTe (and equivalently PbTe for which Sn is replaced by Pb). b) Band inversion in $Pb_{1-x}Sn_xTe$ as a function of x. Pure SnTe is a TCI phase, while pure PbTe is trivial. The transition occurs at $x \approx 0.35$.
a) Adapted from[191] b) Based on[215]

SnTe crystallizes in cubic rock salt structure with a lattice constant of $a_{SnTe} = 0.63\,\mathrm{nm}$[212]. This fcc-type type lattice gives rise to a octahedron bulk Brillouin zone. The mentioned band inversion of the four equivalent points in SnTe happens at direct band gaps at the L-points, the hexagonal face-centers, of this bulk Brillouin zone.
The Hamiltonian of the system can be derived from the D_{3d} symmetry sub-group that leaves the L-points invariant. At a given point L, the conduction and valence band are then formed by two sets of opposite-parity Kramers doublets α, giving rise to a $(3+1)$D low-energy representation[202]

$$\mathcal{H}(\mathbf{k}) = \begin{pmatrix} m & 0 & -iv'k_z & -v\,(ik_x + k_y) \\ 0 & m & v\,(ik_x - k_y) & -iv'k_z \\ iv'k_z & -v\,(ik_x + k_y) & -m & 0 \\ v\,(ik_x - k_y) & iv'k_z & 0 & -m \end{pmatrix}, \tag{3.6}$$

which can be transformed via $k_z \to (v/v')\, k_z$ into a massive Dirac spectrum

$$\mathcal{H}(\mathbf{k}) = m\Gamma_0^{\mathrm{D}} + v \sum_{i=1}^{3} k_i \Gamma_i^{\mathrm{D}}, \tag{3.7}$$

where Γ^{D} are the gamma matrices of the Dirac notation. The band inversion at the interface or surface corresponds to a change in the sign of the mass $m \to -m$ in the Hamiltonian above. Hsieh et al. found from kp-theory calculations that there are crystal momenta which are invariant under reflection about the {110} mirror planes in real space. These momenta can be assigned to six planes spanning from Γ, the center of the bulk Brillouin zone, to arbitrary pairs of the four L-points and the definition of the coordinate system with k_x perpendicular to the invariant plane(s) and k_y, k_z in the plane(s) governs the relation to the low-energy Hamiltonian above.
Hsieh et al.[203] showed that the mirror Chern number $n_{\mathcal{M}}$ for these $k_x = 0$ planes changes by $|\Delta n_{\mathcal{M}}| = 2$ when band inversion occurs. This expresses the fact that the band inversion leads to a simultaneous change in mass at the two equivalent L-points of the invariant plane(s). Therefore, one of the compounds of PbTe and SnTe is a TCI, while the other is trivial. In the same work SnTe was found to be non-trivial from analysis of the DFT band structure. The left panel of fig. 3.9 shows these first-principles calculations for the (001) surface of SnTe.

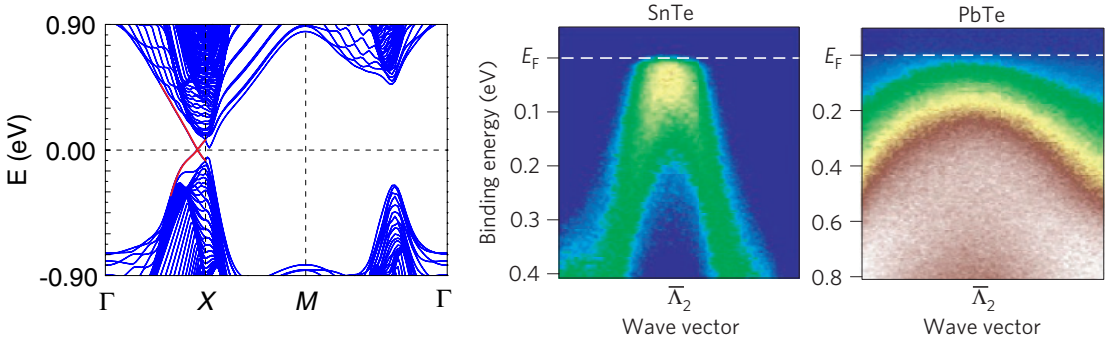

Figure 3.9: Left panel) First-principles calculations of the SnTe band structure along the (001) surface, showing a complicated structure of bulk bands (blue) and the presence of surface states (red). Middle and right panel) ARPES measurements of the (001) surface of SnTe and PbTe, confirming the presence of surface states in the former and the trivial character of the latter. Left) Adapted from[203] Middle and right) Adapted from[215]

Surfaces which are symmetric about the {110} planes hence carry protected topological states in SnTe. As it has been mentioned before, the exact type of surface termination can have implications on the characteristics of corresponding surface states. In SnTe there are three surface terminations which fulfill these symmetry requirements, (001), (110) and (111). Liu et al.[216] found that these three terminations exhibit two different types of surface states, type one for (111) where all four equivalent L-points project to an individual surface point with invariant momentum, and type two for the other

terminations, for which the projections happen pairwise (see fig. 3.10).

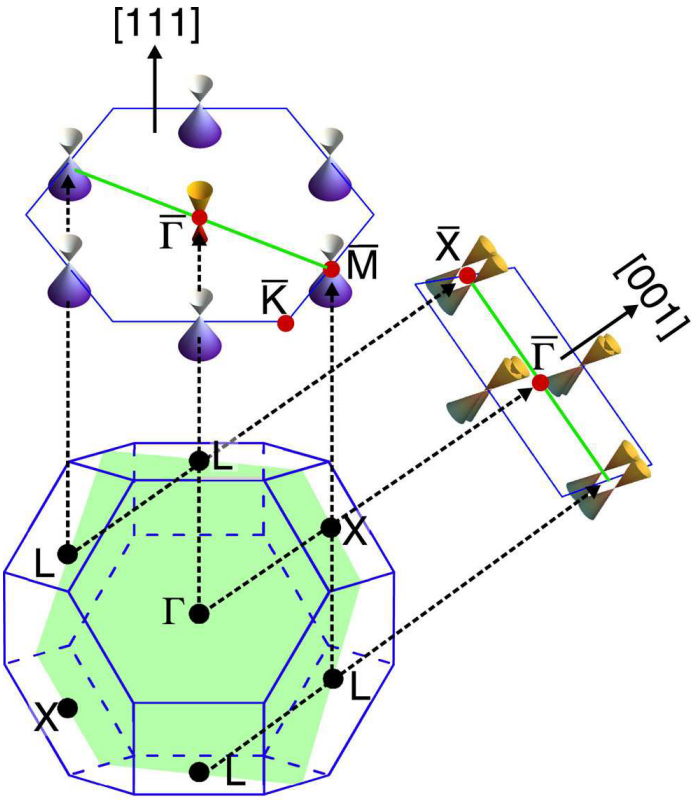

Figure 3.10: The two different types of surfaces in SnTe. On the (111) surface the four bulk L-points project onto individual points with invariant momentum, while the (001) surface has only two pairwise projections, leading to hybridization. The green plane represents the (110) mirror plane in the bulk Brillouin zone and the green lines the projections onto the surface Brillouin zones.
Adapted from [217]

(111) surface states are less complicated because the Dirac states, as long as translational symmetries are maintained, cannot couple in-plane due to their different in-plane momenta. Therefore the four L-point projections onto the surface give rise to four branches of Dirac surface states, located at Γ and M of the surface Brillouin zone. Since preparation of (111) surface is a bit more sublime these states have been experimentally realized later by Tanaka et al.[217] They confirmed Dirac surface states at the given points with ARPES measurements and found a shift in energy between the cones as well as different Dirac velocities which stems from different broadness of the bulk band (projections onto the surface) from which the surface states smoothly emerge.
In the case of (001) surfaces, as an example of type two, the four bulk L-points project pairwise to the X-points of the surface Brillouin zone, leading to hybridization effects of the cones. As a result, a double-cone structure is created with its two cones shifted away from X to Λ_1, Λ_2 on the high-symmetry line $\Gamma - X$. The presence of these states was experimentally confirmed by Tanaka et al.[217] as well, as shown in fig. 3.9 (middle panel).

Interesting features arise from the hybdridization, for instance a topological *Lifshitz transition*, a gradual transition from two disconnected electron pockets to a large electron and a small hole pocket. The transition is accompanied by a van-Hove singularity in the density of states [216].

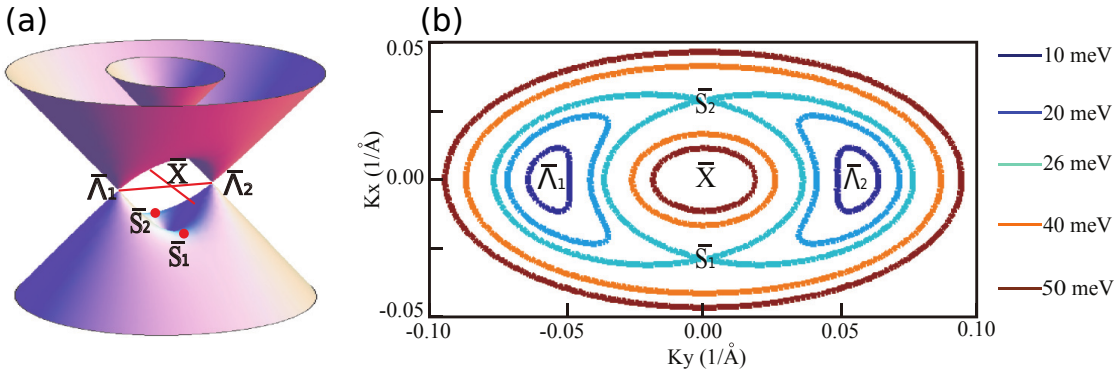

Figure 3.11: a) Double Dirac cone structure created by hybdridization on the (001) surface. b) Constant energy contour lines showing the gradual widening of the two electron pockets at Λ_i and the creation of a large electron pocket and a small surrounded hole pocket at the Lifshitz transition.
Adapted from [216]

The number of surface states can be estimated via weak anti-localization measurements, where each 2D channel should contribute a constant dimensionless parameter $\alpha = -0.5$ to the conductance within the Hikami-Larkin-Nagaoka formalism [218] (HLN),

$$\sigma_{\mathrm{HLN}} = \alpha \frac{e^2}{2\pi^2\hbar} \left[\ln\left(\frac{\hbar}{4eB_\perp l_\Phi^2} \right) - \Psi\left(\frac{1}{2} + \frac{\hbar}{4eB_\perp l_\Phi^2} \right) \right], \tag{3.8}$$

with $B_\perp$ the out-of-plane magnetic field, Ψ the Digamma function and l_Φ the phase-coherence length of the surface channel. It should be pointed out that, even though WAL is of 2D origin, the bulk still plays a very important role by coupling the two surfaces, which is referred to as *inter-surface coupling* [219]. This coupling depends on charge carrier properties of the bulk and hence ultimately on fabrication conditions of the SnTe. Transport can also be influenced by *intra-surface coupling* of Dirac cones on the same surface [220].
Additionally, SnTe is known to have a rhombohedral transition of the crystal structure at low temperatures [221]. The critical temperature of this transition strongly decreases with increasing charge carrier density as well. While the distortion due to the atomic displacement in SnTe is generally small, mirror symmetries can nevertheless be influenced which can introduce small gaps to otherwise gapless surface states. This transition was theoretically studied by Plekhanov et al. [222] who found indication for a rich sequence of phases, ranging from the cubic TCI phase to a time-reversal invariant TI phase and finally to a ferroelectric phase with strong Rashba effect for increasing lattice distortion.

4 Superconductivity and SQUID Physics in Topological Materials

After the discovery of superconductivity by Kamerlingh Onnes in 1911, who found a resistance drop to zero in mercury at liquid helium temperature, physicists struggled to develop a theoretical model that explains this phenomenon. Further discoveries like the Meissner-Ochsenfeld effect [223], the repulsion of magnetic fields inside of a superconductor, or the dependance of the critical temperatures of different superconducting materials on the isotopic mass [224] provided hints that finally led to progress in the description: from the phenomenologic London equations [225] in 1935 to the phenomenologic Ginzburg-Landau theory [154] in 1950, a symmetry-breaking phase transition theory mentioned in section 3.1.1, to the first microscopic description by Bardeen, Cooper and Schrieffer in 1957, the famous BCS theory [155]. The latter is based on attractive interaction of electrons mediated by electron-phonon coupling that creates pair states, the so-called Cooper pairs, which are usually spaced over several hundreds of nanometers and have quasi-bosonic character due to a spin singlet pairing mechanism allowing for symmetric spatial wave functions. This concept is now commonly referred to as *s*-wave superconductivity.
The achievement of a microscopic theory did not end the quest for new phenomena or models in the field of superconductivity. Intrinsic properties of 3D materials, pure elements and compounds, were investigated mainly in order to increase the critical temperature of superconductors. In this context models of different pairing symmetries like *p*-wave or *d*-wave superconductivity were introduced, but these types remained not well understood and practical implementation elusive at first.
With the emergence of microelectronic applications the focus fell on spatial inhomogenities in superconductors. A first evidence of this is the Josephson effect [226], the tunneling of Cooper pairs through thin insulating barriers discovered in 1962. Transport through non-superconducting junctions is, together with quantization of magnetic flux in superconductors, at the heart of the superconducting quantum interference device (SQUID), which can be used to detect magnetization very precisely. Later on junctions were fabricated for example as normal metal layers, which covers different transport mechanisms. Superconducting transport in adjacent normal layers was soon understood via the generalization of Andreev states and the superconducting proximity effect [227] [228] [229]. Especially since the discovery of graphene, CNTs or topological insulators, a more complete picture developed that combines novel materials and unconventional pairing mechanisms to provide many new and interesting phenomena and potential applications, of which the induced superconductivity in TIs is just one example. Already induced s-wave coupling in these materials with their extraordinary electronic properties can produce effects like topological superconductivity and its implications that have been touched in sec. 3.1.3.

4.1 Introduction to Superconductivity and SQUID Physics

4.1.1 BCS Formalism for *S*-Wave Superconductivity

The BCS formalism is based on attractive electron-electron interaction, which seems to be a strange physical concept bearing in mind that Coulomb interactions between equal charge types are repulsive. However, it can be shown that electron-phonon interaction for certain conditions leads to an effective electron-electron interaction that is attractive for electrons near the Fermi surface. This model explicitly requires a symmetric spatial wave function and since the paired electrons still obey fermionic statistics, the total (product) wave function requires the spin contribution to be antisymmetric - a singlet of electrons with opposite spin. Neglecting the dependence on phonon momenta $\mathbf{q}$ and assuming the simplest case of electron pairing with opposite momenta, where the attractive potential is maximized, the BCS Hamiltonian reads

$$\mathcal{H}_{\mathrm{BCS}} = \sum_{\mathbf{k},\sigma} \varepsilon_{\mathbf{k}\sigma} c^{\dagger}_{\mathbf{k}\sigma} c_{\mathbf{k}\sigma} - \sum_{\mathbf{k},\mathbf{k}'} V_{\mathbf{k},\mathbf{k}'} c^{\dagger}_{\mathbf{k}\uparrow} c^{\dagger}_{-\mathbf{k}\downarrow} c_{-\mathbf{k}'\downarrow} c_{\mathbf{k}'\uparrow}, \tag{4.1}$$

This Hamiltonian is usually simplified via a mean-field approximation of anomalous pair values, which represents the picture, that electrons couple pairwise, leading to

$$\mathcal{H}_{\mathrm{eff}} = \sum_{\mathbf{k},\sigma} \varepsilon_{\mathbf{k}\sigma} c^{\dagger}_{\mathbf{k}\sigma} c_{\mathbf{k}\sigma} - \sum_{\mathbf{k}} \Delta(\mathbf{k}) c^{\dagger}_{\mathbf{k}\uparrow} c^{\dagger}_{-\mathbf{k}\downarrow} + h.c., \tag{4.2}$$

where

$$\Delta(\mathbf{k}) = \sum_{\mathbf{k}'} V(\mathbf{k},\mathbf{k}') \langle c_{-\mathbf{k}'\downarrow} c_{\mathbf{k}'\uparrow} \rangle \tag{4.3}$$

is the superconducting gap, the order parameter that describes the superconducting phase. This Hamiltonian still contains anomalous contributions and does not conserve the particle number, which corresponds exactly to the aforementioned spontaneous breaking of $U(1)$ gauge symmetry. It does, however, conserve fermion parity, since creation or annihilation of Cooper pairs does not change the number of electrons from even to odd. $\mathcal{H}_{\mathrm{eff}}$ can be diagonalized by introducing Bogoliubov quasiparticle operators γ as linear combinations of $c, c^{\dagger}$

$$\begin{pmatrix} \gamma_{\mathbf{k},\uparrow} \\ \gamma^{\dagger}_{-\mathbf{k},\downarrow} \end{pmatrix} = \begin{pmatrix} u^{\star}_{\mathbf{k}} & -v_{\mathbf{k}} \\ v^{\star}_{\mathbf{k}} & u_{\mathbf{k}} \end{pmatrix} \begin{pmatrix} c_{\mathbf{k},\uparrow} \\ c^{\dagger}_{-\mathbf{k},\downarrow} \end{pmatrix} \tag{4.4}$$

which obey the Fermi anti-commutation relations

$$\{\gamma^\dagger_{\mathbf{k}\sigma}, \gamma_{\mathbf{k}'\sigma'}\} = \delta_{\mathbf{k}\mathbf{k}'}\delta_{\sigma\sigma'} \quad \text{and} \quad \{\gamma^\dagger_{\mathbf{k}\sigma}, \gamma^\dagger_{\mathbf{k}'\sigma'}\} = \{\gamma_{\mathbf{k}\sigma}, \gamma_{\mathbf{k}'\sigma'}\} = 0. \tag{4.5}$$

The complex u,v are quasiparticle wave functions which also define the BCS ground state $|\Psi_{\mathrm{BCS}}\rangle = \prod_{\mathbf{k}} \left(u_{\mathbf{k}} + v_{\mathbf{k}} c_{\mathbf{k},\uparrow} c_{-\mathbf{k},\downarrow}\right) |0\rangle$ with $\mathcal{H}_{\mathrm{BCS}} |\Psi_{\mathrm{BCS}}\rangle = E_{\mathrm{BCS}} |\Psi_{\mathrm{BCS}}\rangle$. Inserting the transformation reduces the Hamiltonian to

$$\mathcal{H}_{\mathrm{eff}} = \sum_{\mathbf{k},\sigma} E(\mathbf{k}) \gamma^\dagger_{\mathbf{k},\sigma} \gamma_{\mathbf{k},\sigma} + E_{\mathrm{BCS}}. \tag{4.6}$$

The γ operators desribe electron-like and hole-like excitations and do not correspond to the Cooper pairs. In the simple BCS case $E(\mathbf{k}) = \pm\sqrt{(\varepsilon_{\mathbf{k}} - \mu)^2 + |\Delta(\mathbf{k})|^2}$ is simplified by $\Delta(\mathbf{k}) = |\Delta(\mathbf{k})| \exp(i\Phi_S) = \Delta_0$ and a gap of $2\Delta_0$ in the quasiparticle energy spectrum is opened around zero energy. The constant energy contribution E_{BCS} in (4.6) represents the pure condensate without quasiparticle excitations and the gap in the density of states stresses the fact that no low-energy excitations are allowed in the superconducting state for standard s-wave superconductors. It will become clear in the following sections that the presence of appropriate interfaces changes this situation and may even lead to uncommon coupling mechanisms in the case of hybrid systems of superconductors and T(C)Is.

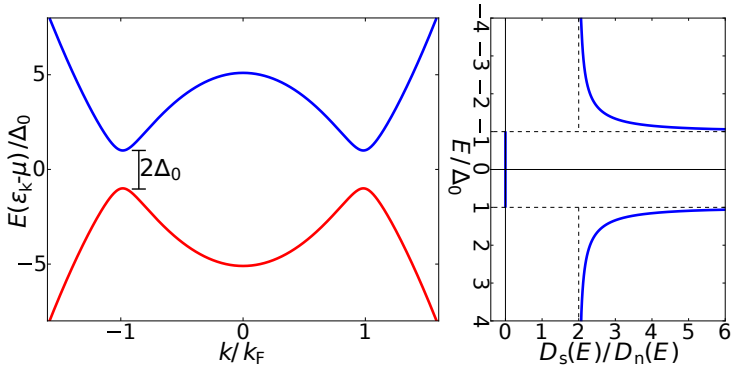

Figure 4.1: Energy spectrum and density of states for s-wave superconductivity in the Bogoliubov quasiparticle picture. The spectrum E_{k} is given for a parabolic dispersion and the resulting energy gap of $2\Delta_0$ is reflected in the superconducting density of states D_{s}, given in units of the normal-state density of states D_{n}.

4.1.2 Bogoliubov-de-Gennes Formalism

In order to describe systems with spatial inhomogenity such as boundaries, interfaces/junctions or impurities, the Bogoliubov-de-Gennes formalism is most conveniently applied. Keeping the spin degree of freedom s, one can write the mean-field Hamiltonian from equation 4.2 as

$$\mathcal{H} = \frac{1}{2} \sum_{\mathbf{k},s_1,s_2} \left(c^\dagger_{\mathbf{k}s_1}, c_{-\mathbf{k}s_1} \right) H_{\mathrm{BdG}} \begin{pmatrix} c_{\mathbf{k},s_2} \\ c^\dagger_{-\mathbf{k},s_2} \end{pmatrix}, \tag{4.7}$$

which is either a $2x2$ or $4x4$ representation, depending on the spin indices of the Bogoliubov-de-Gennes Hamiltonian $\mathcal{H}_{\mathrm{BdG}}$, which reads

$$\mathcal{H}_{\mathrm{BdG}}(\mathbf{k}) = \begin{pmatrix} \varepsilon_{s_1 s_2}(\mathbf{k}) & \Delta_{s_1 s_2}(\mathbf{k}) \\ \Delta^\star_{s_1 s_2}(\mathbf{k}) & -\varepsilon^t_{s_1 s_2}(\mathbf{k}) \end{pmatrix}. \tag{4.8}$$

For singlet pairing the gap function has to fulfill $\Delta(-\mathbf{k}) = \Delta(\mathbf{k})$. One can show that $\mathcal{H}_{\mathrm{BdG}}$ obeys particle-hole symmetry, which implies pairwise occurrence of energy eigenstates at $E_{s_i}(\mathbf{k})$ and $-E_{s_i}(-\mathbf{k})$. This symmetry carries important ramifications for the presence of bound states in the gap that ultimately allows for Majorana modes at superconductor-TI interfaces. In general, interfaces can be treated within this theory by Fourier-transforming $\mathcal{H}_{\mathrm{BdG}}$ into its real-space representation

$$\mathcal{H}_{\mathrm{BdG}}(\mathbf{r}) = \begin{pmatrix} \mathcal{H}_0(\mathbf{r}) & \Delta(\mathbf{r}) \\ \Delta^\star(\mathbf{r}) & -\mathcal{H}_0(\mathbf{r}) \end{pmatrix}, \tag{4.9}$$

where $\mathcal{H}_0(\mathbf{r}) = -(\hbar^2/2m)\nabla^2 - \mu + V(\mathbf{r})$ is the free-electron Hamiltonian. The Schrödinger equation $\mathcal{H}_{\mathrm{BdG}}(\mathbf{r}) \left|\Psi(\mathbf{r})\right\rangle = E \left|\Psi(\mathbf{r})\right\rangle$, where $\Psi(\mathbf{r}) = (\Psi_1(\mathbf{r}),\Psi_2(\mathbf{r}))^T$, is then called BdG equation and allows for the treatment of spatially varying systems $\Delta(\mathbf{r})$, for example metal-superconductor interfaces, from the microscopic point of view, the Andreev reflections. But first we discuss the Josephson effect and the SQUID in a more phenomenologic way.

4.1.3 Josephson Effect

As follow-up of Esaki tunneling in semiconductors, tunneling experiments by Giaever on superconductor-insulator-metal junctions[230] (SIN) and superconductor-insulator-superconductor junctions[231] (SIS) in 1960 confirmed the existence of the superconducting gap. However, transport was only understood in terms of a single-particle picture. It was only in 1962 that the theoretical work of Josephson[226], who predicted the tunneling of Cooper pairs through these thin insulating barriers in SIS junctions, explained this physics as a whole. The Josephson junction is most easily described by superconducting wave functions within the framework of phenomenological theories[232] for both sides of the barrier, $\Psi_j = \sqrt{n_j}\exp(i\theta_j)$, where n_j is the superconducting pair density and θ_j the phase. Substituting the ansatz into Schrödinger's equations,

$$i\hbar\frac{\partial}{\partial t}\Psi_{1,2} = E_{1,2}\Psi_{1,2} + K\Psi_{2,1}, \tag{4.10}$$

with coupling K between the two sides, gives the two Josephson equations, where $2eV = \mu_2 - \mu_1$, $\Phi = \theta_1 - \theta_2$ and $I_c = 2K\sqrt{n_1 n_2}/\hbar$ has been replaced:

$$I = I_c \sin(\Phi) \quad \text{and} \quad \frac{\partial \Phi}{\partial t} = \frac{2eV}{\hbar}. \tag{4.11}$$

These two equations describe the *DC Josephson effect* and the *AC Josephson effect*. For a current-biased junction a supercurrent flows without a voltage drop as long as $I < I_c$ in the case of the DC Josephson effect. I_c is hence referred to as critical current. The dependence of I on Φ is generally called *current-phase relation* (CPR), hence it is a 2π-periodic sine wave in the case of a standard Josephson junction.

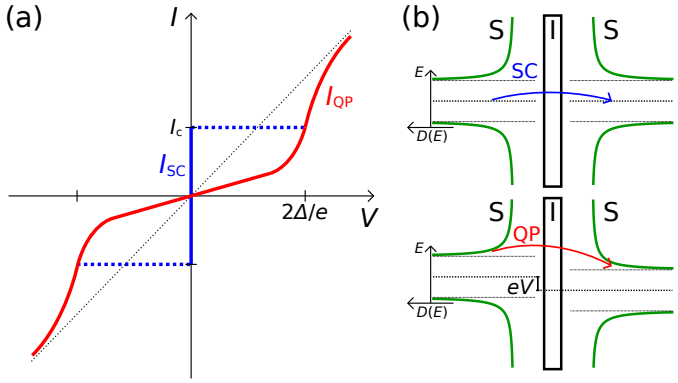

Figure 4.2: a) $I - V$ curve of a Josephson junction. For $I < I_c$ a supercurrent of Cooper pairs tunnels the barrier. For $I \geq I_c$ superconductivity breaks down and the $I - V$ curve jumps onto the quasiparticle branch which approaches Ohmic behaviour for large voltages. Junctions often show hysteretic behaviour. b) Energy scheme of the junction with the density of states, representing the two cases of transport. Cooper pairs exist at the middle of the gap and can tunnel in the superconducting state $I < I_c$. The transport is governed by quasiparticle tunneling for finite voltages at $I > I_c$ and for hysteretic retraces $I < I_c$.

The presence of both types of transport, Cooper pair and quasiparticle tunneling, gives real Josephson junctions both a resistive branch and a capacitance. This is usually taken into account via the *resistively and capacitively shunted junction model* (RCSJ), which describes the system as a circuit of Josephson junction, resistor and capacitor in parallel. The current is given by the sum $I = I_{JJ} + I_R + I_C$ and inserting the Josephson relations gives a equation of motion for the phase Φ,

$$-\frac{I}{I_c} = \frac{\partial^2}{\partial \tau^2}\Phi + \frac{1}{\sqrt{\beta}}\frac{\partial}{\partial \tau}\Phi + \sin(\Phi), \tag{4.12}$$

where $\tau = \omega_p t$ is the with the plasma frequency normalized time and the damping term $1/\sqrt{\beta}$ is determined by the *McCumber parameter* $\beta = \frac{2\pi}{\Phi_0} I_c R^2 C$, which strongly influences the hysteresis. Usually SIS junctions have a large RC and hence small damping and large hysteresis, while the reverse applies for SNS junctions.

In rf-irradiated junctions the *AC Josephson effect* comes to the fore and creates a peculiar pattern in the $I-V$ characteristics. For an applied current-bias the AC contribution with frequency f_{rf} leads to voltage steps and plateaus at integer multiples $V_n = hnf_{\mathrm{rf}}/2e$ which are referred to as *Shapiro steps*[233].

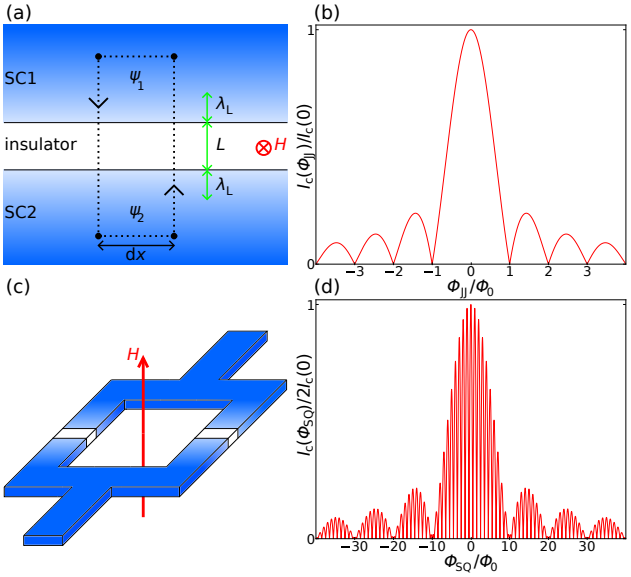

Figure 4.3: a) A Josephson junction of two superconductors spaced by a thin insulating barrier. Magnetic flux is picked up in an effective layer $L + 2\lambda_{\mathrm{L}}$. b) Fraunhofer pattern of a Josephson junction in an external magnetic field. c) The SQUID is a superconducting loop with two Josephson junctions in parallel, the enclosed flux is quantized. d) The SQUID geometry supperimposes a second faster oscillation to the single-junction Fraunhofer pattern. The case of symmetric junctions is shown here, with a SQUID surface area $A_{\mathrm{SQ}} = 10A_{\mathrm{JJ}}$.

4.1.4 Josephson Junctions in a Magnetic Field

One of the particularly interesting features of Josephson junctions arises when they are subject to magnetic fields perpendicular to the current flow. A magnetic field penetrates the barrier layer of thickness L and is screened by the superconductor within the *London penetration depth* λ_{L} to yield an effective magnetic junction thickness $L + 2\lambda_{\mathrm{L}}$. For short junctions the magnetic field, here defined via the vector potential $\mathbf{A}$, can be assumed as uniform and the the junction's phase difference $\mathrm{d}\Phi_x$ of a differentially small part dx with the contour in fig. 4.3a depends on the enclosed magnetic flux

$$\mathrm{d}\Phi_x = \oint \mathbf{A}\mathrm{d}\mathbf{l} = \frac{2\pi}{\Phi_0}\left(L + 2\lambda_{\mathrm{L}}\right)\mu_0 H. \tag{4.13}$$

Integration $\Phi(x) = \int \mathrm{d}\Phi_x \mathrm{dx}$ and maximization of the first Josephson relation $I(x) = I_{\mathrm{c}} \sin\left(\Phi(x)\right)$ gives the critical current for external magnetic flux $\Phi_{\mathrm{JJ}} = A_{\mathrm{JJ}}\mu_0 H$ picked up by the entire junction of area A_{JJ} as

$$I_c(\Phi_{JJ}) = I_c(0)\left|\frac{\sin\left(\pi\frac{\Phi_{JJ}}{\Phi_0}\right)}{\pi\frac{\Phi_{JJ}}{\Phi_0}}\right|. \tag{4.14}$$

Owing to the ressembling shapes of single-slit light diffraction and the sine-dependent oscillation of the Josephson current, $I_c(\Phi_{JJ})$ is usually called Fraunhofer pattern.

4.1.5 The DC SQUID

The effect of quantum interference for two Josephson junctions in a parallel loop configuration was first reported by Jaklevic et al.[234] in 1964. This is exactly the *superconducting quantum interference device* (SQUID). They found a second oscillation within the Fraunhofer pattern of a single junction which corresponds to the interference of the two current paths. In contrast to a single junction, the flux is now picked up by the complete loop area $A_{SQ} \gg A_{JJ}$, leading to a faster modulation which reproduces the double-slit pattern. An important property of superconducting loops is the limitation of the total enclosed flux Φ_{SQ} to integer values of quanta Φ_0,

$$\frac{2\pi\Phi_{SQ}}{\Phi_0} - \Phi_1 - \Phi_2 = 2\pi n, \tag{4.15}$$

where Φ_1,Φ_2 is the flux of the individual junctions. External magnetic fields create screening currents in the loop, which drives the currents through the two junctions apart and hence the critical current of the SQUID is reduced with increasing field. For $\Phi_{SQ} > \Phi_0$ the enclosed flux is increased by one quantum to minimize the system's energy and the screening current switches direction. For symmetric junctions with identical $I_c(0)$ and neglected self-inductance ($\Phi_{ext} = \Phi_{SQ}$), the modulation can be calculated as

$$I_c(\Phi_{SQ}) = 2I_c(0)\left|\cos\left(\pi\frac{\Phi_{SQ}}{\Phi_0}\right)\right|. \tag{4.16}$$

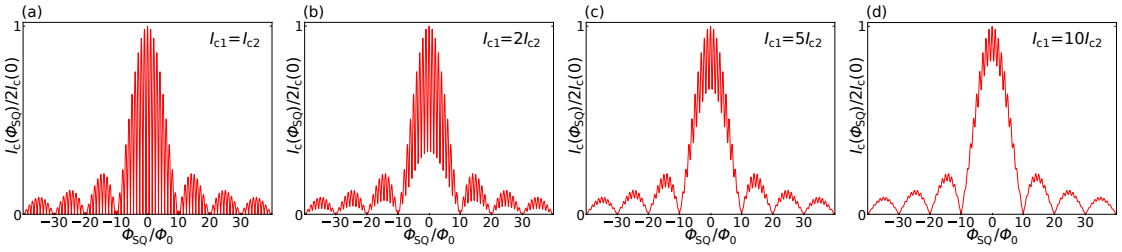

Figure 4.4: a) The ideal SQUID with symmetric junctions has full modulation depth. b-d) The effect of asymmetric junctions on the SQUID modulation for increasing difference in the critical current via each junction, leading to strongly reduced modulation depth.

4.1.6 Non-Standard Current-Phase Relations and SQUIDs

While the appearance of SQUID oscillations is robust to the exact type of junctions forming the ring, deviations result, for instance, from (microscopically unavoidable) asymmetry $I_{c_1} \neq I_{c_2}$. The SQUID modulation then changes to

$$I_c(\Phi_{SQ}) = \sqrt{(I_{c_1} - I_{c_2})^2 + 4I_{c_1}I_{c_2}\cos^2\left(\pi\frac{\Phi_{SQ}}{\Phi_0}\right)}, \tag{4.17}$$

which can lead to strongly reduced modulation depth $\Delta I_c/I_c$ (see fig. 4.4). On the other hand, the asymmetry can in principle be exploited, because these devices are almost exclusively sensitive to the CPR of the smaller junction, while the larger junction only provides an offset. Hence an investigation of junctions made up by tiny objects like atomic point contacts [235] is possible.
Reduced modulation depth and hysteresis also follows from the coil shape of the SQUID, giving rise to a *self inductance* or *geometric inductance* L_g and a corresponding screening factor $\beta_g = \frac{2\pi}{\Phi_0} I_c L_g$, which becomes more influential for larger loops. For large I_c the observation of hysteresis effects is also common, as Joule heating in the resistive state can strongly reduce the retrapping current into the superconducting state.
Beyond this basic notion, the SQUID can be formed by very different types of junctions, leading to deviations from the pattern of fig. 4.3 which only holds for SIS tunnel junctions. Replacing the insulating barrier by a spatially extended weak link can already drastically alter the Fraunhofer modulation due to non-negligible self-field effects [239] of the currents passing the junction area. These effects are thus strongly geometry-dependent and can for instance suppress higher maxima.
But also the CPRs of such junctions are vastly different. In general, junctions of length L can be classified as short or long with respect to superconducting coherence length ξ_{SC} as well as ballistic or diffusive with respect to the electron mean free path l_e. The underlying physics and theoretical description strongly depend on the particular case.
In SQUIDs with superconducting weak links (for example thin film Dayem bridges) or SNS junctions, the CPR usually differs significantly from the sine wave CPR of SIS tunnel junctions. In the case of micro-bridges with dimensions comparable or large with respect to ξ_{SC}, the CPR often takes on a (rounded) triangular shape and the SQUID shows small modulation depth (fig. 4.5a). Hasselbach et al. [240] calculated the relevant quantities of the complete (micro-)SQUID and explained the CPR with a phase drop that extends way over the junction region. Faucher et al. [236] assigned the measured effects to large *kinetic inductances* L_k in the corresponding screening factor $\beta_k = \frac{2\pi}{\Phi_0} I_c L_k$ for those devices. The current via such a junction can be calculated with the Likharev-Yacobson model [241] for the Ginzburg-Landau theory as

$$I(\Phi) = \frac{I_c}{\beta_k}\left(\Phi - \frac{\xi_{SC}^2}{L^2}\Phi^3\right), \tag{4.18}$$

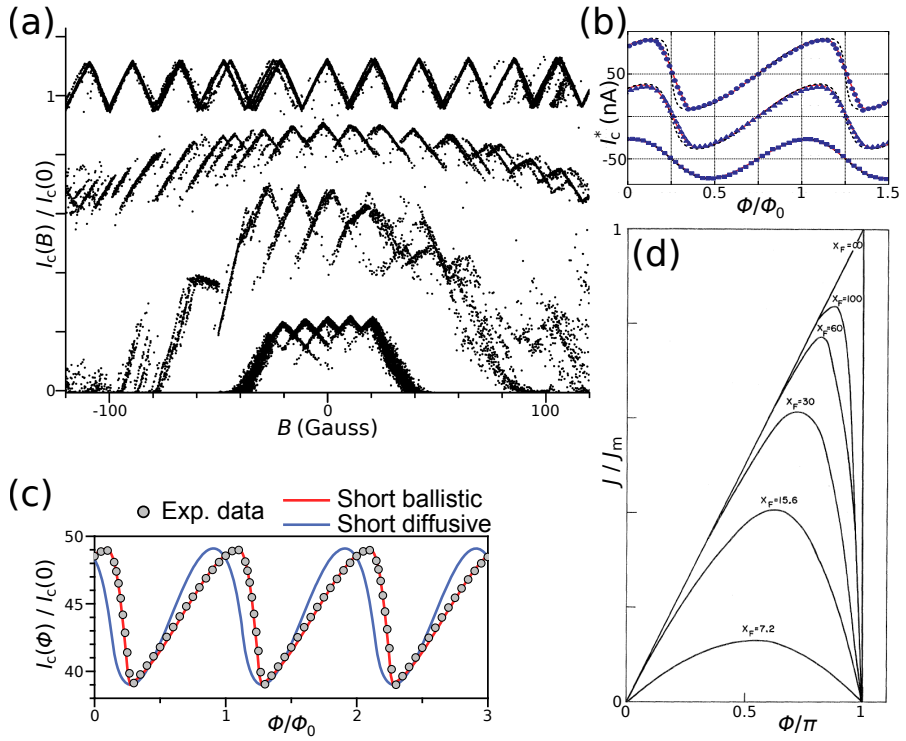

Figure 4.5: a) Niobium micro-SQUID devices with Dayem bridges as weak links. Curves are vertically shifted and correspond to decreasing weak link surfaces and increasing kinetic screening β_k from top to bottom. Triangular CPR and multi-valued switching is observed. b) Three different atomic contacts embedded in a SQUID loop, showing strongly skewed CPR for the presence of highly transmittive channels, while low transmission (lowest curve) ressembles the case of SIS tunnel junctions. c) Graphene can reproduce the expected CPR of short ballistic SNS junctions. The difference to the diffusive case is highlighted, which corresponds to a skewed sine. d) Calculated current density of a long SNS junction with different ratios x_F of bound quasiparticle spacing to k_BT. A sawtooth results for perfect ballistic transport at large spacing and low temperatures.
Adapted from a)[236] b)[235] c)[237] d)[238]

which leads to multivalued critical currents $I_c(\Phi_{SQ})$ for $\beta_k > 1$ such that Φ spans only a limited range before switching into the neighbouring state.

In SNS devices with ballistic transport the CPR becomes a sawtooth with either straight flanks for long channels[238] or rounded flanks for short channels, which can be realized for example in graphene[237]. Disorder also leads to a rounded CPR, which ultimately shifts the CPR back to (skewed) sine-like shapes. Examples of such CPRs are illustrated in fig. 4.5b-d.

Furthermore, there are different types of junctions with respect to at which phase difference Φ the current vanishes. For a normal Josephson junction with $I = I_c \sin(\Phi)$, the ground state $I = 0$ corresponds to $\Phi = 0$, while $\Phi = \pi$ corresponds to an instable state. Some systems have a π-shifted ground state with $I = I_c \sin(\Phi + \pi)$ and are therefore referred to as π-junctions. Here, the definition of the ground state follows from the minimum of the Josephson energy, which reads

$$U_{\mathrm{JJ}}(\Phi) = \frac{\Phi_0}{2\pi}\int I(\Phi)\mathrm{d}\Phi = \frac{2\pi}{\Phi_0} I_{\mathrm{c}}\left[1-\cos\left(\Phi\right)\right], \tag{4.19}$$

in the case of a normal junction with $\Phi = 0$ ground state. The supercurrent can be calculated from the Josephson energy as

$$I(\Phi) = \frac{2e}{\hbar}\frac{\partial U(\Phi)}{\partial \Phi}, \tag{4.20}$$

leading to $I = 0$ for both 0-junction and π-junctions when no phase bias is applied. For non-zero phase bias the π-configuration corresponds to a sign change in the Josephson current.

The most well-known example for such a π-shift occurs in SFS junctions, where a sign change of the superconducting order is caused by exchange interaction in a thin ferromagnetic layer[242]. Other realizations include the sign-changing $s_{\pm}$ gap in the iron picnitide material group[243] or d-wave cuprate superconductors[244], where the effect is usually tied to grain boundaries. Such boundaries give rise to phase discontinuities and pinned fractional vortices, which are of half-integer type for $0-\pi$-transitions.

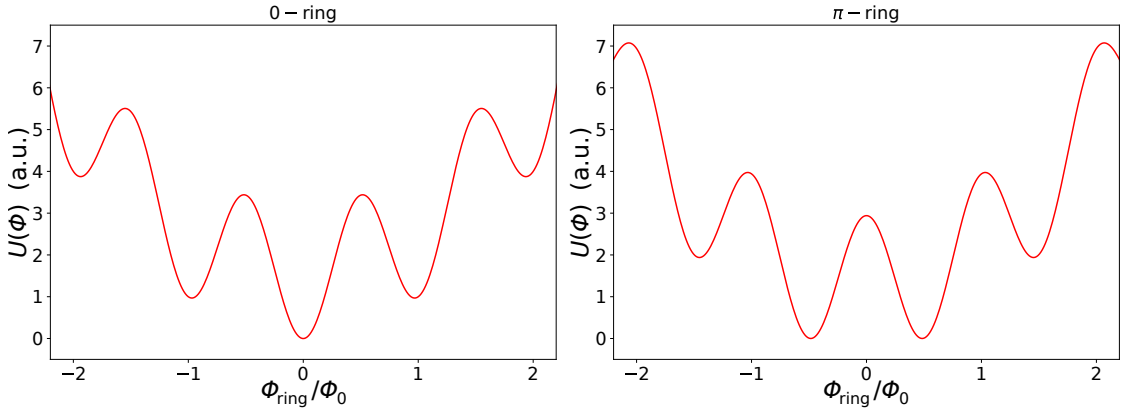

Figure 4.6: Josephson energy in a ring with one intersecting junction and no applied external flux as function of the flux in the ring. a) The standard setup has a non-degenerate ground state at $\Phi_{\mathrm{ring}} = 0$. b) For a phase shift of π two equivalent minima occur, shifted by $\pm\Phi_0/2$ from zero. Based on[244]

With a SQUID setup, such $0-\pi$-transitions of individual junctions are detectable as a phase shift of $\Phi_0/2$ in the modulation pattern when a (0,0) configuration switches to (0,π) or (π,0). For (π,π) the initial pattern is restored[245].

The most general cases of deviation from the standard configuration are the controllable φ-junction[246] with degenerate ground state at $\pm\varphi$ and the φ_0-junction[247], where a non-degenerate ground state at $\varphi_0 \neq 0,\pi$ gives rise to a supercurrent without phase bias. Such devices are of great interest for potential applications in data storage and quantum computation.

4.2 Induced Superconductivity in TI Materials

4.2.1 Andreev Reflection and Andreev Bound States

Since the early days of superconductivity research the possibility of zero-resistance SNS interfaces is well-known. Subsequent studies [248] showed that the interface resistance is critically dependent on the normal layer thickness L such that too thick metal layers break the superconducting state. Bearing in mind that Cooper pairs are non-local objects it was hence concluded that the superconducting pair density extends into the metal where it exponentially decays due to scattering events. Therefore superconductivity can be induced into normal conductors which are spatially close to the interface with the exact length scale ξ_{SC} being dependent on the transport properties of the normal material. On the other hand, it was found that too thin superconducting layers covered by metal also lead to a resistive state, representing the fact that the normal electron density penetrates the superconductor at the interface. These features are categorized as *proximity effect*.
Microscopically the proximity effect can be explained by Andreev reflection (AR) at one NS boundary and Andreev bound states (ABS) in SNS junctions. Starting from the Hamiltonian $\mathcal{H}_{\mathrm{BdG}}$ of eq. (4.9) one can write down the BdG equations as [227]

$$\mathcal{H}_0(\mathbf{r})\Psi_1(\mathbf{r}) + \Delta(\mathbf{r})\Psi_2(\mathbf{r}) = E\Psi_1(\mathbf{r}) \tag{4.21}$$

$$-\mathcal{H}_0(\mathbf{r})\Psi_2(\mathbf{r}) + \Delta^\star(\mathbf{r})\Psi_1(\mathbf{r}) = E\Psi_2(\mathbf{r}), \tag{4.22}$$

which generally have to be solved self-consistently. If one assumes that the potentials describing the system, $V(\mathbf{r})$ in $\mathcal{H}_0(\mathbf{r})$ and $\Delta(\mathbf{r})$ in the superconductor, vary slowly with respect to the mean electron spacing k_{F}^{-1}, the $\Psi_i(\mathbf{r})$ can be decoupled into a slowly varying part $f_i(\mathbf{r})$ and a rapidly varying part,

$$\Psi_i(\mathbf{r}) = f_i(\mathbf{r}) \exp(-i\mathbf{kr}), \tag{4.23}$$

with $|\mathbf{k}| \approx k_{\mathrm{F}}$ for all involved wave vectors, which simplifies the BdG equations to the Andreev equations

$$i\hbar v_{\mathrm{F}}\hat{\mathbf{n}}\nabla f_1 + \Delta f_2 = E f_1 \tag{4.24}$$

$$-i\hbar v_{\mathrm{F}}\hat{\mathbf{n}}\nabla f_2 + \Delta^\star f_1 = E f_2, \tag{4.25}$$

where $\hat{\mathbf{n}}$ is the incident unit vector. For one NS interface those equations can be solved with a technique that is analogous to the potential wall. Assuming the case of an interface at $x = 0$ with a simple s-wave superconductor Δ_0 at $x \geq 0$ and a perfectly ballistic normal metal with constant DOS at $x < 0$, the gap is a Heaviside step function $\Delta(x) = \Delta_0\Theta(x)$ and the wave functions on both sides have to be modelled by taking the

boundary conditions into account. The general solution for $x < 0$ reads

$$f(\mathbf{r}) = \begin{pmatrix} f_1(\mathbf{r}) \\ f_2(\mathbf{r}) \end{pmatrix} = \begin{pmatrix} \exp(i\mathbf{k}_1\mathbf{r}) + r_\mathrm{N} \exp(-i\mathbf{k'}_1\mathbf{r}) \\ a_\mathrm{N} \exp(i\mathbf{k}_2\mathbf{r}) \end{pmatrix}. \tag{4.26}$$

Here, $\mathbf{k}_1 = \hat{\mathbf{n}} E \hbar^{-1} v_\mathrm{F}^{-1} \ll k_\mathrm{F}$ corresponds to incident electrons with $\hat{\mathbf{n}}$ and specular reflection of electrons at the boundary occurs with coefficiant r_N along $\mathbf{k'}_1 = (-k_{1x}, k_{1y}, k_{1z})$. However, one finds $r_\mathrm{N} < 1$, which means that not all of the incident electrons are reflected. There is a non-vanishing contribution from the process a_N which, originating from the second spinor component, corresponds to a reflected spin-down hole in opposite direction to $\hat{\mathbf{n}}$, with $\mathbf{k}_2 = -\hat{\mathbf{n}} E \hbar^{-1} v_\mathrm{F}^{-1}$. So incident electrons can create reflected holes at the interface and vice versa, depending on the definition of $\hat{\mathbf{n}}$. Due to the involved wave vectors $\mathbf{k}_1, \mathbf{k'}_1, \mathbf{k}_2 \ll k_\mathrm{K}$, the reflected hole has almost the same momentum as the incident electron and the phenomenon is commonly referred to as *Andreev reflection*, which is a strongly spin-dependent process.

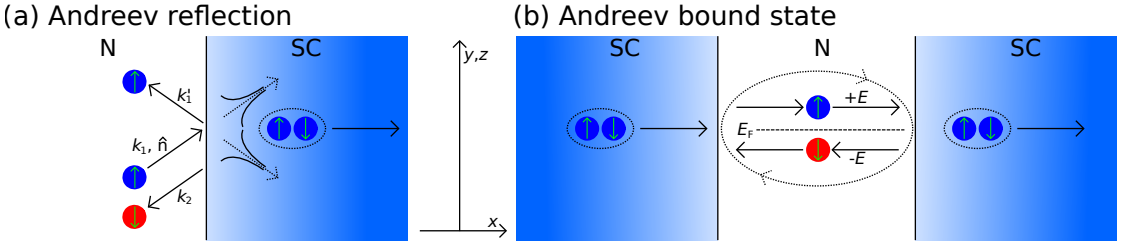

Figure 4.7: a) Andreev reflection at a metal-superconductor interface. An incident electron can be specularly reflected or retroreflected as a hole, by this creating evanescent quasiparticle states and a Cooper pair in the superconductor. b) Multiple such reflections on both sides of a SNS junction lead to the formation of an Andreev bound state, corresponding to the transport of Cooper pairs from left to right.

On the superconductor side, given by $x \geq 0$, the Andreev equations are solved by

$$f(\mathbf{r}) = \begin{pmatrix} f_1(\mathbf{r}) \\ f_2(\mathbf{r}) \end{pmatrix} = c_\mathrm{SC} \begin{pmatrix} \sqrt{1 + v_\mathrm{F} \mathbf{n}\hat{\mathbf{k}}_3 \hbar E^{-1}} \\ -i\sqrt{1 + v_\mathrm{F} \mathbf{n}\hat{\mathbf{k}}_3 \hbar E^{-1}} \end{pmatrix} \exp(i\mathbf{k}_3\mathbf{r}), \tag{4.27}$$

with c_SC a constant and $\mathbf{n}\hat{\mathbf{k}}_3 = \hat{n}_x \frac{1}{v_\mathrm{F}} \sqrt{E^2 - \Delta_0^2}$. For incident electrons with energy $E < \Delta_0$ the result is an evanescent quasiparticle state penetrating the superconductor side. However, this evanescent contribution cannot explain the charge imbalance which is created in the metal in the case of Andreev reflection, where effectively $2e$ is created. The solution for this is the formation of a Cooper pair in the SC for which the second electron is taken from the metal, corresponding to the creation of a hole.
When the situation is extended to two such interfaces in a SNS junction, interesting physics arises: at the second interface there is also a non-zero probability for Andreev

reflection of the formerly reflected hole. This disassiocates a Cooper pair in the left SC and emits an electron into the normal region. Twofold reflection thus leads to the transport of a Cooper pair from the left SC to the right SC, analogous to the Josephson effect in SIS junctions. For multiple reflections *Andreev bound states* are formed, which correspond to the continuous transport of Cooper pairs over the junction at zero bias. If a bias voltage V is applied to the junction, both electrons and holes gain an energy eV for every travel between the interfaces. This means that a quasiparticle entering the metal with an energy below the gap can gain enough energy via a sufficient number of reflections to overcome the gap $2\Delta_0$ and tunnel into an unoccupied state in the right SC, which breaks up the bound state. These events are associated with subgap transport features in electron tunnel spectroscopy. Particularly interesting about these bound states is that they take on the symmetry of the superconductor [249] and also depend heavily on the spectrum of the middle part N. In general, the supercurrent contribution of an ABS with energy spectrum $E(\Phi)$ can be determined according to eq. (4.20) via

$$I(\Phi) = \frac{2e}{\hbar}\frac{\partial E(\Phi)}{\partial \Phi}. \tag{4.28}$$

Since the properties of junctions made from a TI and enclosed by s-wave superconductors were found to strongly resemble the case of $p_x + ip_y$ superconductivity by Fu et al. [175], a quick introduction to this type of gap symmetry is given in the following.

4.2.2 *P*-Wave Superconductivity and Majorana Bound States

In general, the pairing mechanism of the superconducting state is governed by energetical considerations for the underlying materials (crystal) structure. In section 4.1.1 s-wave superconductivity in the BCS picture was introduced as a pairing mechanism of antisymmetric spin singlet states with symmetric spatial wave function to obey Fermi statistics. Furthermore, the gap was assumed constant, $\Delta(\mathbf{k}) = \Delta_0$. This type of superconductivity is by the far the most common and simplest. There are, however, materials where different pairing mechanisms occur. One example is d-wave superconductivity, which can be found in high-T_c cuprates and has a spin singlet structure but a $\mathbf{k}$ dependence of $\Delta(\mathbf{k})$. Another type is the case of spin triplet pairing, usually referred to as p-wave superconductivity, with a gap symmetry $\Delta(-\mathbf{k}) = -\Delta(\mathbf{k})$ and Sr_2RuO_4 as the main candidate. The naming of the pairing types is derived from the analogy of the spatial part of the gap function and the atomic orbitals in quantum mechanics. Nomenclature and symmetries can be summarized as:

name	orbital state L	spatial parity	spin state	spin parity
s-wave	0	even	singlet	odd
p-wave	1	odd	triplet	even
d-wave	2	even	singlet	odd

Table 4.1: Different types of superconductivity and their parities.

A common point of most of these unconventional pairing types are nodes in the superconducting gap which can be specified with $\Delta(\mathbf{k})$. One example is a triplet state of an 1D p-wave superconductor, for instance with symmetry p_x, which has nodes in k_y-direction. An exception in this sense is the triplet $p_x \pm ip_y$ pairing which can appear in 2D, a type that is referred to as *chiral*, showing no nodes [250].

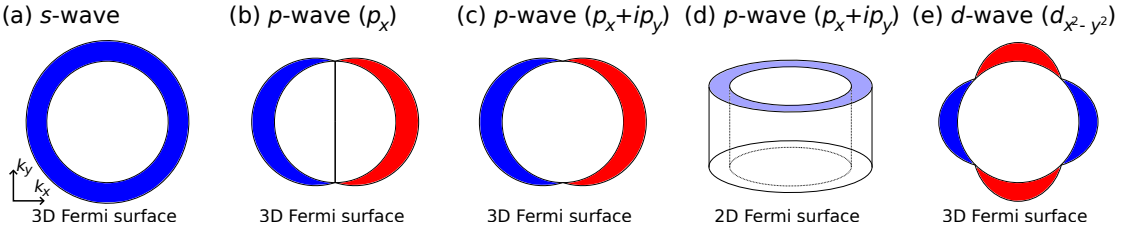

Figure 4.8: Illustration of the superconducting gaps for different symmetries with (a)-(c) and (e) being projections of a 3D spherical Fermi surface into the $k_x - k_y$-plane. Red and blue separate regions with phase difference π of the gap function. a) A *s*-wave gap is isotropic. b) A p_x gap has nodes along the p_y direction (black line). c/d) A $p_x + ip_y$ gap in 3D has nodes, while it is fully gapped in 2D (chiral). e) An example of a *d*-wave gap.
Based on [251] [252]

The symmetry of the pairing can be universally introduced with a spinor expression [253]

$$\Delta(\mathbf{k}) = \begin{pmatrix} \Delta_{\uparrow\uparrow}(\mathbf{k}) & \Delta_{\uparrow\downarrow}(\mathbf{k}) \\ \Delta_{\downarrow\uparrow}(\mathbf{k}) & \Delta_{\downarrow\downarrow}(\mathbf{k}) \end{pmatrix} = i\left(\Delta_{\mathbf{k}}\mathbb{1}_2 + \mathbf{d}(\mathbf{k})\boldsymbol{\sigma}\right)\sigma_y, \tag{4.29}$$

where $\Delta_{\mathbf{k}}$ corresponds to the even singlet contribution, $\mathbf{d}$ is a three-component vector that determines the odd triplet contribution and $\boldsymbol{\sigma}$ and σ_y are (vectors of) Pauli matrices. Also, $\mathbf{d}$ defines a normal plane of equal spin pairing and the gap is $\propto |\mathbf{d}|^2$. In the case of $p_x + ip_y$ pairing with $S_z = 0$ this vector could be given by $\mathbf{d} = \Delta_0\,(0{,}0{,}k_x + ik_y)$. It should be noted that the exact form of $\mathbf{d}$ depends heavily on material crystal symmetries and that these unconventional types of pairing normally break more than just gauge symmetry [251].

A superconducting gap of the p-wave type has important ramifications as it can, under certain conditions, give rise to *Majorana bound states* (MBS) in the material. While the idea of *Majorana fermions*, fermionic particles that are their own anti-particle, is long known, the concept gained a lot more interest when it became clear that there are quasi-particle excitations in solid state physics that obey those peculiar characteristics. As it was shown first by Kitaev [174], a p-wave 1D superconducting chain is exactly such a case, that leads to the creation of MBS at its ends[1]. The spinless[2] (tight-binding) Hamiltonian

1 One should keep in mind the Bogoliubov quasiparticle picture which has excitations of electron and hole contribution. *S*-wave SC quasiparticles do however not fulfill Majorana conditions.
2 Here this means exactly that Δ couples equal spins to triplet states.

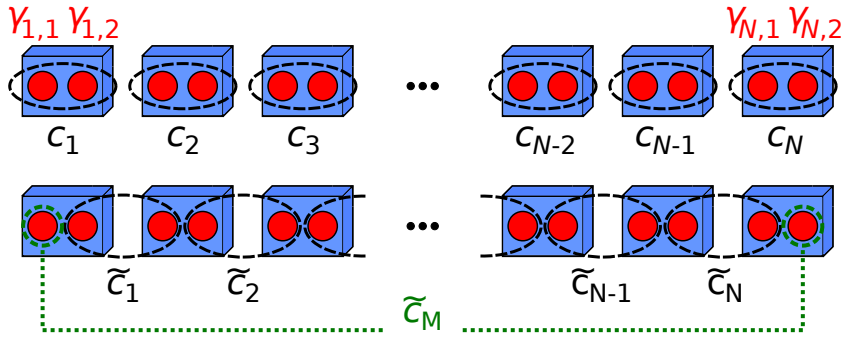

Figure 4.9: The superconducting chain with *p*-wave gap has a Majorana mode at its ends. Fermions on each site i with operators c_i can be each split into two half-fermionic Majorana operators γ. The Hamiltonian of the system is diagonalized by pairing Majorana operators from neighbouring sites, leaving two unpaired Majorana operators at the ends.
Based on [254]

$$\mathcal{H}_{1\mathrm{D}\,p-\mathrm{wave}} = -\mu \sum_{i=1}^{N} n_i + \sum_{i=1}^{N-1} \left(t c_i^\dagger c_{i+1} + \Delta c_i c_{i+1} + h.c. \right) \tag{4.30}$$

can be rewritten by splitting the fermionic operators $c_i^\dagger, c_i$ of the N_i sites of the chain into half-fermionic Majorana operators γ via

$$c_i = \frac{1}{2} \left(\gamma_{i,1} + i\gamma_{i,2} \right) \tag{4.31}$$

$$c_i^\dagger = \frac{1}{2} \left(\gamma_{i,1} - i\gamma_{i,2} \right). \tag{4.32}$$

The inverse easily shows $\gamma = \gamma^\dagger$. This operation is mathematically nothing remarkable and could be performed for arbitrary fermions, just that overlap due to localization of the pair normally cancels any physically measureable effect [254]. In the case of the *p*-wave chain, this operation diagonalizes the (low-energy $\mu \to 0$) Hamiltonian in an again fermionic picture $\tilde{c}^\dagger, \tilde{c}$, when the Majorana operators are paired on neighbouring sites. This operation excludes the two Majorana states at the ends of the chain from the Hamiltonian, which can hence be occupied with zero energy cost and are referred to as *Majorana zero mode*, corresponding to the delocalized fermionic pair state

$$\tilde{c}_\mathrm{M} = \frac{1}{2} \left(\gamma_{N,2} + i\gamma_{1,1} \right). \tag{4.33}$$

This delocalization reflects the topological protection and is thus at the heart of the conceptual fault-tolerant quantum computation. As a generalization of the 1D chain one can find similar results for the 2D case of $p_x \pm ip_y$ superconductivity, which has gapless

chiral edge modes very similar to the quantum Hall edges. Here, Majorana zero modes can occur as zero-energy solutions to the chiral edge modes and/or at vortices [255] [256], where the gap Δ goes to zero and hence allows for such solutions for bound states. Non-degenerate states of this kind automatically fulfill Majorana conditions due to the electron-hole symmetry in the superconductor.
Different to the case of *s*-wave superconductors, fermion parity of the ground states switches at the zero-energy crossings. One can consider the ground state fermion parity in these systems as a topological invariant, indicating the close relation of the concept of Majorana zeromodes and *topological superconductivity*. It is long known that the Josephson current via such states is 4π-periodic in the superconducting phase, owing to the change in fermion parity, which is one of the most striking features of MBS and a stark contrast to the common 2π-periodicity of *s*-wave coupled SIS junctions (see eq. 4.11).

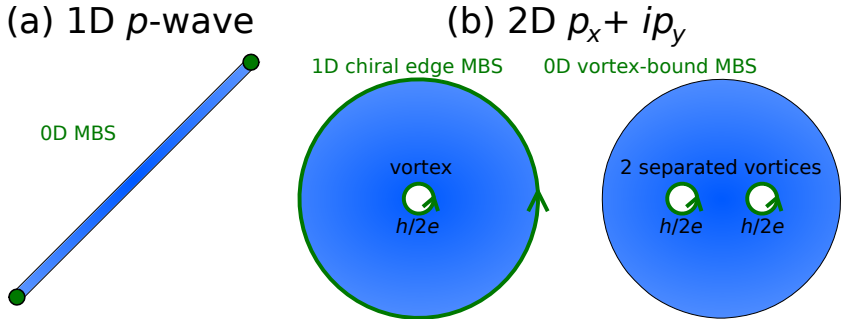

Figure 4.10: Spatially separated MBS in *p*-wave superconductors. a) In the 1D *p*-wave chain 0D MBS appear at the ends. b) The 2D $p_x + ip_y$ has chiral Majorana modes at vortices.

Kwon et al. [257] calculated the ABS energy spectra and resulting supercurrent of realistic SIS junctions of different geometries and couplings, for example in 1D,

$$E(\Phi) = \pm\Delta_0\sqrt{1 - D^2\sin^2(\Phi/2)} \tag{4.34}$$

$$E(\Phi) = \pm\Delta_0\sqrt{D}\cos(\Phi/2), \tag{4.35}$$

resulting in a 4π-periodic spectrum for *p*-wave structures, whereas a non-vanishing interface barrier (transmission $D < 1$) opens up a gap in the case of *s*-wave coupling which creates two separated 2π-periodic branches. According to eq. 4.28, the Josephson current has the same periodicity as the energy spectrum. Kwon et al. also found 4π-periodicity for 2D *p*-wave structures of specific alignment and related this periodicity to a fractional AC Josephson effect at half-frequency $eV/\hbar$.
As mentioned already in sec. 3.1.3, a similar experimental platform can be realized in nanowires with strong (Rashba) spin-orbit coupling and induced superconductivity. A key signature of MBS is a zero-bias conductance peak, which was observed by Mourik et al. [176] for InAs nanowires and by Das et al. [258] and Deng et al. [259] for InAs. There is, however, still an ongoing discussion surrounding these measurements, since the conductance of

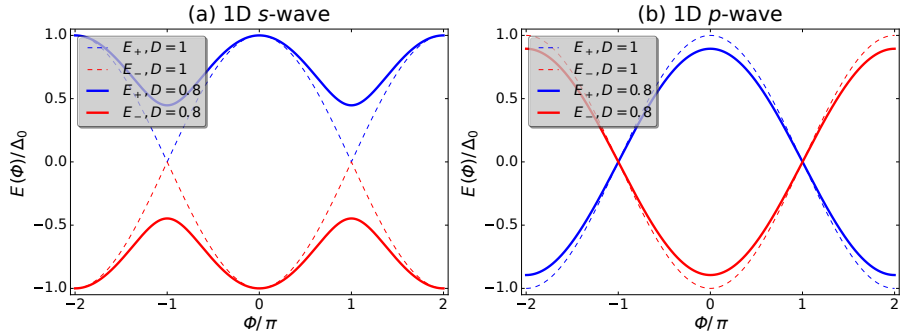

Figure 4.11: Andreev bound states of a 1D superconductor with a) *s*-wave coupling, for which a gapped 2π-periodic energy spectrum emerges, and b) *p*-wave coupling, which shows a 4π-periodic spectrum. In both cases the modes are separated by the bulk of the system, with finite size effects giving rise to (exponentially) small gaps, shifting the energy levels away from zero. Based on [257]

the zero-bias peak is predicted by theory to be robust at $2G_0$ for $T \to 0$, no matter the barrier strength. This quantized conductance was not observed so far, and distinguishing between trivial ABS and MBS remains a very delicate problem in real experimental systems [260] [261].

4.2.3 Superconductor-TI Interfaces

While the concept of Majorana physics in *p*-wave superconductors is enticing, the rareness of these materials still hinders serious progress. Fortunately, the close relation to the topological insulator class allows to take a shortcut as topological superconductivity can indeed be realized via the proximity effect in these systems. As Fu et al. [175] showed for the particular example of a 3D TI, one only needs to induce a common *s*-wave superconducting gap to the surface spectrum of a TI to create a system that effectively obeys $p_x + ip_y$ symmetry[1].
To incorporate the spin dependence of the TI and the electron-hole symmetry of the superconductor, this problem is usually treated in the Nambu presentation in four dimensions, where the total Hamiltonian is given by

$$\mathcal{H} = \frac{1}{2}\Psi^\dagger \mathcal{H}_{\text{eff}} \Psi. \tag{4.36}$$

Here, $\Psi = \left((\psi_\uparrow, \psi_\downarrow), (\psi_\downarrow^\dagger, -\psi_\uparrow^\dagger)\right)^{\mathrm{T}}$ with the electron field operators ψ and $\mathcal{H}_{\text{eff}}$ is composed of the TI surface Fermi arc and a Cooper pair tunneling contribution,

1 Similar concepts hold for the relation of 1D *p*-wave chain and induced superconductivity in the helical edge modes of a 2D QSH insulator.

$$\mathcal{H}_{\text{eff}} = \mathcal{H}_{\text{TI}} + \mathcal{H}_{\text{SC}} \tag{4.37}$$
$$= \hbar v_{\text{F}} \tau^z \otimes \boldsymbol{\sigma}\mathbf{k} - \mu_{\text{TI}} \tau^z \otimes \mathbb{1}_2 + \Delta_0 \left(\tau^x \cos\Phi + \tau^y \sin\Phi\right) \otimes \mathbb{1}_2, \tag{4.38}$$

a matrix of dimension $D = 4$ in the chosen representation. The τ are Pauli matrices mixing the ψ and $\psi^\dagger$ blocks of Ψ, hence operating in the electron-hole space. It can be shown that $\mathcal{H}_{\text{eff}}$ obeys time-reversal symmetry and particle-hole symmetry and the spectrum is given by

$$E(\mathbf{k}) = \pm\sqrt{(\pm\hbar v|\mathbf{k}| - \mu_{\text{TI}})^2 + \Delta_0^2}, \tag{4.39}$$

which gives rise to a low energy spectrum that resembles the $p_x \pm ip_y$ superconductor for $\mu_{\text{TI}} \gg \Delta_0$. This analogy becomes clearer for diagonalization via a transformation into a system which rotates with $\mathbf{k} = k_0 \left(\cos\left(\theta_k\right) + \sin\left(\theta_k\right)\right)$. This is done by using the relation $c_{\mathbf{k}} = \left(\psi_{\mathbf{k}\uparrow} + \exp\left(i\theta_{\mathbf{k}}\right)\psi_{\mathbf{k}\downarrow}\right)/\sqrt{2}$, resulting in

$$\mathcal{H}_{\text{eff}} = \sum \left(v|\mathbf{k}| - \mu_{\text{TI}}\right) c_{\mathbf{k}}^\dagger c_{\mathbf{k}} + \frac{1}{2}\Delta_0 \left(\exp\left(i\theta_{\mathbf{k}}\right) c_{\mathbf{k}}^\dagger c_{-\mathbf{k}}^\dagger + h.c.\right), \tag{4.40}$$

which is formally equivalent to a spinless $p_x \pm ip_y$ superconductor with the exception of time-reversal symmetry conservation for the TI. Fu et al. concluded that the SC-TI interface should hence show MBS similar to the case of vortices in the $p_x \pm ip_y$ superconductor. Here, the Majorana partner state resides at the opposite surface of the 3D TI which hosts the second Dirac cone (see fig. 4.12a).
Fu et al. also showed that a line junction of a 3D TI between two s-wave superconductors, sketched in fig. 4.12b, should give rise to gapless nonchiral Majorana modes at a phase difference of π between the superconductors. One could imagine breaking TRS via a Zeeman field, which could experimentally be done with a deposited ferromagnetic layer[1], to induce an insulating gap in the surface spectrum and create chiral Majorana edge states.
The aforementioned calculations were done for the case of a perfectly topologically insulating state, having no doping, $\mu_{\text{TI}} = 0$. Experimentally it is difficult to realize such systems since known TI materials are usually strongly doped. Snelder et al. [262] studied the practically more relevant case of $\mu_{\text{TI}} \gg \Delta_0$ and showed that MBS are still present at this limit, but their existence may be masked. The characteristics of available 4π-periodic channels now strongly depend on the mismatch of the chemical potentials μ_{TI} and μ_{SC}: for zero mismatch or perfectly transparent barriers, all trajectories give rise to a 4π-periodic ABS, while for non-zero mismatch all trajectories with an angle of incidence are gapped out and hence 2π-periodic.

1 This layer is ideally electrically insulating to avoid shunting of the TI junction.

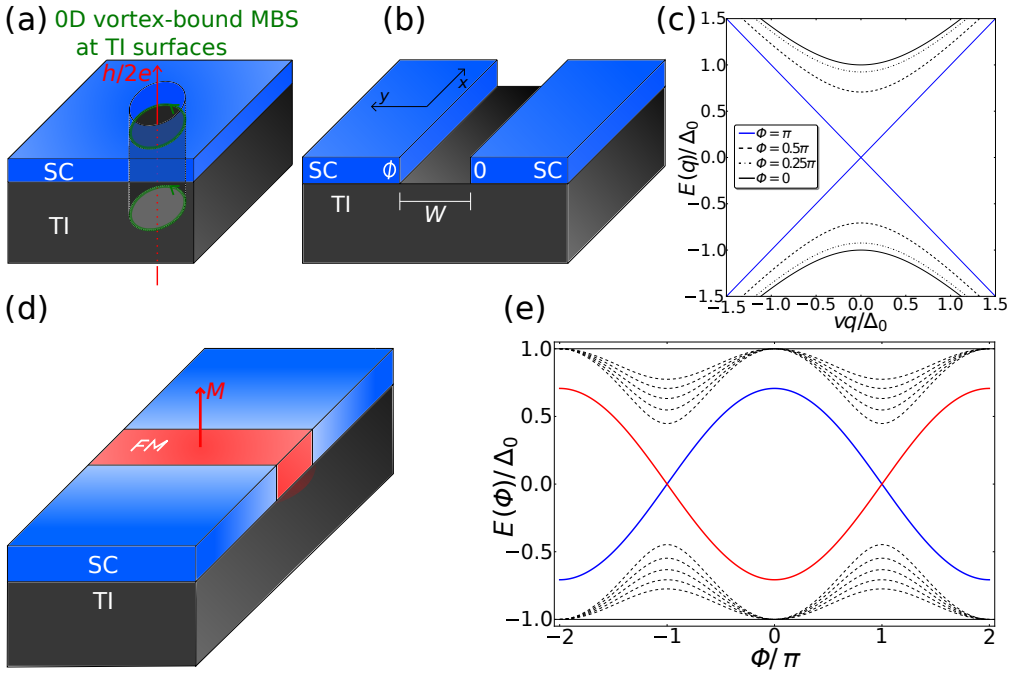

Figure 4.12: a) The interface of a *s*-wave SC on a 3D TI has Majorana zero modes bound to vortices, located at the two surfaces of the TI. b) A line junction can host nonchiral Majorana modes with dispersion parallel to the interface. c) Energy dispersion of such a junction for $W \to 0$ with wave vector $\mathbf{q}$ in y-direction. For $\Phi = \pi$ gapless mode are present (blue lines), while a phase different from π gaps out the modes. d) Model system for the study of MBS in topological junctions. A *s*-wave superconductor (SC) and a ferromagnetic layer (FM) are deposited on top of the TI. e) Spectrum of the 4π-periodic ABS modes $E_\pm$ (blue and red lines), decoupled from the continuum of states $|E| \geq |\Delta_0|$ (solid black lines) and the 2π-ABS modes (dashed black lines). c) Based on [175]

This gap renders the 4π-effect as single channel, making it almost impossible to measure within the ensemble of available modes, especially in real systems, which might even show bulk conductivity owing to strong doping. Furthermore, relaxation in the thermal equilibrium, as it is the case for DC measurements, destroys the 4π-periodic Josephson effect. This is possible because the ground state of the 4π-mode switches between two values $E_\pm$ when the phase Φ is changed. For particle exchange with the continuum, like metallic leads, an effect called *quasiparticle poisoning* arises. This relaxation changes the fermion parity of the mode back to its initial state, by this rendering the mode 2π-periodic.

In principle, the flip of fermion parity due to poisoning can be avoided with AC measurements like Shapiro[1], where the 4π-mode should only contribute at double-integer steps with respect to the 2π-modes. However, angle averaging of the supercurrent usually leads to vanishingly small contributions even in the rf case.

1 The measurement time needs nevertheless to be fast than the quasiparticle lifetime.

Snelder et al. suggested ferromagnetic layers to reduce the gap arising at the interface for charge carriers with non-zero angle of incidence, which should promote small-gap 2π-modes to 4π-modes via Landau-Zener tunneling when a bias is applied. According to the theoretical studies of Veldhorst et al.[263], this change of the interface gap should then be detectable, even in a DC SQUID, by means of a (slight) change in the CPR. Another effect of the magnetic field is the decoupling of the 4π-modes from the continuum via a decrease of the maximum energy, $E_{\pm} < \Delta_0$, which helps to reduce relaxation via exchange.

In this context it is important to distinguish between *broken* 4π-modes, for example due to interface missmatch or finite size effects of the bulk, and inherently 2π-periodic modes, which can disguise as 4π-periodic due to Landau-Zener tunneling at larger bias. The latter can give misleading information regarding the presence of Majorana modes in the system, but do not fulfill the criteria.

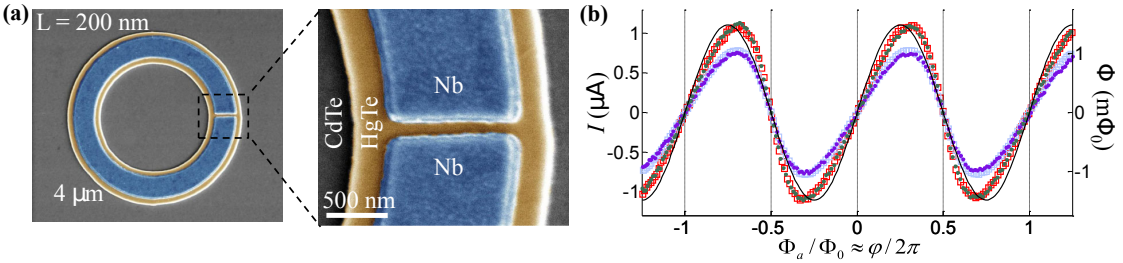

Figure 4.13: a) False-color SEM image of a representative device. A Nb loop is divided by a $L \approx 200\,\mathrm{nm}$ 3D HgTe junction whose flux state is measured by a pickup loop. b) The CPRs of four different measured devices show forward skewness with respect to the perfect sinusoidal CPR (black line).
Adapted from[264]

Experimentally, the first tries of measuring any influence of unconventional transport due to the presence of 4π-periodic surface states were nevertheless done in DC setups of induced superconductivity in either a single Josephson-like junction or in a SQUID. Kurter et al.[265] from the University of Illinois investigated the effect of non-sinusoidal contributions in (gated) Bi_2Se_3 devices and discussed the lifting of nodes in the Fraunhofer and SQUID patterns as possible evidence for the presence of such states. Sochnikov et al.[264] from Stanford measured strained 3D HgTe junctions with scanning SQUID microscopy techniques and found a skewness of the CPR which might arise due to transport via surface states. While being possibly related to unconventional bound states, these results remained quite ambiguous.

In 2015 Wiedenmann et al.[266] from the group of Molenkamp reported on irregular Shapiro patterns of rf-exposed strained 3D HgTe as first clearer evidence of a 4π-periodic effect, manifesting itself as disappearance of the first Shapiro step, as it is shown in fig. 4.14. In 2016 similar effects were found by the same group[267] for the 2D QSHI, where, due to the limited number of edge transport channels, the pattern extends beyond the first Shapiro step and show up to five vanishing odd-integer steps.

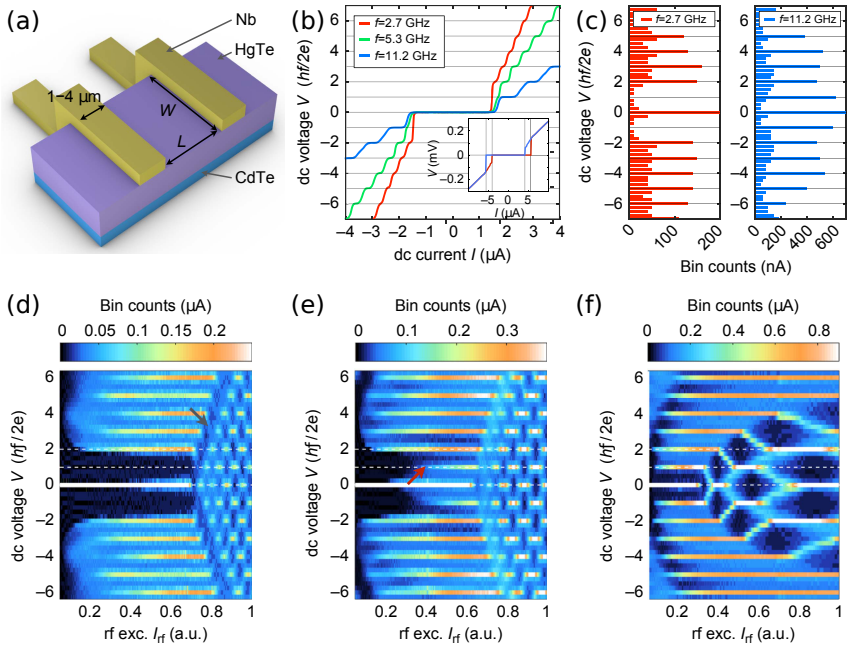

Figure 4.14: a) Schematic of the HgTe Josephson junction device. b) Shapiro steps in the $I-V$ curves for three different frequencies show a weakened or vanishing first step for lower frequencies. The inset represents the case of no rf-irradiation. c) Binning of the voltage data shows the Shapiro steps as peaks. While all steps are visible for 11.2 GHz, the first step vanishes for 2.7 GHz. d-f) The progressive disappearance of the first Step can be seen in the power dependence for lower frequencies.
Adapted from [266]

4.2.4 Superconductor-SnTe Interfaces

Due to the gapless Dirac surface states in SnTe TCI, Majorana zero modes can appear in SnTe TCI just as it is the case for the 3D TI. There is, however, one distinct difference, which is the number of Dirac cones per surface. In the common 3D TI there is one cone, resulting in a Z_2 classification of vortex-bound 0D states: there are either one or zero Majorana modes bound to the vortex core, while pairs of Majorana modes hybridize and gap out. Fang et al. [268] theoretically demonstrated that this is not the case for the TCI class, which allows for $n_{\mathcal{M}}$ non-hybridized Majorana modes with $n_{\mathcal{M}}$ being the mirror Chern number introduced in sec. 3.3.1.
For the (001) surface termination of SnTe, which has four cones, as it was shown in sec. 3.3.2, this classification gives rise to four Majorana modes at a single vortex core, of whom two are protected by symmetry, while the other two are gapped. This system requires the presence of a mirror-symmetric lattice, mirror-symmetric and TRS invariant Cooper pairing and an external magnetic field or Zeeman field parallel to the mirror plane and the result holds for chemical potentials inside the bulk gap as well as doping. There is a critical chemical potential, located at the conduction band minimum, at which a quantum phase transition extends the 0D Majorana end states of the vortex into the bulk of the vortex line, leading to hybridization.

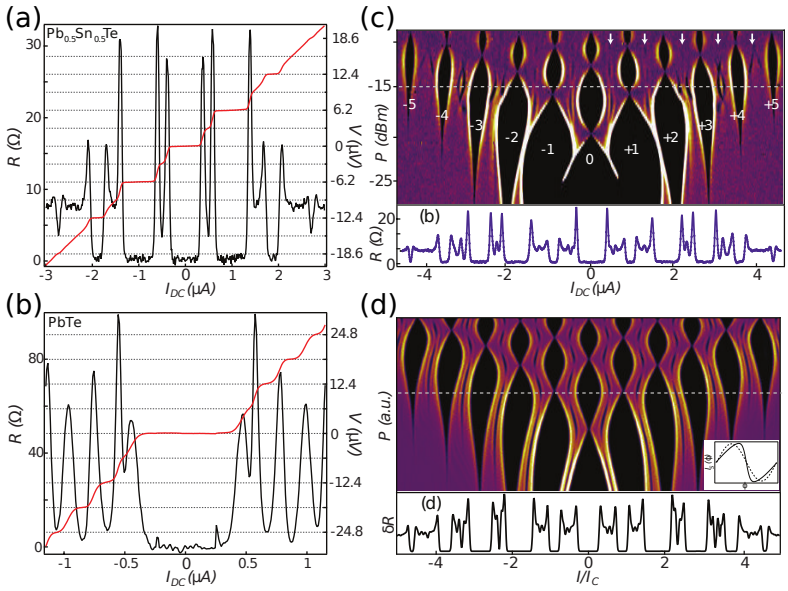

Figure 4.15: Shapiro measurements at 3 GHz with peaks in the resistance R and steps in the numerically integrated voltage V (red curves) indicate a) additional features at fractional values $V \neq 6.2\,\mu\text{V}$ for $Pb_{0.5}Sn_{0.5}Te$ and b) no additional features for PbTe. Comparison of c) the power-dependent Shapiro pattern at 2.2 GHz with d) numerical RSJ calculations for a skewed CPR (see inset) indicate the presence of higher harmonics in the critical current.
Adapted from [269]

There are very few experimental studies on the effect of induced superconductivity in SnTe TCI. In a recent pre-print from the end of 2017, Snyder et al. [269] reported on Josephson junctions made from MBE-grown $Pb_{0.5}Sn_{0.5}Te$ layers and their differences to topologically trivial PbTe layers. Superconductivity was induced with aluminum electrodes and found to be fully present at low temperatures. A study of the AC Josephson pattern revealed additional steps at fractional values for $Pb_{0.5}Sn_{0.5}Te$, features which were not observed for the trivial compound PbTe. Snyder et al. compared the pattern to numerical simulations of a RSJ model based on a CPR including higher harmonics. They concluded that this skewed CPR is necessary to explain their experimental findings and discussed disorder-induced helical states as a possible origin of their non-sinusoidal CPR.

4.2.5 The Effect of In-plane Magnetic Fields and Spin-Orbit Coupling

In sec. 3.2, strong spin-orbit coupling (SOC) was introduced as a crucial component to induce band inversion in topological insulators. For the class of time-reversal invariant topological matter (2D QSHI, 3D TI) with inversion symmetry of the bulk band structure, the underlying interactions are $\Delta_{\text{SOC}} \propto \mathbf{LS}$, which preserve these symmetries.
More recently, a more complete picture has developed, which generalizes the interplay between spin-orbit and magnetic fields in low-dimensional systems, to deduce the occurrence of phenomena, which are closely related to the ones predicted and measured in the symmetry-protected topological materials. Particularly the presence of spin-orbit fields

related to broken inversion symmetry has shown to be of great impact. Such fields are usually discussed in terms of Dresselhaus-type bulk (BIA) and Rashba-type structural inversion asymmetry (SIA), which also lock the charge carrier's spin to its momentum, similarly to the spin-momentum locking in the topological insulator material class [270]. In this context, the effect of induced p-wave coupling in such materials was suggested [271], as well as the formation of Majorana bound states when a 2DEG is coupled to s-wave superconductor electrodes and subject to Zeeman fields [272]. This should not come as a surprise, as already the aforementioned topological nanowire systems [176] rely on exactly this type of physics. Nevertheless, a widely ramified field, combining topology and spin-orbit effects, is created and the interplay (and possible engineering) of superconductivity and exotic spin textures, resulting in unconventional order parameters, is of great interest. However, contributions in real systems, where effects often blur with bulk activation and fabrication-induced disorder, are difficult to assign.

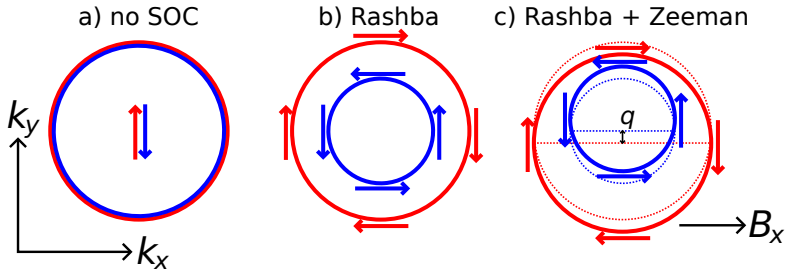

Figure 4.16: a) In absence of SOC, the Fermi contours of spin-up and spin-down are degenerate. b) Rashba SOC lifts the degeneracy. c) In-plane Zeeman fields shift the contours with respect to eachother to realize finite momentum $\mathbf{q}$ of pairs.

One phase, which has emerged in recent years within this field, is Cooper pairing with finite momentum of the center of gravity $\mathbf{q} \neq 0$. This concept was introduced as *FFLO phase* (from Fulde-Ferrell-Larkin-Ovchinnikov) [273] [274] in 1964, where a strong Zeeman field, originally incorporated as exchange coupling to magnetic impurities, can create a finite-$\mathbf{q}$ pair state between separated Fermi surfaces and a spatially modulated superconducting order parameter. Experimental evidence of such a state, with the most researched platform being heavy fermion superconductors, was for a long time elusive, but predictions [275] of realizations in low-dimensional electron systems, stabilized by Rashba SOC induced SIA (see fig. 4.16), or topological insulators have revived this quest, which is further boosted by the outlook of Majorana physics in such sytems.
Indeed, recent experiments on HgTe (2D QSHI) quantum wells in large in-plane fields by Hart et al. [276] provided good evidence for the manifestation of spatially modulated order parameters: Comparison between measurements and theory, the latter including the effects of structural (SIA) and bulk (BIA) inversion asymmetry as well as Zeeman couplings, indicate that the nodal suppression of the supercurrent in-plane, shown in fig. 4.17c, is result of finite $\mathbf{q}$.
A quite similar effect was observed in Bi_2Se_3 3D TI even more recently, where an intensity shift of the Josephson pattern towards outer branches is induced by in-plane fields across the junction. In a 2018 pre-print, Chen et al. [277] explained their findings with combined

contributions of Zeeman modulation, closely related to FFLO physics, and orbital flux modulation. The latter results in a phase modulation encircling the circumference of the 3D TI and can be seen as a manifestation of an Aharonov-Bohm effect.

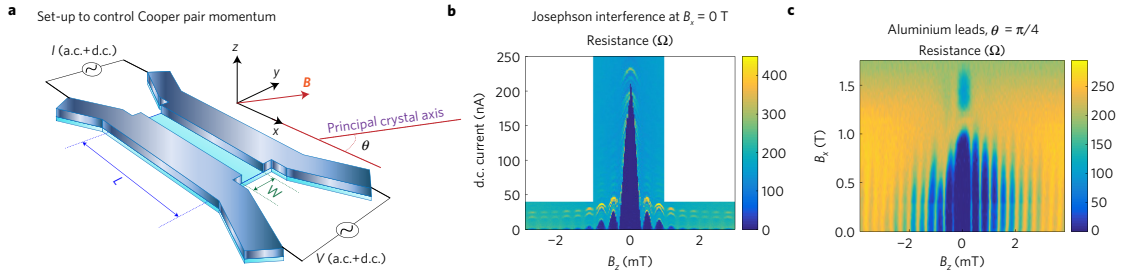

Figure 4.17: a) The HgTe quantum well device of $L = 4\mu m$ and $W = 800\,\mathrm{nm}$. b) The device is driven in the strongly n-doped regime and shows common Fraunhofer oscillations in B_z. c) At nodal fields of $B_x \approx 1.1\,\mathrm{T}$, superconductivity is suppressed due to finite Cooper pair momentum. Adapted from [276]

The Zeeman effect of in-plane fields $B_{\mathrm{ip}} = (B_x, B_y)$ on the Dirac spectrum is given as [203]

$$\mathcal{H} = -\hbar v_{\mathrm{F}} \left(k_x - \frac{g_y \mu_{\mathrm{B}} B_y}{\hbar v_{\mathrm{F}}} \right) \sigma_y + \hbar v_{\mathrm{F}} \left(k_y + \frac{g_x \mu_{\mathrm{B}} B_x}{\hbar v_{\mathrm{F}}} \right) \sigma_x, \tag{4.41}$$

which modulates the gap as $\Delta = \Delta_0 \exp(2iqx)$ with $q = \frac{g_y \mu_{\mathrm{B}} B_y}{\hbar v_{\mathrm{F}}}$ for $B_{\mathrm{ip}} = (0, B_y)$, attributed to the induced finite momentum. This shift of the Fermi contours is very similar to the idea presented for Rashba SOC in fig. 4.16, which is a consequence of spin-momentum locking in TIs.

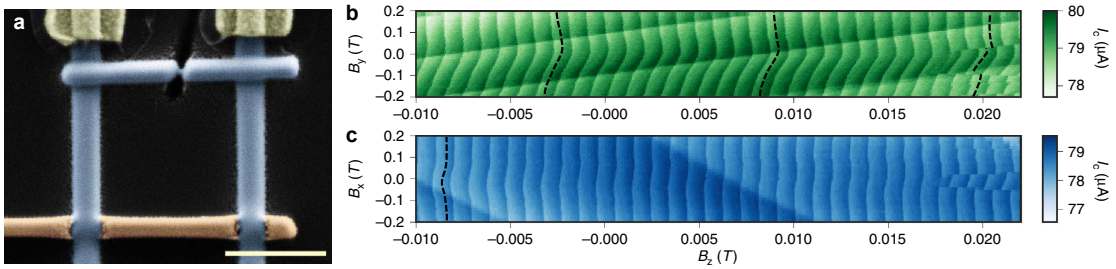

Figure 4.18: a) The asymmetric SQUID of superconducting tungsten wires (blue) and the Bi wire. b,c) In-plane fields B_x, B_y induce phase drifts φ_0 (dashed lines) and sudden $0 - \pi$-jumps. Adapted from [278]

In-plane field response was also probed in monocrystalline topological Bi nanowires in an asymmetric SQUID configuration. Aside from sawtooth CPR explained by ballistic transport in the few-channel device, $0 - \pi$-transitions and φ_0-shifts of the SQUID modulation was observed, visible as changing drifts of the phase in fig. 4.18b,c.
A common characteristic of the used materials is large SOC and g-factors, which facilitates the breaking of chiral symmetries that preserve conventional phase relations. Consequently, φ_0-SQUID behaviour was also found in InSb nanowires [247].

Part II

Sample Fabrication and Measurement Setup

5 Carbon Nanotube Devices

5.1 Contextual Introduction to Carbon Nanotube Sample Fabrication

The very first approaches of carbon nanotube synthesis were based on high-energy physical evaporation methods. In Iijima's original report [50], for instance, CNTs from *arc discharge evaporation* were used, where a high current is passed through two graphitic electrodes placed within a low-pressured argon vessel. The created plasma enables the formation of oriented carbon structures at the negatively charged electrode. These structures are mainly multi-wall CNTs, but carbon whiskers, fullerenes or amorphous carbon can also be observed.
A similar technique is the *laser ablation deposition*, where a graphitic target in a furnace is decomposed via laser pulses. The soot material is then transported onto a cooled copper target by a flow of inert gas [279].

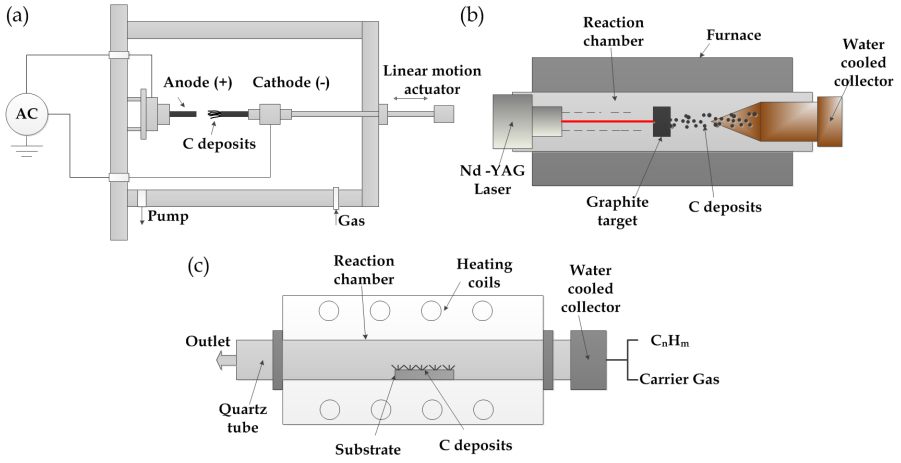

Figure 5.1: Three established fabrication methods for carbon nanotubes, a) arc discharge evaporation, b) laser ablation deposition and c) chemical vapour deposition.
Adapted from [280]

Both techniques have in common that the yield usually has to undergo post-growth treatments for selection and subsequent dispersion in solution, in order to transfer the nanotubes onto a device chip where further processing is realized. This post-growth processing can strongly deteriorate the theoretically very low inherent disorder in carbon nanotubes. Exposition to solutions, photoresists and electron beams but also contact to the substrate surface can lead to adsorbates or increased amounts of amorphous carbon, which expresses itself in large hysteresis effects, unipolar charge characteristics or the breakdown of the quasi-one-dimensional character into chains of quantum dots at low

temperatures [84] [85] [57]. SWCNTs can also be obtained via doping of the graphitic targets but individual and clean SWCNTs are generally hard to produce, which ultimately led to the focus on chemical approaches mainly for the use in more advanced nanoelectronic applications. As of today, the dominant fabrication process is *chemical vapour deposition* (CVD). This process allows for a high yield of single SWCNTs and is generally more easily integrated into the fabrication process, owing to the possibility of growing nanotubes directly on-chip.
However, the thermal requirements for the fabrication of nanoscale circuits remain rather high, leading to usually complicated process developments. The CVD growth itself and its embedding into the fabrication of complex nanoscale devices is described in the following parts.

5.1.1 The CVD Growth Process

The growth of carbon nanotubes by CVD is based on catalytic decomposition of carbon feedstock at high temperatures and in the absence of oxygene, a process called *pyrolysis*. The carbon precursor molecules, for example methane (CH_4), are split into radicals by the chemical reaction [281]:

$$\mathrm{CH_4} \rightarrow \mathrm{H_3}C^{\bullet} + H^{\bullet} \rightarrow \mathrm{H_2}C^{\bullet\bullet} + 2H^{\bullet} \rightarrow \mathrm{H}C^{\bullet\bullet\bullet} + 3H^{\bullet} \rightarrow C^{\bullet\bullet\bullet\bullet} + 4H^{\bullet}. \tag{5.1}$$

Because the other byproducts diffuse away in the gaseous phase, the end product of this process is pure carbon which can form various structures, like single-wall and multi-wall CNTs, carbon whiskers or amorphous carbon, with the latter ones usually being unwanted. The exact outcome delicately depends on several process parameters: The thermal energy provided via the temperature regulation promotes the breaking of the atomic bonds of the precursor and thus the number of radicals. But also the overall amount of process gases and the ratio of its components regulates the growth, since a surplus of hydrogen rebinds hydrocarbon radicals [282] :

$$\mathrm{H_3}C^{\bullet} + \mathrm{H_2} \rightarrow \mathrm{CH_4} + H^{\bullet}. \tag{5.2}$$

The catalytic effect lowers the thermal decomposition temperature, by this reducing the amount of produced amorphous carbon. Catalyst particles, usually transition metals like Fe, which strongly bind the created carbon radicals due to an unfilled d-shell, serve as the cell of growth. Therefore the catalyst particle size determines the nanotube diameters [283]. To improve the dispersion of catalytic particles, the catalyst is often provided in a matrix of supporting oxide like $\mathrm{Al_20_3}$ [284].
The exact growth mechanism of SWCNTs during the CVD process is not approved without a doubt but generally believed to be of the *vapour-liquid-solid* (VLS) type [283]. Its particular stages are illustrated in fig. 5.2. In contact with the hot metal catalyst gaseous hydrocarbon is catalytically decomposed into hydrogen and carbon radicals as

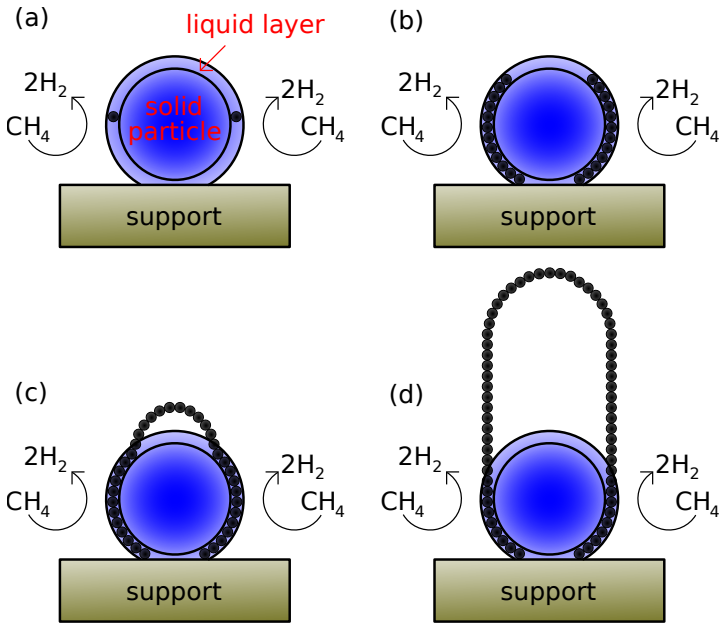

Figure 5.2: VLS mechanism for CNT growth with methane: a) Gaseous CH_4 is adsorbed and decomposed on the catalyst surface. b) Carbon diffuses into the liquid surface layer. c) Oversaturation leads to the formation of the CNT cap. d) Continued CNT growth.
Based on [284] [285]

a first step. The catalyst surface is assumed to be liquid despite of CVD temperatures well below the bulk melting point, owing to small particle size and the fact that the decomposition process is exothermic. The adsorbed carbon is dissolved and then diffuses into the liquid surface layer, while the excess hydrogen is carried away in the gaseous phase. As soon as a supersaturated state of carbon in the liquid surface layer is reached, the carbon precipitates and crystallizes in tubular sp^2-bonds, which is energetically favorable due to the absence of dangling bonds. This forms the cap of the CNT and the growth continues until either the gas flow is stopped or the catalyst loses its activity for decomposition.

5.1.2 CVD-based Fabrication Approaches

Initially, CVD-based fabrication techniques followed a similar concept as the ones using CNTs gained from other growth mechanisms like laser ablation. While the latter ones usually where deposited on the substrate from solution, this step could be replaced by depositing catalyst and subsequently growing the CNTs directly on-chip. However, the CNTs still had to be localized and selected via AFM imaging and subsequently contacted from the top via individually adapted designs. The possibility to fabricate CVD-grown suspended SWCNTs with low disorder following the standardized approach of Cao et al.[92] facilitated the discovery of rich CNT quantum properties which have been described in chapter 2.

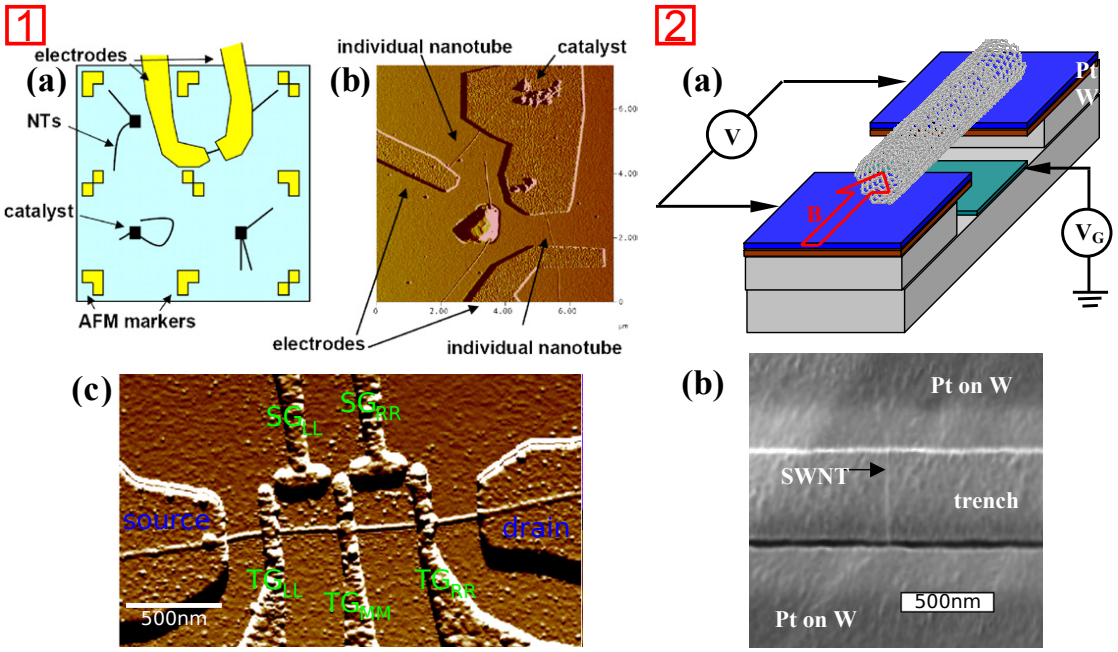

Figure 5.3: 1) Early CVD-based CNT devices: a) schematic of an individual design organized within an area defined by AFM alignment markers b) AFM image of an actual device c) double quantum dot device realized with palladium contacts and aluminum top and side gates 2) Suspended CNT devices: a) schematic of the sample layout b) a suspended CNT spanning over the gap between source and drain
1) Adapted from [104] 2) Adapted from [92]

On the other hand, a dilemma was brought to the fore by the need for smaller and more complex circuits for more advanced quantum physics: the fabrication of those circuits is scarcely compatible with growth of clean CNTs due to the thermally very demanding conditions of the CVD process, which does not only limit the device miniaturization but also the choice of materials. This led to a new school of thoughts, deviating from the predominant on-chip growth principle, and the fabrication of devices via a two-step process, where CNTs are grown on second chip and subsequently transferred onto the circuit chip. These types of processes are usually referred to as *stamping*. In order to explain the differences and limits of used fabrication approaches, the most prominent examples are briefly introduced in the following.

The Early Tries of Stamping

In a first report on the transfer of CNTs in 2005 Hines et al. [286] realized devices by adapted nanoimprint lithography and transfer printing techniques at the University of Maryland. Metal electrodes as well as CVD-grown nanotubes (and other organic semiconductor compounds) were transferred stepwise from silicon(oxide) transfer substrates onto flexible device substrates made of plastic. These devices showed ambipolar charge behaviour and small hysteresis effects, indicating a low CNT disorder. However, the approach was

limited to plastic substrates and relatively large scales of several μm at first. Additionally, there was no mechanism included to control either the number of transferred CNTs or their direction, since CNTs are grown without pre-patterning, thus making the alignment of the CNTs and electrodes relatively random. The printing technique requires a modest heating of 140 °C and high pressures of $200 - 400$ psi.

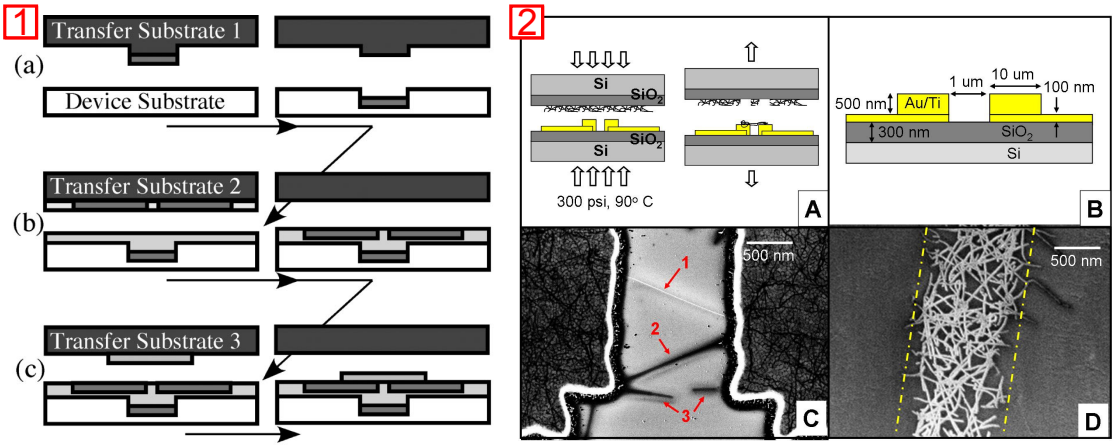

Figure 5.4: 1) Transfer printing technique for carbon nanotube transistors on flexible substrates of Hines et al.: a) the printing of an embedded gate electrode b) the printing of the gate dielectric and source and drain electrodes c) the printing of the carbon nanotubes 2) Stamping of CNTs onto silicon device chips of the same group: a) the two chips are pressed against eachother for three minutes to transfer CNTs b) the optimized layout for ideal CNT yield c) SEM image of a device after stamping, showing one suspended CNT (red arrow 1) d) SEM image of a transfer substrate after the stamping process
1) Adapted from [286] 2) Adapted from [287]

In 2008 the group realized a similar transfer technique for suspended devices on silicon substrates [287]. In this approach the CNTs from the transfer chip were stamped onto gold electrodes with a high yield of up to 20 % for single nanotube devices and a strong tendency for gaps to be bridged by multiple tubes. Direct stamping of the transfer chip onto the metallic electrodes required the latter ones to be sufficiently malleable, limiting this approach to relatively large scales and simple circuits.

Towards a Controlled Transfer

In 2010 Wu et al. [288] from the University of Michigan reported on an improved transfer technique under ambient conditions. In contrast to former approaches, they patterned pillars on a quartz transfer substrate by plasma etching in order to avoid direct contact with the device electrodes and permit controlled directionality of suspended CNTs. The alignment of the two chips was achieved with an optical contact alignment system. The gold electrodes were deposited on top of 1 µm high pillars of SiO_2/Si_3N_4 with an undercut created by selective etching to prevent electrical contact to the gate formed inside of the gap. Nanotube channel lengths were designed to be in the range of $1 - 3$ µm, smaller than the quartz pillar distance in order to cut the nanotubes at the contact points on

the substrate surface behind the electrodes. By doing so, suspended tubes spanned over the gap. Wu et al. stated a yield up to 20-40 % for single SWCNTs, yet the approach remains stochastic and spatial dimensions relatively large.

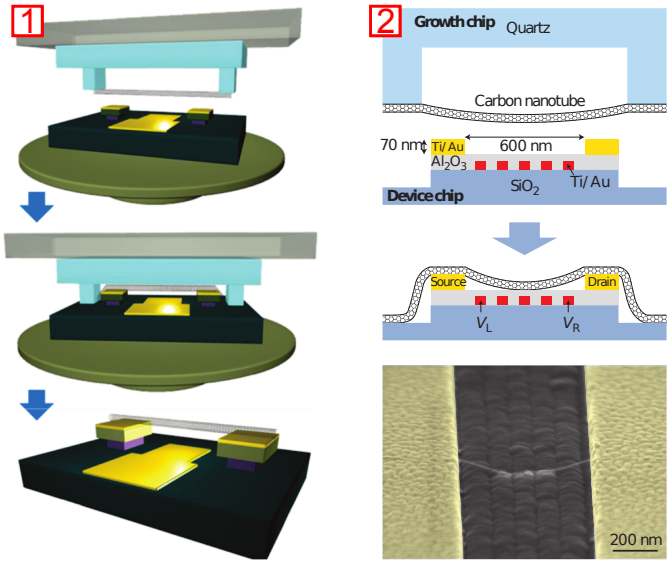

Figure 5.5: 1) Schematic of the transfer technique of Wu et al.: Carbon nanotubes grown suspendedly over quartz pillars are attached to a blank mask of a mask alignment system, with the device chip mounted on the movable stage. The alignment is done optically and pressing the two chips against eachother cuts off the nanotubes on the substrate surface such that they span over the electrodes fabricated on two mesas. 2) The refined method of Pei et al.: The fabrication of the device circuit on one mesa allows for a reduction of the spatial dimensions and the addition of local gates. The SEM image shows a CNT suspended over such a device.
a) Adapted from [288] [60]

Based on the work of the Michigan group, Pei et al. [60] developed a similar approach at the Delft University. While also using etched quartz pillars for the growth of nanotubes and an optical alignment system, they considerably reduced the spatial dimensions by placing all device structures on one etched 1 µm high mesa. This allowed for the insertion of five local gates inside of the 600 nm wide gap and additionally reduced the distance of the gates to the nanotubes.

Controlled Transfer of Single Nanotubes

Waissman et al. [96] from the Weizmann Insitute of Science (in Rehovot, Israel) found fault in the practical relevance of the former approaches, noting that the stochastic nature and inherent low yield of these techniques is not very suitable for more complex circuit designs. In 2013 they thus developed a deterministic transfer method based on a scanning probe setup. Nanotubes were grown parallely without slack over wide trenches on the transfer chip while the electrical circuits were fabricated on narrow cantilevers. The cantilever could then be mounted onto a scanning probe microscope and driven into the trenches where the distance of the two chips was controlled via a capacitance-based detection scheme and piezoelectric elements. Contact to carbon nanotubes could be

detected *in-situ* at 4 K via transport measurements and selected nanotubes cut via a high current through an additional pair of adjacent electrodes. This technique allowed for the selection of very clean nanotubes only and the use of relatively arbitrary circuits - with the implicit understanding that the fabrication of these circuits has to be feasable within the spatial restrictions of a cantilever.

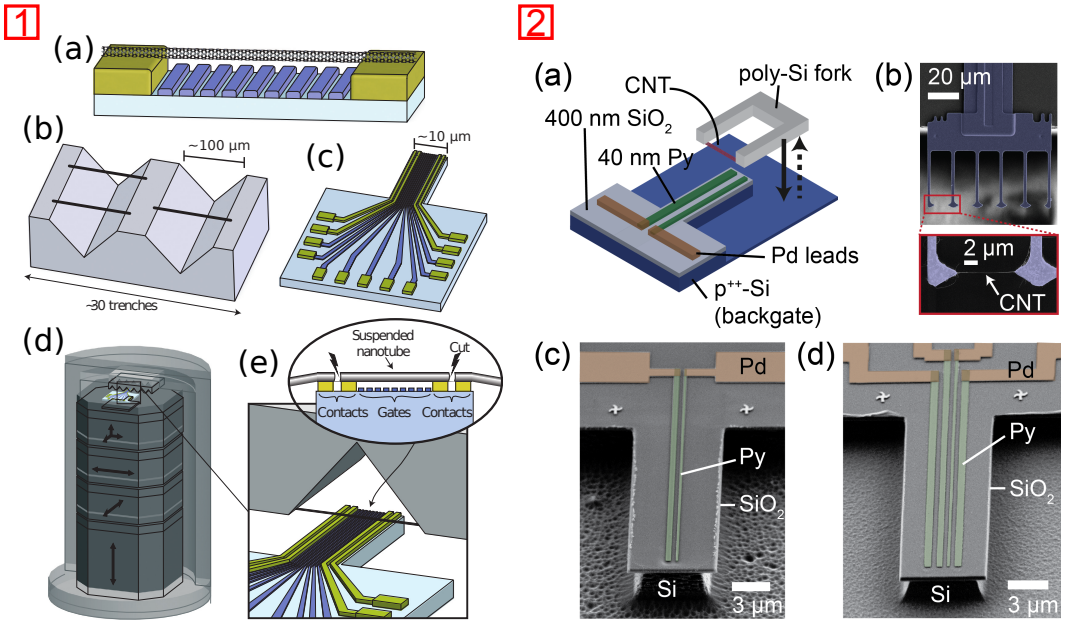

Figure 5.6: 1) The scanning probe technique developed at the Weizmann Institute: a) a resulting device of an ultra-clean carbon nanotube connected to source and drain and suspended over several local gates b) the transfer chip where nanotubes are grown over wide trenches c) the device chip shaped as a cantilever for the scanning probe microscope d) the scanning prope microscope setup where nanotubes can be detected *in-situ* at 4 K e) close up of (d): the cantilever is driven in to the trenches to pick up a CNT 2) The fork stamping method of the University of Basel: a) schematic of the sample layout and the transfer principle b) false color SEM image of a fork where CNTs grow between the individual arms c) SEM image of a two-terminal device with ferromagnetic Py leads where the CNT cutoff is done mechanically d) SEM image of a four-terminal device where the CNT cutoff is current-induced
1) Adapted from [96] 2) Adapted from [289]

Gramich et al. [289] from the University of Basel presented a comparable approach in 2015 which they called *fork stamping*. Nanotubes were grown over a movable polycrystalline silicon fork structure of 8 µm and optically aligned to the device chip fabricated on an etched mesa under ambient conditions. Transport measurements gave direct indication of successful connection to a nanotube, a process which could be repeated several times to find and select very clean nanotubes. Undesired tubes were removed with the help of a large bias voltage and the cutoff of the selected nanotubes was done either mechanically for two-electrode chips or via a current on adjacent electrode pairs in line with the technique of the Weizmann Institute.

The Conventional Outlier

In 2013 Jung et al.[290], the same group from the University of Basel, presented results of clean carbon nanotube devices following a conventional lithography process on one chip. They combined pre-patterning of local gates and suspended CNT elements with post-treatment to locate and contact the nanotubes. To do so two rhenium gates were plunged into 100 nm deep trenches created in the SiO_2 substrate layer. Then CNTs were grown and connected via conventional lithography processing for top contacts after the growth, with a total channel length of 700 nm and two suspended elements of 100 nm each therein. They found CNT qualities comparable to techniques where the nanotubes are placed as the last step of processing, suggesting that the disorder potentials of adsorbates and resist residues might be too small compared to the quantum dot energy to become noticeable.

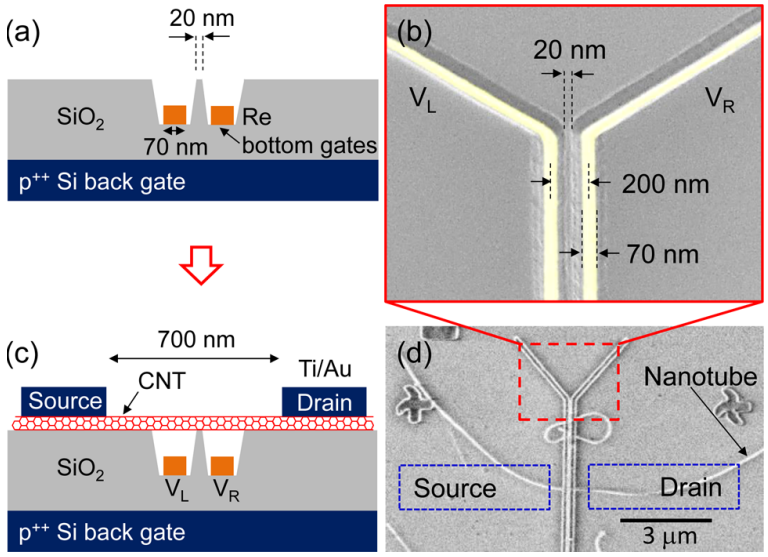

Figure 5.7: The process of Jung et al.: a) schematic of the two recessed Re bottom gates b) tilted SEM image of the gate structures c) schematic of the complete device with a CNT and subsequently deposited source/drain contacts d) SEM image taken after the CNT growth
a) Adapted from [290]

Summary of CNT Fabrication Approaches

To conclude this section a comparison of the main characteristics of the two predominant approaches, the on-chip growth and the two-chip stamping, is provided in table 5.1. Those approaches are further classified with respect to the presence or absence of post-growth treatment for the former and with respect to stochastic or controlled nature of the CNT transfer for the latter.

conventional techniques (on-chip growth)		stamping (two-chip techniques)	
growth as final step	post-growth treatment	stochastic	controlled
clean CNTs possible?			
yes	normally no (but hybrid approaches like Jung et al.)	yes	yes
yield of CNTs?			
moderate	high	moderate (practically hard to achieve)	low (single devices)
complex circuits possible?			
limited in types and spatial dimensions (thermal exposure)	yes (only top and side gates)	yes (limitations due to alignment)	yes (restrictions due to cantilevers)
material choice?			
very limited	normally free	free	free

Table 5.1: Characteristic advantages and disadvantages of different fabrication approaches.

5.2 Fabrication of Carbon Nanotube Devices with Multiple Local Gates

This section is dedicated to our own fabrication technique. First the requirements for our samples and hence the reasoning for the chosen approach are discussed, then the individual steps are explained in detail.

5.2.1 The Requirements and Approach for our Samples

Conventional processes with post-growth treatment are dismissed directly, not only due to their limited CNT cleanliness but also owing to a very particular requirement of our samples: it must be feasible to deposit the molecular magnets directly onto the CNTs. This is not the case for devices where the CNT is capped by an insulating oxide layer for the use of top gate electrodes. While the gates could be realized alongside the CNT, this concept is limited in alignment precision and therefore distance to the nanotube and gate efficiency.
Further implications come from the molecule deposition step since there is no reliable controlled technique to this day. It is rather a highly stochastic process that requires a reasonable yield of CNT junctions. Taking this into account controlled transfer techniques for single devices are not well suited for our needs, beyond the reasoning of technical feasibility at our facilities. While one could think of the hybrid approach of Jung et al.[290] as a reasonable way to combine relatively clean CNTs and complex circuit

structures, it carries one disadvantage not yet mentioned. Nanotubes have to be selected by imaging techniques before the contacts are fabricated and the layout has to be modified individually, making this process very time consuming, especially if one keeps the low yield of subsequent SMM deposition in mind. It is thus preferable to automatize the fabrication process by using just one layout and select the devices at the very end by conductance measurements.
These considerations hence leave to options, conventional CVD-growth as the last step or stochastic stamping approaches, and the decision boils down to one single question: Is it easier to achieve a complex sample layout under the thermal restrictions given by the CVD process or a reasonably high yield of nanotubes via stamping? In this context it should be pointed out that the goal is obviously to minimize gate size and distances to enable a maximum of control of the molecules which have the spatial dimension of 1 nm. Both approaches have been investigated to that effect within the last years in our group. The development of the stamping technique goes back to the work of former postdoc Oksana Gaier in 2013/2014 just before the start of this PhD project, following the idea of Pei et al.[60]. However, the on-chip CVD growth approach, started in parallel in 2015, showed more promise early on. As a result, the stamping technique was put aside for the time being and the focus is set here on the on-chip growth process. An overview of the particular steps is given in fig. 5.8, with the details being discussed in the following.

5.2.2 The Metal Circuit

As mentioned previously, the difficulty in combining on-chip growth of CNTs with complex metallic circuits stems from the thermal conditions during the CVD process. At typical growth temperatures of $\approx 800\,^{\circ}\mathrm{C}$ many metals regularly used for nanofabrication, such as Au, Al or Ti, are unsuitable due to melting or chemical reactions. Metals which can typically withstand such conditions are Pt, W, Mo, Cr, Re and Pd. However, factors as ability to contact CNTs, adhesion to substrates or mere availability further restrict our choices. Additionally, the required spatial dimensions are close to the practical limit such that a certain randomness is introduced by the used equipment. The leading thought is therefore to keep the fabrication process as simple as possible and as clean as possible to ensure a high enough reproducibility.
However, it should be noted that extended downtimes of all relevant machines at the Néel facilities, summing up to about one year, exacerbated this problematic and made it very difficult to improve the parameters of fabrication or even just replicate former results. As backup during downtimes, a lot of tries were done at the PTA cleanroom of the CEA Grenoble, which admittedly changed the fabrication conditions for various reasons like different machines and even materials. While some of the steps were less prone to failure under changing conditions, the fabrication of the small local gate lines turned out to be particularly difficult to reproduce without more rigorous changes of the recipe.

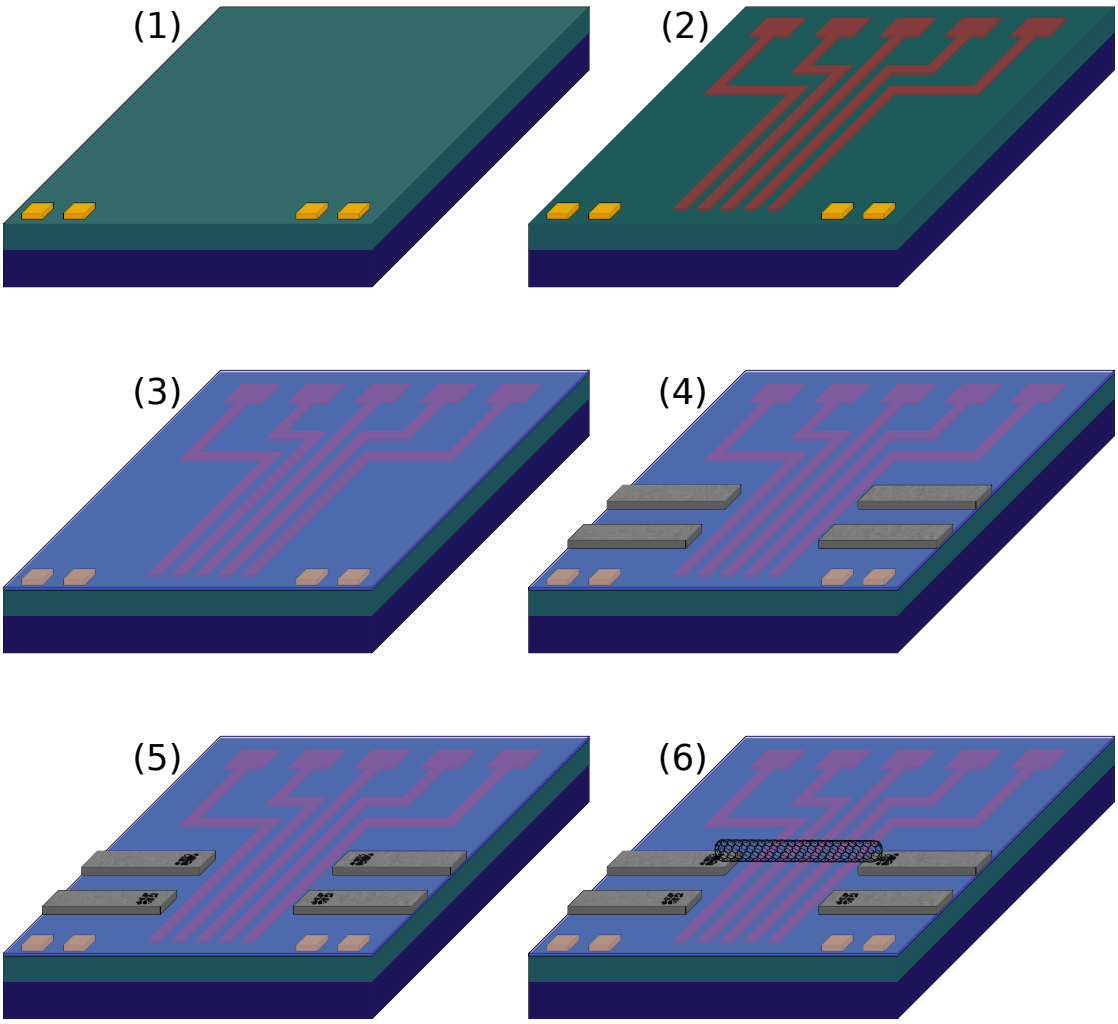

Figure 5.8: Schematic overview of our fabrication approach: 1) Gold markers are fabricated by laser lithography. 2) Local gates are written by electron beam lithography and deposition of molybdenum. 3) Al_2O_3 is deposited globally by atomic layer deposition (ALD). 4) Molybdenum-platinum source/drain electrodes are aligned alongside the gates. 5) Small islands are defined on top of source/drain by laser lithography for the CVD catalyst. 6) CVD growth of CNTs bridges connects electrodes stochastically.

The Effect of Substrate and Layout on Leakage Currents

First criterion for our approach is the possibility of having back gate control via the substrate. While not absolutely crucial, a global back gate does not only provide an additional control parameter for transport measurements at low temperatures, but also strongly facilitates the selection of suitable nanotube junctions at room temperature. This is because the gate-dependent conductance $G(V_{\mathrm{bg}})$ serves as signature of the nanotube4s quality, a principle which is explained in more detail in sec. 5.2.4.

Typically used substrates for this kind of application are doped silicon chips coated by a silicon oxide layer as gate dielectric. Doping is necessary in order to increase the inherently low charge carrier density of pure Si and can be of p-type or n-type. For relatively thin oxide layers of a few 100 nm, dry thermal oxidation is preferred over wet oxidation due to its superior quality. The lower growth rate of a dry process produces less dangling bonds which can act as charge traps that create leakage currents along the surface. While oxide thicknesses available for dry processing are usually limited, the cutoff does not coincide with our requirements.

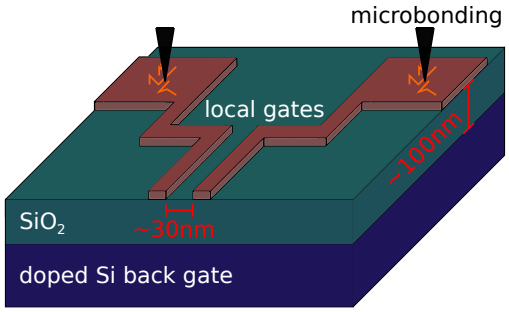

Figure 5.9: Leakage between the local gates is determined by the distance of the nanoscale lines but also by shortcuts to the back gate, which can appear due to microbonding.

Prevention of leakage currents is the most crucial part of the fabrication with the small gate lines being the most delicate parts. Two bottlenecks for such structures are highlighted in fig. 5.9. Obvious is the nanoscale middle part with minimal distance, where leakage via the SiO_2 surface or the ALD layer can occur, dependent on the gate line distance and the efficiency of the insulating material at low temperatures.
But the local gate bonding pads are critical as well, since mechanical impact of microbonding can reduce the effective gate oxide or even break through to the global back gate when the protecting oxide layer underneath is too thin. This is more pronounced for thin layers of relatively hard metals and therefore inevitably an implication of our approach. On the other hand, too thick oxide layer could impede the electron beam lithography process of the small gate structures due to charging effects and hence limit spatial dimensions. The substrate has thus to be chosen with due diligence.
This point was not entirely evident at the beginning of the process development, where a relatively simple test indicated the feasibility of the approach, although the interpretation of the underlying mechanism was in fact incorrect. The mentioned test consisted of measuring the leakage current between just two such lines, similar to the technique presented in fig. 5.10. Those variously spaced lines were fabricated on a 100 nm SiO_2 substrate from either 10 nm molybdenum or palladium due to their availability in the electron beam evaporator of the Néel cleanroom. Subsequently the lines (including the bonding pads) were covered by an ALD-deposited Al_2O_3 insulator layer of 10 nm or 20 nm and exposed to the actual CVD growth conditions.
The test revealed high room temperature leakage for Mo and a even higher one for Pd with insulator thickness up to 10 nm. At cryogenic temperatures these currents severly

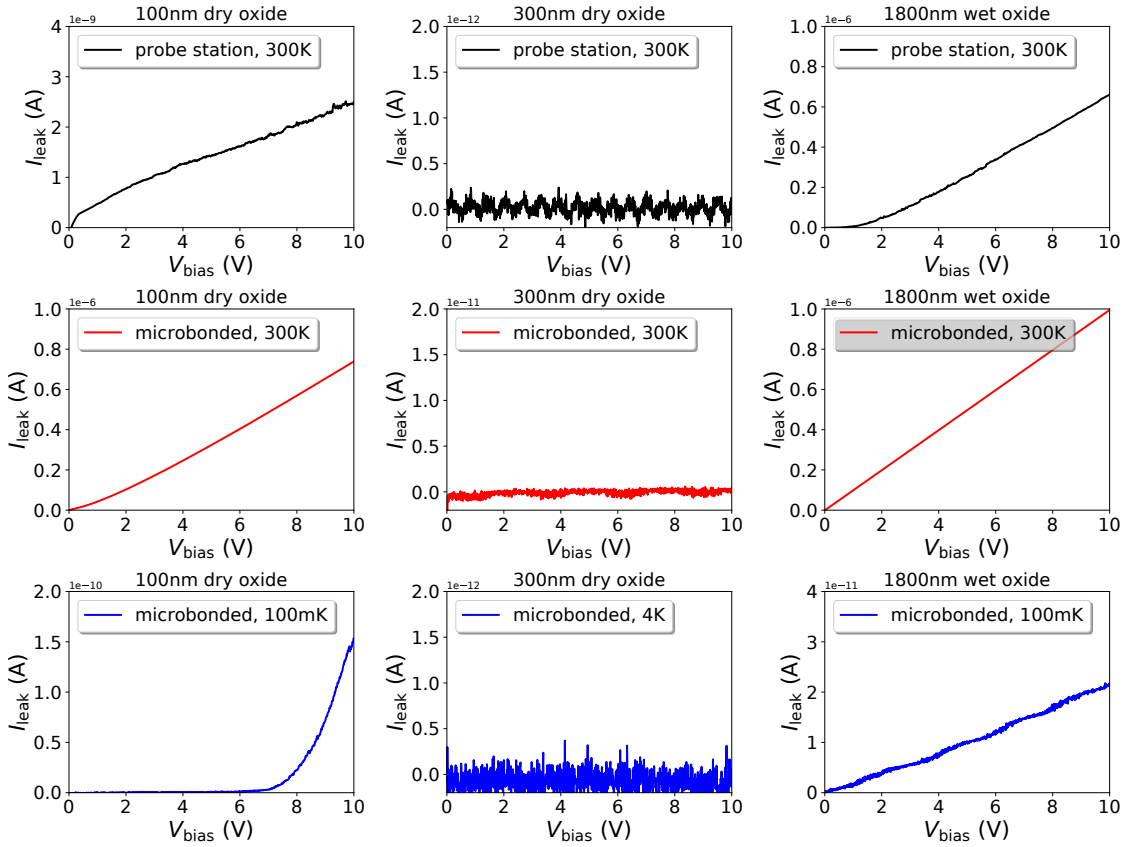

Figure 5.10: Leakage currents for three different substrates, each shown in a different column, measured via a $10\,\mathrm{M\Omega}$ preresistor corresponding to $I = 1\,\mu\mathrm{A}$ at $V = 10\,\mathrm{V}$. Additional resistance contributions stem from the substrate/oxide layer. The $100\,\mathrm{nm}$ substrate (left) has decreased resistance when microbonded, at low temperatures the breakthrough is at $7\,\mathrm{V}$. The $1.8\,\mu\mathrm{m}$ substrate (right) has surface transport processes greatly reducing the resistance at room temperature, at low temperature there is a low but constant increase in $I(V)$. The $300\,\mathrm{nm}$ substrate (middle) has no leakage higher than our detection precision.

decreased and no leakage was detected up to breakthrough voltages in the range of $7 - 9\,\mathrm{V}$. For $20\,\mathrm{nm}$ of oxide a drastic improvement was observed. However, it turned out afterwards that the measured leakage was the one created by the substrate itself and the linespacing was in fact still too big to dominate the characteristics for this particularly chosen substrate. Likewise, the improvement of the thicker insulator layer can be ascribed to the fact that this layer is not necessarily completely broken by microbonding and thus adds a resistance which does not correctly reflect the value at the small gate lines itself. After cleaning up the initial misinterpretations of this test and its reasoning one can at least conclude the following points: The substrate itself should not become the limiting factor, but optimized as well. This has been evaluated in the last subsection. Furthermore, an insulator thickness of much more than $10\,\mathrm{nm}$ is not necessarily useful due to limitations of the microbonding.

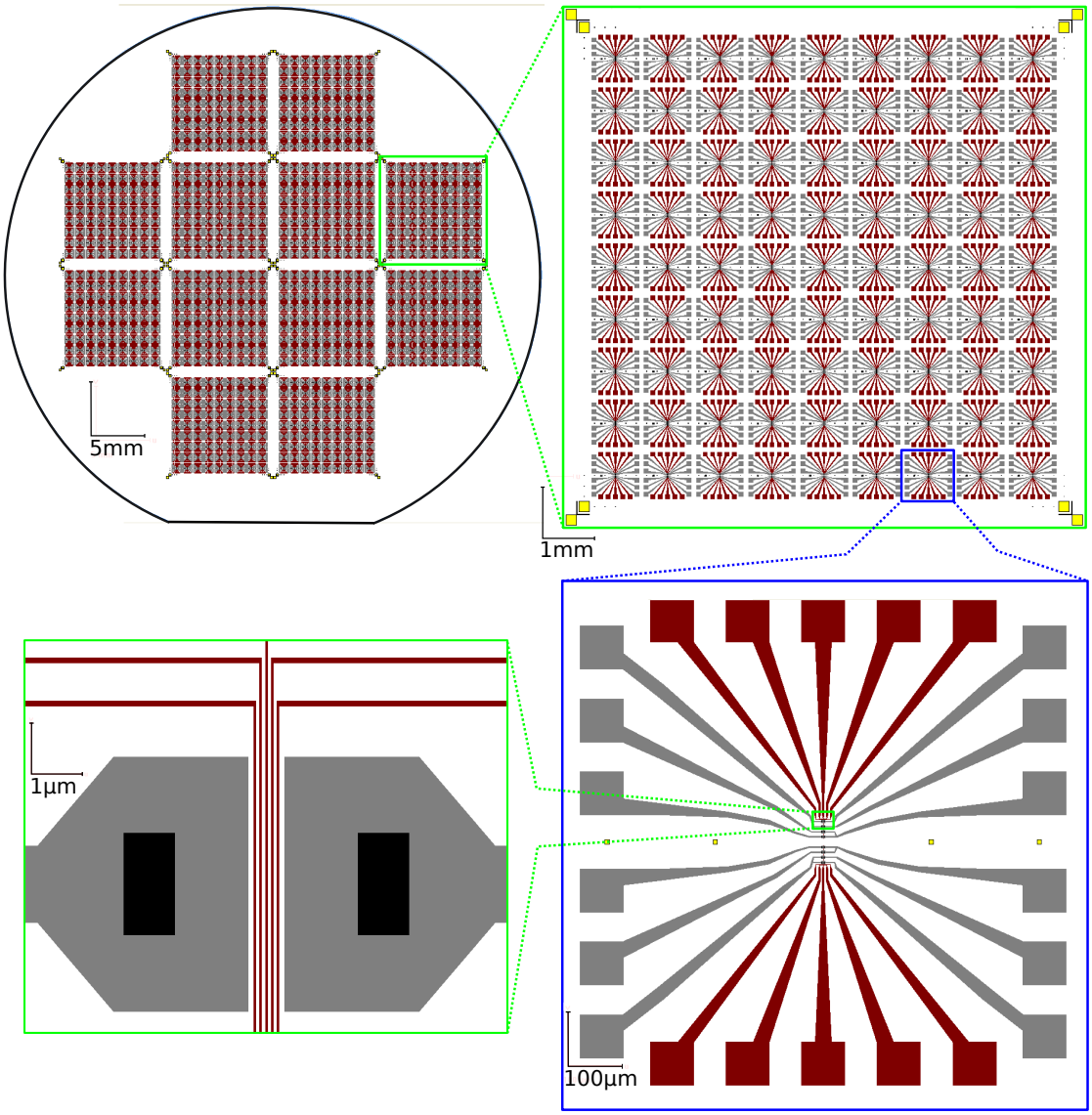

Figure 5.11: Layout of the samples: Markers are written on a complete two-inch substrate, then it is cut into $1\,\mathrm{cm}^2$ chips for further proceeding. These chips contain 81 groups of 8 possible junctions (grey structures), aligned around 5 local gate lines (redbrown structures).

Three different substrates have been tested to this effect, two with 100 nm and 300 nm layers of dry SiO_2 and one with 1.8 µm of wet SiO_2. By using probe station tips and microbonding onto the 'bare' SiO_2, the leakage current between two points on the surface for voltages up to 10 V was detected, measured via a 10 MΩ preresistor to protect the detection input from a potential breakthrough of the oxide layer. It can be seen from fig. 5.10 that microbonding on a 100 nm SiO_2 layer reduces the effective oxide thickness and thus creates leakage which is naturally smaller at low temperatures. In contrast,

this effect is not seen for the 300 nm oxide where leakage currents are well below the precision of the detection scheme already at room temperature. The substrates of 1.8 µm wet oxide show a distinct surface leakage which is much more strongly pronounced at room temperature. The larger oxide thickness does not overcome this disadvantage even at low temperatures, making the 300 nm substrates the most suitable candidate.
However, final optimized devices still regularly showed leakage between the local gates and the back gate after microbonding, which is not explicable by anything else than locally substandard oxide quality of the used lot of substrates. These *type-1* substrates were thus finally replaced by *type-2* (see table 5.2), also facilitating the coordination of the project with the KIT (Karlsruhe Institute of Technology, Germany), where it is continued in Wolfgang Wernsdorfers new group.

substrates		
type	1	2
material	Siltronix Si polished, CZ process N-phosphor doping	Siegert Si polished, CZ process P-boron doping
coating	frontside SiO_2 300 nm ± 30 nm backside Cr/Au 100 nm	frontside SiO_2 290 nm no backside coating
parameters	thickness 250 − 300 µm resistance 0.001 − 0.005 Ωcm	thickness 525 µm ± 20 µm resistance 0.001 − 0.01 Ωcm

Table 5.2: The used substrates.

markers		
step	type	characteristics
1	cleaning	3 min heating of substrate to 200 °C
2	spincoating	LOR3A, 6000 rpm, 4000 rpm/s, 30 s, 240 nm 2 min bake at 200 °C S1805, 6000 rpm, 4000 rpm/s, 30 s, 400 nm 1 min bake at 115 °C
3	lithography	LASER in Heidelberg DWL 66fs (diode, 405 − 410 nm)
4	development	1min in MF26A 1min in distilled water, N2 drying 6 s O_2 plasma
5	deposition	6 nm Ti in PLASSYS EBE 52 nm Au in PLASSYS EBE
6	lift-off	2 h in PG remover at 80 °C 10 s ultrasonic in acetone rinsing in isopropane, N_2 drying
7	cutting	Scriber, 1 cm^2 samples, 648 junctions

Table 5.3: The particular steps of the marker fabrication.

As a first step markers are fabricated on a complete two-inch wafer of this substrate. This is done by laser lithography (Heidelberg Instruments DWL 66fs) and subsequent deposition of Ti/Au. The markers are required for the electron beam lithography steps and consist of sets of four $8x8\,\mu m^2$ squares where each set defines a group of eight possible junctions and a corresponding area of approximately $1\,mm^2$. On a field of $1\,cm^2$, highlighted by big crosses in each corner, there are 81 of these sets grouped together and the substrate is cut accordingly to facilitate the subsequent steps.

Local Backgates and Gate Insulator

Incorporating the aforementioned factors puts the focus on the small gate line parts. It is obvious that statistical variations on the nanoscale can drastically change the outcome. These variations can be caused by technical parameters such as electron beam focus and alignment or metal deposition and insulator quality and hence diffusion effects. An optimization towards smallest possible structures at highest possible yields is certainly feasable, but it should be pointed out that this process remains delicate and prone to unanticipated aberrations. The output thus has to be high enough and every sample has to be checked individually. This is, to a certain extent, by design since the process envisions minimal yet realistic spatial dimensions to cope with the tiny molecules.
From the available materials, a choice of molybdenum[1] over palladium seems reasonable due to the higher melting point of Mo at 2623 °C, compared to 1555 °C for Pd. Despite of a melting point well above the CVD growth temperature, diffusion effects play a crucial role. The metal thickness should hence be minimized in order to reduce the amount of material that is even available for diffusion. We found that 10 nm thick Mo still constitutes an efficient metallic layer for electrostatic gating.
Under these conditions and in the best cases we can fabricate local gate lines of approximately 50 nm width at our facilities, owing to the use of a NanoBeam NB5 80 kV electron beam lithography system. These lines can reliably support voltages $\geq 5\,V$ without leakage which is easily enough, considering that already $\pm 1\,V$ usually drives the spatially close nanotubes from p- to n-states with multiple charges (see sec. 8). However, the margin of error for this step is small. Gate lines with distances $\lessapprox 30\,nm$ regularly showed huge leakage currents after CVD growth, making them entirely unworkable.
The first samples were designed with three of these lines, later the process was improved to five lines (see fig. 5.12 for a *scanning electron microscopy* image (SEM) of such a structure). The thin 10 nm electrodes are sufficient for efficient gating and furthermore the lift-off is facilitated. Ultimately this also lowers the barrier over which nanotubes have to grow to form suspended devices. A short oxygen plasma cleaning before the deposition clearly enhances the yield of uninterrupted lines, but was unfortunately not always available.

1 Straightforward replacement of the Mo by Cr deposited at the PTA cleanroom did not reproduce the same results, but imperfect lift-off of the small gate lines occurred repeatedly. Replacement of the Mo with Re from a different UHV evaporator at the Néel Institute also failed due to a too high deposition temperature charring the resist.

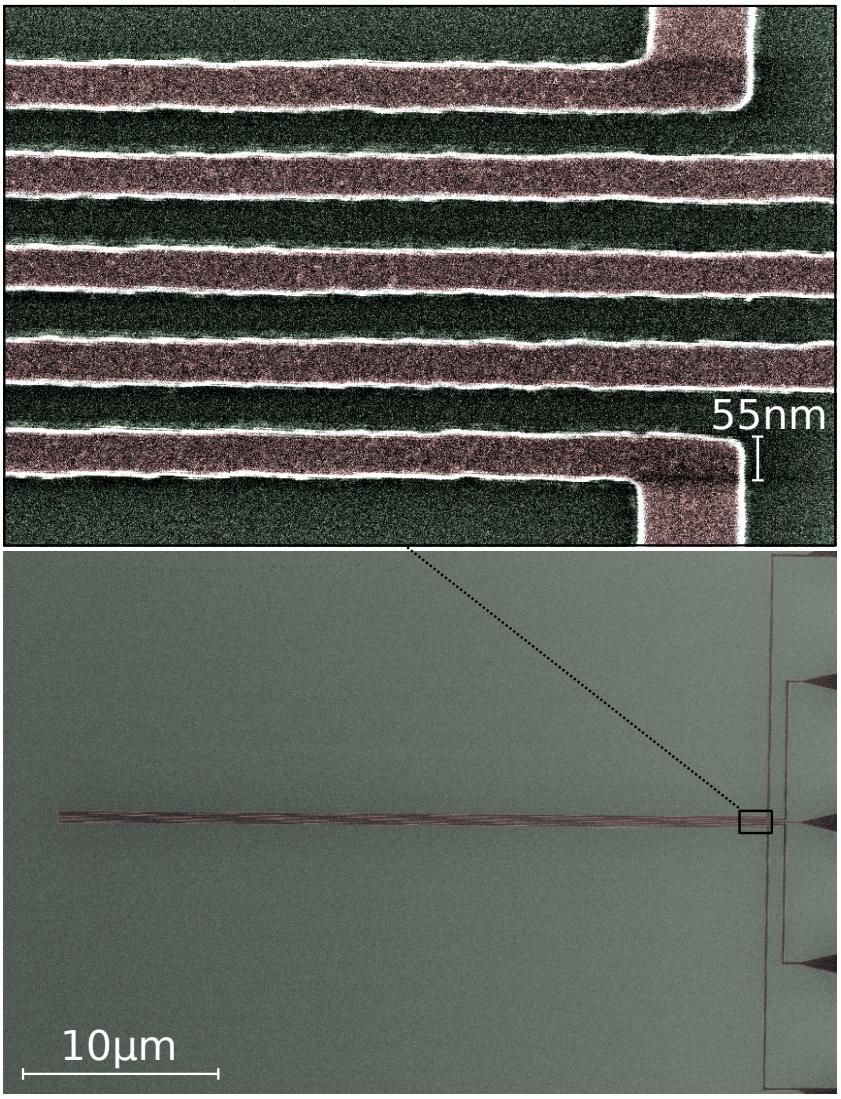

Figure 5.12: False color scanning electron microscope image of the five local gate lines, showing a sample of 55 nm line width.

12 nm of Al_2O_3 is deposited as gate insulator by atomic layer deposition, whose mechanism is depicted in fig. 5.13. This layer is required in order to avoid shortcuts between nanotubes and local gates in case of not fully suspended devices, but also between source/drain electrodes and local gates in the case of non-ideal alignment. Temporary tries with the theoretically superior HfO_2 were stopped due to inexplicable and randomly occurring melting of the source/drain electrodes deposited on top, an effect that could clearly be assigned to the oxide layer underneath. In our approach the oxide is deposited on the entire surface in order to achieve a better and homogeneous layer, without putting stress on the delicate local gate parts during a possible ALD-layer liftoff.

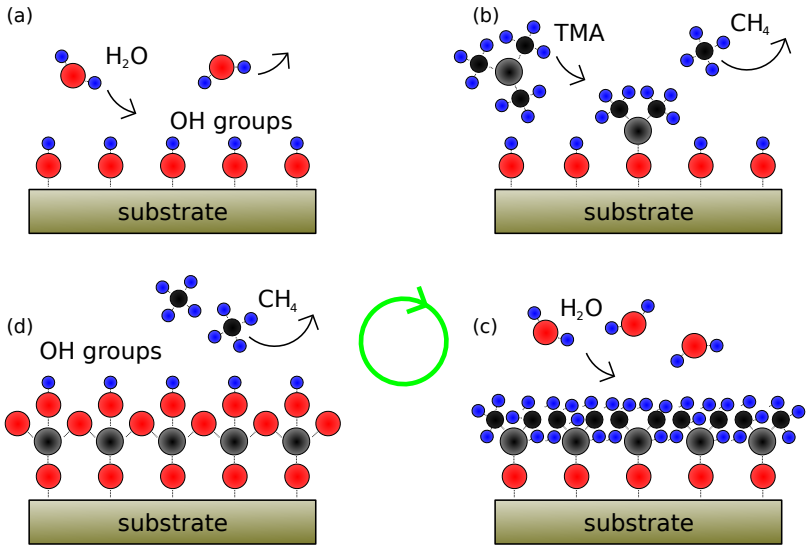

Figure 5.13: Principle of the atomic layer deposition (ALD) of Al_2O_3, for which two precursors, water vapour and trimethylaluminium (TMA), are injected alternatingly. The process is self-limited and redundant precursor as well as gaseous reaction products are removed after every reaction step. a) Water vapor covers the surface and builds hydroxyl groups (OH). b) TMA binds to these groups and frees up CH_4. c) Water vapor reacts with the surface-bound TMA complexes. d) A single layer of Al_2O_3 grows with CH_4 as reaction product. The surface is again terminated with OH groups which can bind TMA.

There is, however, one clear drawback of this technique, which is the undependable microbonding of the local gates that has to break through the Al_2O_3. While leakage to the backgate can be attributed to insufficient SiO_2 quality, the probability of bonding to 10 nm thick Mo gates is still too low to reliably achieve devices with maximum number of working gates. To counter this issue, three different slight modifications of the described fabrication technique have been studied, disregarding a lithography step for the ALD layer, a measure which could bedevil the established process. Ordered by increasing complexity or effort of these changes are:

- **Increased gate deposition thickness of 15 nm**: No considerable increase of effort or complexity of the device is required. The modification slightly changes the conditions for suspened devices, probably to a negligible degree as well. Noticable yet limited improvemet of the contacting was observed and other methods were thus tried out.
- **Redepositing of gate pads during source/drain step**: This does not change the gate thickness or number of lithography steps, but only an increase of writing time. However, reinforced gate pads peeled off the surface after the CVD process when trying to microbond onto them. High numbers of material interfaces, here $Mo/Al_2O_3/Mo/Pt$, should hence be avoided.

- **Additional lithography to reinforce gate pads**: One more lithography is done to (re)write the gate pads after the fabrication of the small lines, allowing for cleaner Mo/Mo interfaces. Due to the lower requirements this step is done optically. Connectivity of gates was noticeably increased and the recipe adjusted accordingly.

local gate lines		
step	type	characteristics
1	cleaning	10 s O_2 plasma at 20 W 3 min prebake at 180 °C
2	spincoating	PMMA 2%, 4000 rpm, 4000 rpm/s, 30 s, 70 nm 5 min bake at 180 °C
3	lithography	ebeam in NB5 at 80 kV and 1 nA/1 nA
4	development	1 min in MIBK/isopropane (1:3) 5 s + 1 min in isopropane, N_2 drying approx. 6 s O_2 plasma at 10 W
5	deposition	10 nm Mo in PLASSYS EBE
6	lift-off	2 h in NMP at 80 °C 10 s ultrasonic in acetone rinsing in isopropane, N2 drying
gate bonding pads		
step	type	characteristics
1	cleaning	10 s O_2 plasma 3 min prebake at 180 °C
2	spincoating	LOR3A, 6000 rpm, 4000 rpm/s, 30 s, 240 nm 2 min bake at 200 °C S1805, 6000 rpm, 4000 rpm/s, 30 s, 400 nm 1 min bake at 115 °C
3	lithography	LASER in Heidelberg DWL 66fs (diode, 405 – 410 nm)
4	development	1min in MF26A 1min in distilled water, N2 drying 20 s O_2 plasma at 10 W
5	deposition	40 nm Mo in PLASSYS EBE
6	lift-off	2 h in PG remover at 80 °C 10 s ultrasonic in acetone rinsing in isopropane, N_2 drying
gate oxide		
step	type	characteristics
1	cleaning	10 s O_2 plasma at 20 W
2	deposition	12 nm Al_2O_3 in Cambridge ALD 120 cycles of 20 s at 250 °C

Table 5.4: The particular steps of the local gate and gate oxide fabrication.

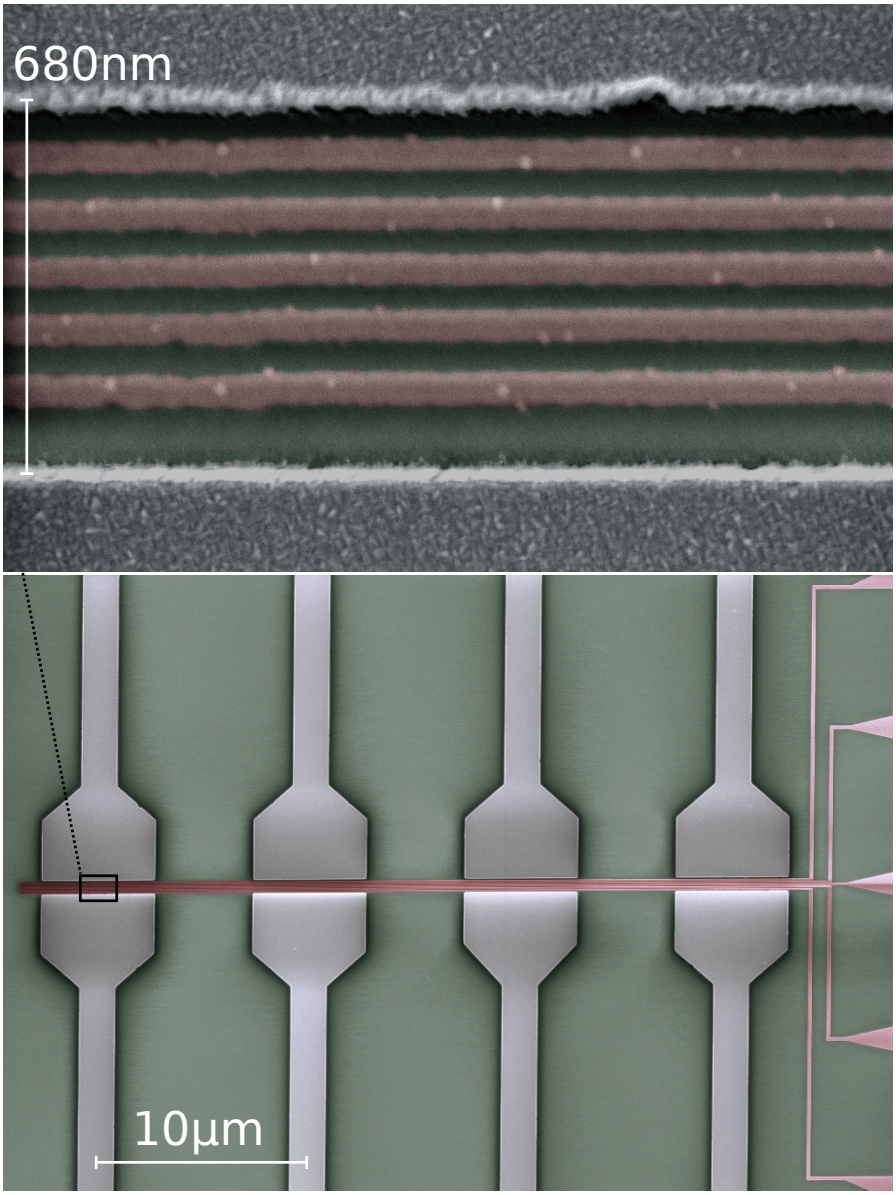

Figure 5.14: False color scanning electron microscope image of the source/drain electrodes aligned along the local gate lines, showing a sample of 680 nm gap width.

Source and Drain Electrodes

The source/drain electrodes are subsequently aligned pairwise along the small local gate lines with a gap of about 650 nm. In contrast to the fabrication of the tiny local gates, this step is less prone to failure because of electron beam focus quality. Nevertheless a good alignment and material quality is still absolutely crucial and the process has to be realised in the cleanest possible manner in order to reduce the risk of burning the samples

in the CVD. As it has been mentioned in sec. 2.2.1, carbon nanotubes grown by CVD make good contact to platinum, which is hence the preferable material. However, the adhesion of Pt to silicon substrates or substrates functionalized with SiO_2 or Al_2O_3 layers is very poor, a problem that gets amplified for small structures but can be tackled by an additional metallic adhesion layer. Commonly used Ti does not meet the requirements, since also the adhesion layer has to endure the CVD growth conditions. Both Mo and Cr have been used to this effect, giving similar results up to a deposition thickness of 10 nm of adhesion layer with 70 nm of Pt. Above, the lift-off with Mo becomes risky for the used resist system due to limited adhesion to the substrate, making it necessary to modify the resulting undercut of the lithography.
The use of plasma cleaning before the metal deposition has shown to be from very high importance, both to improve the adhesion of the material and to avoid the destruction of interfaces that comes with PMMA residues under the metal layer during the CVD growth.
For the sake of simplicity, first samples were fabricated with lower density of electrodes, also having just 15 nm thick electrodes to facilitate the lift-off. Both of these parameters were subsequently increased after first signs of success in order to optimize the yield of (suspended) CNT devices. For the resulting electrode gap width of $650 - 700$ nm and our CNT growth conditions, nanotubes showed to be mostly clean for 80 nm thick electrodes, owing to at least partial suspension, and giving a good yield of clean, suspended devices for 100 nm.

source/drain electrodes		
step	type	characteristics
1	cleaning	10 s O_2 plasma at 20 W 3 min prebake at 200 °C
2	spincoating	PMMA/MAA 6%, 6000 rpm, 4000 rpm/s, 30 s, 230 nm 5 min bake at 180 °C PMMA 3%, 6000 rpm, 4000 rpm/s, 30 s, 120 nm 5 min bake at 180 °C
3	lithography	ebeam in NB5 at 80 kV and 1 nA/40 nA
4	development	1 min in MIBK/isopropane (1:3) 5 s + 1 min in isopropane, N_2 drying 10 s O_2 plasma at 10 W
5	deposition	10 nm Mo or Cr in Plassys EBE 70 nm Pt in Plassys EBE
6	lift-off	2 h in NMP remover at 80 °C 10 s ultrasonic in acetone rinsing in isopropane, N_2 drying

Table 5.5: The particular steps of the source/drain electrodes fabrication.

5.2.3 Carbon Nanotube Growth

Carbon nanotubes are grown in a *FirstNano EasyTube 2000* CVD system with modified load, which was installed at the Néel institute in 2009. Optimization of the growth was done by former members of the NanoSpin group, Viet-Ngoc Nguyen and Jean-Pierre Cleuziou. Different catalyst types and compositions, different growth precursors as well as growth conditions were studied, which established a recipe that remained the same over time in many of its aspects. The used catalyst composition or the type of precursors are since unchanged. However, a degraded quality of nanotubes in 2016 sparked a complete revision of the CVD growth conditions.

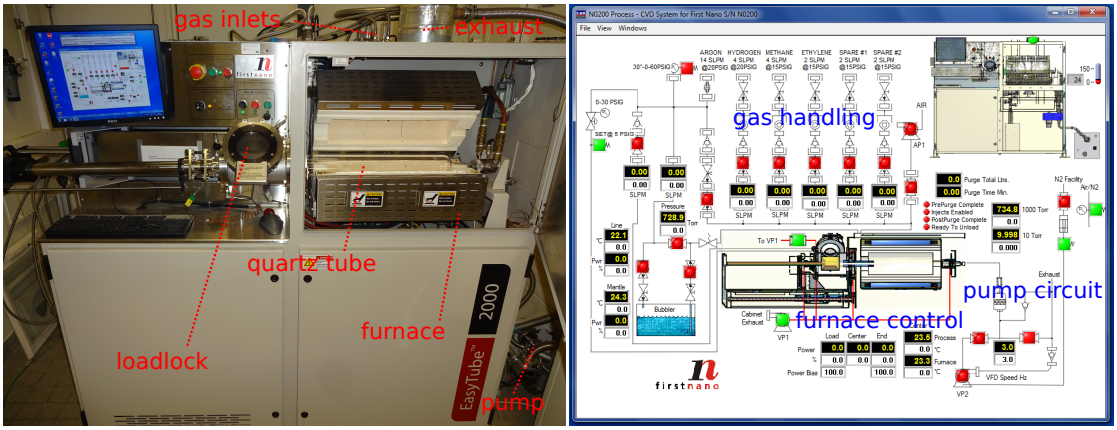

Figure 5.15: a) CVD setup b) Software interface to program and monitor the growth

Catalyst Deposition

Viet-Ngoc Nguyen studied the CNT growth with Fe-based catalyst particles in a bimetallic dilution with both Mo as well as Ru particles [285]. These non- or weakly catalytic elements showed to strongly alter the yield, quality and selectivity of the grown nanotubes. This can be vividly explained by the high rates of hydrocarbon decomposition compared to carbon solubility of Fe, which tends to poison the catalyst particles and can lead to formation of non-tubular carbon structures or stop the growth process altogether. The impact of Mo and Ru was ascribed to the formation of a homogeneous solid phase and thus a doping effect at CVD temperatures, which mainly alters these rates.
However, the exact dependencies of the growth process are very difficult to analyse microscopically due to various involved processes, high temperatures and high reaction rates. It was found that Fe:Mo catalyst with low Mo ratio can vastly improve the carbon solubility and thus the overall CNT yield, single-wall to multi-wall ratio, CNT cleanliness and also the diameter distribution. On the other hand, too high ratio of Mo leads to the formation of different carbon compounds.
In contrast to the effect of Mo on the carbon solubility, Fe:Ru catalyst shows lower decomposition of hydrocarbon and thus lower yield and usually shorter nanotubes, but very high cleanliness and small diameters. In order to reach a high yield and good

quality our nanotubes are hence grown with the Fe:Mo catalyst suspended in an Al_2O_3 matrix and dissolved in methanol with the exact atomic ratios shown in table 5.6. The comparably large and porous Al_2O_3 particles serve as a solid support for the Fe:Mo that helps the catalyst dispersion and creates a multitude of catalytic sites, while the methanol is used to deposit the catalyst in a homogeneous way and avoid big clusters.

catalyst composition	
component	atomic ratio / mass per fill
$Fe(NO_3)_3 \cdot 9H_2O$	1 / 40 mg
MoO_2	0.09 / 1.1 mg
Al_2O_3	3 / 30 mg
CH_3OH	dilute with $\geq$ 20 g

Table 5.6: The used catalyst composition, established by Viet-Ngoc Nguyen [285].

To bring up catalyst onto the desired spots, islands of $\approx 1.5\,\mu m \times 3\,\mu m$ are defined on top of the source/drain electrodes, as shown in fig. 5.16. It is crucial to maintain a alignment precision good enough to not have catalyst in or very close to the gap, in order to not impede the lift-off process and spoil the cleanliness of the devices. While being close to the limit of feasibility, this step can still be done optically by laser lithography, therefore facilitating the fabrication. On one hand optical lithography is much faster to perform, on the other it allows for an standardized use of typical resists like LOR3A. This is of big advantage, because PMMA resists used for electron beam lithography get dissolved by methanol which is used for the catalyst dilution. The catalyst can then be spincoated onto the surface, a step that should be repeated at least once or twice, depending on the density of the dilution and verified after each deposition.

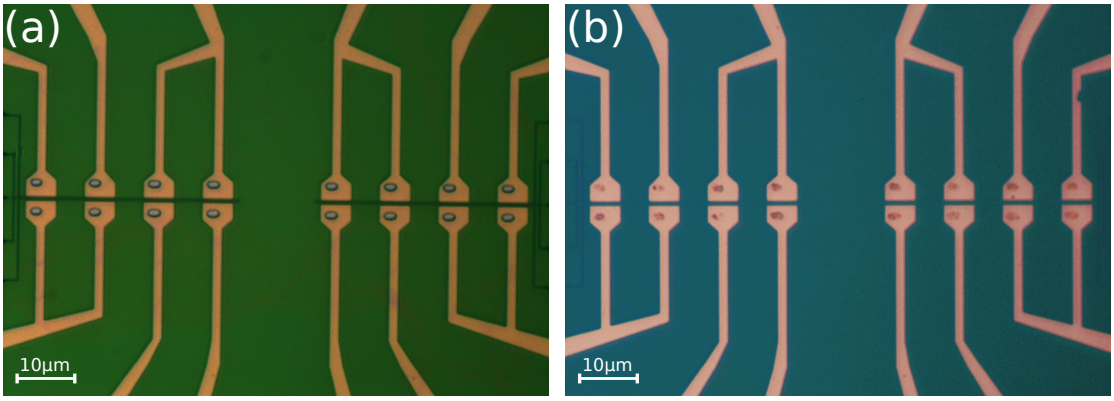

Figure 5.16: a) Optical microscope image of the micro-scale islands on top of the electrodes, defined by laser lithography in optical resist. The used spatial dimensions are at the limit of this technique. b) The situation after deposition of catalyst particles and lift-off. Nanotubes are subsequently grown from these islands in arbitrary direction to bridge the gaps.

While the used catalyst and CVD growth conditions strongly affect the average yield of nanotubes, it is nevertheless the case that each catalyst island or even single growth

site produces CNTs arbitrarily in length and direction. Large amounts of catalyst thus improve the chances to bridge the gaps between source and drain with nanotubes, but one should keep in mind that the ideal result is exactly one CNT making the connection. Furthermore, the catalyst particles tend to create thick and stable layers that can hardly be lifted anymore, especially since high-power ultrasonic baths should be avoided due to the underlying sensible circuit structures. It is therefore of big importance to find a good balance for the used amount of catalyst.

catalyst islands		
step	type	characteristics
1	cleaning	10 s O_2 plasma at 20 W 3 min prebake at 200 °C
2	spincoating	LOR3A, 6000 rpm, 4000 rpm/s, 30 s, 240 nm 2 min bake at 200 °C S1805, 6000 rpm, 4000 rpm/s, 30 s, 400 nm 1 min bake at 115 °C
3	lithography	LASER in Heidelberg DWL 66fs (diode, $405 - 410$ nm)
4	development	1min in MF26A 1min in distilled water, N2 drying
5	cutting	Scriber, 1 cm^2 chip into 4 samples
6	cleaning	30 s O_2 plasma at 10 W 1min in acetone to lift S1805 rinsing in isopropane, N2 drying
7	deposition	catalyst solution, 2000 rpm, 30 s 1 min bake at 80 °C repeat 1-2 times
8	lift-off	2 h in PG remover at 80 °C 10 s ultrasonic after 5 min, upright positioning 10 s ultrasonic in acetone rinsing in isopropane, N_2 drying
9	cutting	Scriber, samples of $\approx 6 - 10\,mm^2$, $\approx$ 50-70 junctions
CVD process		
step	type	characteristics
1	cleaning	5 min O_2 plasma at 20 W
2	CVD growth	5 min at 810 °C 1000 sccm CH_4 feedstock, 800 sccm H_2 background

Table 5.7: The particular steps of the catalyst deposition and CVD growth.

Cutting of the samples before and after the catalyst deposition is done such that big enough pieces for the spincoating technique are maintained and that samples retained from the CVD can be connected on the sample holder (see chapter 7 and fig. 7.2) directly and without further mechanical or electrical stress. To remove any organic residues that could impede the CNT growth from the catalyst surface, the samples are cleaned in

an oxygen plasma (RIE) right before the CVD growth. It should be mentioned that replacing this step on an interim basis by a non-accelerated plasma cleaning (Diener surface plasma) almost entirely stopped the growth of nanotubes, indicating that there is an activation process of the catalyst present. This is sometimes realized by calcination in oxygen atmosphere at high temperatures, a step that we want to avoid in order to limit further thermal stress on the circuit. Nevertheless, a change of the electrode surface texture is generally observed after the CVD, indicating the modification to platinum carbide structrues. An example of a finished device is presented in fig. 5.17.

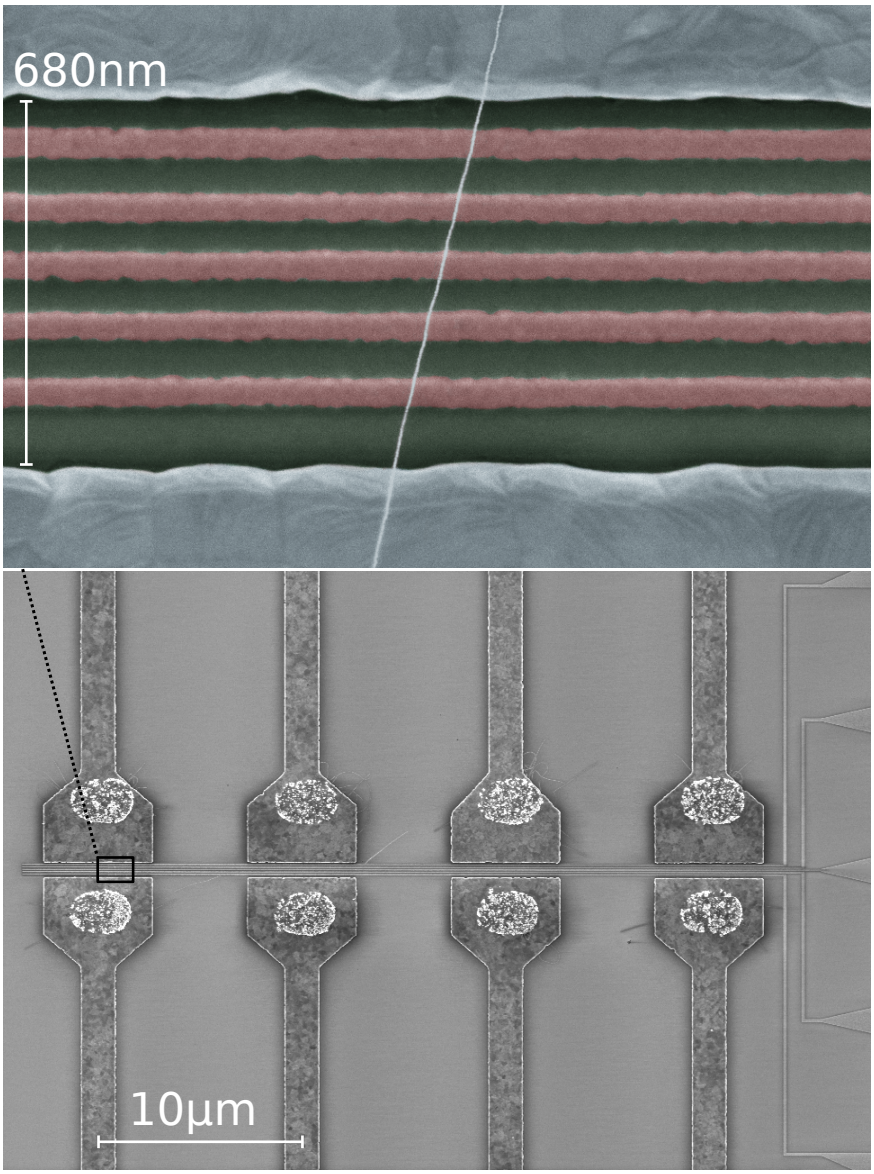

Figure 5.17: Bottom) SEM image of a junction group after the CVD, where CNTs grow arbitrarily from the catalyst islands. Top) False color SEM of a junction crossed by a single CNT.

CVD Process

CVD growth of carbon nanotubes in our setup is based on methane (CH_4) and hydrogen (H_2) precursors. The gas handling system also provides argon (Ar), which is mainly used to purge the chamber before and after the growth and for cooldown of the sample in an ArH_2 atmosphere to avoid the deposition of amorphous carbon after the growth is finished. In his work[285], Viet Ngoc-Nguyen established growth parameters of $770 - 800\,°C$ during usually 10 min, with gas flows of 1200 sccm of CH_4 and 700 sccm of H_2. Those conditions produce mainly SWCNTs with diameters in the range 1.6 ± 0.6 nm and they remained unchanged until 2016.
The yield of CNTs bridging the gap does not only depend on CVD growth conditions and local variations in the chamber, the cleanliness of the chamber and the purity of the precursors, but also on the quality and density of catalyst as well as the nature of the samples itself. It is evident that bridging a longer gap with a suspended nanotube is statistically less likely than bridging a short gap without restrictions for suspension. As a result, the exact conditions are hardly reproducible for separate processes. Our expectancy, gained from averaging over different types of sample geometries, is therefore a yield of $\geq 5\,\%$ junctions with usable CNTs per chip. Noticeable deviation to lower values is hence an indication of a deficient process.
The initial growth conditions were established with studies of SEM imaging, as well as *transmission electron microscopy* (TEM), Raman spectroscopy and transport measurements[285]. The latter serve as significant all-in-one and non-compromising tool to directly monitor the quality of completed devices. Monitoring of the CVD growth conditions, however, has to be realized with the former techniques to exclude the sample itself as source of error.
This was exactly the in for 2016, where a strongly degraded CNT quality fueled a full revision of the CVD process parameters. Raman analysis of CNTs grown on bare Si/SiO_2 at that point indicated a shifted growth temperature. After replacement of all the quartz parts, precursor gases and thermometry components, the CVD parameters were then recalibrated by more detailed Raman studies for different temperatures and gas flows, followed by SEM and TEM verification as well as transport measurements. As new CVD parameters, resulting from these studies, we chose 810 °C during 5 min, with gas flows of 1000 sccm of CH_4 and 800 sccm of H_2. More details on this study can be found in appendix A.1.
The cleanliness of nanotubes can generally be deduced from the ratio of the G-band and D-band in Raman spectra[291], with the D-band ideally vanishing almost entirely. Fig. 5.18 shows such a Raman spectrum of nanotubes grown in our setup. There is still a considerable D-peak visible at $1351\,cm^{-1}$, however the spectrum is taken for an arbitrary position of the Si/SiO_2 surface where CNTs were grown globally. It is therefore reasonable to assume an ensemble of tubes giving rise to the measured spectrum, inevitably increasing the disorder signal compared to single isolated CNTs. This assumption of several measured CNTs is supported by the broadened G-peak at $1593\,cm^{-1}$. Its saddle at the left flank can indicate semiconducting character of CNTs but might also stem from different contributions of the ensemble in this particular case.

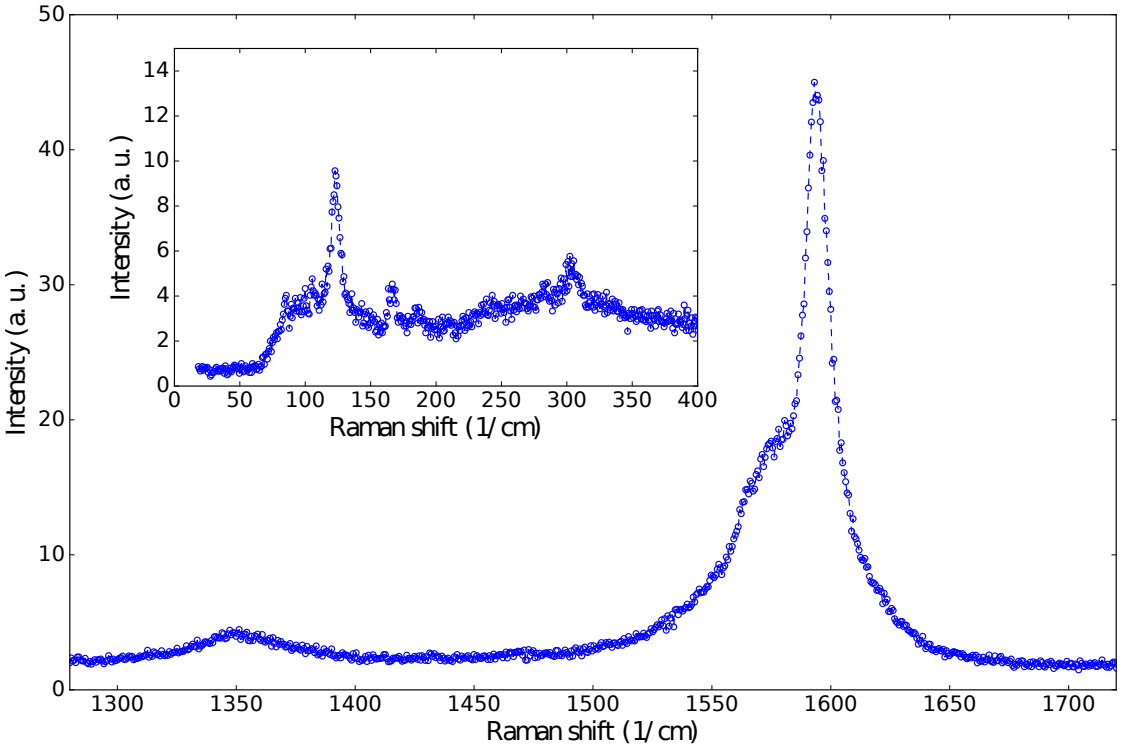

Figure 5.18: Raman spectrum of CNTs on SiO_2. The small but distinct D-band can be attributed to contribution of several tubes, growing as aggregations with disorder arising from overlap. The inset shows the RBM peak at $123\,\mathrm{cm}^{-1}$ as indication of single-wall properties. Another weak contribution is visible at $169\,\mathrm{cm}^{-1}$, corresponding to a nanotube of $\approx 1.5\,\mathrm{nm}$ diameter.

The presence of a pronounced *radial breathing mode* (RBM), shown in the inset of fig. 5.18, characterizes the measured CNT(s) as single-wall. Its frequency of $123\,\mathrm{cm}^{-1}$ can be related to the nanotube's diameter d with $\omega_{\mathrm{RBM}} = 248\,\mathrm{cm}^{-1}/d$ for isolated CNTs [292] on SiO_2 or $\omega_{\mathrm{RBM}} = 234\,\mathrm{cm}^{-1}/d + 10\,\mathrm{cm}^{-1}$ for bundles [293]. Both formulas result in $d \approx 2\,\mathrm{nm}$, in line with former analysis of the CNT width distribution [285].
In fig. 5.19 transport spectroscopy measurements of a CNT at low temperatures are presented, performed on suspended CNT devices grown over a 100 nm gap. Having no further complicated on-chip circuitry, these devices are very useful to monitor the electronic properties of grown CNTs. The regularity and sharpness of the Coulomb diamonds features present in these measurements indicate the high cleanliness and quality of the CNT, with the band gap being unquestionable confirmation of tunability between p- and n-type transport. Further manifestation of the high quality can be seen in the presence of exited states, visible as parallel lines outside of the diamonds.

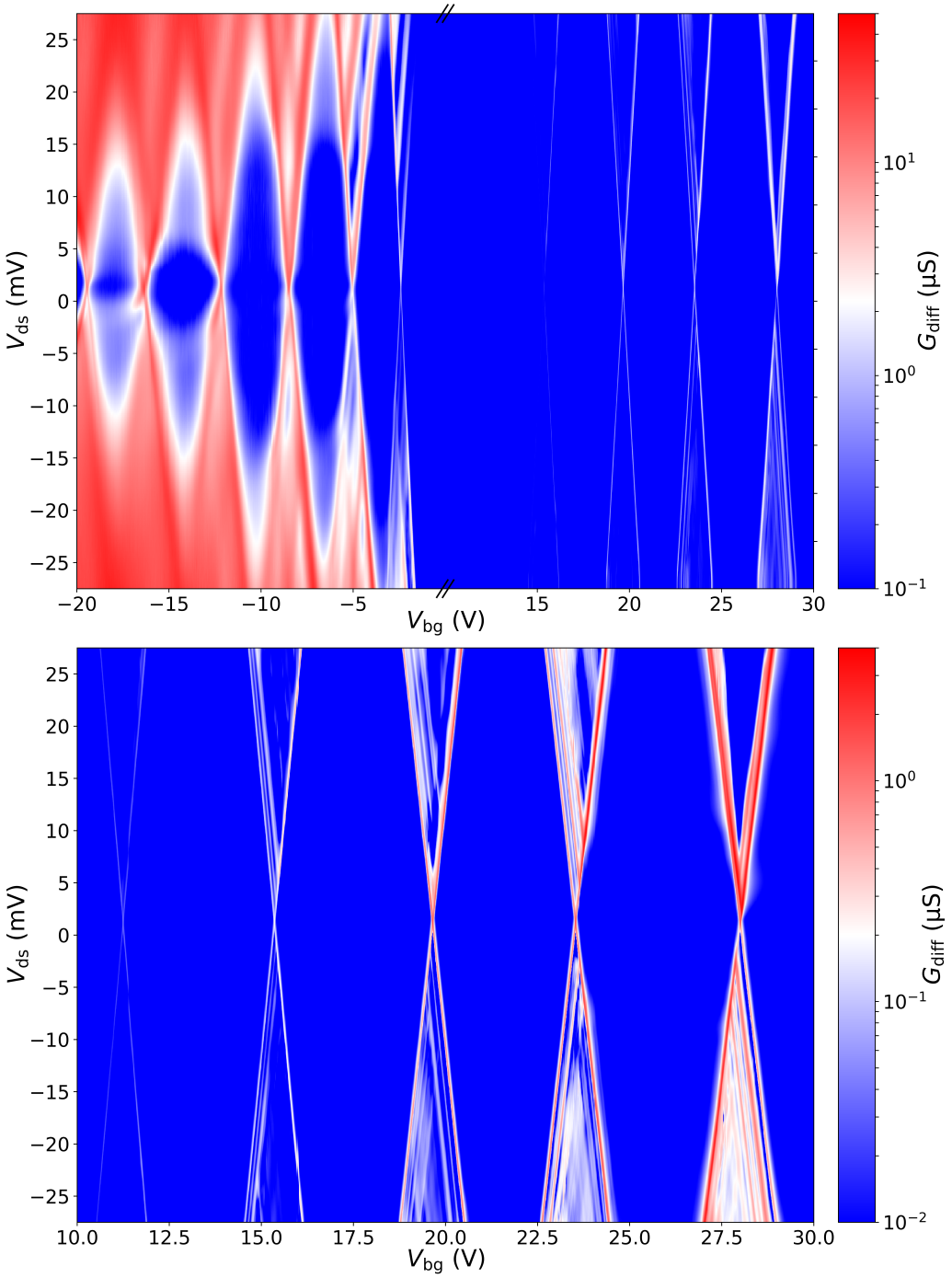

Figure 5.19: Top) Conductance map at $100\,\mathrm{mK}$ of a CNT grown in our setup. The CNT is suspended over a $100\,\mathrm{nm}$ gap and controlled with a global back gate V_{bg}. The CNT can be tuned from p-type to n-type transport features over a pronounced band gap. Very regular Coulomb diamonds in the n-region indicate the high quality of the nanotube. The large diamonds are a manifestation of the relatively big distance to the global back gate and the short nanotube itself, giving rise to limited coupling and large charging energy respectively. Bottom) Close-up of the n-type region, where excitations can be seen as lines parallel to the Coulomb diamond edges.

5.2.4 CNT Device Selection at Room Temperature

While the chosen growth conditions, together with composition and geometry of the junctions, strongly influence the properties of the produced ensemble of carbon nanotubes, such as length, diameter, cleanliness or electronic classification, each single junction's outcome remains entirely stochastic. There may or may not be a CNT connecting source and drain, it may have metallic character or a band gap and differ in cleanliness. Every junction thus has to be characterized beforehand to preselect suitable samples. This preselection is done at room temperature via transport measurements. To do so, the differential conductance over back-gate is detected for both trace and retrace in the probe station measurement setup (see sec. 7.2).

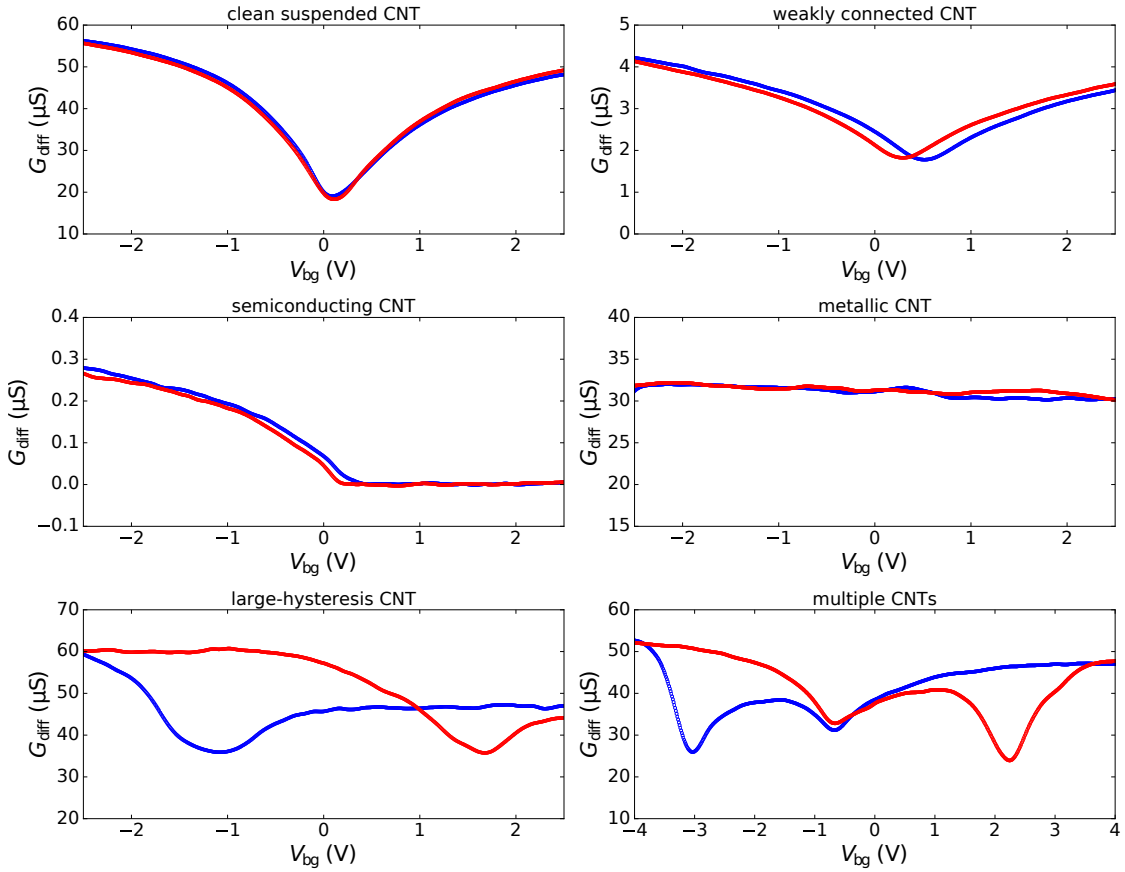

Figure 5.20: Conductance measurements in dependence of the back gate voltage, showing the different types of grown CNTs. Clean devices, comparable to example (a), are preferably used for low-temperature measurements and/or molecule deposition.

As a first criterion, junctions with non-zero conductance but without (sufficiently strong) gate dependence are neglected, since those correspond to either metallic nanotubes or other bridging objects that cannot be tuned. Next in line are the CNTs with band gap, which can be classified as either small-gap or large-gap, with the latter ones being

classified as *semiconducting*. Semiconducting CNTs are discarded due to the not accessible n-branch and often diverging resistance at low temperatures. Remaining CNTs are then ordered by cleanliness, which can be inferred from their hysteresis in gate measurements, being preferably as small as possible.
Last, the conductance (or resistance) value is taken into account. Junctions with $G \gtrapprox 150\,\mu\text{S}$ (or $R \lessapprox 6.5\,\text{k}\Omega$) exceed the perfect channel transmission presented in sec. 2.2 and hence cannot be single CNTs. On the other hand, $G \lessapprox 5\,\mu\text{S}$ (or $R \gtrapprox 200\,\text{k}\Omega$) already at room temperature corresponds to badly connected CNTs whose resistances often diverge at low temperatures. Practically, a realistic range for suitable single CNTs is $G \approx 10 - 100\,\mu\text{S}$ (or $R \approx 10 - 100\,\text{k}\Omega$).
The best CNTs are then either directly microbonded for low-temperature measurements or functionalized with single-molecule magnets before.

5.3 Functionalization with Single-Molecule Magnets

As last step of the fabrication process the carbon nanotubes are functionalized with single-molecule magnets, here usually $TbPc_2$. While this step could principally be done already before the explained procedure of CNT preselection, functionalization as the very last action allows for more reliable monitoring of the results of previous steps.

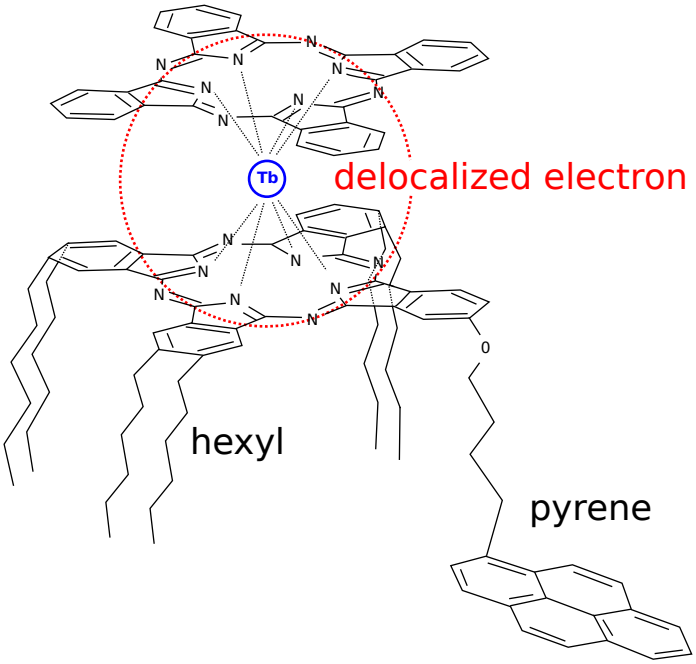

Figure 5.21: Chemically engineered $TbPc_2^{\bullet}$ molecule, where one ligand is modified with six hexyl groups and a pyrene arm to promote grafting to carbon nanotubes.
Based on [39]

5.3.1 Supramolecular Grafting of $TbPc_2$ to Carbon Nanotubes

Neutral $[TbPc_2]^0$ has an electron delocalized over the two ligand planes [294]. This radical can bind to the delocalized $\pi-$orbitals of sp^2-type carbon structures via $\pi-\pi$ interactions. However, unsubstituted $[TbPc_2]^0$ tends to self-assemble on metallic or graphitic surfaces as aggregates without molecular ordering [295]. With chemical engineering of the Pc ligands one can strongly increase the grafting to particular surfaces and obtain $TbPc_2$-CNT complexes, as shown by the group of Mario Ruben, which synthesizes the used SMMs [39]. In this case the ligands are modified with a pyrene arm which binds non-covalently via $\pi-$stacking to SWCNTs, in order to avoid possible insertion of local defects to the detriment of the CNT transport properties [62]. Further modification with six hexyl groups increases adhesion via van-der-Waals forces. The steric hindrance induced by this particular type of ligand prevents recrystallization of the molecules, now labeled $TbPc_2^\bullet$, on the nanotube surface [63].

5.3.2 The Deposition Process

Ideally, the deposition process of molecules is well-controlled, such that only a small amount of molecules is attached to each nanotube and that additional contamination is very limited. The $G(V_{bg})$ data at room temperature should then be very similar to the case of clean CNTs, since the energy scales introduced by a small number of molecules do not affect the CNT much under these conditions. However, in our case the molecules are deposited from solution, which is generally an intrusive process on delicate nanosystems like CNTs, especially suspended ones. Non-ideal deposition processes may hence mask problems that arose already in previous steps, for example during the catalyst deposition or CVD growth. It is therefore preferable to monitor the CNT quality before and after the functionalization to gain information on the entire fabrication process.
$TbPc_2^\bullet$ molecules are provided as dark green powder from synthesis. Small amounts of such grains are then dissolved in organic solvent dichloromethane CH_2Cl_2. Technically, the molecules are most easily deposited by dropcasting of this solution and subsequent nitrogen drying. However, this technique can only give reliable results for CNTs grown non-suspendedly and with metallic top contacts already in place. In the case of suspended devices the approach usually results in a too large amount of molecules grafted to the tubes or, even more often, the nanotubes are destroyed altogether. Strong cohesive forces at the surface of the droplets can rip the nanotubes apart when the surface moves across the tube during the drying process.
Such effects can be avoided with quite high reliability by using a supercritical point dryer, in our case a *Tousimis Autosamdri-815*, shown in fig. 5.22b. For this technique the sample is placed in $TbPc_2^\bullet$-CH_2Cl_2 solution for several minutes, then rinsed in pure CH_2Cl_2 and isopropane to remove weakly grafted excess molecules and finally transferred to the isopropane-filled chamber of the supercritical point dryer. It is absoluty crucial to keep the sample covered with liquid at all times during this sequence of transfers. Supercritical drying is based on the properties of CO_2 which are illustrated in the (p,T) phase diagram of fig. 5.22a.

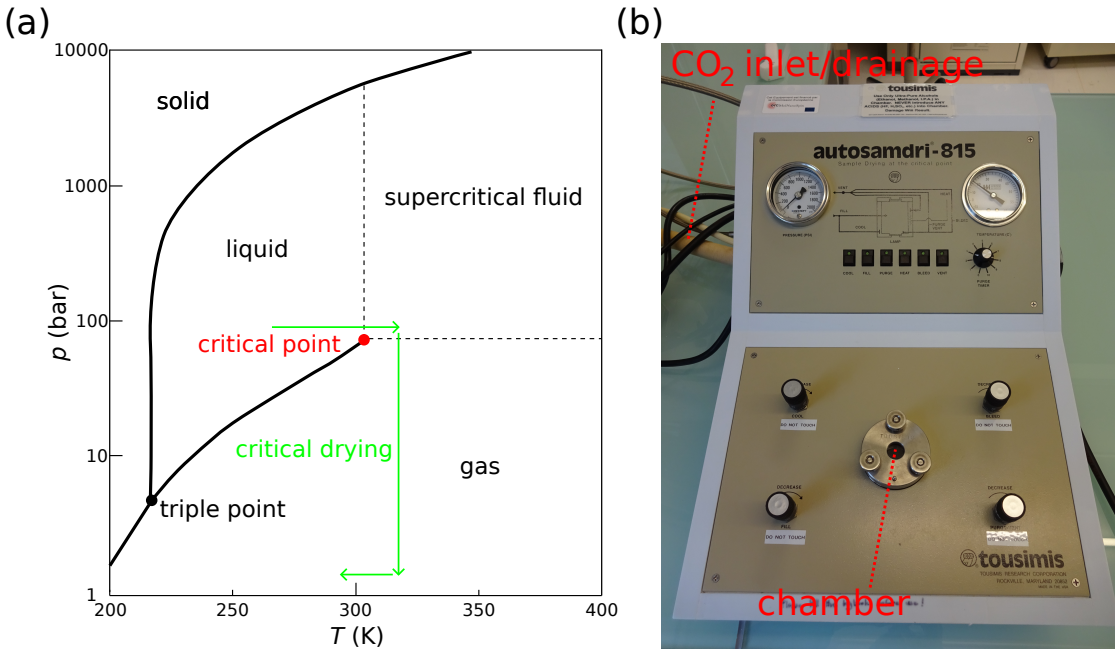

Figure 5.22: a) The (p,T) phase diagram of CO_2, in which the supercritical drying process is schematically drawn. During this process CO_2 undergoes a transition from the liquid to the gaseous phase without crossing the corresponding phase separation line. b) The used supercritical point dryer.

First the chamber is cooled to $\leq 260\,\mathrm{K}$ by a flow of cold CO_2 which then replaces the isopropane in the chamber, resulting in a pressure rise to $80\,\mathrm{bar}$. By increasing the temperature beyond the critical point ($T_{\mathrm{sc}} = 304.25\,\mathrm{K}$, $p_{\mathrm{sc}} = 73.9\,\mathrm{bar}$) without crossing the liquid-gas phase transition line, a supercritical fluid phase is reached. Lowering the pressure in this phase and subsequent cooldown back to room temperature brings the CO_2 into the gaseous phase, omitting surface tensions that are generated at the liquid-gas boundary. The gas can then be removed easily from the chamber. The whole process takes approximately one hour, keeping nanotubes intact in $\gtrapprox 80\,\%$ of the cases.

6 Tin Telluride Thin Film Samples

The investigation of thin film tin telluride devices was realized as a collaboration with the University of Bielefeld, mainly PhD student Robin Klett and successor Denis Dyck, and later on the KIT in Karlsruhe. Fabrication of devices as well as structural characterization studies were conducted in Bielefeld by the two mentioned PhD students, while low-temperature measurements were performed in Grenoble. In this context only a shortened summary of the fabrication part is provided in this chapter. The reader is explicitely invited to look up further details given in the appended publication ""Proximity-Induced Superconductivity and Quantum Interference in Topological Crystalline Insulator SnTe Thin-Film Devices" or the thesis manuscript of Robin Klett.

6.1 Tin Telluride Thin Films

6.1.1 Fabrication and Structural Characterization of SnTe Thin Films

The SnTe thin films investigated in this project are prepared by co-sputtering of Sn and Te in a Bestec system with layer thicknesses of $20 - 70\,\mathrm{nm}$. As substrates, both MgO with (001) crystallographic direction and Si (001) with 50 nm of thermal SiO_2 are used. *X-ray diffraction* measurements (XRD), presented in fig. 6.1, reveal growth of the SnTe with strong (001) texture for both cases. Stoichiometric properties can be deduced from *x-ray fluorescence* (XRF) and *energy-dispersive x-ray spectroscopy* (EDX), indicating a ratio of $49.1\,\% \pm 1.1\,\%$ Sn to $50.9\,\% \pm 1.9\,\%$ Te.
Atomic force microscopy (AFM) studies of the surface yield an average roughness of 0.48 nm on MgO and 0.27 nm on Si. To further study the crystallographic properties of the samples, a goniometer is used for XRD scans. The angle-resolved measurements confirm the strong (001) texture of the SnTe and reveal polycrystalline structure in-plane. The AFM plots and Euler cradles can be found in the supporting material of the mentioned publication.
Transmission electron microscope imaging (TEM) of the layers, presented in fig. 6.2, gives access to the average grain size $d \approx 27\,\mathrm{nm}$ of the crystallites in in-plane direction and shows that only one crystallographic phase is formed in perpendicular direction.

6.1.2 Electrical Characterization of SnTe Thin Films

The deposited SnTe thin films were also characterized electrically by means of temperature-dependent transport measurements of a Hall bar geometry. Fig. 6.3 illustrates the transport properties derived from such measurements for a 40 nm layer. Resistivity measurements (fig. 6.3a) reveal metallic behaviour of the films in spite of SnTe being

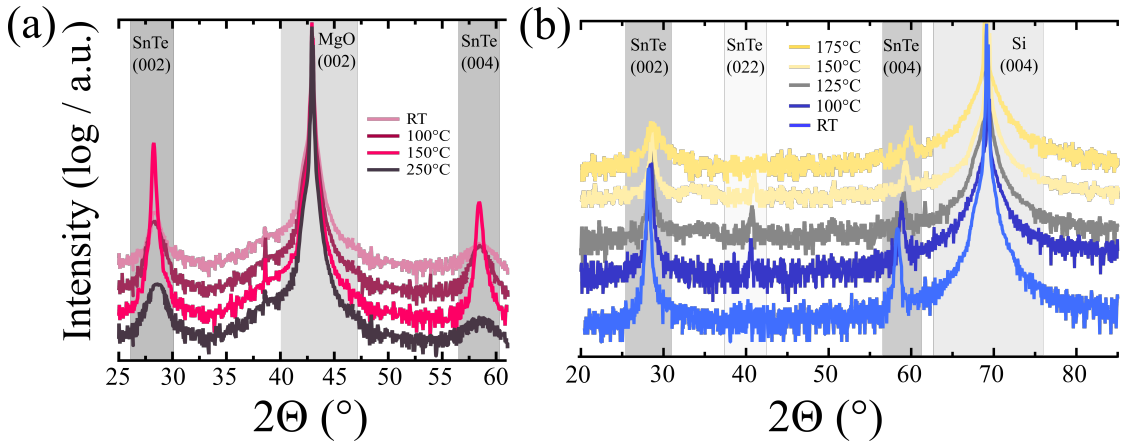

Figure 6.1: XRD measurements of $40\,\mathrm{nm}$ SnTe thin films on a) MgO (001) and b) Si (001) show texture in (001) direction and no further phases. Ideal growth temperatures of $140\,^{\circ}\mathrm{C}$ for MgO and room temperature for Si are deduced.

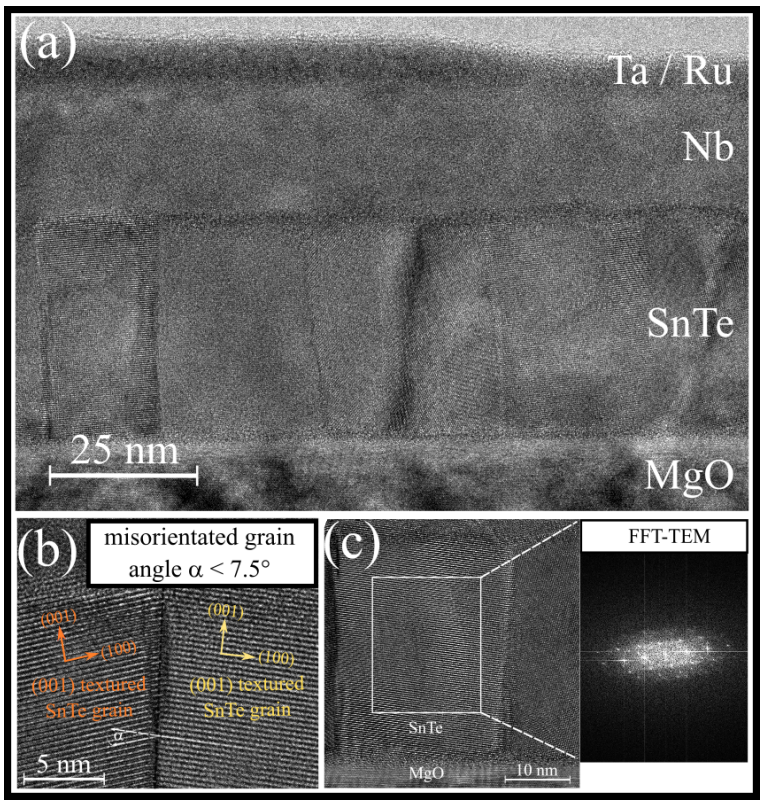

Figure 6.2: a) TEM profile of a MgO/SnTe/Nb/Ru multilayer thin film shows homogeneous crystallites in growth direction (001) and grains in-plane with average size $27\,\mathrm{nm}$. b) Close-up of a grain boundary between two crystallites with an angle missmatch of $7.5\,^{\circ}$. c) The high symmetry of the peaks in the Fourier transformed TEM image is a hallmark for good crystal quality of the individual grains.

classified as a semiconductor with small band gap. This is consistent with findings of other groups, e.g. Shen et al.[214], and can be explained by the aforementioned tendency to Sn vacancies of this compound, leading to strong p-type doping which drives the Fermi energy deep into the valence bands. Furthermore the absence of any pronounced kink in $\rho(T)$, a fingerprint of a rhombohedral phase transition[214], is emphasized, validating the assumption of small influence of such a transition on the transport in the measured samples.

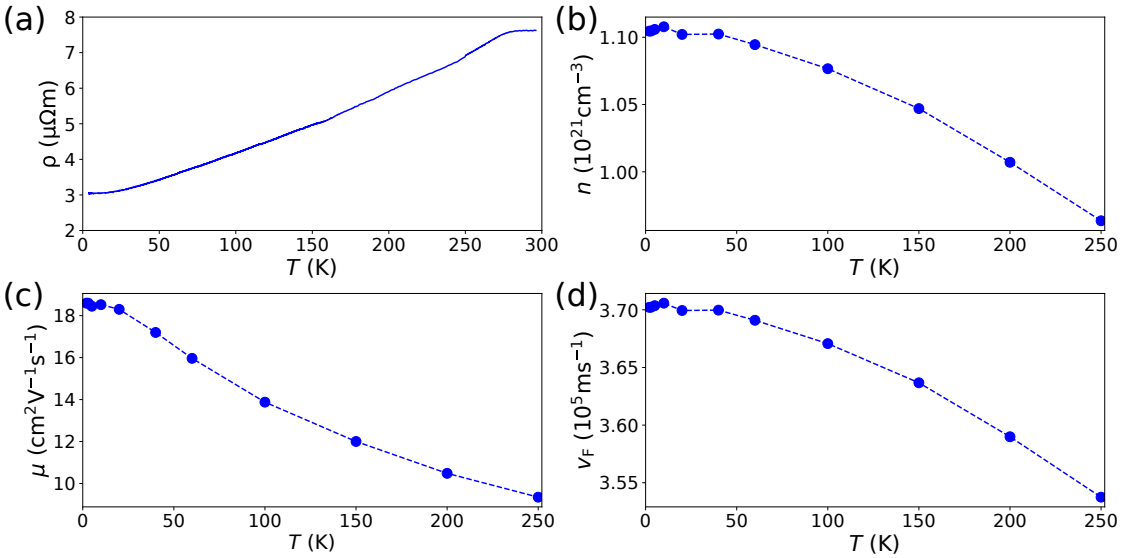

Figure 6.3: Electrical characterization of a Hall bar structure patterned from a 40 nm thick SnTe layer. a) Resistivity measurements ρ reveal metallic rather than semiconducting behaviour with the Fermi energy expected to reside in the valence band due to Sn vacancies. b) Hall measurements indicate fairly high charge carrier density n of the specimen, consistent with the metallic characteristics. c) Mobility μ calculated from ρ and n is limited by the large number of charge carriers. d) Calculation of the Fermi velocity from n, which would need to be corrected with an effective mass as argued in the main text.

Hall measurements give direct access to charge carrier densities (fig. 6.3b) and reveal approximately constant and fairly high[1] carrier concentrations $n \approx 10^{21}\,\mathrm{cm}^{-3}$ for the measured specimen, again supporting the theory of strong p-doping and consistent with the metallic behaviour. As a result, mobilities $\mu = 1/ne\rho$ are limited.
We can also estimate the Fermi velocity with $v_\mathrm{F} = \hbar(3\pi^2 n)^{1/3}/m_0$, but it has to be pointed out that the resulting values, presented in fig. 6.3d, are mostly determined by valence band properties and thus would need to take an effective mass $m_0 \to m_\mathrm{eff}$ into account which we cannot easily access. For the sake of completeness one could assume a light-hole mass of $m_\mathrm{lh} \approx 0.16 m_0$ and a heavy-hole mass $m_\mathrm{hh} \approx 1.92 m_0$ for SnTe as done in common models, e.g. by Zhang et al.[296], to result in a possible range of

1 Tanaka et al. reported a carrier density $n \approx 2 \cdot 10^{20}\,\mathrm{cm}^{-3}$ for their modified Bridgeman growth method. Assaf et al.[220] achieved values down to $n \approx 8 \cdot 10^{19}\,\mathrm{cm}^{-3}$.

$v_\mathrm{F} \approx 2 \cdot 10^5\,\mathrm{ms}^{-1} - 2 \cdot 10^6\,\mathrm{ms}^{-1}$ at low temperatures. For the Dirac velocity related to the (001) surface cone Hsieh et al.[203] calculated $v_\mathrm{F} \approx 1.7 \cdot 10^5\,\mathrm{ms}^{-1}$, whereas Tanaka et al.[215] derived $v_\mathrm{F} \approx 4.5 - 7.8 \cdot 10^5\,\mathrm{ms}^{-1}$ directly from the ARPES slopes.
Finally, the mean free path l_h of the charge carriers can be assessed with $l_\mathrm{h} = \mu v_\mathrm{F} m_\mathrm{eff}/e \approx 4\,\mathrm{nm}$, which is clearly corresponding to a diffusive transport regime.

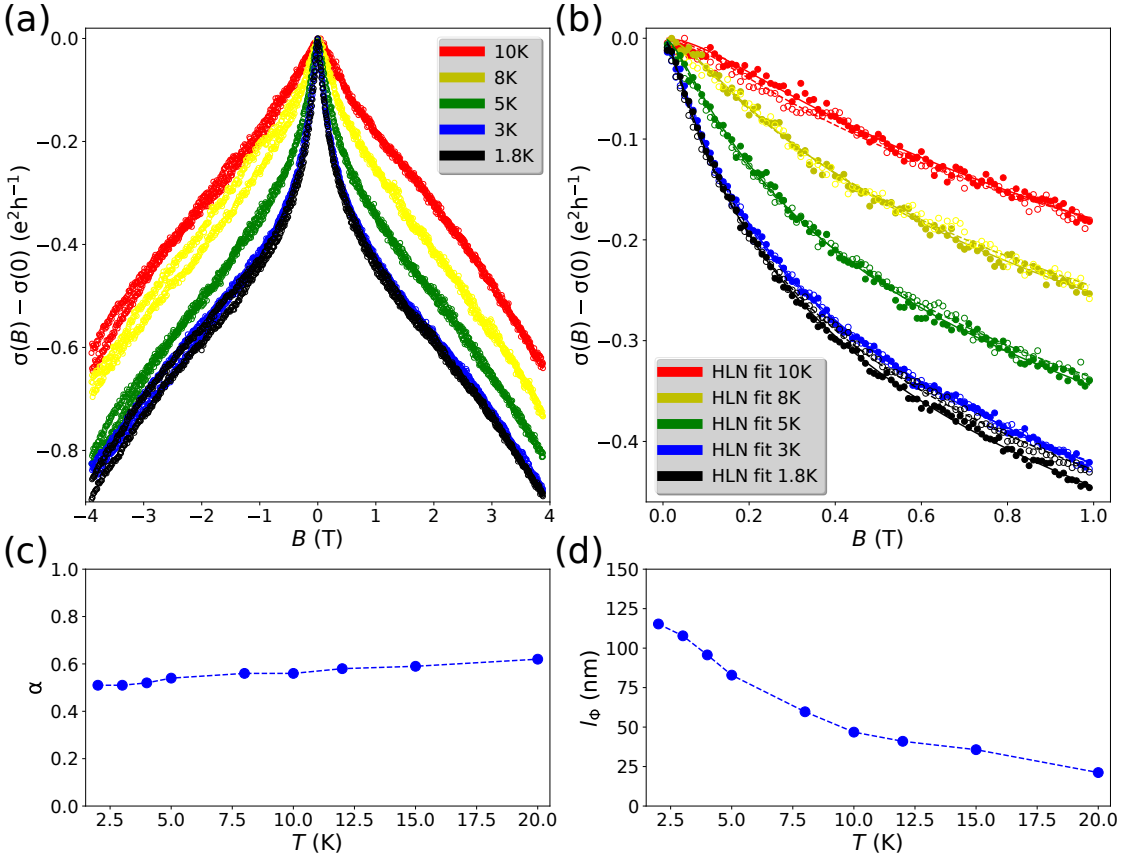

Figure 6.4: Magnetoresistance measurements for a $40\,\mathrm{nm}$ thick SnTe layer and derived quantities. a) The relative magnetoconductivity shows cusp-like structure, which is consistent with WAL effects. The effect vanishes with increasing perpendicular magnetic field B and increasing temperature. b) The data in (a) can be fitted with the HLN formalism, giving access to α and l_Φ as fit parameters. c) The number of contributing surface states is one, corresponding to $\alpha \approx 0.5$ at low temperatures and approximately consistent in the whole temperature range. The presence of only one such channel can be attributed to coupling mechanisms of the different SnTe Dirac cones. d) The phase coherence length l_Φ continually increases for decreasing temperature, reaching a value $l_\Phi \approx 120\,\mathrm{nm}$ at $T = 2\,\mathrm{K}$.

As it has been introduced in sec. 3.2.2 and 3.3.2, an established tool[297] to gauge the presence of topological surface states are weak anti-localization effects which may be present in the longitudinal magnetoresistance. The results of such measurements are shown in fig. 6.4a, clearly indicating anti-localization in the investigated specimen. Fitting of the relative change of magnetoconductivity $\sigma(B) - \sigma(0)$ at different temperatures with

the HLN formalism of eq. 3.8 gives access to two parameters, the dimensionless transport parameter α and the coherence length of the material $l_{\Phi,\mathrm{SnTe}}$. We find $l_\Phi \approx 120\,\mathrm{nm}$ at low temperatures[1], which is substantially bigger than the crystallites' size observed in TEM studies as well as the layer thickness of 40 nm, supporting the validity of the purely two-dimensional model and suggesting that surface states are indeed present and influencing transport. Each separate coherent transport channel should contribute [218] [297] with a value of 0.5 to α, while deviations can indicate the coupling to bulk states near the surface, possibly contributing with WL rather than WAL.
Our measurements (see fig. 6.4c) hence suggest the presence of one such channel. As introduced in 3.3.2, SnTe should form four independent cones on the (111) surface and pairwise hybdridized cones on the (001) surface. Taking two surfaces into account one would naively expect $\alpha = 4$ or $\alpha = 2$. The much smaller measured α thus indicates the coupling of these states, both intra-valley and inter-valley, such that one coherent transport channel is formed. This result is consistent with the findings of other groups for SnTe [220] [298] and was mainly attributed to high bulk carrier densities. Similar coupling was also observed in other topological matter like 3D TIs [219].

6.2 Fabrication of Tin Telluride SQUIDs and Josephson Junctions

6.2.1 Superconducting Thin Films

In order to investigate induced superconductivity in SnTe, the films described before are functionalized with bulk superconducting material, deposited by DC sputtering at room temperature. This step is done in-situ in order to ensure a high interface quality, as low contact resistances are crucial for the propagation of superconducting properties into adjacent normal layers. Used bulk superconductors are niobium (Nb) and tantalum (Ta), both *s*-wave type materials, deposited also as thin films of 30 nm thickness.
The superconducting transition of these films was studied beforehand by the use of bare layers and the results are illustrated in fig. 6.5. Critical temperatures of $T_\mathrm{c}^\mathrm{Nb} = 5.8\,\mathrm{K}$ and $T_\mathrm{c}^\mathrm{Ta} = 2.8\,\mathrm{K}$ were measured. Those values are perceivably lower than the ones given in literature [299], $T_\mathrm{c}^\mathrm{Nb} = 9.25\,\mathrm{K}$ and $T_\mathrm{c}^\mathrm{Ta} = 4.39\,\mathrm{K}$, which is an effect often observed for films produced by sputtering, usually attributed to interstitial impurities introduced during the deposition process [300]. Reports on Nb/Ta films produced by electron beam evaporation [301] reveal critical temperatures close to the reported bulk ones, but these techniques were obviously not available for our bilayer material system.
Especially Nb tends to be further affected by chemical reactions that may arise in the deposition chamber due to the presence of other elements. Such undesired modifications make it quite delicate to maintain the quality of deposited films [302]. Chemical reactions may also occur during subsequent patterning steps, which can further reduce the critical

1 Akiyama et al. [298] reported $l_\Phi \approx 200\,\mathrm{nm}$ and Assaf et al. [220] measured $l_\Phi \approx 180 - 300\,\mathrm{nm}$ for comparable layers. Both groups are using molecular beal epitaxy growth methods (MBE) on BaF_2 substrates.

temperature of finished devices.
First SnTe-based devices were fabricated with Nb films. In 2017 the Nb was replaced by Ta, initially as sustained problems with the superconducting transition of the deposited layers made the change to an element less prone to chemical degradation necessary.

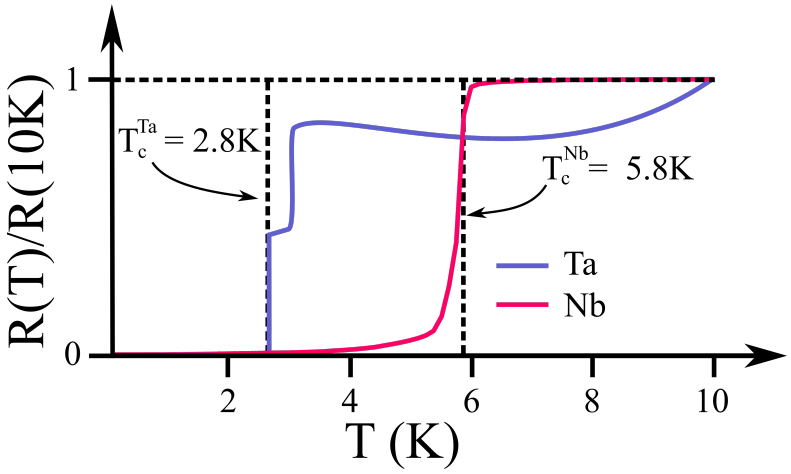

Figure 6.5: Resistance measurements of bare Nb and Ta films of 30 nm thickness in the temperature range close to the transition show critical temperatures of $T_c^{Nb} = 5.8\,K$ and $T_c^{Ta} = 2.8\,K$.

6.2.2 Patterning of Devices

Thin films of SnTe/superconductor bilayers were deposited on entire substrates. While some samples were patterned with positive resist techniques and lift-off of Ta to similar success, most devices were fabricated using negative resist masks and physical dry etching techniques. It is important to take the thermal properties of SnTe for the patterning steps into account, as Te tends to degas at temperatures above 140 °C, an effect which reduces the layer quality.
Etching of the structures is done in an Ar^+ milling chamber, equipped with a secondary ion mass spectrometer to detect the removed materials. The first processing is stopped as soon as no spectroscopic signal of the superconductor is observed anymore. Very first devices were kept in this state, with the SnTe layer untouched and still globally present below the superconducting structures. For newer series of samples the SnTe was confined to the area adjacent to the junction(s) by a second processing of lithography and subsequent Ar milling.
Using these techniques, single junctions and SQUIDs were patterned[1]. For newer samples the design was altered to enable several devices on one chip at once, realized by shared electrodes on one side of the junctions. Such a device is presented in fig. 6.6.

1 The previously discussed Hall bar structures were produced similarly, etched from bare SnTe films.

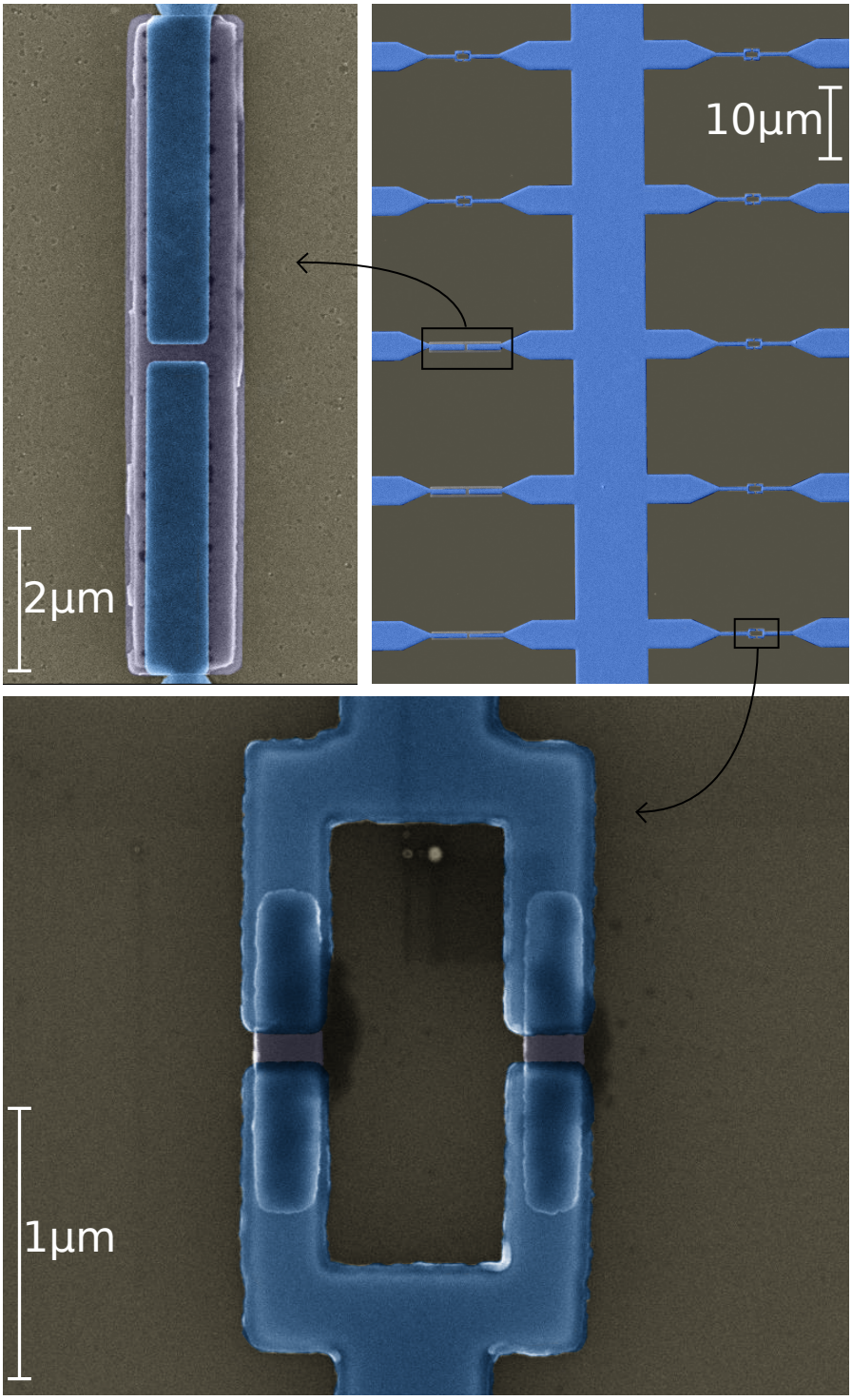

Figure 6.6: The evolved layout of the samples to allow for several Josephson junctions and SQUIDs on one chip. Ta (blue) is used as parental superconductor and the SnTe is restricted to the junction areas.

7 Measurement Setup

In this chapter an overview of the experimental setup used to carry out the measurements is provided. This includes an introduction to the data aquisition method, which is generally based on ADwin sytems, the probing of samples at room temperature and also a distinction of relevant connection schemes for highly resistive nanotube samples and low-resistance superconducting samples. Finally, the cryostats, which are used to conduct transport measurements at low temperatures, are briefly presented.

7.1 ADwin and NanoQT

Transport measurements in our group are generally handled with an ADwin setup, a single device with both voltage source and lock-in detection functionality that synchronizes tasks with very small delay and can therefore be used to perform measurements with several output or input signals at high precision. The all-in-one design furthermore reduces the noise level in comparison to interconnected devices which tend to have ground loops. ADwin units of the used generation consist of a 300 MHz digital signal processor (DSP) which controls a variable amount of output and input signal cards, most often one of each type. Its processor operates with 3 ns precision. The output and input cards are voltage-based digital-to-analog (DAC) and analog-to-digital converters (ADC) with 16 bit and 18 bit precision respectively, applied over a range of $\pm 10\,\mathrm{V}$, thus providing minimal voltage steps of $20/2^16 \approx 305\,\mu\mathrm{V}$ at the output and $20/2^18 \approx 76\,\mu\mathrm{V}$ at the input. ADwin also provides a numerical lock-in detector which further simplifies the assembly.

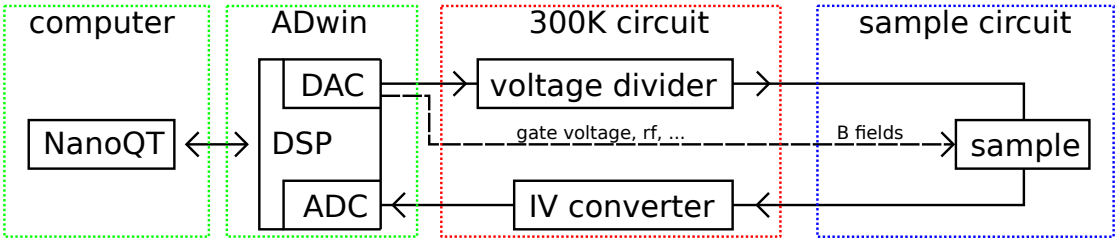

Figure 7.1: General scheme of the transport measurement setup based on ADwin. ADwin is controlled by a standard computer via NanoQT and provides voltage output signals towards the sample or additional signal generators. The sample can be placed in the room temperature setup or microbonded and cooled down in a cryostat.

Internally, the ADwin box operates with *ADwin basic* code, which can be controlled by a standard computer via Ethernet and the NanoQT interface. This interface was developed (and still is improved) at the Néel Institute by E. Bonet, C. Thirion and R. Picquerel and it consists of two levels of accessibility: a first level, based on JavaScript, which allows

for the creation of adapted measurement scripts by the user and a second level which translates the scripts into C++/Adwin basic.
By installing additional voltage-controllable signal generators, this setup can now be used to carry out measurements under various conditions. In fig. 7.1 a simple conductance measurement is schematically illustrated: a voltage output signal is applied to the sample via an (optional) voltage divider. The resulting current is transformed into a voltage and amplified and then detected at an ADwin input channel.

7.2 Room Temperature Probing and Sample Connection

In order to select suitable carbon nanotubes (see sec. 5.2.4), to provisionally monitor the outcome of individual fabrication steps, for example leakage of the small gate lines, or to verify resistance values of (potentially superconducting) metallic samples at room temperature, an ADwin-controlled *LakeShore TTPX* probe station setup is used. Our setup is equipped with several microscale BeCu and W tips which are movable in 3D by the help of a camera and therefore allow the probing of samples via the connection pads (see for example fig. 5.11). Back gate measurements can be realized by mounting samples with conducting adhesive tape or silver paint to the stage, where an electric signal can be applied. While it is possible to cool the setup down to 4.2 K or heat it to 475 K, our standard operation is at room temperature and under vacuum. This allows to quickly conduct tests or measure a large number of junctions, but also protects the samples from detrimental environmental influences. Particularly nanotubes, ore more importantly the hybrid structures of CNTs and SMMs, are easily affected by adsorption, oxydation or electric discharges, which can deteriorate or even destroy the devices.

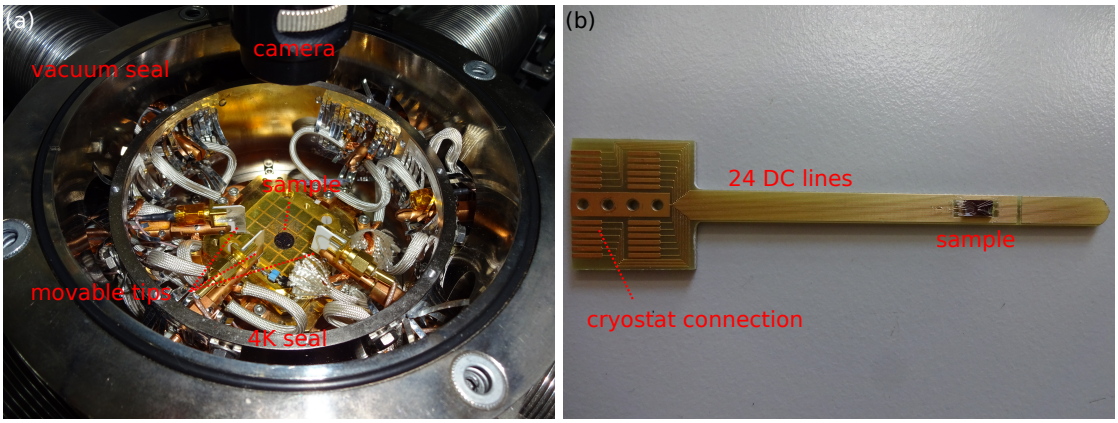

Figure 7.2: a) The probe station in an open state. Movable tips can be connected via BNC. The signals are handled by ADwin. b) A sample holder of the *Diluette* cryostat, consisting of 24 DC lines, with a microbonded sample.

Once selected and/or tested for functionality, the samples need to be connected on a suitable sample holder for the low-temperature measurement setup. Our sample holders generally provide a maximum of 24 small DC strip lines from which the connection

pads of source/drain or the nanotube local gates can be microbonded. For this purpose Al- and Au-based *WestBond* stations with high precision, owing to a continously free 3D control, are available. Nevertheless, this step is delicate and can easily destroy the samples, especially the frail CNT devices, where electric discharges or the breakthrough of the gate insulation urgently need to be avoided. Also leakages due to incautious arrangement of the wires can become an issue. Since each individual CNT device with full number of local gates requires already 7 wires, the number of devices that can be connected at once is severely limited and the connection has to be done thoughtfully. This is corroborated by the practical experience that a cycle of cooldown and warming usually deteriorates CNT samples which can thus not be used again. In contrast, the tin telluride samples showed to reproduce the same results for repeated cooldowns and are generally less prone to failure.

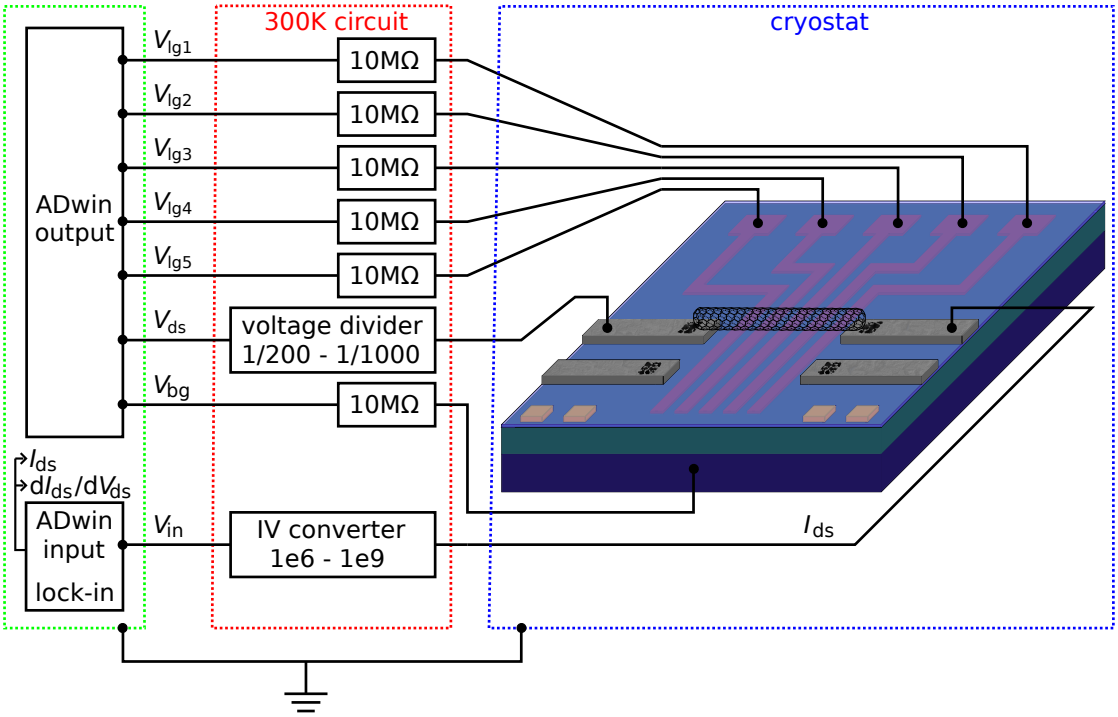

Figure 7.3: Voltage-biased 2-point conductance measurement for typical CNT samples with 5 local gates and a global back gate. The capacitively coupled gates are charged via protecting preresistors and the bias is applied via a voltage divider which improves the internal step size of ADwin. The current has to be converted back into a voltage for the ADwin input.

7.3 2-Point Measurement Technique

Measurements of highly-resistive CNT samples are done in a voltage-biased 2-point connection based on the simple scheme of fig. 7.1. For the case of a multi-gate device, the exact circuit is depicted in fig. 7.3. Individual ADwin output voltages are assigned

to the local gates and the global back gate via 10 MΩ preresistors in order to protect the sample in case of a breakthrough of the oxide, where a leakage current would now be limited by the series resistor. Nanotubes are usually measured in a bias range of $|V_{ds}| \leq 30\,\text{meV}$, which does not only include all the important transport features but also limits the danger of combustion of the CNT. In this context the voltage divider inserted into the bias circuit serves two purposes: On one hand, it limits the applied voltage to the CNT since the maximum voltage is, for instance, $V_{ds} = \pm 10\,\text{V}/200 = 50\,\text{meV}$. On the other, the precision of the measurement is improved because the minimum voltage step at the ADwin output is divided in the same manner, $V_{ds,min} = 305\,\mu\text{V}/200 \approx 1.5\,\mu\text{V}$. The IV converter inserted after the sample converts the current I_{ds} passing the CNT into a voltage, which can be handled by ADwin. Additionally it serves as a low-noise preamplifier. Internal numerical lock-in detection of ADwin allows for the display of the derivate input, the differential conductance dI_{ds}/dV_{ds}. All the output generators and input detectors of ADwin share a common ground, which can be appointed to the ground of the cryostat as well to reduce noise sources due to ground loops.

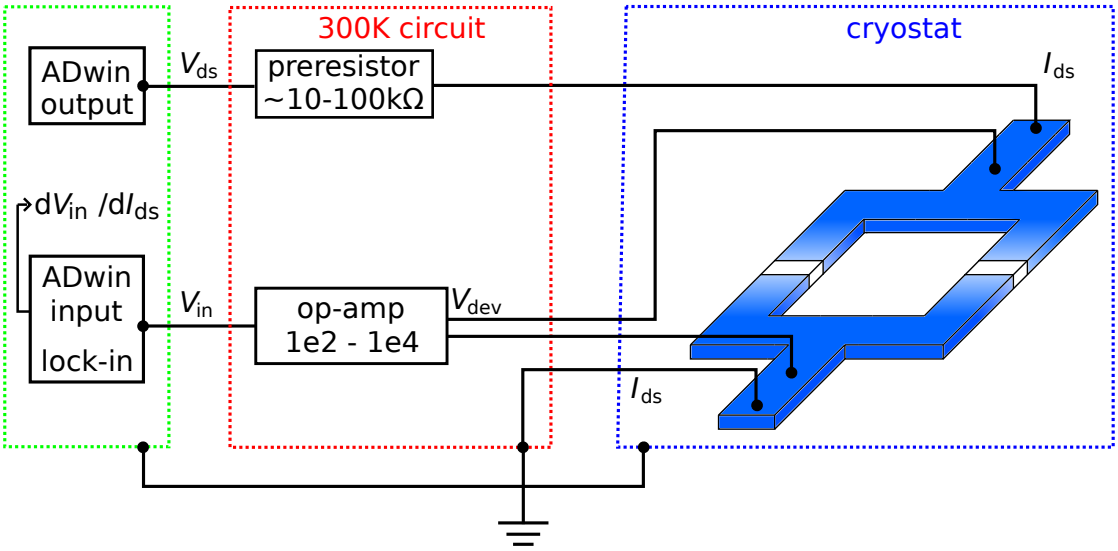

Figure 7.4: Current-biased 4-point resistance measurement setup for low-resistive SQUIDs or junctions based on ADwin. The ADwin output voltage is fed to the sample via a comparably large preresistor. The voltage drop of the device itself can then be measured without masking due to the contact resistances.

7.4 4-Point Measurement Technique

Current-biased 4-point measurement is a standard technique for low-resistive samples and is generally applied when comparably large resistance contributions of leads and contacts obscure the measurement of the sample itself. One of these cases are transport measurements of SQUIDs or Josephson junctions, where there is no voltage drop in the superconducting state. Switching into the normal state often goes along with small

contributions due to micro- or even nanoscale spatial dimensions and the fact that the materials at hand have metallic properties in their normal state. This technique was thus applied for the measurements of the superconducting SnTe samples.
Most generally, the idea of this measurement circuit is to feed a current through the sample via two outer contacts and detect the voltage drop at two contacts in between with a voltmeter. Owing to the high impedance of the voltmeter, there is only minimal current flow in this loop of the circuit and the detected small voltage drop corresponds to the sample while contributions of contacts and leads are omitted.
To realize this configuration with the ADwin setup, the output voltage V_{ds} is applied to a preresistor $R_{\mathrm{pre}} \propto \mathrm{k}\Omega \gg R_{\mathrm{dev}}$ in series with the device before being led off to the ground. By doing so a stable current bias $I_{\mathrm{ds}} = V_{\mathrm{pre}}/\left(R_{\mathrm{pre}} + R_{\mathrm{dev}}\right) \approx V_{\mathrm{ds}}/R_{\mathrm{pre}}$ of the sample is ensured. The voltage drop at the inner contacts is amplified with a homebuilt low-noise operational voltage amplifier and then detected with the ADwin voltage input where the used lock-in technique displays the differential resistance $dV_{\mathrm{in}}/dI_{\mathrm{ds}}$.
As standard configurations preresistors of 121 kΩ and 14.8 kΩ were used, allowing for the application of a maximum current bias of ≈ 80 µA and ≈ 675 µA, respectively.

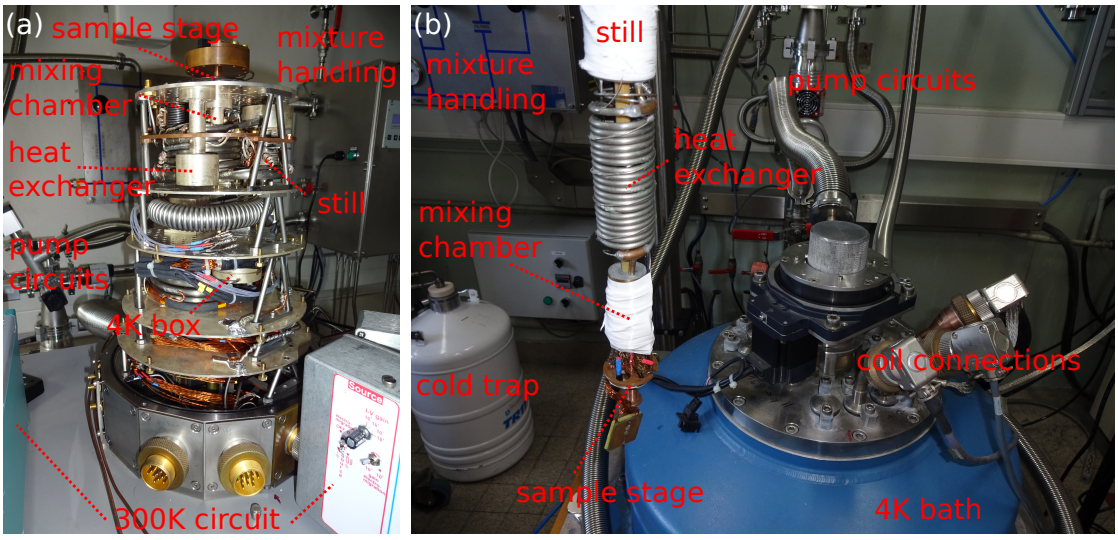

Figure 7.5: a) The open *Sionludi* cryostat. b) The open *Diluette* cryostat.

7.5 Cryogenic Setup

The low-temperature measurements were carried out in three different dilution cryostat units. The preferentially used cryostats in our group are fabricated at the Néel Institute and carry the colloquial name *Sionludi*, arising from the inverted construction in comparison to common dilution refrigerator units.
The Sionludi has a compact table-top design, two separate cooling cycles and a fast cooldown of approximately three hours, nevertheless a base temperature of approximately 30 mK. It can be equipped with a homemade 3D vector magnet. Two cryostats of this

type but different generation were used during this PhD, of which one was equipped with a fast SQUID-optimized electronics, which can measure critical currents at kHz frequencies.
The second type, the *Diluette* cryostat, is based on the common principle of a ^{4}He bath, into which the cryostat is inserted. Compared to the first type it has a longer cooldown time, mainly owing to the long pumping time of the exchange gas and a lower cooling power. Two magnetic coils are installed in the ^{4}He bath, allowing for 2D sweeps of the magnetic field. With the cryostat tube having rotational freedom around the x-axis, the third field direction is also accessible.

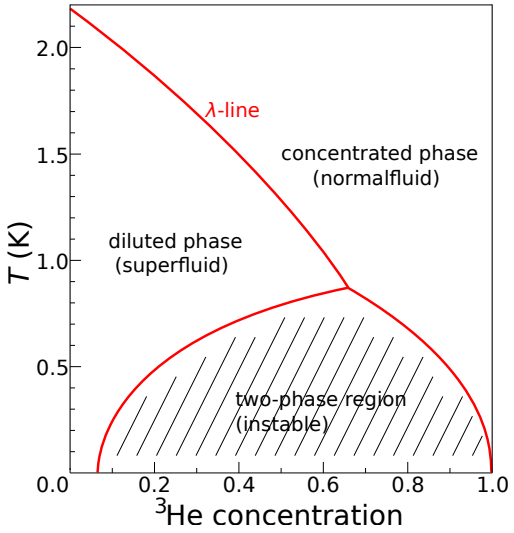

Figure 7.6: The low temperature phase diagram of ^{3}He/^{4}He mixture at vapour pressure, where phase separation into a diluted phase and a concentrated phase occurs below $\approx 800\,\mathrm{mK}$. The minimum concentration of ^{3}He in ^{4}He is finite, $X_{\min} \approx 0.06$.
Based on [299]

7.5.1 Helium Dilution Cooling Mechanism

The cooling mechanism of dilution refrigerators is based on the very particular properties of ^{3}He/^{4}He mixtures that can be derived from the low-temperature phase diagram in fig. 7.6. From 2.17 K at saturated vapour pressure ^{4}He starts to undergo a transition to the superfluid phase with the exact transition temperature being dependend on the ^{3}He concentration of the mixture. At a temperature of approximately 800 mK the mixture separates into two distinct phases: a heavier superfluid ^{4}He phase with low ^{3}He concentration, the *diluted phase*, and a normal fluid phase with high ^{3}He concentration, the *concentrated phase*. Due to a non-zero minimum concentration of ^{3}He in the diluted phase, continued pumping on it drives the dilution out of thermal equilibrium. This is because mainly lighter ^{3}He is removed. Equilibrium is reestablished via diffusive transport of ^{3}He from the concentrated phase. Due to the higher enthalpy of ^{3}He in the diluted phase this transfer removes energy from its environment and thus cools down

parts that are thermally connected to the occuring phase separation. When the removed ^{3}He is continuously reinjected, this mechanism can create temperatures of a few mK with the exact temperature being a practical limit of the experimental setup, determined by thermal leakage and spatial dimensions and not by the dilution cooling principle itself. Practically this mechanism can be exploited in a closed Helium flow circuit which, apart from technical details of the realisation, always operates according to the same underlying mechanism. Its main components are the *mixing chamber*, where the phase separation occurs, and the *still*, supported by heat exchangers, flow impedances and an external pump and compressor. In order to start the dilution cooling process it is necessary to cool down the system to the temperature where phase separation occurs. As a first step the cryostat hence needs to be pre-cooled with either a external bath or a secondary circuit of ^{4}He or even cryogen-free (with pulse tubes) to approximately 4 K. Further lowering of the temperature can be achieved by pressuring the mixture with a compressor and sending it through a flow impedance. The pressure gradient leads to *Joule-Thomson expansion* behind the impedance which reduces the internal energy of the mixture and hence cools it down just as the temperature of still and mixing chamber are lowered by a continuous flow as well. At this point ^{4}He starts to condense in the mixing chamber and evaporative cooling occurs when the vapour is pumped away. Counter-heat exchangers of the cold vapour phase cool down the incoming mixture and more and more ^{4}He condenses until the lower parts of the cryostat up to the still are filled entirely. At low enough temperature phase separation occurs and the dilution cooling starts.

7.5.2 The *Sionludi* Table-Top Cryostat

The *Sionludi* consists of 6 stages spaced upon another, each at a lower temperature than the one below. More precisely, there is a 300 K or room temperature stage, a 100 K, 20 K and 4 K stage, topped by a 1 K stage and the actual 20 mK stage, where the samples are installed. The cooling down to cryogenic temperatures is enabled by several aluminum radiation shields, encapsulating the 4 K, the 30 K and the 80 K stage to prevent heat transfer to the upper, colder stages. An additional outer hull around the 300 K stage maintains the vacuum.
The cooling process involves two separate cycles. The ^{4}He cycle, or secondary cycle, pre-cools the lower parts of the system to 4.2 K during approximately two hours by injection of liquid ^{4}He from a dewar underneath the cryostat. ^{4}He is channeled into the 4 K box which is in thermal contact with the 4 K stage, thus cooling down this stage. Evaporated ^{4}He then leaves the cryostat via a spiral heat exchanger. By doing so, the two stages below are also cooled. To achieve sufficiently large flow rates and thus cooling power for the cooldown, the ^{4}He is pumped. In contrast, the flow created by the overpressured dewar is sufficient to maintain enough cooling power for the stable operating state at low temperatures.
Two different components make up the primary cooling cycle of ^{3}He/^{4}He mixture: fast injection and normal injection. Both are led through capillaries in the counter-flow heat exchanger of the secondary cycle, thus gradually reaching a temperature of 4.2 K before being thermalized with the upper stages. The fast injection is transferred without further

processing to pre-cool the upper parts, including the still and the mixing chamber, to 4.2 K and it is stopped before the actual dilution cooling of the mixture is initialized. The normal injection is first pressured to 4 bar and expanded at a flow impedance above the 4 K stage where the *Joule-Thomson effect* reduces the temperature further. Discrete heat exchangers cool down the incoming mixture and cooling due to condensation sets in.

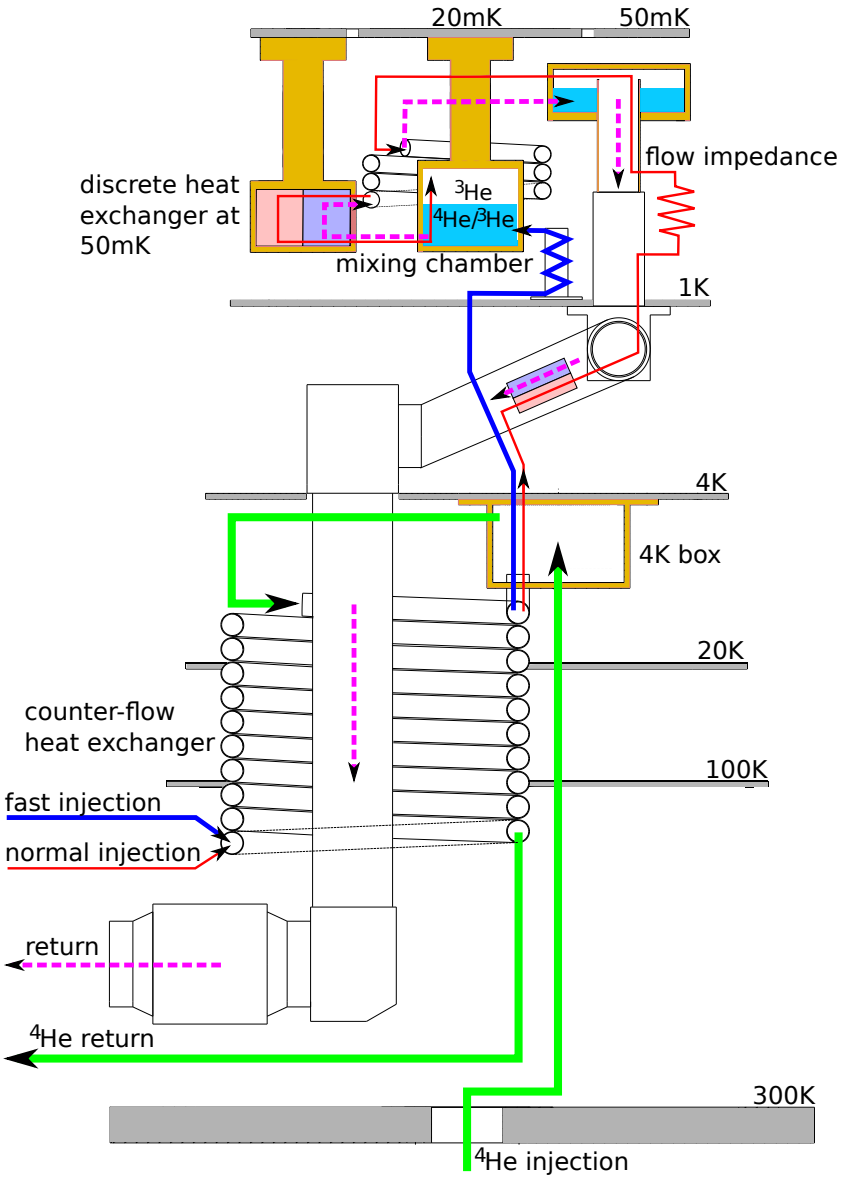

Figure 7.7: Schematic of the inverted *Sionludi* cryostat. The secondary cooling circuit (green) pre-cools the primary circuit consisting of fast injection (blue) and normal injection (red). In the operating state, ^{3}He is injected via the normal injection into the ^{3}He rich phase of the mixing chamber and extracted from the diluted phase (purple).
Adapted and modified from [303]

7.5.3 The *Diluette* Cryostat

In contrast to the *Sionludi*, the *Diluette* cryostat only has one closed ^{3}He/^{4}He circuit, as illustrated in fig. 7.8. Pre-cooling is achieved by evacuation of the outer tube and subsequent filling with ^{4}He exchange gas before lowering the unit into a bath of liquid ^{4}He. This well-proven principle allows for fast and uncomplicated cooldown to 4.2 K, however the tube has to be evacuated from exchange gas again in order to decouple the lower stages from the bath and enable further cooling.
After evacuation of the exchange gas, the ^{3}He/^{4}He mixture can be injected from a tank at room temperature. It is first compressed into the circuit and thermalized at the upper part of the cryostat which is still coupled to the bath. Subsequently the mixture is subject to the Joule-Thomson effect at two separate flow impedances. Heat exchange with the cold gas and the liquid phase of the still, as well as the coupling to the rising liquid in the continuous heat exchanger, leads to further cooling of the incoming mixture until the dilution cooling mechanism starts.

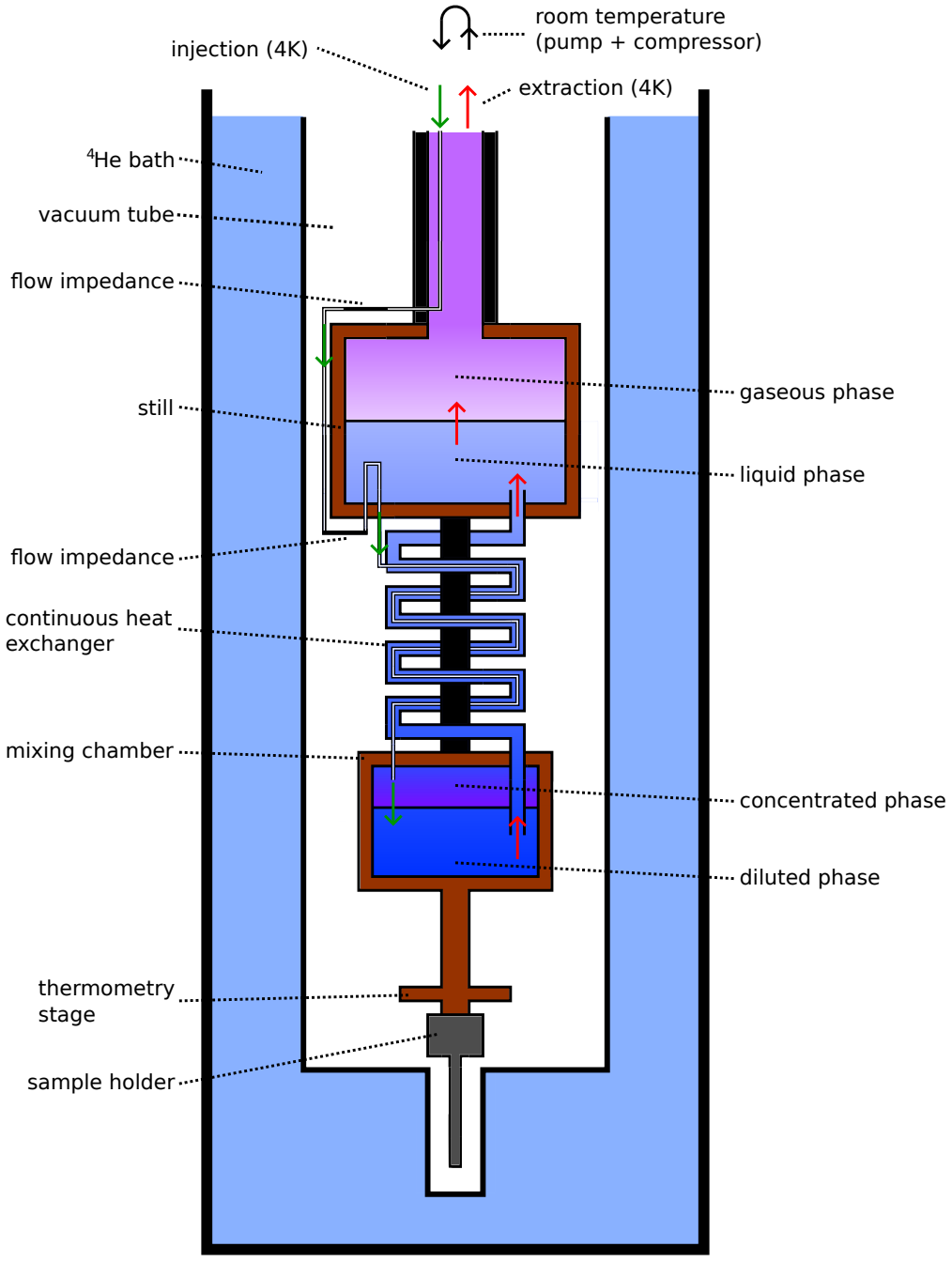

Figure 7.8: Schematic of the lower parts of the *Diluette* cryostat and its cooling mechanism when inserted into the ^{4}He bath. Incoming ^{3}He/^{4}He mixture is thermalized at the $4.2\,\mathrm{K}$ parts and further cooled down via flow impedances and heat exchange, first with the gaseous and liquid phase of the still and then with liquid rising from the mixing chamber to the still in the continuous heat exchanger. The osmotic pressure at the phase boundary due to pumping of mainly ^{3}He in the mixing chamber leads to cooling down to temperatures $\leq 40\,\mathrm{mK}$ at the sample stage.

Part III

Experimental Results

8 Tunable Double Quantum Dots in Multi-Gated Carbon Nanotube Devices

In this chapter the measurements of the multi-gated carbon nanotube samples are presented, whose fabrication scheme was explained in detail in sec. 5.2. While the focus was put on the description of the final recipe of the developed approach, certain intermediate steps were mentioned in order to reason for the chosen approach and included modifications towards this recipe.
In a similar way, characteristic data on samples of the three distinguishable major generations is presented in the following. In this way, demonstration of the working principle is not only provided on the basis of a final result, but milestones are highlighted, which should help to shed light on challenges and requirements that can typically arise and hence contribute towards are more instrumental description.
The functionality of the CNTs as controllable carriers is demonstrated by means of a double quantum dot configuration, tunable from p- to n-type characteristics, which allows for the realization of different coupling scenarios. The resulting charge configurations are explained in most detail for the second of this sample generations, which first met these mentioned requirements.

8.1 Generation 1

As it was alluded in sec. 5.2.2, the earlier generations of devices had reduced number of gates and source/drain electrode thickness in order to probe feasibility and first principles of the approach. In early 2016, first CNT devices with 5 gates and 15 nm thick electrodes were realized. Fig. 8.1 illustrates the charcteristics of these still early tries for an example of length $L \approx 620nm$ and 4 working local gates.
Conductance measurements in dependence of V_{bg} revealed large hysteresis nanotube transport properties dominated by disorder. While parts of this derogation can be attributed to the very limited source/drain height and hence nanotubes gradually following the device height profile, leading to induced disorder at contact points with the oxide, a considerable amount was found to be caused by degraded growth conditions at this point in time, which was subsequently resolved (see sec. 5.2.3 and appendix A.1).
Interestingly, the envisioned principle of tuning the nanotube's charge states in a double quantum dot (DQD) configuration nevertheless held, albeit for deviating physical reasons. Due to the absence of a pronounced band gap in the accessible regime of these devices, characteristics are mainly dominated by arbitrarily positioned and disorder-induced barriers and not by pn-barriers arbitrarily tunable over the entire device length.

Regardless, a short segment of sufficiently low disorder between local gates V_{lg2} and V_{lg4} could be realized, as indicated by the fingerprint of a strongly coupled configuration in fig. 8.1b. In this segment, a barrier could be induced with $V_{\mathrm{lg3}} = 1\,\mathrm{V}$ to create a weakly coupled regime (fig. 8.1c) and additional application of $V_{\mathrm{lg5}} = 1\,\mathrm{V}$ allowed for a strong pinch-off of current over the sample (fig. 8.1d), leaving the coupling almost unaffected. Thus, first principles of gate-tunable DQD devices could be verified, which are surprisingly robust even in the presence of strong disorder.

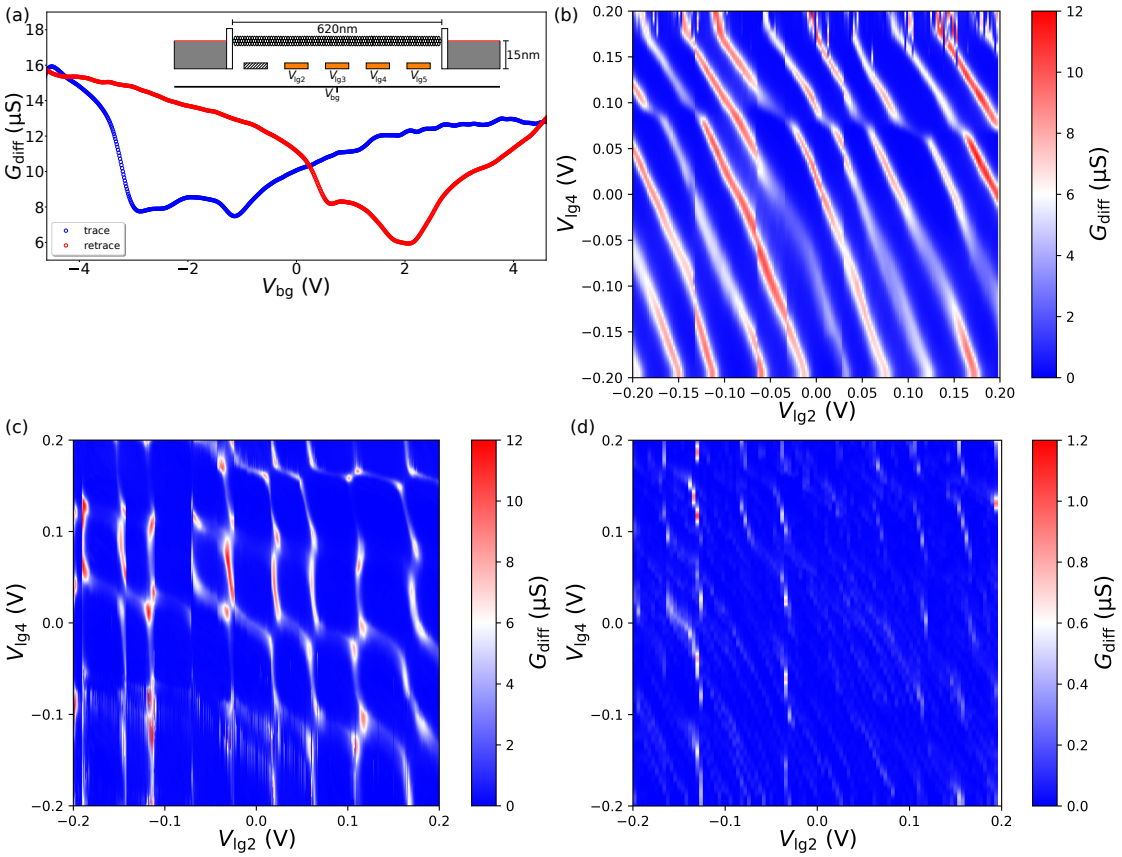

Figure 8.1: Representative example for a CNT sample with $15\,\mathrm{nm}$ source/drain electrodes, controlled by 4 working local gates V_{lg2}, V_{lg3}, V_{lg4}, V_{lg5} plus back gate control V_{bg}. a) Conductance measurement in dependence of V_{bg} at room temperature. Large hysteresis is observed, attributed to the growth profile and intrinsic disorder. b) Conductance in dependence of V_{lg2} and V_{lg4} with $0\,\mathrm{V}$ applied to the remaining gates. A strongly coupled segment is created, but no sign of tunability via the CNT band gap is noted. c) Application of $V_{\mathrm{lg3}} = 1\,\mathrm{V}$ induces a barrier in the segment and a weakly coupled scenario is realized. d) $V_{\mathrm{lg5}} = 1\,\mathrm{V}$ leads to a strong pinch-off of the transport.

8.2 Generation 2

After the first successful demonstration of the working principle, the CNT growth conditions were revised and the height of the source/drain electrodes increased stepwise to 80 nm in order to support at least partially suspended CNTs of higher cleanliness. In spring 2017, first working devices of this type were obtained. Remaining issues at this point were the yield of functional local gates and CNTs which mostly do not yet show ultra-clean properties. The former can, apart from a certain randomness of lithographic failures, mainly be attributed to occurring leakage due to substandard silicon wafers before the realized change of substrates, but also to the problematic of contacting the thin gate pads before modification of the pattern, as it was described in sec. 5.2.2. The latter expresses itself in limited but recognizable hysteresis effects which is attributed to disorder arising at the nanotube-substrate interface, where the CNTs are expected to follow to some extent the varying height profile of the multigate structure in case of not fully suspended devices.

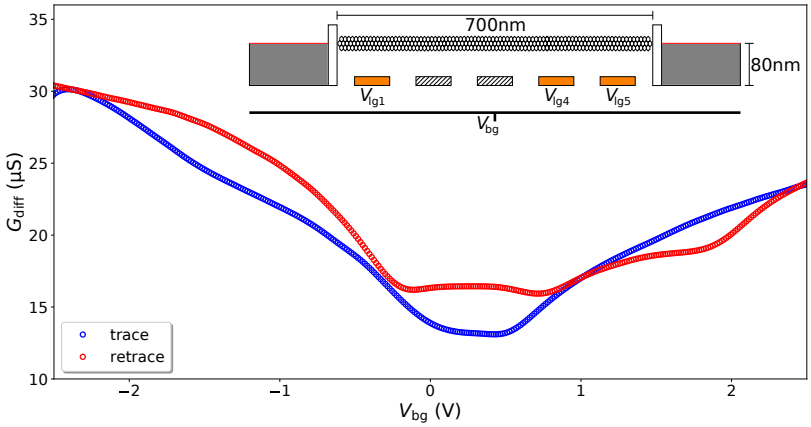

Figure 8.2: Sample *CNT-s6-2017* with a 700 nm CNT on 80 nm source/drain electrodes, controlled by 3 working local gates V_{lg1}, V_{lg4}, V_{lg5} plus back gate control V_{bg} (inset). Main) Conductance measurement in dependence of V_{bg} at room temperature. The moderate hysteresis is mostly attributed to a not fully suspended CNT.

Accordingly, non-vanishing hysteresis in $G_{\mathrm{diff}}\,(V_{\mathrm{bg}})$ at room temperature of fig. 8.2 is visible, obtained for sample *CNT-s6-2017*, a representative example of this type.
In order to systematically manipulate the CNT in a double quantum dot configuration (DQD), it is crucial to have both control of multiple gates and a CNT band gap to allow for induced pn-barriers and hence different coupling scenarios. This is most easily characterized in the single-gate configuration shown in fig. 8.3, for which the remaining gates are kept at $V_{\mathrm{g}} = 0\,\mathrm{V}$. These maps confirm a transition from p- to n-type transport regimes for all 4 gate parameters with a distinct, but small band gap, which is estimated from the bias maps as $E_{\mathrm{g}} \approx 30\,\mathrm{meV}$. Coulomb diamonds of similar dimensions and very similar shell filling are observed for all 3 local gates in the n-region ($V_{\mathrm{lg}} \gtrapprox 0.4\,\mathrm{V}$), with ≈ 8 electron states added within the shown gate range. Transport characteristics in this weakly coupled regime are hence dominated by single-electron effects.

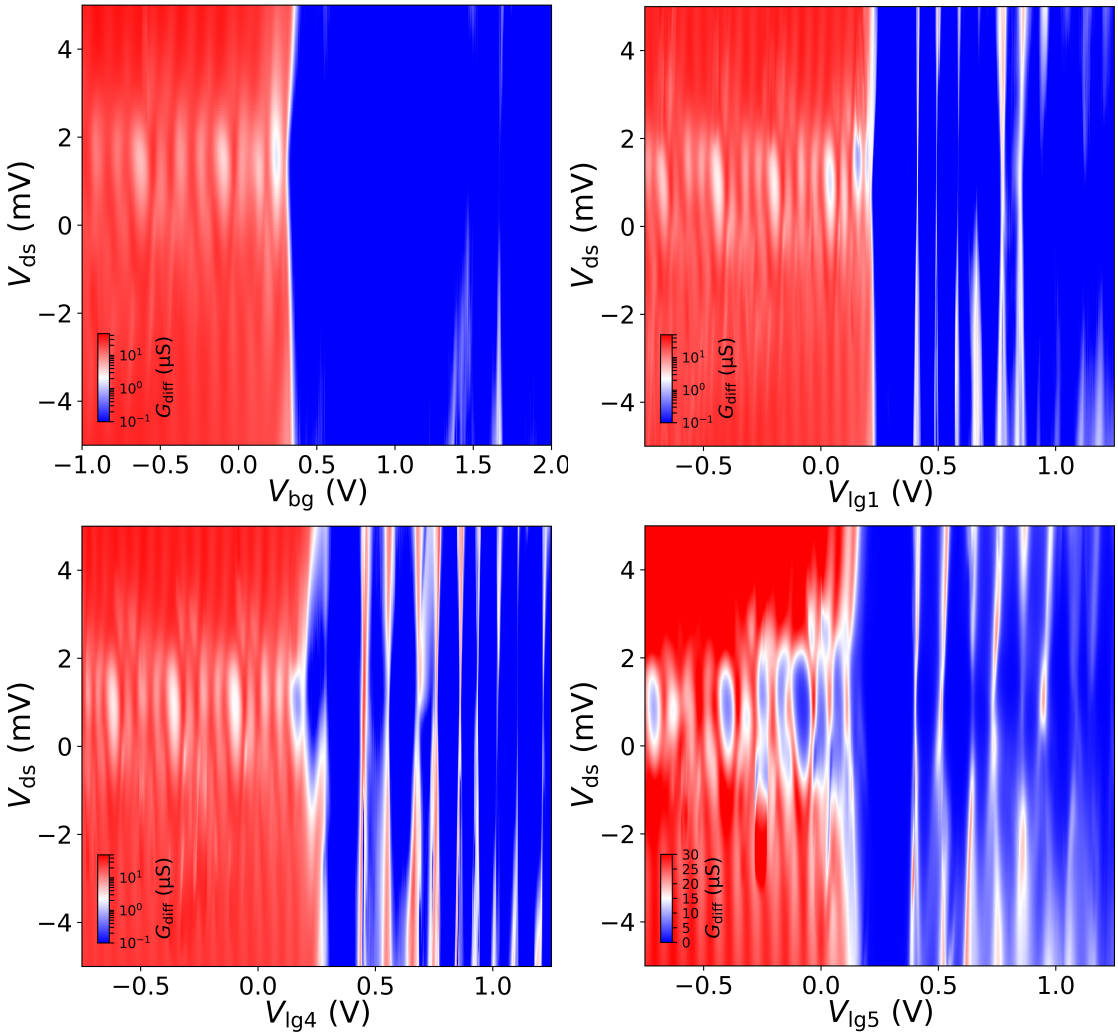

Figure 8.3: Single-gate conductance maps of sample *CNT-s6-2017* for the 4 available gate voltages at $T = 100\,\mathrm{mK}$. For each measurement of a single gate parameter, the other 3 are kept at a potential $V = 0\,\mathrm{V}$.

For negative voltages comparably large conductance is observed and evidence of a fourfold shell filling is noted, as well as a (still weak) shaping of a meshed pattern. Here, the transport characteristics can be attributed to the interplay of single-hole transport and Fabry-Perot resonances, indicating an intermediate coupling regime, which is often observed in clean CNT devices with small band gap [101]. Following eq. 2.13, the length of a CNT segment tuned by a single local gate can be estimated with $L = \hbar v_\mathrm{F}/2\Delta E$, with level spacing $\Delta E \approx 1\,\mathrm{meV}$, valid in a regime of linear dispersion far away from the band gap. This yields $L \approx 280\,\mathrm{nm}$, which is a realistic value, considering a device length of $\approx 700\,\mathrm{nm}$ and a field distribution that is expected to extend beyond patterned dimension of $\approx 50\,\mathrm{nm}$ of a local gate in this scenario.

These different regimes can be realized for voltages $V_{\mathrm{lg}} \lessapprox \pm 1.25\,\mathrm{V}$, which verifies good efficiency of our local gate electrodes and easily allows us to manipulate charge states in a wide range, still far away from potential leakage, which usually does not occur for $V_{\mathrm{lg}} \lessapprox \pm 5\,\mathrm{V}$. A considerably better efficiency of the local gates compared to the back gate is noted, which is a consequence of the reduced distance. Also, a slight shift of the band gap towards positive gate voltages is observed, which gives rise to a p-doping of the CNT at all gate voltages $V_{\mathrm{g}} = 0$. In this context the weak features of n-type transport in the V_{bg} measurement can be understood: the local gates induce an efficient p-type doping in the CNT, which creates pn-barriers with respect to n-type regions induced by V_{bg}.

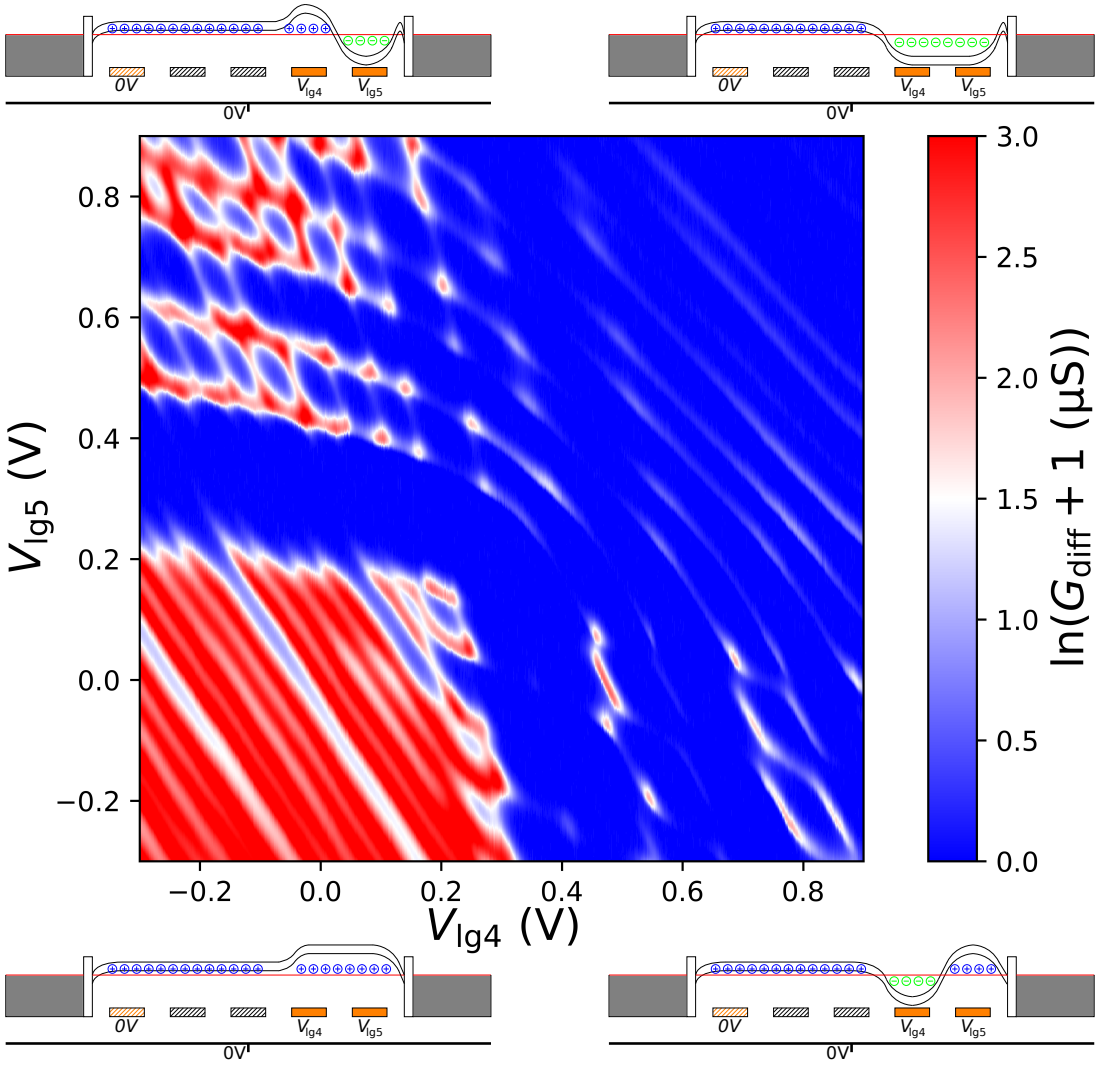

Figure 8.4: Conductance map of *CNT-s6-2017* in dependence of V_{lg4} and V_{lg5} at $T = 100\,\mathrm{mK}$. 4 different transport regimes of the DQD can be realized, (p,p), (n,p), (p,n) and (n,n), indicated by the band diagram schematics in the respective corners. Due to the small spacing of the individually tuned dots, a strongly coupled (n,n) state arises.

With the 4 available gate control parameters, DQD states of different configurations can now be realized. As first scenario, the case of local dots above gates V_{lg4} and V_{lg5} is investigated, shown in fig. 8.4. In this case, the effect of the source/drain electrodes work functions, but also $V_{\mathrm{bg}} = 0$ and $V_{\mathrm{lg1}} = 0$ give rise to a (slight) p-doping of the nanotube segments which are not controlled by V_{lg4} and V_{lg5}.
In light of this, the 4 different occurring DQD regimes, separated from eachother by the band gap, can be understood. The used logarithmic transformation of the conductance data is pointed out, which was done to enable the proper identification of the regimes in one plot, despite strongly altering values between the regimes. As a guide, the two essential coupling scenarios, which have been discussed in sec. 2.16 in more detail, are illustratively recalled in fig. 8.5.

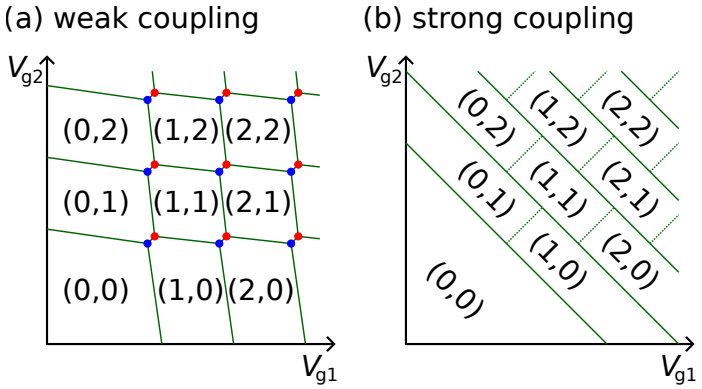

Figure 8.5: The fingerprint of the two predominant coupling scenarios of a double quantum dot, as discussed in sec. 2.4. The pattern can be observed in transport measurements.

In the lower left corner, where both V_{lg4} and V_{lg5} are negative, the entire CNT is driven into p-type transport, giving rise to one large (p,p) quantum dot and high maximum conductance. The latter characteristic can be understood in terms of higher p-type conductance in both single dots and no created barriers within the CNT. Upon increasing only one of those two local gate voltages beyond the band gap, (n,p) and (p,n) states are created, where the DQD is in a weak coupling regime, as indicated by the comb-like pattern.
Finally, one large (n,n) dot can be created by increasing both voltages to positive values, visible as the restored pattern of repeating straight lines of non-vanishing conductance. The conductance level in this regime is very low in comparison to the (p,p) dot, as both internal pn-barriers and low single dot conductance limit charge transport. The DQD of this setup of neighboured gates can hence be seen as one object isolated from the p-type nanotube.
It is interesting to compare these results to the case of furthest spaced gate pairs V_{lg1} and V_{lg5} in order to investigate the possibility to induce barriers and coupling between any segments of the CNT. This configuration is depicted in fig. 8.6. Again, unvaried gates are held at zero, $V_{\mathrm{bg}} = 0$ and $V_{\mathrm{lg4}} = 0$, which now induces p-type doping in the extended middle part of the CNT.

Just as it was the case for the first presented configuration, 4 different regimes can be distinguished. No different behaviour is observed for (p,p) charging of the DQD, as strong coupling and high conductance indicate. Also, the weakly coupled (n,p) and (p,n) regimes are reproduced in a fairly similar way, with different angles of the comb-like pattern being a result of different relative efficiencies of the used pair of gates.

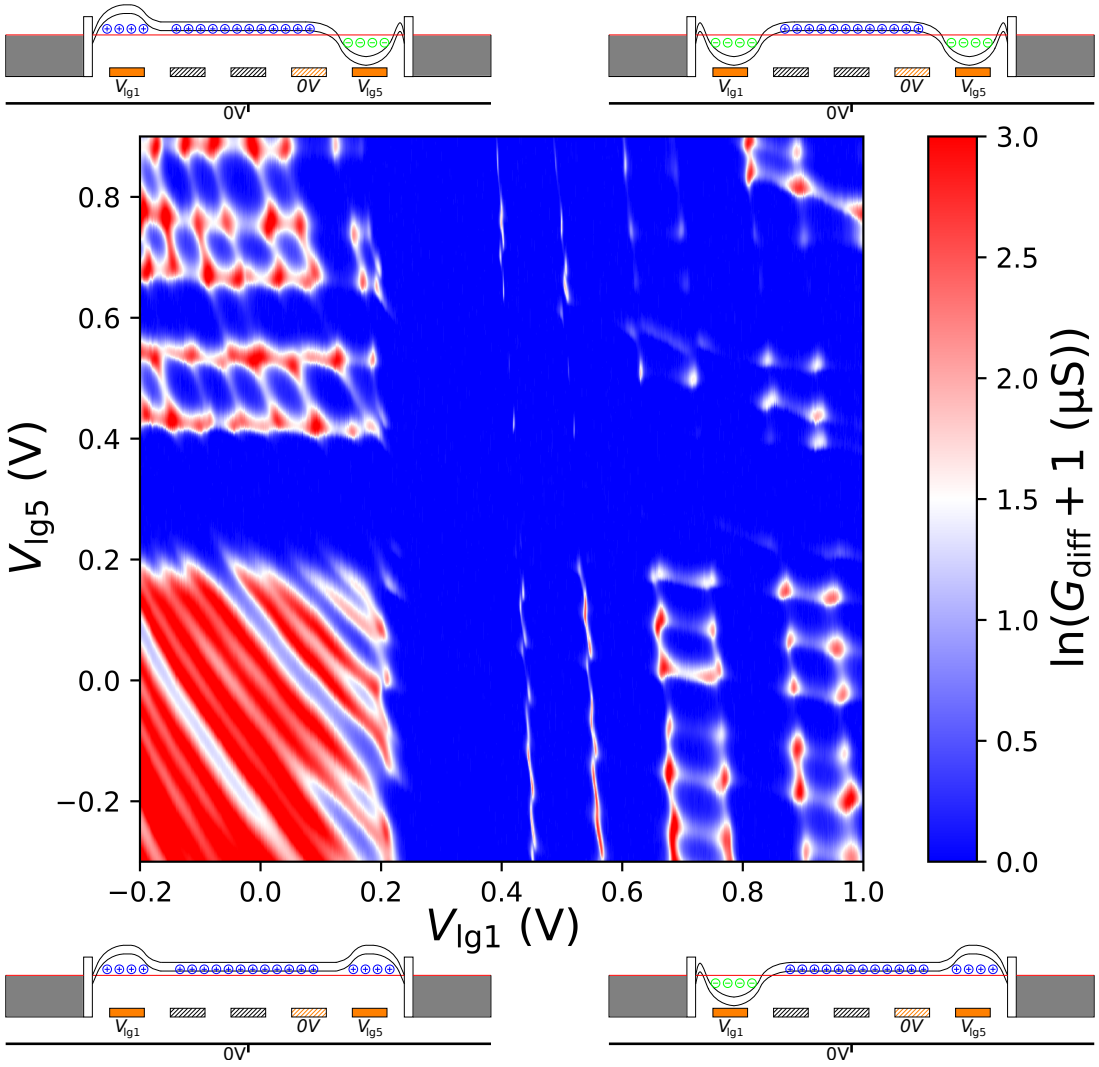

Figure 8.6: Conductance map of *CNT-s6-2017* in dependence of V_{lg1} and V_{lg5} at $T = 100\,\mathrm{mK}$. Again, (p,p), (n,p), (p,n) and (n,n) regimes are created. As the individually tuned dots are now spaced out to opposite ends of the CNT, the (n,n) state is weakly coupled due to pn-barriers at the middle segments.

A different behaviour is observed in the (n,n) state. For the now spaced quantum dots, a (very) weakly coupled state emerges. This variation of coupling can be explained by the creation of pn-barriers towards the middle p-type part of the CNT. One can thus conclude that the control of DQD configurations holds for the entire device length.

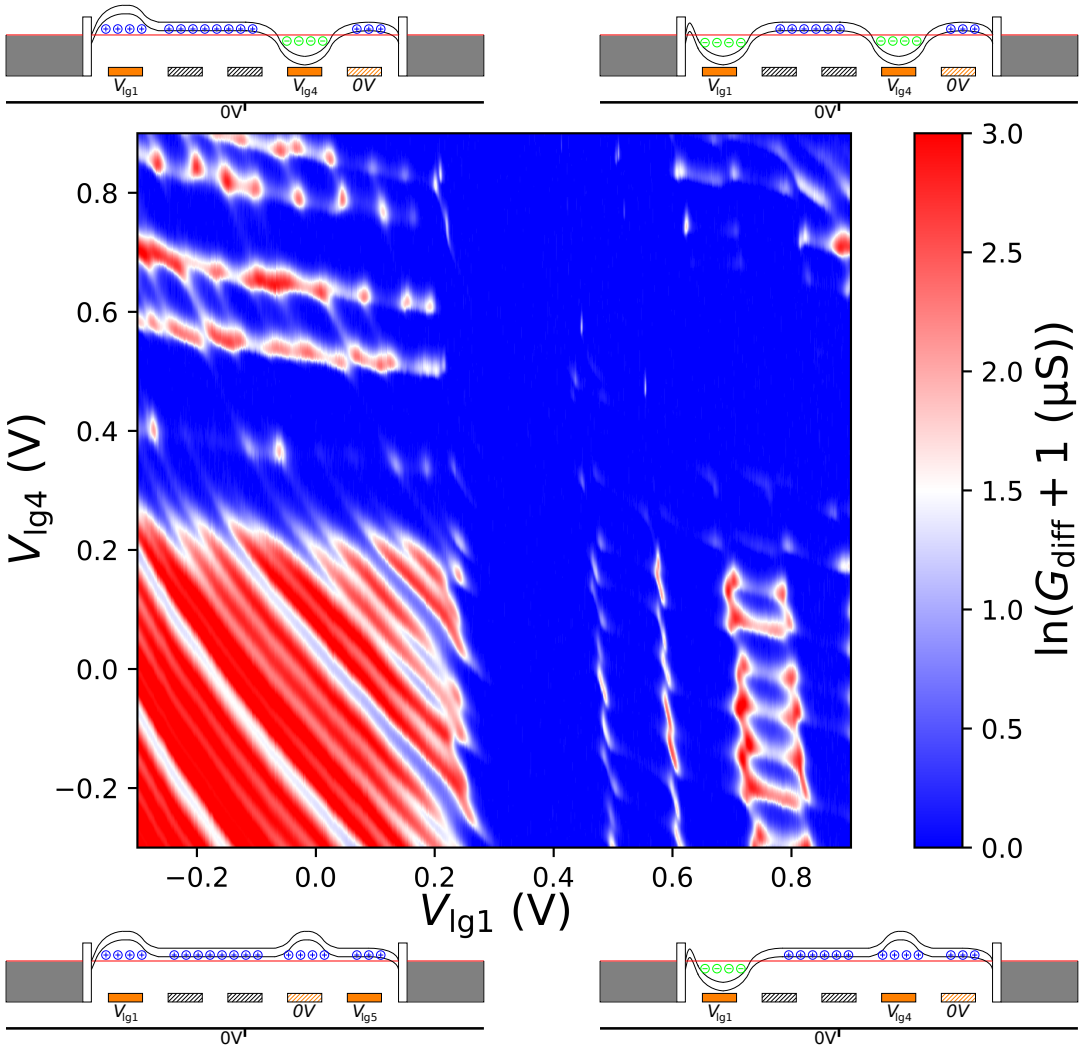

Figure 8.7: Conductance map of *CNT-s6-2017* in dependence of V_{lg1} and V_{lg4} at $T = 100\,\mathrm{mK}$. The same qualitative behaviour of the 4 regimes is observed as for the case of V_{lg1} and V_{lg5} gate pairs.

This mechanism is confirmed for the case of local dots tuned by V_{lg1} and now V_{lg4} instead of V_{lg5}, as can be seen in fig. 8.7: the characteristics of the 4 different regimes are exactly reproduced.

One can now use the remaining gate parameters to induce pn-barriers and hence modify the coupling of spaced pairs of local dots. At the example of a DQD controlled by V_{lg1} and V_{lg5}, the impact of V_{lg4} is demonstrated in fig. 8.8. Compared to the case of p-doping for $V_{lg4} = 0\,\mathrm{V}$ of fig. 8.6, a n-type barrier is now induced with $V_{lg4} = 1\,\mathrm{V}$. As a result, the coupling of the (p,p) regime is strongly reduced, while the opposite is true for (n,n). Here, the barrier strength of the middle segments are now decreased such that a sufficiently high positive voltages V_{lg1} and V_{lg5} strongly couple the spaced DQD.

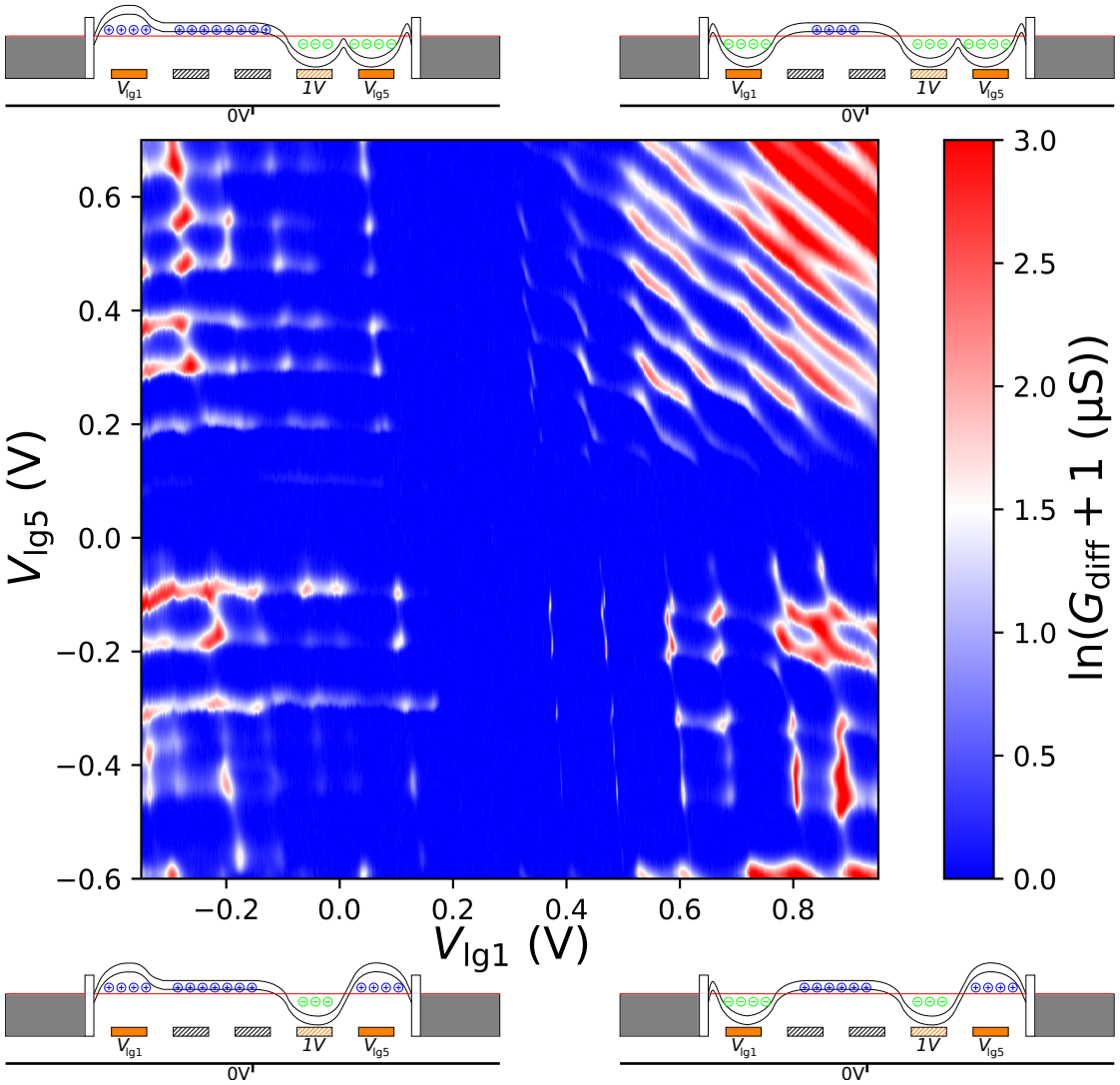

Figure 8.8: Conductance map of *CNT-s6-2017* in dependence of V_{lg1} and V_{lg5} at $T = 100\,\mathrm{mK}$. A n-type segment and hence pn-barriers are created with $V_{\mathrm{lg4}} = 1\,\mathrm{V}$, by this rendering the (p,p) regime weakly coupled and enabling strong coupling in the (n,n) configuration.

Finally, the back gate can be used to demonstrate that, in principle, this coupling can be engineered with all available parameters. Using the setting of fig. 8.8 as initial point, the middle segments of the CNT can be more strongly p-doped by application of $V_{\mathrm{bg}} = -1\,\mathrm{V}$, by this again increasing the pn-barriers that determine the coupling of the DQD system located at positions 1 and 5. As a result, the (n,n) configuration is again driven to a weak coupling regime, while the other three configurations remain qualitatively unaffected. This case is shown in fig. 8.9). It is pointed out that this scenario could be more efficiently realized by using additional local gates instead of the back gate, which were, however, not connected in this particular device.

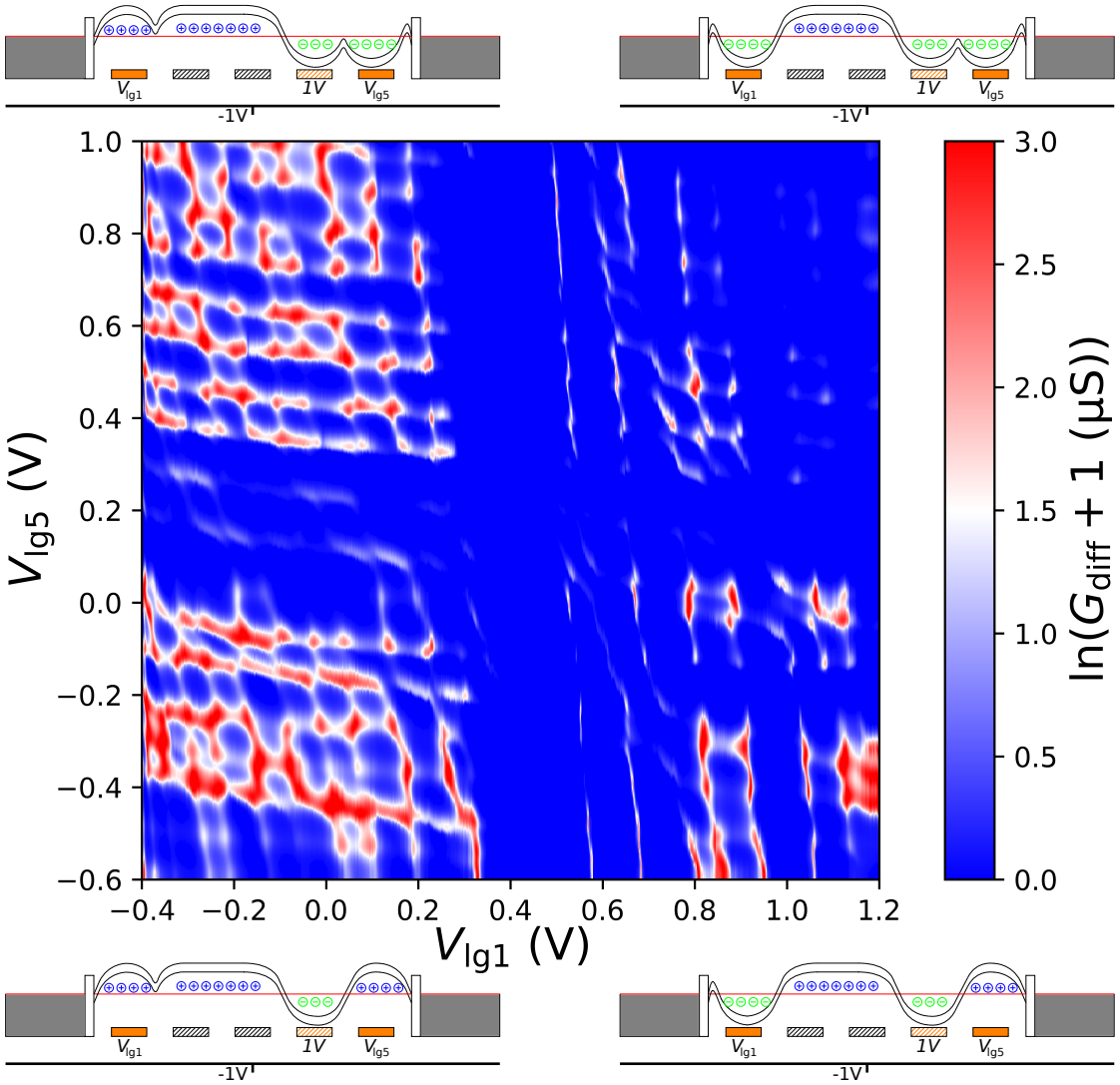

Figure 8.9: Conductance map of *CNT-s6-2017* in dependence of V_{lg1} and V_{lg5} at $T = 100\,\mathrm{mK}$. Additionally to the barriers induced by $V_{\mathrm{lg4}} = 1\,\mathrm{V}$, the remaining middle segments are now driven at $V_{\mathrm{bg}} = -1\,\mathrm{V}$. The resulting pn-barriers restore the weakly coupled case for (n,n).

With our growth conditions, typical junctions lengths of $L \approx 700\,\mathrm{nm}$ and an electrode thickness of 80 nm, room temperature characterization via the back gate measurements $G_{\mathrm{diff}}\,(V_{\mathrm{bg}})$ suggests the yield of both relatively clean CNTs, as the one of 8.2, and ultra-clean ones, having basically no hysteresis, as illustrated for another sample of the same generation in fig. 8.10.
The assumption of nanotubes just on the verge of being suspended thus stands to reason, which is in line with the chosen device parameters, as CNTs are expected to grow with a certain slack and a difference in height of $\approx 70\,\mathrm{nm}$ from the source/drain level to the gate oxide does not leave a big margin.

On the other hand, low-temperature measurements with the local gates of these devices of varying room temperature hysteresis do not indicate a substantial difference in cleanliness, as it becomes clear from comparison of the previously shown data for *CNT-s6-2017* and the data of *CNT-s9-2017* in fig. 8.11.
Again, evidence of Fabry-Perot contributions are found in the p-type region of the single-gate measurements (fig. 8.11a1,a2), which are here slightly more pronounced due to lower contact resistance of this sample, manifesting itself as higher conductance levels. The n-region is dominated by single-electron transport and shows Coulomb diamonds of similar size, regularity and local gate coupling. A more strongly featured n-branch in this device is noted. A double quantum dot characterization for local gates 2 and 5 is shown in fig. 8.11b, which is most comparable with the scenario presented in fig. 8.7 due to the equivalent lateral gate distance. Again, strongly coupled (p,p) and weakly coupled (n,p), (p,n) and (n,n) regimes are observed, in line with the reasoning given before, albeit with more strongly pronounced transport features.
As a matter of fact, basically all of the measured devices in a range of moderate to vanishing room temperature hysteresis revealed very similar low-temperature characteristics. It is therefore sensitive to assume that the presence of the local gates can interfere with $G_{\mathrm{diff}}\,(V_{\mathrm{bg}})$ characterization measurements at room temperature. These local gates constitute metallic structures between the back gate and the CNT after all and should therefore impact these measurements with screening effects, dependent on the microscopic alignment of the structures. While $G_{\mathrm{diff}}\,(V_{\mathrm{bg}})$ remains a good indicator to facilitate the room temperature selection process, only low-temperature measurements with V_{lg} can undoubtedly shed light on specific CNT properties of these devices.
However, as the results of this section confirm, our approach allows for reliable fabrication of clean nanotube devices which are suitable for the envisioned purpose of a carrier in supramolecular systems.

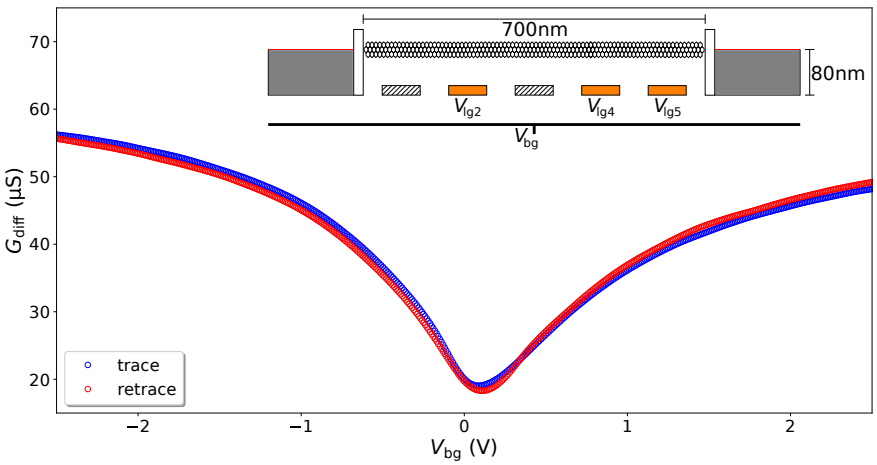

Figure 8.10: Sample *CNT-s9-2017* with a 700 nm CNT on 80 nm source/drain electrodes, controlled by 3 working local gates V_{lg2}, V_{lg4}, V_{lg5} plus back gate control V_{bg} (inset). Main) Conductance measurement in dependence of V_{bg} at room temperature. Lack of any hysteresis indicates ultra-clean properties, possibly caused by full suspension of the device.

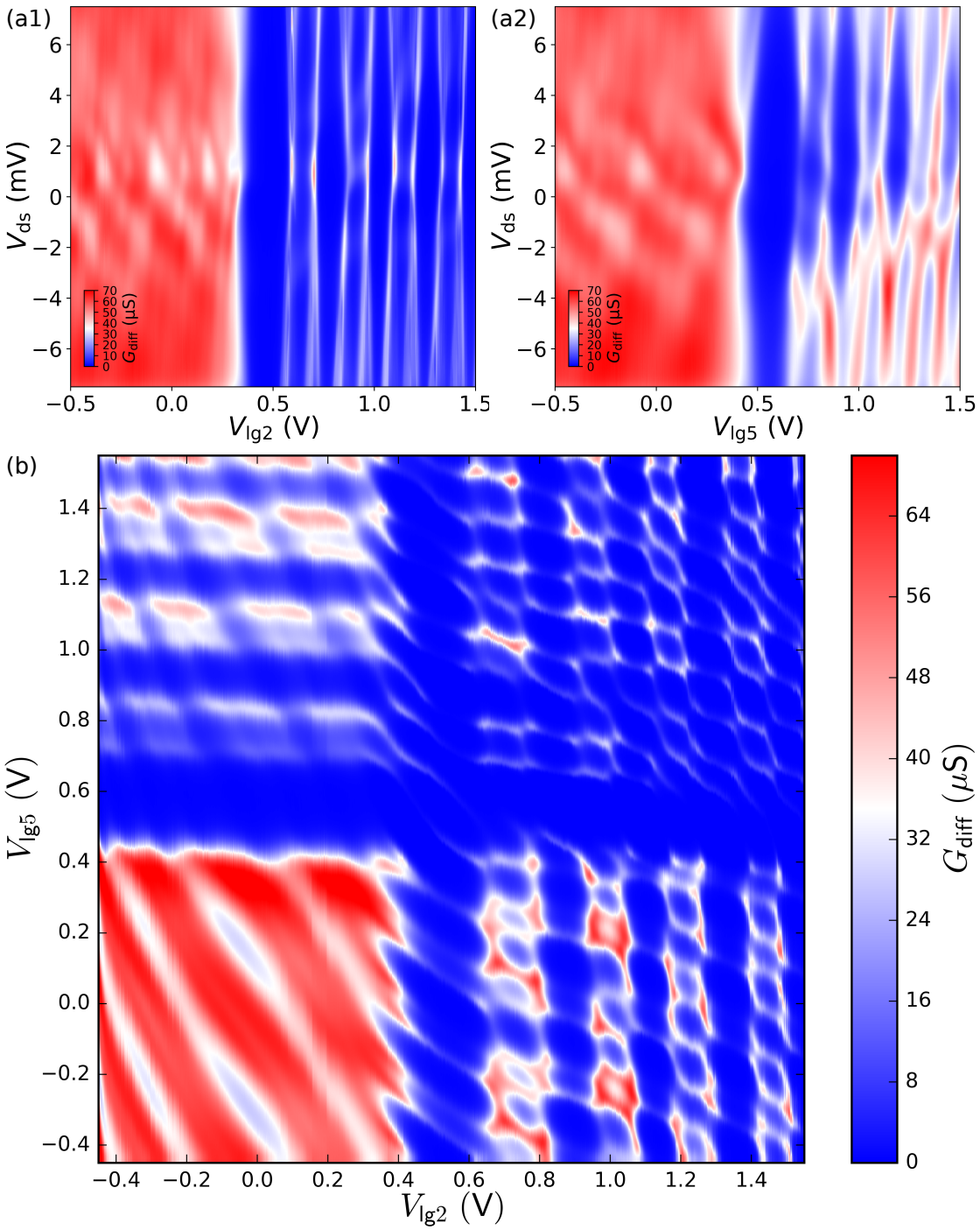

Figure 8.11: Low-temperature measurements of *CNT-s9-2017* at $T = 100\,\mathrm{mK}$. a1,a2) Single-gate conductance maps of sample *CNT-s6-2017* for V_{lg2} and V_{lg5}, analog to the ones of fig. 8.3. b) Conductance map of the DQD configuration, showing again 4 transport regimes, (p,p), (n,p), (p,n) and (n,n). The latter 3 reveal weak coupling due to pn-barriers.

8.3 Generation 3

As final measure, the remaining issue of local gate yield was tackled by replacement of the defective substrates and a redeposition step of the gate pads, to minimize leakage and improve the contact probability (see sec. 5.2.2). Furthermore, the height of the source/drain electrodes was increased to 100 nm to boost the ratio of clean nanotubes. With these changes, we can now reliably produce high-quality nanotube devices with 4-5 working local gate electrodes. One representative example is shown in the following. Since the electronic properties and gate tunability strongly ressemble the generation 2 samples, albeit with generalization to 5 gates, only an overview is provided.

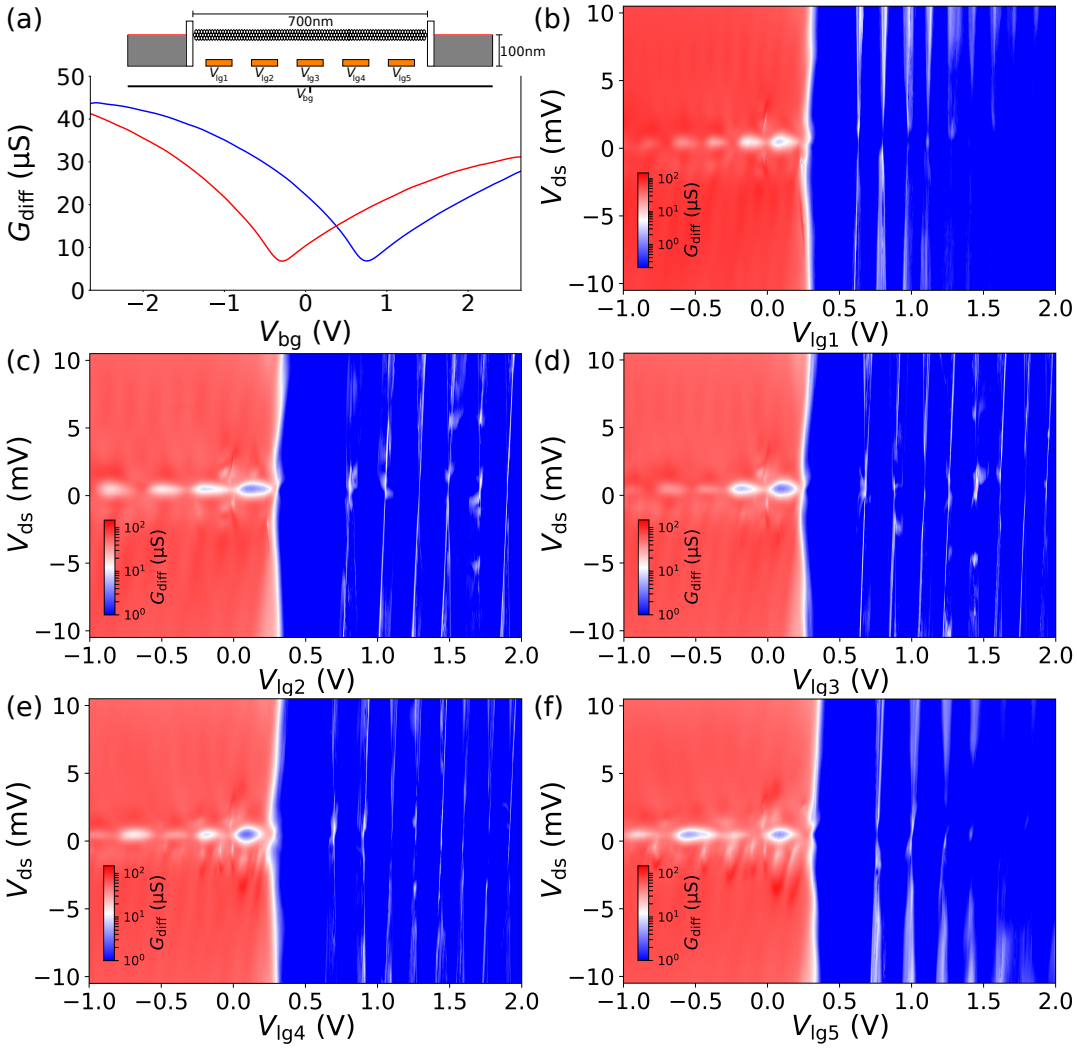

Figure 8.12: a) $G\,(V_{\mathrm{bg}})$ at room temperature for sample *CNT-s3-2018*. The device has the full control of 5 local gates. Moderate hysteresis is observed, similar to the discussion of the samples of generation 2. b-f) Single-gate conductance maps of the device for all 5 gates, measured at $T = 40\,\mathrm{mK}$, showing very similar electronic characteristics in all cases.

Again, distinct hysteresis is present in room temperature characteristics $G\,(V_{\mathrm{bg}})$ of fig. 8.12, which does not carry over to low-temperature measurements. We find very similar conductance, gap position and width as well as Coulomb diamond patterns for all 5 local gates, which verifies the clean properties and stable tunability of the CNT.

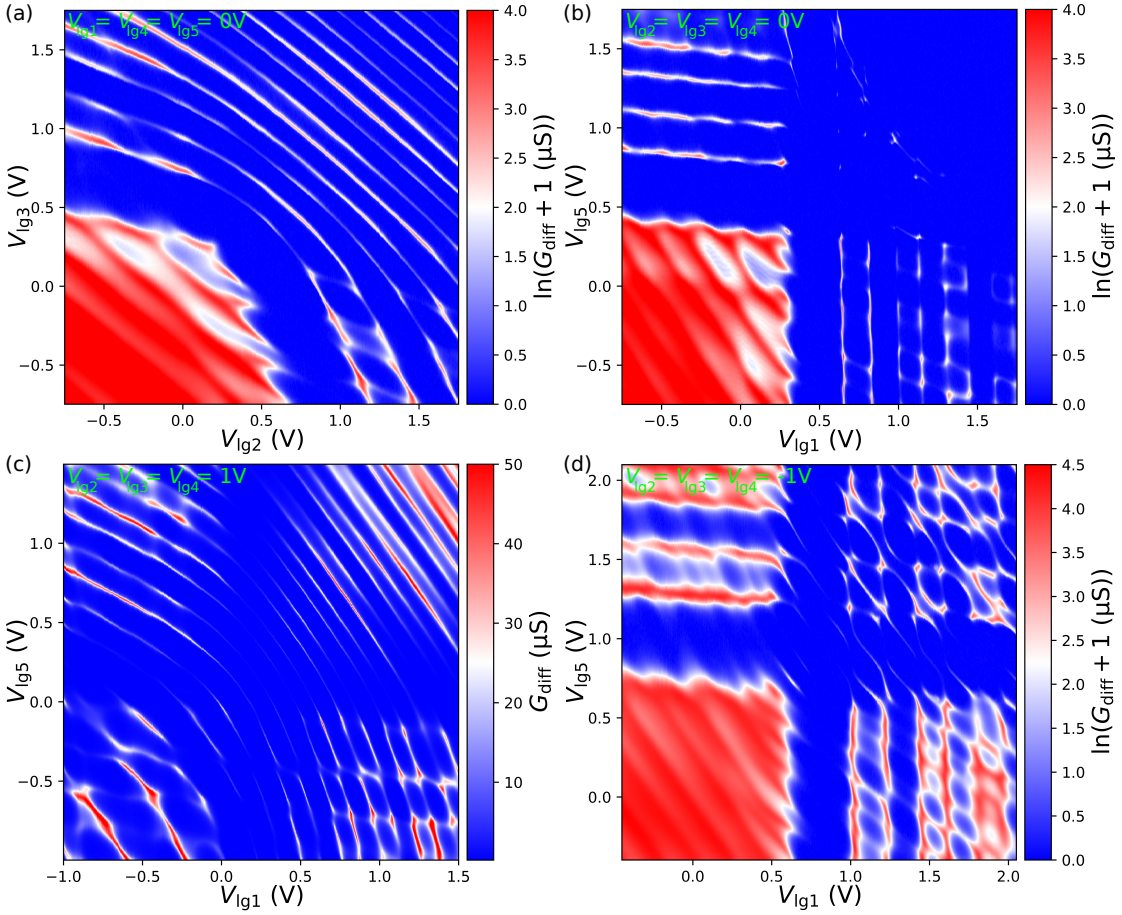

Figure 8.13: DQD configurations of sample *CNT-s3-2018*, which is again p-doped for $V_{\mathrm{g}} = 0\,\mathrm{V}$. a) For two nearby CNT segments, controlled by V_{lg2} and V_{lg3}, a strongly coupled (n,n) regime is observed. b) For two CNT segments at opposite ends of the CNT, controlled by V_{lg1} and V_{lg5}, pn-barriers in the middle govern a weakly-coupled (n,n) regime. c) With $V_{\mathrm{lg2}} = V_{\mathrm{lg3}} = V_{\mathrm{lg4}} = 1\,\mathrm{V}$ the coupling scenarios of (p,p) and (n,n) are reversed. c) With $V_{\mathrm{lg2}} = V_{\mathrm{lg3}} = V_{\mathrm{lg4}} = -1\,\mathrm{V}$ the coupling ressembles (b), but with increased conductance level.

In line with the presented case of the previous section, the characteristic DQD configurations of two adjacent (fig. 8.13a) and two spaced CNT segments (fig. 8.13b-d) are reproduced. The intrinsic p-doping of the CNT at $V_{\mathrm{g}} = 0\,\mathrm{V}$ gives rise to strong coupling in (p,p) for all cases without gate-induced pn-barriers. Only for n-doped middle segments with $V_{\mathrm{lg2}} = V_{\mathrm{lg3}} = V_{\mathrm{lg4}} = 1\,\mathrm{V}$ this is lifted (fig. 8.13c). In the (n,n) regime, strong coupling can be realized for exactly this case or for the choice of two nearby segments (fig. 8.13a) without any induced barriers.

As last case, one can study the most general DQD configuration with the controlled dots above V_{lg2} and V_{lg4} and tunable barriers above the remaining 3 separating CNT segments. Three possible configurations are shown in fig. 8.14. When no barriers are induced, $V_{\mathrm{lg1}} = V_{\mathrm{lg3}} = V_{\mathrm{lg5}} = 0\,\mathrm{V}$ (fig. 8.14a), the pattern of the 4 regimes strongly ressembles the case of fig. 8.13 with the exception that large positive voltages V_{lg2} and V_{lg4} can drive the (n,n) part into a strongly coupled state, which is a consequence of the comparably smaller lateral spacing of the two segments.
Here, a positive voltage on the segment separating the dots, $V_{\mathrm{lg3}} = 1\,\mathrm{V}$ (fig. 8.14b), reverses the coupling of mostly (p,p) and (n,n), while for negative voltage $V_{\mathrm{lg3}} = -1\,\mathrm{V}$ (fig. 8.14c) a strong pn-barrier is induced between the two controlled segments, which blocks the transition into a strongly coupled (n,n) regime at large positive voltages V_{lg2},V_{lg4} observed in the case of $V_{\mathrm{lg3}} = 0\,\mathrm{V}$.

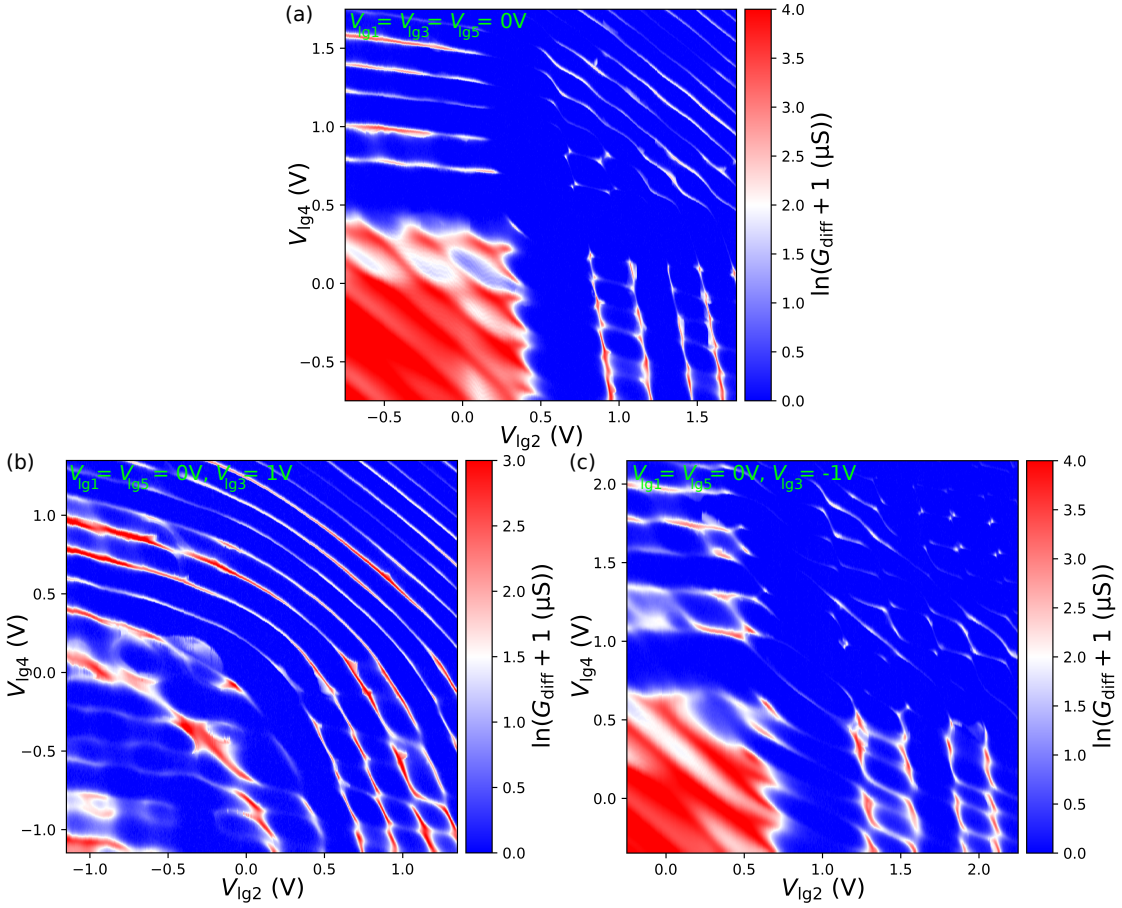

Figure 8.14: DQD configurations for V_{lg2} and V_{lg4}. a) $V_{\mathrm{lg1}} = V_{\mathrm{lg3}} = V_{\mathrm{lg5}} = 0\,\mathrm{V}$ creates strongly coupled (p,p) and weakly coupled (n,p), (p,n) and (n,n) regimes. For large enough positive voltages, the weak coupling in (n,n) is lifted. b) With $V_{\mathrm{lg3}} = 1\,\mathrm{V}$ the coupling of (p,p) and (n,n) is reversed. c) With $V_{\mathrm{lg3}} = -1\,\mathrm{V}$, the induced pn-barrier between the dots hinders a regime of strong coupling for larger voltages in (n,n).

Finally, two possible coupling scenarios resulting from voltages on all 5 local gates are presented. When an additional $V_{\mathrm{lg1}} = V_{\mathrm{lg5}} = 1\,\mathrm{V}$ is applied, the strong coupling in (n,n) of fig. 8.14b is preserved, but the addional barriers at the outmost segments drive the (p,p), (n,p) and (p,n) regimes in a more weakly coupled configuration. Switching the middle barrier with $V_{\mathrm{lg3}} = -1\,\mathrm{V}$ decouples (n,n) and slightly increases coupling in (p,p). The clear DQD charge states in the entire voltage range is pointed out, which is similar to the presented case Steele et al.[135] in fig. 2.18. This scenario is also similar to the one of fig. 8.9, where the reduced number of working local gates was compensated with the global back gate of the device.
The back gate constitutes another available parameter to tune the device, which was however not used here. It is also pointed out that for the presented measurements fixed values of $V_{\mathrm{g}} = \pm 1\,\mathrm{V}$ were applied to the barrier segments. This was done in order to simplify the discussion on possible coupling scenarios, but generally there is no restriction to these particular values. A variable choice of the barrier voltage should allow for a more continuous tuning of the configurations and their coupling.

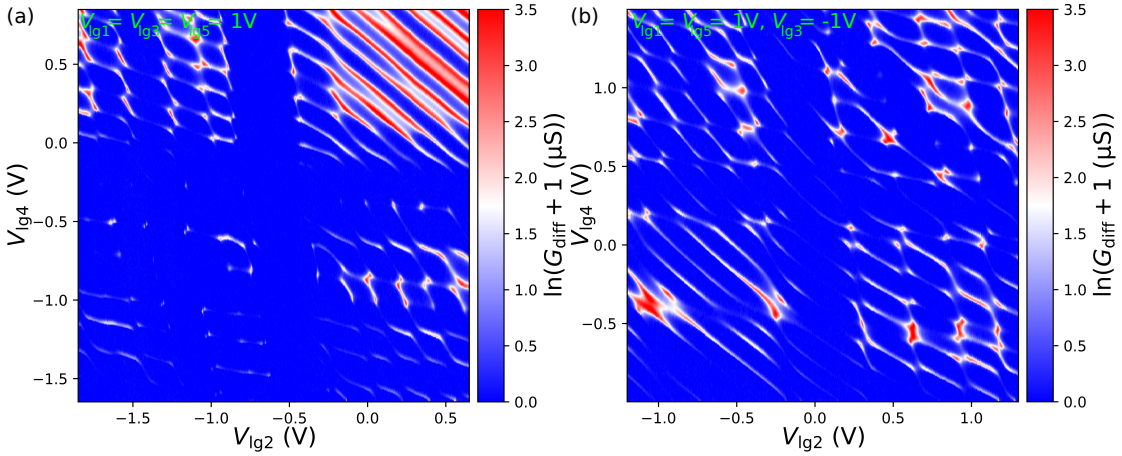

Figure 8.15: DQD configurations for V_{lg2} and V_{lg4} for the use of all 5 local gates. a) $V_{\mathrm{lg1}} = V_{\mathrm{lg3}} = V_{\mathrm{lg5}} = 1\,\mathrm{V}$ decouples (p,p), (n,p) and (p,n) more strongly. b) Switching of $V_{\mathrm{lg3}} = -1\,\mathrm{V}$ creates weak coupling in all 4 regimes.

To summarize the presented measurements of this section, we have shown that the developed fabrication technique allows us to realize clean CNT devices with a maximum of 6 gate control parameters, the 5 small local gates and the back gate of the substrate. Particularly the local gates enable efficient and leakage-free tuning of the electronic configuration via the transition from p- to n-type charge states of the CNT and hence allow for realization of a large variety of DQD systems with different coupling scenarios. In detail, we can control (p,p), (p,n), (n,p) and (n,n) charge configurations. The DQD can be created with arbitrary local gate pairs and the expected coupling holds for DQD over the entire device length. The remaining gate parameters can be used to induce pn-barriers and by this freely modify the coupling of the charge configurations or control the conductance levels of the CNT.

9 Proximity-Induced Superconductivity in SnTe Topological Crystalline Insulator

In this chapter the experimental results on induced superconductivity effects in SnTe are presented. First of all, the characteristics of proximity coupling in our system is characterized in terms of parental superconducting materials Nb and Ta, temperature dependence, spatial dimensions of the SnTe weak links and perpendicular magnetic fields. As our weak antilocalization measurements, discussed in sec. 6.1.2, indicate the presence of topological surface states, measures to elicit their impact in the abovementioned regime are investigated and discussed. In this context, the effect of rf irradiation and electrostatic gating is discussed.
In the second part the current-phase relation of the weak links, obtained from phase-sensitive measurements, is discussed within the concept of kinetic inductance. Finally, the effect of applied in-plane magnetic fields on CPR and SQUID behaviour is investigated, indicating the occurrence of unconventional superconducting pairing in SnTe devices.

9.1 Characterization of SnTe/Nb and SnTe/Ta Hybrid Devices

This section is dedicated to the characterization studies of induced superconductivity in SnTe. The experimental data presented within is almost exclusively gained from measurements in the *Diluette* cryostat, consisting of transport measurements supported by magnetic fields and rf irradiation.

9.1.1 SnTe/Nb Hybrid Devices

Dependence of Induced Superconductivity on Temperature and Junction Length

As first measure, a series of samples based on 40 nm SnTe covered by 30 nm of Nb superconductor was investigated. These devices were patterned as SQUID rings with an average area of $\approx 4 \times 4\,\mu\mathrm{m}^2$ with the SnTe still present on the entire surface, as shown in fig. 9.1a. Current-biased 4-point measurements, along the lines of the principles explained in sec. 7.4, were performed to obtain $R_{\mathrm{diff}}(I)$ curves at different temperatures for samples with different junction lengths, later on also assisted by magnetic fields. The notion of R_{diff} stems from the differential lock-in measurement technique, but, for the sake of simplicity, will be mostly denoted less formally as *resistance* R.
Induced superconductivity expresses itself as a state of $R = 0\,\Omega$ in the originally resistive device, with critical temperature T_{c} and critical current I_{c} strongly dependent on the explicit material system and interface quality, but also spatial dimensions. Originally,

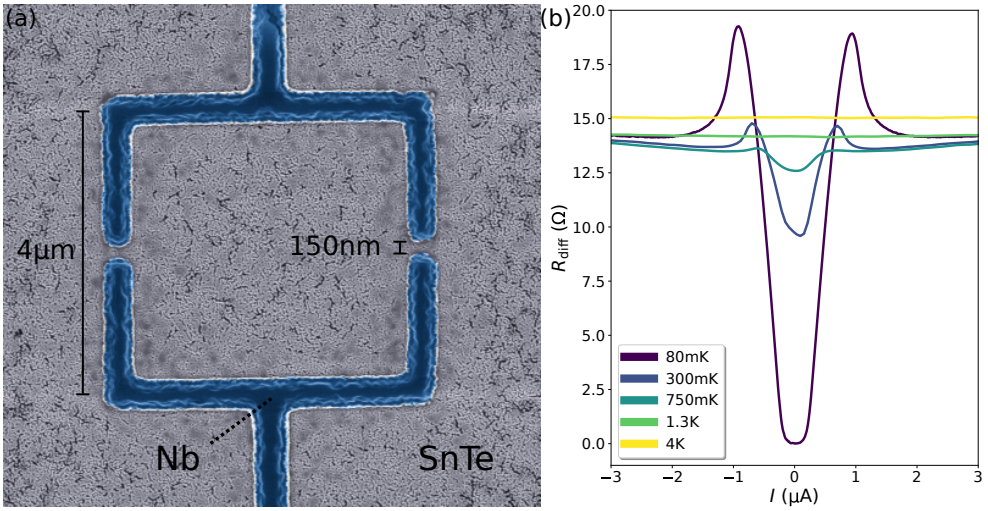

Figure 9.1: a) False color SEM image of a typical SnTe/Nb SQUID device of area $A \approx 4 \times 4\,\mu\mathrm{m}^2$, where the Nb is patterned on top of SnTe (grey). b) Resistance measurement at different temperatures, showing the transition from resistive to fully superconducting state for a sample of junction length $L = 150\,\mathrm{nm}$. A fully superconducting state is only realized for $T =\leq 80\,\mathrm{mK}$.

the concept of interface *barrier strength* was introduced to describe such physics [229]. In the case of our SnTe/Nb thin films we observe a transition to a proximity-induced superconducting state in SnTe just at temperatures well below $T_c^{\mathrm{Nb}} = 5.8\,\mathrm{K}$ of the bare Nb films, starting at $T \approx 1.3\,\mathrm{K}$, with $R = 0\,\Omega$ only manifesting itself after sufficient thermalization at $T \leq 80\,\mathrm{mK}$, as shown in fig. 9.1b.

Both the presence of a zero-resistance state and the magnitude of I_c was found to strongly depend on the junction length L, as resistance measurements at 80 mK in fig. 9.2 indicate. For a comparably long junction of $L = 200\,\mathrm{nm}$, a small dip in R around zero current is visible, but a high resistance $R \approx 55\,\Omega$ is preserved. For the three junctions with $L \leq 150\,\mathrm{nm}$ a fully superconducting state is observed. Comparing these characteristics to the phase coherence length $l_\Phi \approx 120\,\mathrm{nm}$ obtained from the WAL measurements (see chapter 6), one can conclude a likely correlation between the occurrence of induced superconductivity and the coherence of surface currents in the normal state.

For the junctions with $L = 150\,\mathrm{nm}$ and $L = 120\,\mathrm{nm}$ similar behaviour is observed, as both devices have $I_c \lessapprox 1\,\mu\mathrm{A}$. These values are in line with results of other groups, for instance the presented work of Snyder at al. [269] on MBE-grown PbSnTe/Al devices. Interestingly, the transition does not manifest itself as a sharp peak, but rather a broad one that is tilted outwards. Comparable line shapes have been observed in other topological matter [304], surmised to indicate contribution of non-s-wave coupling. More cautiously, such effects could stem from the participation of several SnTe bands and hence different induced superconducting gaps for junctions $L \approx l_\Phi$.

One can estimate the induced gap with the Ambegaokar-Baratoff relation [305] as $\Delta_{\mathrm{SnTe}} = 2eI_cR_n$, which gives 3.4 µeV and 6.4 µeV for the two junctions of 150 nm and 120 nm. Those values are very small, but the used relation often tends to underrate the gap and

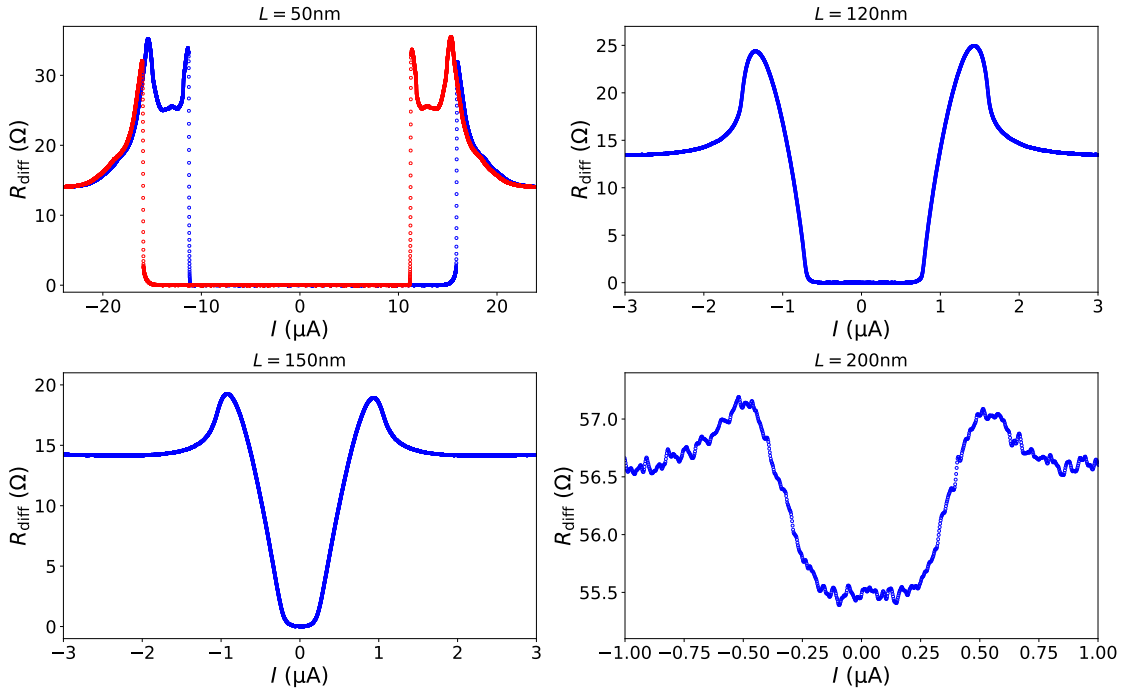

Figure 9.2: Resistance measurement of 4 Nb-based devices of different junction length L at $T = 80\,\mathrm{mK}$, showing a fully superconducting state only for $L \lessapprox 200\,\mathrm{nm}$. Upon reducing L to $50\,\mathrm{nm}$, an enhancement of the critical current is observed. A higher R_n of the $200\,\mathrm{nm}$ sample is noted. Due to the existing but not profound dip in R we attribute this to finite contact resistance of this particular measurement.

is originally introduced for SIS junctions, so it cannot provide more than a rough idea. In this context, the normal state resistance R_n should be looked at more closely, for instance at the example of fig. 9.1. At $T = 4\,\mathrm{K}$ we have $R_\mathrm{n} \approx 15\,\Omega$, which is not fully restored at $T = 80\,\mathrm{mK}$ directly after the transition into the normal state. There is hence bulk superconducting material that remains in a $R = 0\,\Omega$ state for comparably still small currents. On the other hand, the plateau of $R_\mathrm{n} \approx 13.5\,\Omega$ is too large to be made up by the weak links only, which indicates that switching of the weak links and the smaller Nb structures, probably the ring, occurs simultaneously. Due to the unknown current distribution in the global SnTe layer, it is not possible to properly estimate the weak link contribution to R_n in these samples.

Features arising due to possible contribution of topological surface states to the transport should be most prominent for $L \ll l_\Phi$. The first conspicuous property of the junction with $L = 50\,\mathrm{nm}$ is a significantly increased I_c, as well as a pronounced hysteresis effect, which was entirely absent in other samples. Due to the relatively large critical current, this hysteresis is most likely of thermal origin, as self-heating effects lower the retrapping current in such mesurements, an effect commonly observed in proximity-coupled metal junctions[306]. A more peculiar feature is the additional peaks appearing at the flanks of the transition. Hashimoto et al.[307] theoretically predicted the appearance

of mirror-protected surface ABS, hosted in superconducting TCI on the (001) surface if an unconventional odd-parity superconducting potential is realized. However, no direct conclusion can be drawn from our current-biased measurements, as these characteristics would need to be verified by scanning tunneling spectroscopy in order to be precisely related to the specified case. As the mentioned peaks only occur for decreasing current, a two-step retrapping due to asymmetry in the device arms or due to separate transitions for weak links and Nb ring, in line with the considerations above, is a much more probably explanation for the measured effect.

Magnetic Field Dependence

Following this first characterization of superconducting properties, we investigated the response of the patterned SQUIDs to perpendicular magnetic fields B_z. As it has been introduced in sec. 4, particularly in eq. 4.16, such a scenario should give rise to oscillations of the critical current I_c with magnetic flux quanta Φ_0 threaded through the loop.
In fig. 9.3 these measurements are shown for the $L = 150\,\mathrm{nm}$ device, demonstrating clear oscillations over a large range in the top panel. On the other hand, no higher-order Fraunhofer peak, corresponding to a slower periodicity of the envelope function, are observed in the field range $B_z \leq 15\,\mathrm{mT}$, beyond which the oscillations break down abruptly, indicating the suppression of induced superconductivity in SnTe and possibly related to self-field effects in the relatively large junction area of these devices. Similar effects will be discussed for Ta-based samples in more detail.
The periodicity of the fast SQUID oscillations is given by $\Phi_{SQ}/\Phi_0 = A\Delta B_z/\Phi_0$, which is dependent on the SQUID ring area A. For conventional 2π-periodic oscillations and the given loop area $A \approx 4 \times 4\,\mu\mathrm{m}^2$, one would thus expect a field modulation of $\Delta B_z \approx 125\,\mu\mathrm{T}$, while the case of 4π-periodic transport governed by topological surface states would give rise to 250 mT modulation. In the case of both types contributing, a superposition of predominant 2π-character would arise. However, as it was explained in sec. 4.2.3, DC measurements are expected to gap out potentially present 4π-periodic modes, since such as setting does not conserve the parity of surface states.
The lower panel of fig. 9.3 verifies that transport in our system in this measured DC regime follows indeed purely the conventional 2π-characteristics, showing no sign of topological surface state contribution. This is not very astonishing, since significant shunting of possible topological transport by bulk channels can be expected, according to our previously presented characterization studies, making 2π-contributions the entirely dominating part. Further poisoning of possibly occurring quasiparticles governing 4π-periodic transport via surface states is to be expected, explaining the observed pattern. Similar results[1] were obtained for the device with $L = 120\,\mathrm{nm}$, shown in the appended article "Proximity-Induced Superconductivity and Quantum Interference in Topological Crystalline Insulator SnTe Thin-Film Devices".

1 Strangely, the transition of the $L = 50\,\mathrm{nm}$ device was not found to be sensitive to SQUID modulation.

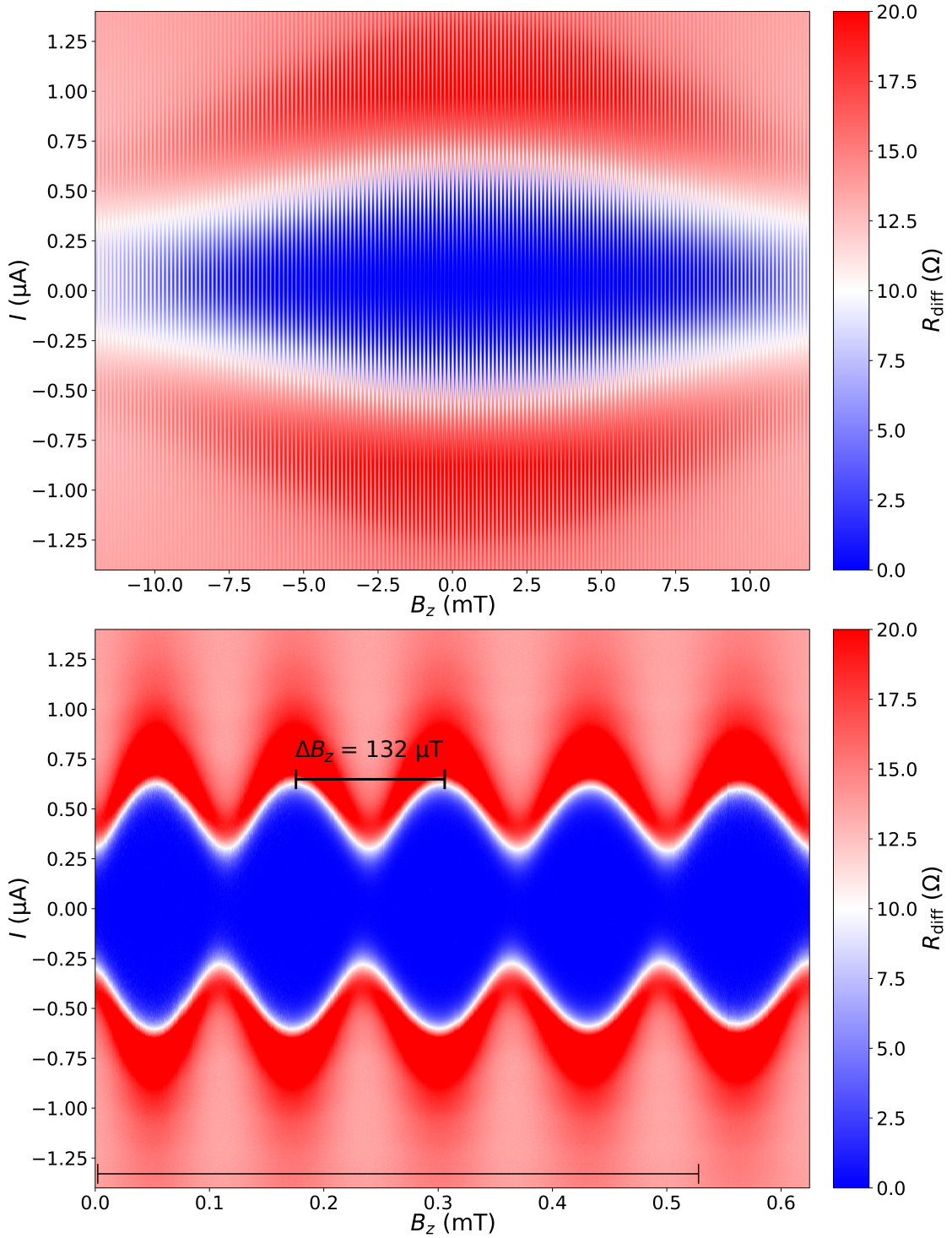

Figure 9.3: Resistance map showing the response of the SQUID from fig. 9.1 to applied perpendicular magnetic fields. The superconducting state persists in the blue area, separated from the normal resistive state (red). Top) SQUID oscillations are observed over a large range of field B_z. Bottom) Close-up on the fast SQUID oscillations, where the data is slightly offset. The pattern follows a perfect 2π-periodic field modulation of $\Delta B_z \approx 132\,\mu\mathrm{T}$, showing no evidence of topological surface state contribution.

These results are consistent with observations of other groups for different topological matter, for instance 3D HgTe[308] or Bi_2Te_3[309]. In fact, so far no evidence of topological transport in such type of experiments has been found. Yet, the measured robust proximity-induced superconductivity with distinct zero-resistance state in these topological devices is an important demonstration, which can be seen as starting point for further investigation of this material system.

9.1.2 SnTe/Ta Hybrid Devices

From here on we turn towards devices with Ta as parental superconducting material. This change was initially done by virtue of technical problems of the Nb deposition, on the grounds that Ta is known to be less prone to chemical degradation. All correctly patterned Ta devices, fabricated in a time span of about one year, did indeed show superconducting behaviour. At the same time, the fabrication pattern was changed to restrict the SnTe to only small patches at the junction areas by a second step of dry etching, in order to reduce possible disturbing influence of current trajectories passing the SQUID loop itself. The results presented in this section are mostly based on the device shown in fig. 9.4, consisting of 40 nm SnTe and 30 nm of Ta, but similar characteristics were obtained for several very similar samples.

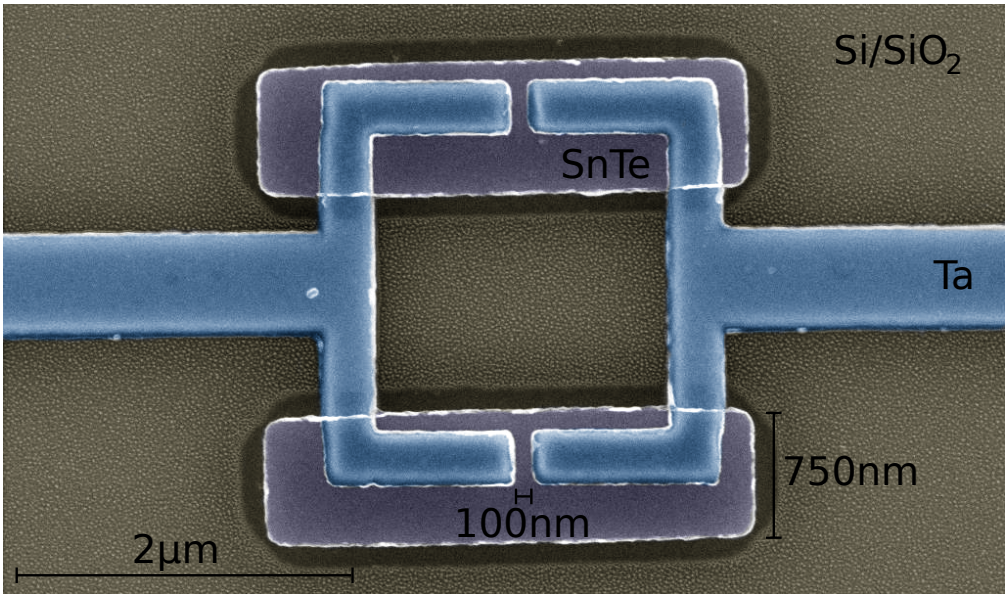

Figure 9.4: False color SEM image of a typical SnTe/Ta SQUID device of area $A \approx 2 \times 2\,\mu\mathrm{m}^2$, where the SnTe is constricted to patches forming the junctions.

Evaluation of the Temperature-dependent Multi-valued Switching

In fig. 9.5 $R(I)$ measurements are presented over a wide range of temperatures. First of all, normal state resistances $R_\mathrm{n} \approx 340\,\Omega$ are obtained at temperatures above the

transition of Ta, here illustrated for $T = 2.6\,\mathrm{K} > T_\mathrm{c}^\mathrm{Ta}$, significantly larger than $R_\mathrm{n} \approx 15\,\Omega$ of the Nb-based samples (fig. 9.1). While a part of this can be explained by slightly modified dimensions of the SQUID arms as well as the changed material, it is nevertheless reasonable to assume reduced contributions of leakage currents via the now removed SnTe surface.

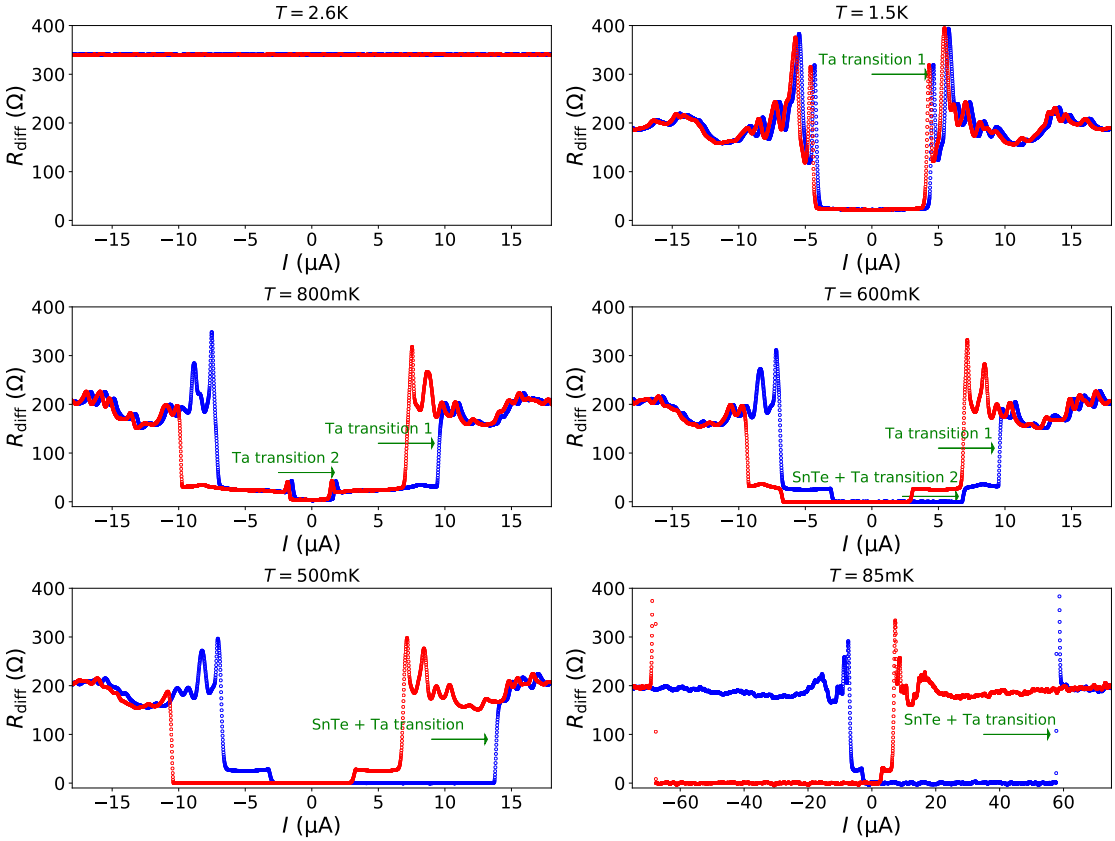

Figure 9.5: Evolution of $R(I)$ with temperature for the sample of fig. 9.4. The transition of Ta, observed at $T = 1.5\,\mathrm{K}$, is slightly lowered by the presence of SnTe and the patterning with respect to the bare films. However, the device resistance remains finite. Below $T = 800\,\mathrm{mK}$ a second transition with moderate I_c can be observed, which we attribute to the smaller SQUID ring. At lowest temperatures, I_c increases drastically and only one switch occurs. Due to the large I_c, dissipated heat breaks superconducitivity in the Ta extending beyond the SQUID ring.

A first transition into a low-resistive state is observed for $T \gtrapprox 1.5\,\mathrm{K}$. As this transition does not realize $R = 0\,\Omega$ it is attributed to larger Ta structures, while the current density in the finer structures is still bigger than the critical current density, hence preserving a finite resistance of the device. Again, the normal resistance of $R_\mathrm{n} \approx 340\,\Omega$ is not yet restored in the presented current range, indicating that the biggest Ta structures remain superconducting. At $T \gtrapprox 800\,\mathrm{mK}$ a second transition is observed and the one of Ta has shifted to $I_\mathrm{c} \approx 10\,\mu\mathrm{A}$. In this temperature range we obtain $R = 0\,\Omega$, as can be seen more easily in the left panel of fig.9.6. This transition will be discussed in more detail shortly.

Upon cooling further, these two mentioned transitions begin to merge and a tremendous increase in proximity coupling is observed, represented by critical currents reaching values of $60\,\mu\mathrm{A}$ at $T = 85\,\mathrm{mK}$ in the mentioned device and even more ($\geq 100\,\mu\mathrm{A}$) in others. The jump into a resistive state then appears as one pronounced peak without further distinct features, but the large I_c gives rise to huge thermal hysteresis effects. At this point, the created heating power $P_\mathrm{n} = R_\mathrm{n} I_\mathrm{c}^2$ cannot be dissipated quickly enough anymore[1], leading to the switch that extends beyond the SQUID ring into the bulk Ta.
This high I_c in comparison to Nb is puzzling, since the *strength* of proximity-induced superconductivity should to a large extent depend on T_c of the parental material and $T_\mathrm{c}^\mathrm{Nb} > T_\mathrm{c}^\mathrm{Ta}$. However, these values were measured for bare films and Nb tends to undergo chemical modifications, which could be more pronounced at interfaces with SnTe, for which already moderate temperatures can induce degassing processes. On the other hand, the measured I_c is also very high in comparison to other material systems in the same field, indicating that the interface barrier, created by scattering due to mismatch of band structure or impurities, is very low in our multilayers. Yet, a high I_c, albeit being indicative of very good coupling, is detrimental to our measurements, as thermal hysteresis masks interesting effects. Several of the subsequently presented measurements are thus conducted at $500 - 700\,\mathrm{mT}$ in order to counter this issue, which certainly constitutes a trade-off in terms of induced thermal broadening. Furthermore, this range coincides with the second transition of the small SQUID parts, which exhibits some peculiar details.

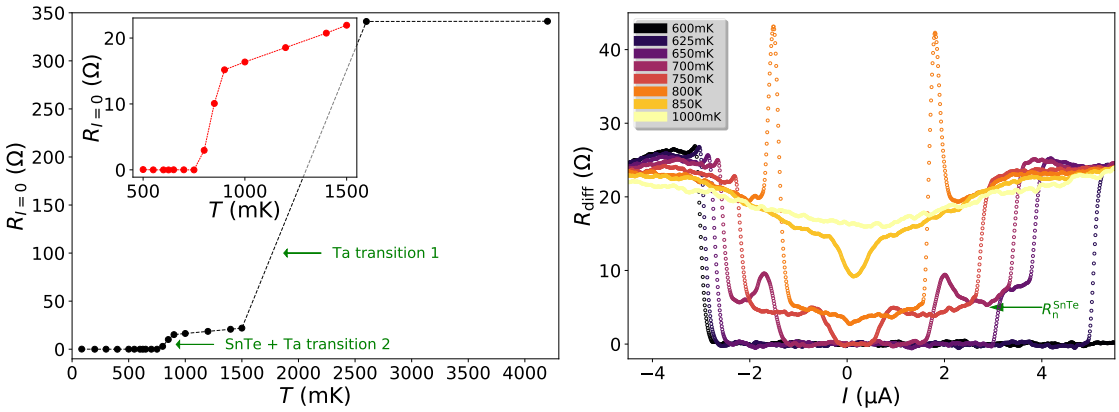

Figure 9.6: a) Resistance at $I = 0$ for temperatures $T \leq 4\,\mathrm{K}$, highlighting the two larger transitions, which are attributed to the bulk Ta and the smaller SQUID structures. The inset is a zoom on the SQUID transition. b) Close-up on the $R(I)$ curves of the second transition. A third smaller transition occurs at $T = 750\,\mathrm{mK}$ which is attributed to the weak link only. For $T \lessapprox 650\,\mathrm{mK}$ this transition merges with the one of the Ta ring.

In the right panel of fig. 9.6 a close-up the $R(I)$ curves in the mentioned range is shown. Interestingly, the already discussed transition at $T = 800\,\mathrm{mK}$ still does not

1 This effect should be enhanced by the etching of the excess SnTe

create $R_\mathrm{n} \approx 0\,\Omega$, and, just as it was the case for the Nb devices, the resistance plateau of $22 - 25\,\Omega$ is higher than expected values for the SnTe weak links only. We hence attribute this to remaining contributions of the Ta, probably the SQUID ring, switching simultaneously with the junctions.
Just below, at $T = 750\,\mathrm{mK}$, a very small third transition appears, now leading to $R = 0\,\Omega$ and a resistance plateau of $5\,\Omega$. As weakest of the contributions towards a fully superconducting state, this transition should correspond to the SnTe weak link, $R_\mathrm{n}^\mathrm{SnTe} = 5\,\Omega$. This claim is supported by expected resistances of $R \approx 10\,\Omega$ for one SnTe patch, as can be calculated from the low temperature resistivity $\rho_\mathrm{SnTe} \approx 3\,\mu\Omega\mathrm{m}$ (see fig. 6.3a) for a structure of 750 nm width, 100 nm length and 40 nm thickness. For the parallel circuit of two SQUID arms, this corresponds very well to the measured plateau of $5\,\Omega$. However, the transition attributed to the weak link only persists in a narrow temperature window and merges quickly with the one of Ta upon decreasing T.
In any case, the concept of R_n cannot be treated carelessly, as the finer features of these measurements ressolve.

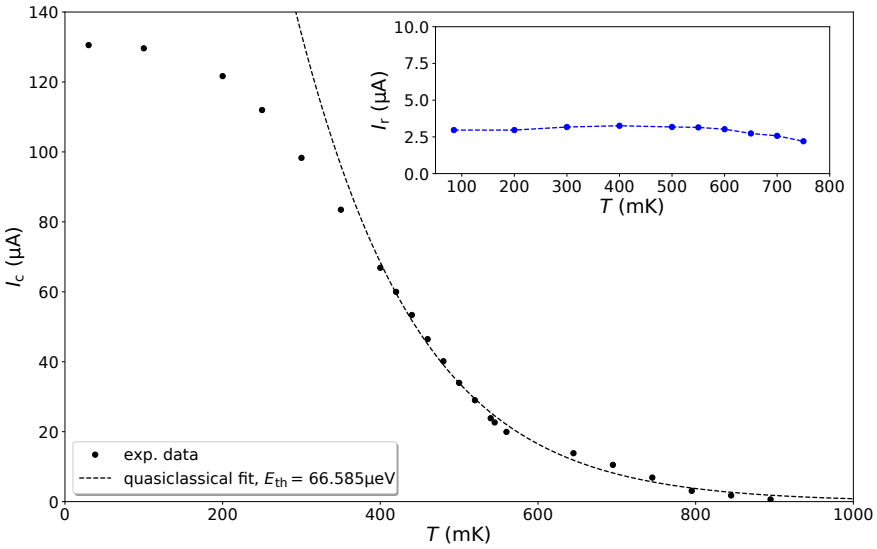

Figure 9.7: $I_\mathrm{c}(T)$ data extracted from the measurements in the *Sionludi* cryostat. The I_c data is shifted about 150 mK with respect to the *Diluette* cryostat data presented before due to lower thermal noise. For $T \geq 300 - 400\,\mathrm{mK}$ a reasonable agreement with the quasiclassical model of eq. 9.2 is obtained, which allows the estimation of the Thouless energy $E_\mathrm{th} \approx 70\,\mu\mathrm{eV}$. The inset shows the retrapping current I_r, which is almost constant at low temperatures.

Evaluation of the Transport Regime

The junctions of the sample from fig. 9.4, a representative example for the measured specimens, constitute the case of length $L \approx 100\,\mathrm{nm}$ and width $W = 750\,\mathrm{nm}$ of the entire SnTe flake. Even if the supercurrent distribution over the junctions and hence the effective junction width might be slightly limited by the 300 nm wide Ta electrodes, clearly a case of $W > L$ is realized. However, the influence of the width should mostly

show up in magnetic field measurements as modification of the Fraunhofer pattern and the transport will be determined by L.
In contrast to the Nb samples, for which induced superconductivity broke down for devices with $L > 150\,\mathrm{nm}$, no such limitation is observed for Ta. We measured samples up to $L = 400\,\mathrm{nm}$ (for instance the second junction of fig. 9.10, discussed for magnetic field response later) with no qualitative difference, indicating that fully gapped superconductivity in the SnTe/Ta hybrids is present for (much) larger length scales.
Generally, transport in mesoscopic SNS junctions can be classified by two limiting cases, ballistic transport in the clean limit and diffusive transport in the disordered limit. The clean limit can be described by an N channel model of Beenakker [310], but even for a maintained bulk gap [311] $2\Delta_{\mathrm{Ta}}(0) = 1.3 - 1.4\,\mathrm{meV}$, a high number of channels $N \geq 200$ is required to reproduce our measured order of magnitude in I_{c}. Validity of ballistic transport can only be assumed for few contributing channels, as it is regularly the case for nanowire junctions of high quality [312]. Due to the large bulk contribution in our samples, this scenario is hence very unlikely. The diffusive case is often approached with the (linearized) Usadel equations [313] [312], but does not converge on a solution with realistic parameters here. This should, however, not dismiss the possibility of diffusive transport in our system.
In order to determine if the devices are in the *short junction* regime $L \ll \xi_{\mathrm{N}}$ or *long junction* regime $L \gg \xi_{\mathrm{N}}$, the superconducting coherence length in the normal region needs to estimated with $\xi_{\mathrm{N}} = L\sqrt{(E_{\mathrm{th}}/\Delta)}$. This is equivalent to the perception of the smallest energy scale of the system determining the characteristics [314], either the (induced) superconducting gap Δ or the Thouless energy E_{th}. Despite being introduced as a quasiclassical theory for disordered systems, E_{th} was found to be the predominant characteristic for many mesoscopic systems, SNS Josephson junctions amongst others [315]. It can also describe, to some extent, the quantum mechanical regime of ballistic transport in such systems [316].
To derive E_{th} one can evaluate the $I_{\mathrm{c}}(T)$ dependence, plotted in fig. 9.7. SNS junctions dominated by bulk-shunted transport are often well described by [317]:

$$I_{\mathrm{c}}(T) \propto \sqrt{T}\exp\left(-\frac{2\pi k_{\mathrm{B}}T}{E_{\mathrm{th}}}\right). \tag{9.1}$$

Application of eq. 9.2 to our data results in a reasonable fit for $T \geq 300\,\mathrm{mK}$ and $T \geq 400\,\mathrm{mK}$ for the respective data sets, which is acceptable under the premise that the model loses its validity for lowest temperatures $k_{\mathrm{B}}T < E_{\mathrm{th}}/2\pi \propto 130\,\mathrm{mK}$ anyhow. One can extract E_{th} as $\approx 70\,\mu\mathrm{eV}$ from this analysis, which is in the same order of magnitude as for other topological matter with bulk-shunted transport [318].
The superconducting gap of a *s*-wave BCS superconductor like Ta can be calculated as $\Delta = 1.76 k_{\mathrm{B}}T_{\mathrm{c}} \approx 380\,\mu\mathrm{eV}$ for a transition temperature $T_{\mathrm{c}} \approx 2.5\,\mathrm{K}$. We hence find $\Delta/E_{\mathrm{th}} = 5.4$ and $\xi_{\mathrm{N}} \approx 40\,\mathrm{nm}$, which places our junctions in the (moderate to) *long* regime. One can also point out the corresponding temperature equivalent of $E_{\mathrm{th}} \propto 800\,\mathrm{mK}$, which coincides with the transition temperature of our SnTe weak links.

It is noted, that the retrapping current is almost constant at temperatures below 750 mK with $I_r \approx 3\,\mu A$. Such a plateau was explained with combined admittance effects for SIS junctions[319], here we expect it to be mainly of thermal cause: As introduced in sec. 4.1.3, large hysteresis $I_c/I_r \approx RC\omega_p \gg 1$ in SIS junctions can be observed for large RC products. According to Angers et al.[320] one can derive an equivalent expression for SNS junctions from the RSJ model as $I_c/I_r = \sqrt{(2eR_nI_c/E_{th})} \equiv Q$. Here we get $Q \approx 4.3$, while the measurement at $T = 30\,mK$ yields $I_c/I_r \approx 43$, rising the conclusion that thermal effects lower the intrinsic retrapping current, even though intrinsic hysteresis may still be present.
In the table below some characteristic values of the described sample are summarized.

L(nm)	W(nm)	Δ(μeV)	E_{th}(μeV)	ξ_N(nm)
100	750	380	70	40

Dependence of Induced Superconductivity on Layer Thickness

Finally, we also measured devices of different SnTe film thickness. Fig. 9.8 presents the $R(I)$ curves at $T = 80\,mK$ of three such layers of 20 nm, 40 nm and 70 nm. Interestingly, the strength of induced superconductivity appears to be strongly reduced for the thinnest among these layers, considering the magnitude of I_c, while the thickest one has even $I_c \geq 150\,\mu A$.

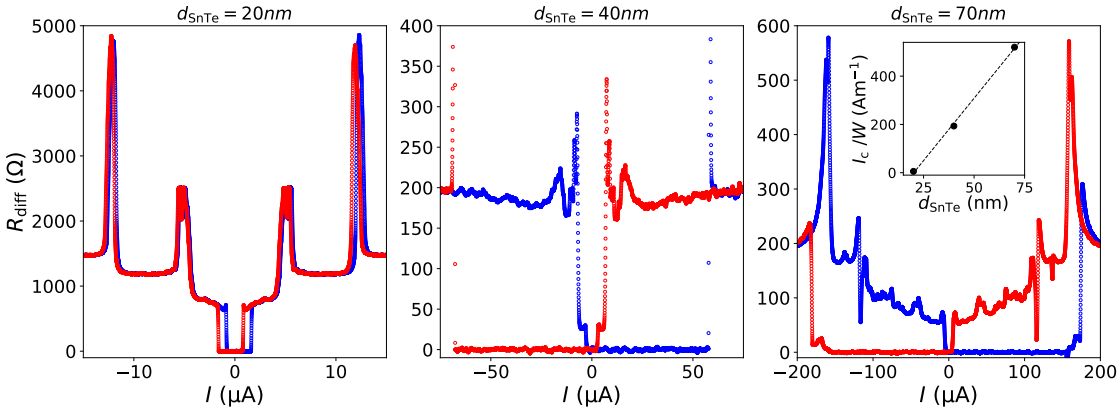

Figure 9.8: $R(I)$ curves for 3 layers of different thickness d_{SnTe}. A strong increase of I_c with d_{SnTe} is observed. The inset shows the linear evolution of the ratio $\frac{I_c}{W}(d_{SnTe})$. The increase of critical current with d_{SnTe} thus appears to be of bulk origin, but a lower limit for breakdown of induced superconductivity may nevertheless exist.

It remains ambiguous whether this reduced coupling is purely a result of modified bulk parameters of SnTe, for instance charge carrier density n, or partly an influence of topological states, as critical minimum thicknesses for the preservation of topology in such systems are commonly observed[208] [209]. Bearing in mind the rather high amount of bulk carriers in our system, the former is more likely to be the case. This claim is supported by the evolution of $\frac{I_c}{W}(d_{SnTe})$, with $W \approx 300\,nm$ being the width of the

junctions, which appears linear and thus indicates a constant critical current density, albeit for a small statistical sample size. Nevertheless, adjustments of the layer thickness also seem to be a viable option to modify the conditions of induced superconductivity in these systems.

Magnetic Field Dependence

As for previous Nb-based samples, the magnetic field response was investigated. In line with the reasoning provided before, these measurements were mostly carried out at elevated temperatures, here $T = 625\,\mathrm{mK}$ for the sample of fig. 9.4. Again, SQUID oscillations persist over a wide range in applied perpendicular field[1] A field modulation of $\Delta B_z \approx 500\,\mathrm{mT}$ is expected for purely 2π-periodic behaviour and the corresponding SQUID area. As shown in the lower panel of fig. 9.9 and similar to the case of Nb, also the Ta-based devices clearly exhibit such characteristics.
For comparably small values of $B_z \lessapprox \pm 10\,\mathrm{mT}$, transitions into the resistive state at I_c happen simultaneously for both the SnTe weak link and parts of the Ta structures. According to the zero-field $R(I)$ sweeps and corresponding normal state resistance as well as switching current values for the respective temperature regime, this Ta is assigned to the (extended) SQUID ring.
As the temperature of the measurement is just slightly below the small transition of SnTe (see fig. 9.6b), increased values of B_z induce a split-up of the switching. The first small transition obeys the 2π-periodic SQUID pattern, while the second transition into the $R \approx 22\,\Omega$ state is insensitive to magnetic modulation other than a gradual suppression of I_c. The resistance of $R = 5\,\Omega$ at the white plateau just after the first switch gives strong evidence, that this trasition can indeed be assigned to the weak links only.
We interpret this behaviour as instantaneous heat avalanche which switches the nearby Ta structures in case of switching at large critical currents, which is generally the case for low temperatures or for higher temperatures and small fields. For switching at small I_c, the heat can be dissipated in the Ta structures without causing a transition to a resistive state of the latter.
Interestingly, the oscillation pattern shows strongly reduced modulation depth, ressembling the scenario of asymmetric junctions $I_{\mathrm{c}1} \neq I_{\mathrm{c}2}$, as it was introduced in fig. 4.4. Similar observations can be made for the Nb sample of fig. 9.3. While deviations of the fabrication process on the nanoscale are unavoidable, our approach should yield rather symmetric devices which do not possess such significant asymmetry to produce the observed patterns. This is further supported by the fact that the entire ensemble of measured equivalent[2] SQUID devices does not differ more than a factor of 2 in I_c. It is hence reasonable to look for explanations of this effect beyond geometric influences. We assess this feature as first distinctive mark of large kinetic inductances in our devices, which will be discussed in more detail in sec. 9.2.

1 Measurements at $T = 80\,\mathrm{mK}$ also showed SQUID oscillations, but a much more ragged pattern. Also, just one switching current is observed in this case.
2 This notion refers to the layer thickness of SnTe and the SQUID ring dimensions.

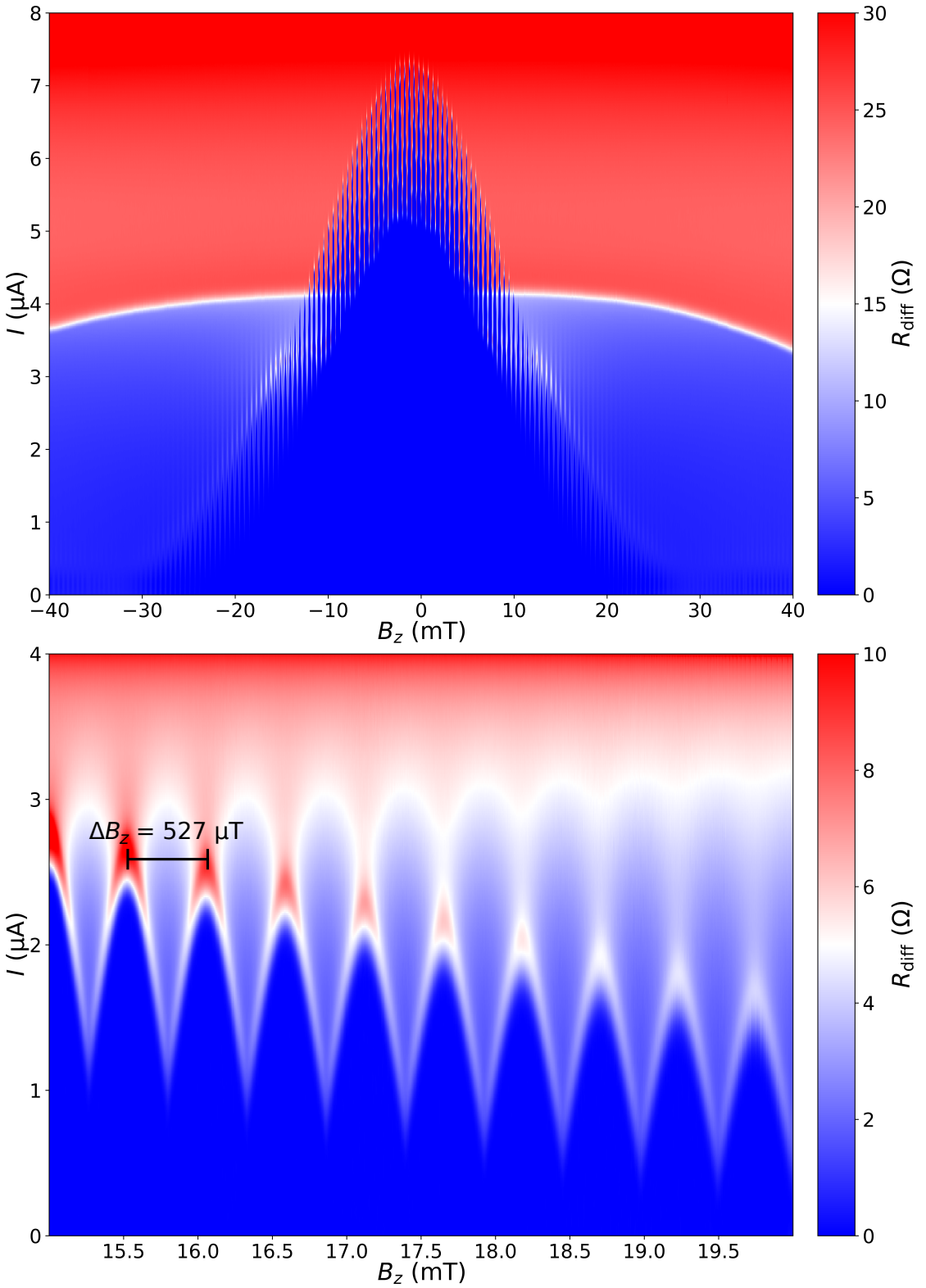

Figure 9.9: Resistance map showing the response of the SQUID from fig. 9.4 to applied perpendicular magnetic fields. Again, 2π-periodic SQUID oscillations are observed over a large range. The effect of larger fields is a split-up of the switching events, of which the first one (lower panel) can be attributed to the weak links.

We also studied single Josephson junctions in order to eliminate possible influence of asymmetry in the respective SQUID arms on the magnetic response. In fig. 9.10 the Fraunhofer pattern of 3 junctions with different geometry is shown, all similar to the one of fig. 6.6. The green dashed contour represents the ideal 2π-periodic pattern of junctions with areas A_{JJ} deduced from the SEM images, while the black one corresponds to a fit of the zero-order maximum, giving rise to a slightly different effective area. Overall, those 3 junctions clearly follow the expected 2π-pattern, although a small offset with respect to the expected progression is observed, manifesting itself as differences between the green and the purple insets. This offset is most likely of geometrical origin, produced by a deviation of the effective area from the anticipated value, which was taken as the absolute possible maximum, hence producing a faster oscillation.
Opposed to the measurements of Williams et al.[321] for Bi_2Se_3, no squeezing of the zero and first-order maxima in B_z is noted. However, a strong suppression of higher maxima of the Fraunhofer pattern is observed in our measurement data of all 3 devices. Similar results have been obtained by other groups for such systems, for example by Qu et al.[309] in Bi_2Te_3. They attributed the deviation from the expected pattern to a non-uniform supercurrent distribution in the junction, which could stem from supercurrents passing the side parts of the junction area.

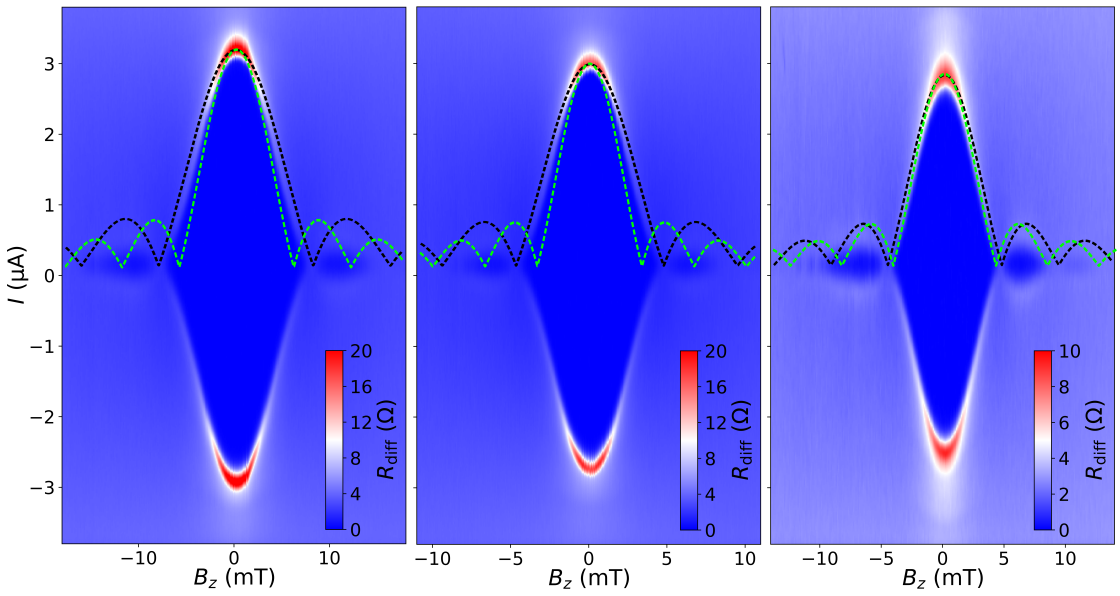

Figure 9.10: Resistance maps at $T = 700\,\mathrm{mK}$ showing the response of 3 different single SnTe/Ta junctions to applied perpendicular magnetic fields. The green contour corresponds to 2π-periodic pattern of maximum possible junction area, the black one to a fit of the zero-order Fraunhofer peak. The measured patterns follow a 2π-periodic characteristic, but deviation from the expected pattern is observed as a strong suppression of higher-order maxima.

A small but recognizable asymmetry of the first-order maxima in (c) is pointed out. Asymmetry can arise in such thin film systems as a result of screening of flux in the superconducting leads or the junctions, usually referred to as *flux focusing*. Flux focussing

can manifest itself as field-dependent node spacing [322] and/or shift of the nodes [320]. Due to the lack of higher-order maxima we cannot say with certainty whether the observed effect stems from flux focusing or fabrication-related disorder or asymmetry, but the observed shift of the nodes towards higher field values could also explain the deviation from the expected pattern (green contour).

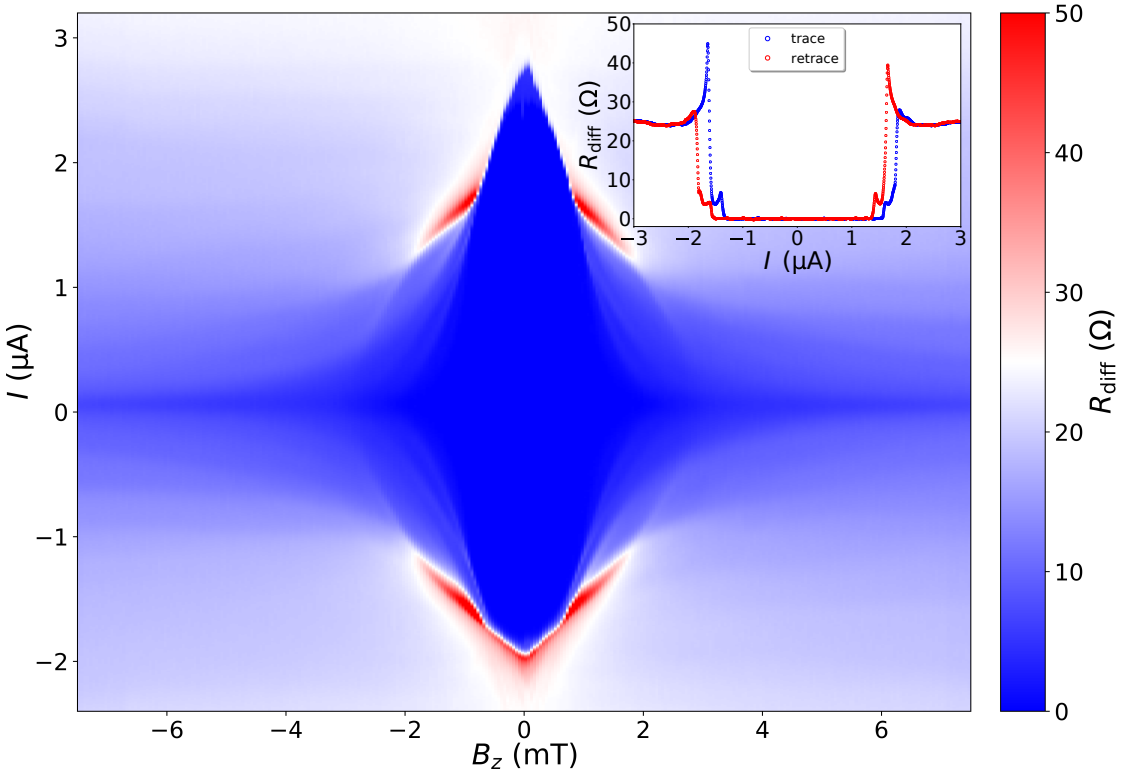

Figure 9.11: Resistance map of a Cu/Ta single junction at $T = 40\,\mathrm{mK}$ and single sweep at zero-field (inset). The observed maximum critical current of $I_c \approx 1.5\,\mu\mathrm{A}$ is almost two orders of magnitude smaller than for Cu/Ta and smaller critical fields are measured as well. Only the major Fraunhofer maximum is observed in these devices.

Cu/Ta Reference Devices

In order to exclude that material properties of purely the Ta from our sputtering chamber cause the measured effects of our hybrid devices, the large coupling expressed by I_c among others, reference samples with copper (Cu) were measured as well. These samples are fabricated entirely equally to the SnTe ones and also of comparable dimensions. We do not find remotely comparable behaviour, as the $L = 200\,\mathrm{nm}$ single junction measurements of fig. 9.11 confirm. A superconducting transition is only realized for $T \leq 200\,\mathrm{mK}$ and the critical current of $\approx 1.5\,\mu\mathrm{A}$ at $T = 40\,\mathrm{mK}$ is much smaller compared to the case of SnTe. While one cannot entirely exclude the possibility of barriers induced by oxidation effects of the Cu to limit induced superconductivity in this system, neither the fabrication

procedure per se nor the observed normal resistance $R_N \approx 25\,\Omega$ strongly suggest such explanations. Since we can also rule out the possibility of remaining Ta islands in our SnTe/Ta devices due to different used fabrication techniques, including Ta lift-off, we hence conclude that the measured coupling is a feature of this particular hybrid system.

The Effect of RF Irradiation

A commonly used tool for the investigation of the influence of surface states on the transport characteristics of topological matter are AC Josephson measurements. As it was introduced in sec. 4.2.3, supported by experimental evidence on other topological systems like 3D TI [266] and QSHI [267], such measurements are ideally insensitive to poisoning of quasiparticle states responsible for the researched transport effect, which inevitably occurs in DC-driven measurements. The presence of topological surface states should then be detectable as an irregular Shapiro pattern with respect to common 2π-periodic transport, manifesting itself as disappearance of (a finite number of) odd steps[1].
In order to realize this scenario, the device is hence exposed to microwave irradiation, applied via a rf antenna and a Rohde & Schwarz SMA100A signal generator (9 kHz-6 GHz). In fig. 9.12, measurement data on the second Josephson junction of fig. 9.10 is shown. Similar results were obtained for the other two devices. The measurement is again conducted with lock-in technique, which gives rise to the appearance of peaks at currents corresponding to the voltage associated with the Shapiro step spacing $hf_{rf}/2e$. The plateaus of $R = 0\,\Omega$ are labelled by n. Due to the rather large thermal broadening, plateaus with $n > 4$ do not recover a fully non-resistive state.
Shapiro peaks could only be observed at temperatures $T \approx 700\,\mathrm{mK}$, corresponding to a working point where the weak link is again separately switchable at moderate I_c. We attribute the infeasibility of Shapiro measurements at lower temperatures to the large I_c, creating instant heat dissipation in the device that masks the researched features. Application of supporting in-plane fields to reduce I_c was tried, but did not create sufficient improvement. The chosen working point comes with a clear drawback of thermal broadening $\approx 60\,\mu\mathrm{eV}$, which greatly reduces the resolution of rf-induced effects for an expected Shapiro spacing at $f_{rf} = 1\,\mathrm{GHz}$ of $hf_{rf}/2e \approx 2\,\mu\mathrm{eV}$. For $R_n \approx 5\,\Omega$ of the SnTe junction, the resulting current step of $\approx 400\,\mathrm{nA}$ is nevertheless easily detectable.
We observe no missing odd values n = 1,3,... of Shapiro peaks/plateaus in the low-power regime and thus no indication of half-frequency AC Josephson effect being present in our devices. Hence, the observation of topological surface states is still derogated by non-ideal conditions of thermal broadening, bulk activation and unwanted coupling effects of the rather inefficient rf antenna to the environment at required high power P_{rf}. These effects leads to a quick fade-out of steps a higher power values $P_{rf} \gtrapprox 10\,\mathrm{dBm}$.
Recent studies by Snyder et al. [269] on $Pb_{0.5}Sn_{0.5}Te$, introduced in sec. 4.2.4, also reported the preservation of all Shapiro steps. However, they observed additional features in

1 According to theoretical calculations [323] and in line with the few experimental observations [266] [267], this effect should be restricted to rather low frequencies.

between the main steps, which they attributed to the presence of higher harmonics in the CPR, possibly created by the presence of surface states. Such features, if existent in our system, might be masked by the experimental conditions.

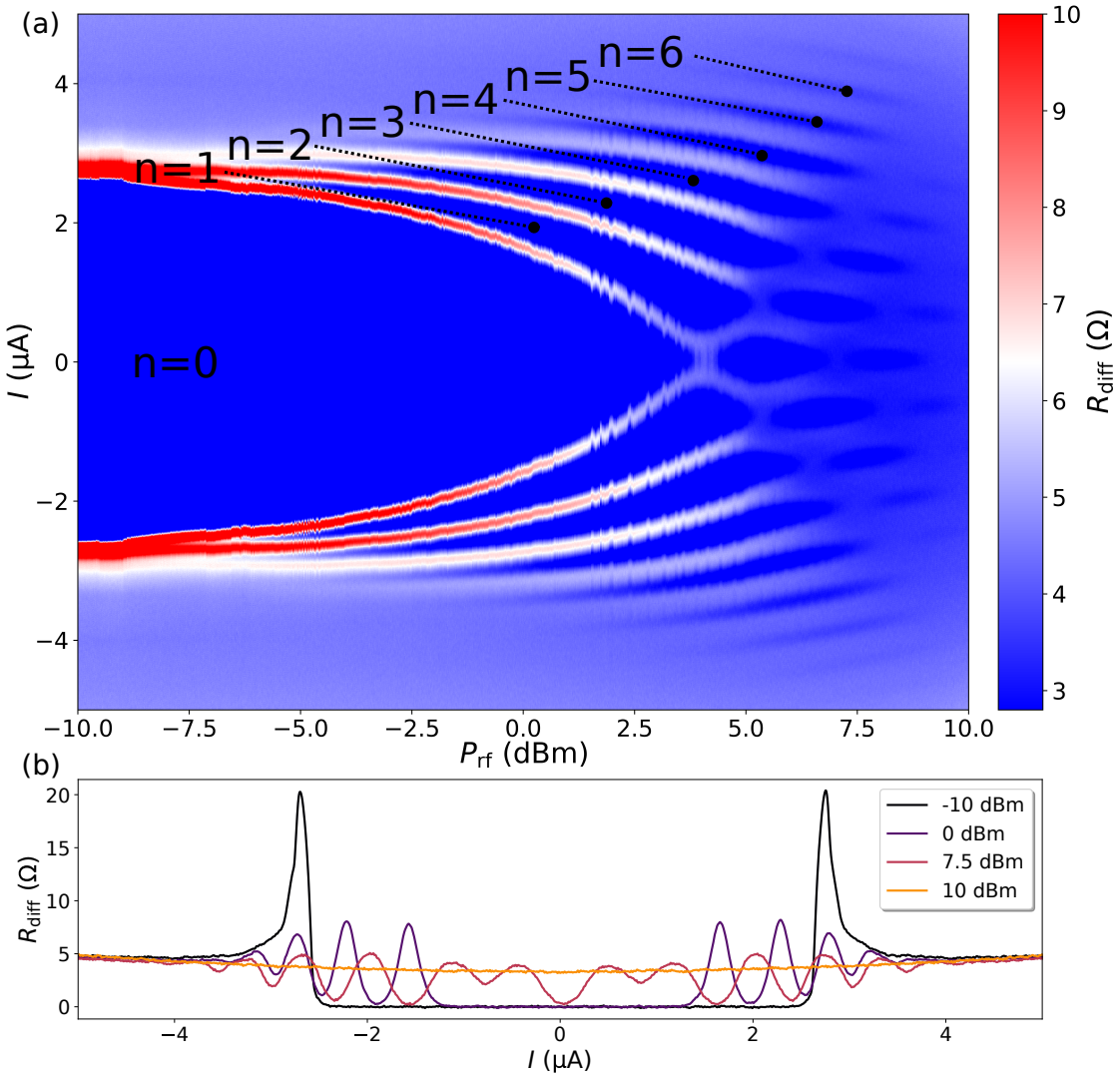

Figure 9.12: a) Resistance measurement of a single Josephson junction device in dependence of the microwave power P_{rf} of an applied $f_{\mathrm{rf}} = 1\,\mathrm{GHz}$ rf signal at $T = 700\,\mathrm{mK}$. Shapiro steps appear as peaks in the differential measurement, separating plateaus (dark blue) labelled by n. No missing odd peaks/plateaus are observed in our device, which would have been expected for transport governed by topological surface modes. b) b) Single sweeps at 4 different P_{rf}. At higher powers the Shapiro steps fade out quickly.

The Effect of Electrostatic Gating

Another approach to tune topological matter from bulk dominated transport to a regime, where the behaviour is sufficiently influenced by topological surface states to be detectable, is electrostatic gating. The underlying principle is the shift of the chemical potential μ, which is usually buried deeply inside of the bulk bands, closer to or into the bulk band gap by application of electric fields. While some success has been achieved for gating of 3D TIs, huge fields are required [324] and/or the impact is mostly rather small [325]. Nevertheless, we fabricated samples with local gate electrodes on top of the two junctions of Ta-based SQUIDs (see fig. 9.13a), made of 5 nm Ta and 75 nm Au and separated from the weak link by 100 nm of Al_2O_3. The latter is grown by ALD at the Néel Institute, analogously to the layers used for the carbon nanotube local gates. On the other hand, ALD on Nb-based samples with global SnTe layer only produced easily breakable and/or rather conductive layers. We suspect chemical reactions of the Nb/SnTe in the ALD chamber to be the cause of this problem. Here, the contacts were covered by PMMA and the growth temperature therefore decreased to 120 °C in order to not being forced to connect the samples through this thick oxide layer. In several measured devices, this preparation technique allowed for application of $\approx \pm 30$ V, limited by breakdown of superconductivity due to leakage currents.

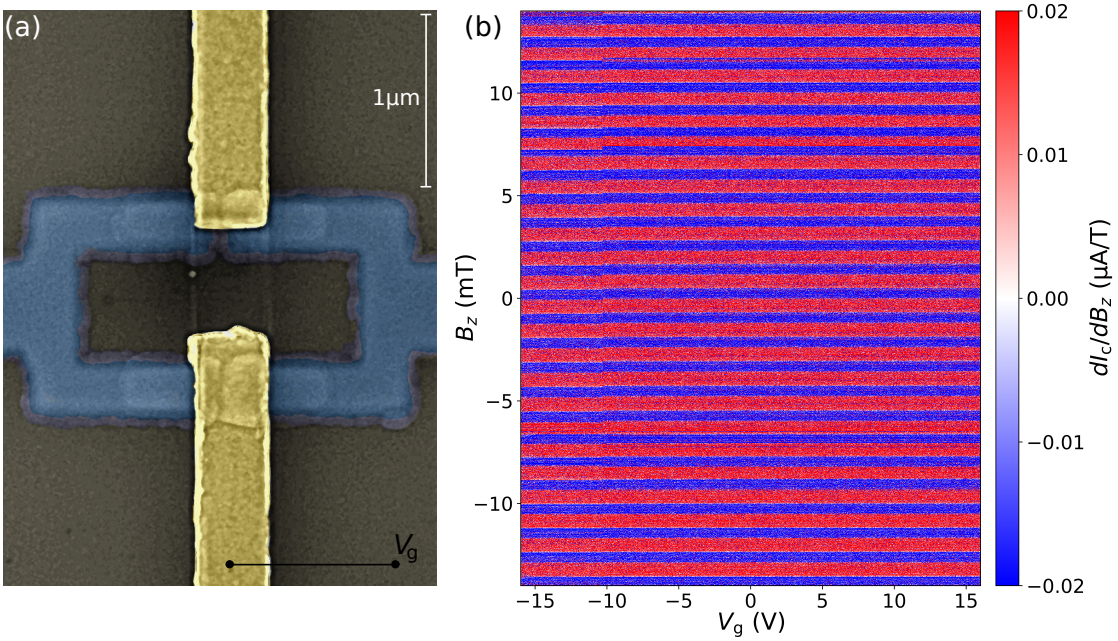

Figure 9.13: a) False color SEM image of an $A \approx 2 \times 1\,\mu m^2$ SQUID on 20 nm of SnTe with local gate electrodes on top of the two junctions. The gates are made from 5 nm Ta and 75 nm Au on ALD-grown Al_2O_3 gate oxide. b) Phase-sensitive measurement of the critical current, plotted as derivative $dI_c\,(dB_z)$, as a function of the applied gate voltage. No effect of the electrostatic field on the CPR is observed for this or any other measured device, confirming the presumption of a chemical potential deeply burried in the bulk bands.

Phase-sensitive data of the critical current $I_c(B_z)$ was taken in order to investigate possible influence of the gating. In fig. 9.13b the $V_g = \pm 16\,\mathrm{V}$ range of such a measurement is shown, plotted as derivative $dI_c\,(dB_z)$ to enhance the contrast. We do not find any impact of the gate voltage on our devices.
The lack of any gate controllability can be attributed to the strong p-doping in our samples, exacerbated by large charge carrier densities which can screen the effect of applied electric fields. A route towards gate-tunable devices could be the use of counter-doped $Pb_xSn_{1-x}Te$ systems of high cleanliness [269] [326]. On the other hand, recent synchrotron and XRD characterization studies [327] of $Sn_{1-x}Te$ reveal high dependence of transport properties in this material on very specific sample conditions which could turn out to be a huge obstacle for reliable device fabrication.

9.2 Current-Phase Relation and Kinetic Inductance Effects

The aforementioned phase-sensitive measurements $I_c\,(dB_z)$ give direct access to the characteristic CPR of the device. In fig. 9.14 such measurements are shown for the sample of fig. 9.4 in the temperature range $30 - 560\,\mathrm{mK}$. It has to be pointed out that this data is taken in the *Sionludi* cryostat. As it was mentioned before, the effective electron temperature of this system is approximately 150 mK lower, which needs to be taken into account when comparing absolute values to previously presented measurements.
Apart from the steep temperature-related increase of $I_c(0)$, a significant deviation from sine wave behaviour is noticed. A regime of single-valued triangular-shaped CPR can be distinguished, generally present for higher temperatures $T \geq 440\,\mathrm{mK}$ and for lower temperatures and small fields B_z. For lower temperatures and small fields, a transition to a CPR is observed, which resembles a sawtooth at first glance.
Naively, one could assume a regime of realized ballistic channels for the latter, as such behaviour is ideally expected for transport governed by topological surface states [162] [328]. However, this assumption is hardly reconcilable with previous reasoning of bulk-dominated characteristics. Also, our data indicates the presence of multivalued switching at the crossover of the two mentioned regimes. We thus attribute the effects to large kinetic inductances in our weak links, even though the experimental data is not entirely unambigous in terms of possible ballistic contribution. Kinetic inductance can be the dominant mechanism in high-mobility transport of charge carriers, such as superconductivity.
To pursue that line of thought, the results of sec. 9.1.2 should be called to mind, where the SnTe weak link could be separated from the ring and also from larger Ta structures for higher temperatures and moderate fields, while a single switching current was observed at small fields (or very low temperatures). In this regard, the regime of sawtooth CPR corresponds to the scenario, where the weak link is exactly not controlled separately, but dominated by the Ta, which makes the conception of ballistic transport very unlikely.
Furthermore, strongly reduced modulation depth $\Delta I_c/I_c$ is observed, which falls in line with the concept of junctions that are dominated by kinetic effects. Such physics has been observed for SQUIDs with spatially extended micro-bridges as junctions [236] which obey $L \geq \xi_N$. We infer from the similarity that a related scenario is realized for our

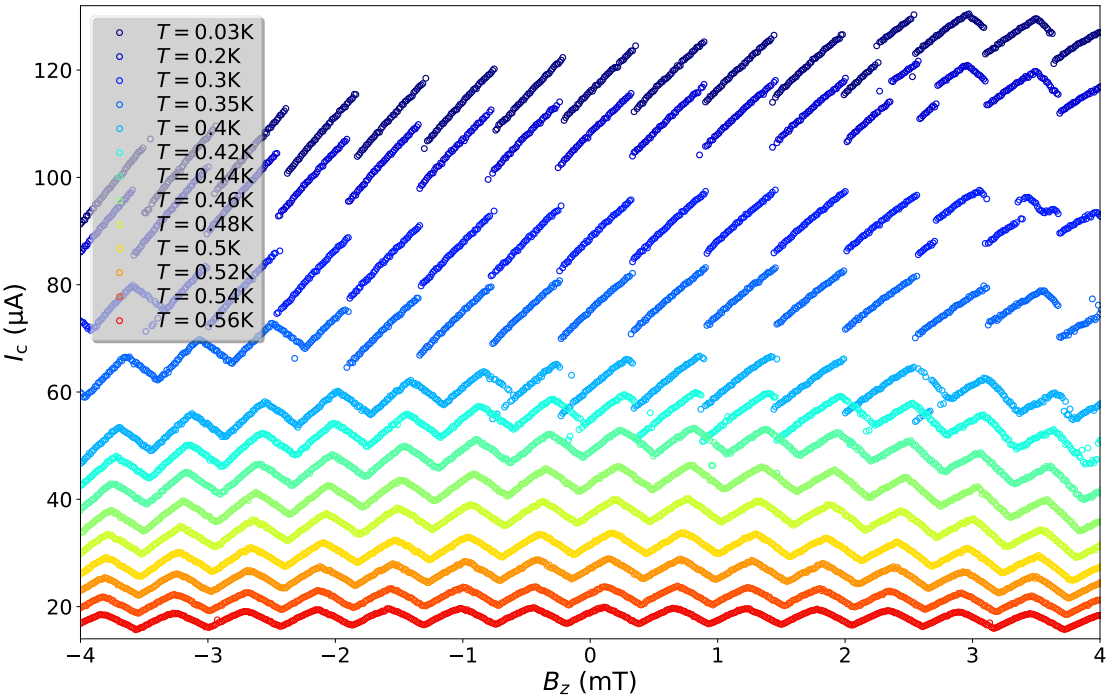

Figure 9.14: $I_c\,(dB_z)$ measurements of the sample of fig. 9.14 for different temperatures $30 - 560\,\mathrm{mK}$. Two different regimes of CPR are visible. At higher temperatures, a triangular CPR is found, which transforms into a sawtooth-like CPR for lower temperatures. Signs of multivalued switching is found at the crossover. The observed effects are strong evidence for transport dominated by kinetic inductance.

junctions in the Ta dominated regime. As it was mentioned before, asymmetry arising from the fabrication process is not able to realistically produce strong damping of the modulation depth as it is observed in our devices.
In order to separate respective contributions of geometric and kinetic origin, the geometric inductance is estimated with [329]

$$L_g = \mu_0 W_{SQ} \frac{2}{\pi} \left[\frac{1}{2} + \ln\left(\frac{W_{SQ}}{w_{SQ}} \right) \right], \tag{9.2}$$

which constitutes an approximate solution for square-shaped rings of dimension W_{SQ} and width w_{SQ} of the superconducting arms. L_g can be considered constant and explicitely independent of temperature. For all our measured devices the equation yields relatively modest values of a few pH:

Nb $16\,\mu m^2$	Ta $4\,\mu m^2$	Ta $2\,\mu m^2$
8.25 pH	3.84 pH	1.74 pH

Following the concept of Faucher et al. [236], one can derive the total inductance L_{tot} as

the inverse slope of the CPR with $L_{\mathrm{tot}} = d\Phi_{\mathrm{SQ}}/dI_{\mathrm{c}} = A_{\mathrm{SQ}} dB_z/dI_{\mathrm{c}}$. For the triangular CPR at $T = 530\,\mathrm{mK}$, shown in a close-up in fig. 9.15, one obtains a modulation depth $\Delta I_{\mathrm{c}}/I_{\mathrm{c}}^{\mathrm{max}} \approx 15\,\%$ and $L_{\mathrm{tot}} = 454.55\,\mathrm{pH} \gg L_{\mathrm{g}} = 3.84\,\mathrm{pH}$. At this temperature, $\beta_{\mathrm{g}} = 2\pi L_{\mathrm{g}} I_{\mathrm{c}}/\Phi_0 \approx 0.17 \ll 1$, but transport characteristics are dominated by the large kinetic inductance $L_{\mathrm{k}} = L_{\mathrm{tot}} - L_{\mathrm{g}} = 450.71\,\mathrm{pH}$ and $\beta_{\mathrm{k}} \approx 20.12 \gg 1$.
Upon reducing the temperature to $T = 400\,\mathrm{mK}$ the regime of multivalued switching is realized and the modulation depth falls to $\approx 7.6\,\%$. The kinetic inductance is $L_{\mathrm{k}} = 192.24\,\mathrm{pH}$, resulting in $\beta_{\mathrm{k}} \approx 39.03 \gg 1$. At $T = 30\,\mathrm{mK}$ the modulation depth is even further reduced to $\approx 4.6\,\%$ and the kinetic inductance $L_{\mathrm{k}} = 162.83\,\mathrm{pH}$ gives rise to $\beta_{\mathrm{k}} \approx 64.55 \gg 1$. The occurrence of multivalued switching can be understood in the context of increasing β_{k}, which induces an inclination in the sine-like supercurrent $I(\Phi)$ of a single junction, which can overlap adjoining oscillations [241].

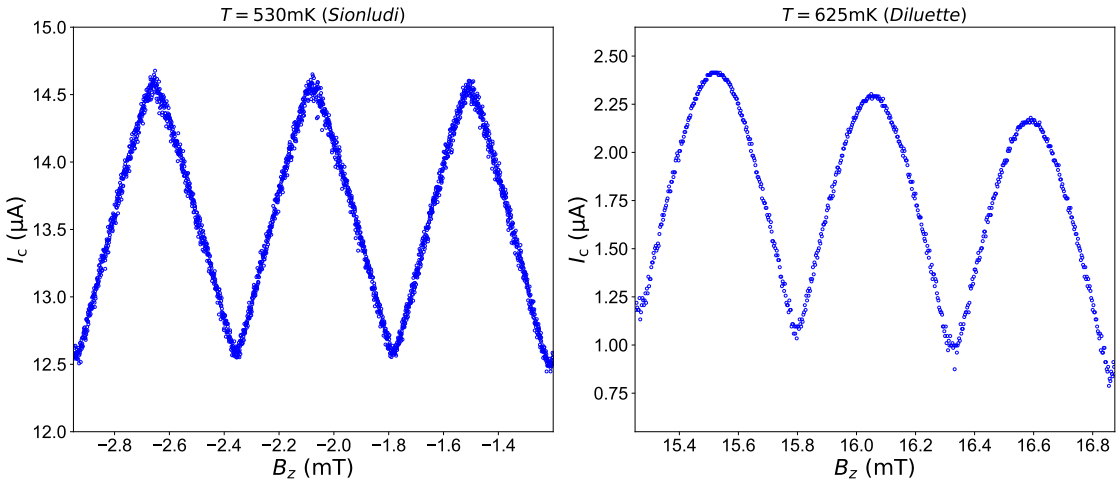

Figure 9.15: Left panel) Close-up on $I_{\mathrm{c}}(B_z)$ at $530\,\mathrm{mK}$, showing an almost perfect triangular CPR, attributed to Ta dominated transport and large kinetic inductance. Right panel) The CPR at $625\,\mathrm{mK}$ (plus additional thermal leakage in the used setup), extracted from the B_z map of fig. 9.9, is cosine-like. In this regime the SnTe weak link determines the properties.

The decrease of kinetic inductance with lower temperatures is stressed, which is the expected evolution, as L_{k} of a conductor with cross section A and length L can be expressed as $L_{\mathrm{k}} = \frac{Lm_{\mathrm{e}}}{Ane^2}$. Here, n is the charge carrier density, in this case Cooper pairs. As n increases for lower temperatures and larger (induced) superconducting gaps, a decrease of L_{k} follows. Using the obtained data for $T = 530\,\mathrm{mK}$ as a cross check, one finds $n \approx 2.6 \cdot 10^{21}\,\mathrm{cm}^{-3}$, which is of the same order of magnitude as the measured (single particle) charge carrier density $n_{\mathrm{SnTe}} \approx 1.1 \cdot 10^{21}\,\mathrm{cm}^{-3}$ from Hall bar studies. It is noted, that the influence of kinetic effects nevertheless increases for lower temperatures due to the dependence of β_{k} on I_{c}.
On the other hand, the geometric influence is not negligible anymore for low temperatures. While $\beta_{\mathrm{g}} \approx 0.17 \ll 1$ at $530\,\mathrm{mK}$, we find $\beta_{\mathrm{g}} \approx 0.78$ and $\beta_{\mathrm{g}} \approx 1.52$ for $T = 400\,\mathrm{mK}$ and $T = 30\,\mathrm{mK}$, respectively. Nevertheless, $\beta_{\mathrm{k}} \gg \beta_{\mathrm{g}}$ for all realized conditions.

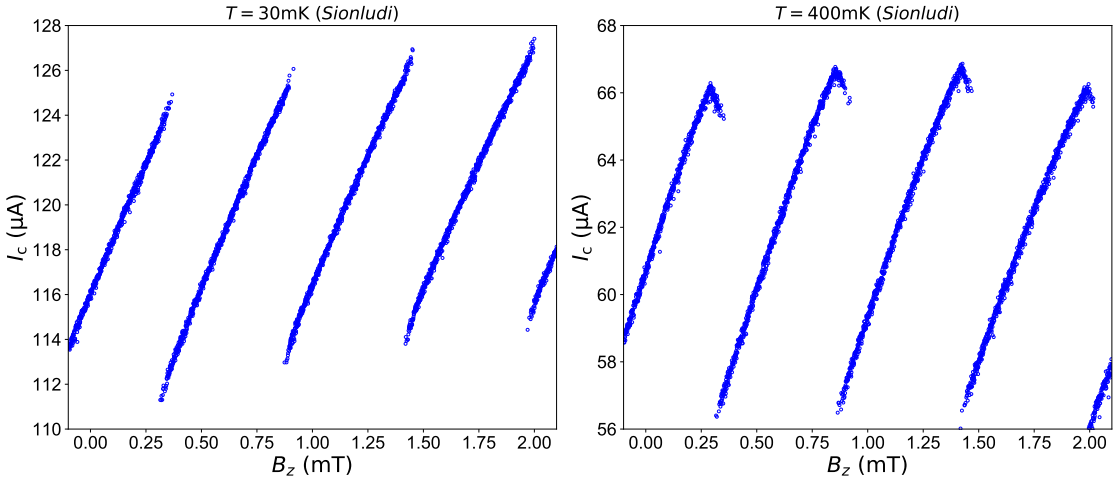

Figure 9.16: Close-up on $I_\mathrm{c}\,(dB_z)$ at $30\,\mathrm{mK}$ and $400\,\mathrm{mK}$. The CPR appears as a sawtooth, but not well-ressolved multivalued switching is present, masking the effect of the triangular CPR.

So far, the three presented temperatures and their CPR comprise only the situation of collective switch of SnTe weak link and (at least the ring of) Ta. This is due to the lower effective electron temperature in the used cryostat. The range of higher T is not directly accessible here, as the fast electronics is limited to sufficiently large critical current values ($I_\mathrm{c} \gtrapprox 10\,\mu\mathrm{A}$) for proper detection.

In order to gain insight on the weak link CPR in the discussed regime, we hence extract I_c from the data of fig. 9.9, which is shown in the right panel of fig. 9.15. A noticeable change is observed, as the CPR now has cosine-wave character, in line with the SQUID relation of eq. 4.16, indicating a crossover from bulk-superconductor-dominated transport to a regime, where the weak link determines the characteristics. Higher harmonics of order m, which should show up with contributions $\propto 1/m$ even for diffusive long SNS junctions, are mostly suppressed in symmetric SQUID setups [330].

Due to the larger applied field $B_z \approx 15\,\mathrm{mT}$ and thus a more strongly suppressed supercurrent, the derived values for the inductance are not directly comparable to the ones discussed before for lower temperatures and smaller fields, but a steep increase of the modulation depth to $\approx 50\,\%$ is pointed out anyhow, indicating a significant decrease of kinetic effects under those conditions.

As a summary, the obtained values for the inductances and β of the sample of fig. 9.4 are tabulated in the following:

T(mK)	L_g(pH)	β_g	L_k(pH)	β_k
530	1.74	0.17	450.71	20.12
400	1.74	0.78	192.24	39.03
30	1.74	1.52	162.83	64.55

9.3 Field-induced $0-\pi$-Transitions in SnTe SQUIDs

Due to the sample's insensitivity to applied gate voltages, a result of strongly metallic behaviour of the not depleted SnTe bulk, a significant knob to drive the device into a non-trivial regime is lost. As introduced in 4.2.5, the impact of magnetic (in-plane) fields can, however, in some cases compensate for the lack of gate tunability and induce effects related to the often peculiar spin texture of topological matter. We hence turn towards investigation of the SnTe weak links in auxiliary in-plane magnetic fields B_x,B_y.
Most significantly, the in-plane field is found to tune the phase of the junctions such that $0-\pi$-transitions of the SQUID device are realized. The occurrence of these transitions is then discussed in the context of comparable phenomena recently observed in other topological systems.

9.3.1 The $0-\pi$-SQUID

In fig. 9.17b $I_\mathrm{c}\,(B_z, B_x)$ is shown, taken for $B_x \pm 0.4\,\mathrm{T}$ for the sample of fig. 9.4. The alignment of sample and field are illustrated in fig. 9.17a, with B_x parallel to the trajectories traversing the junction of length $L = 100\,\mathrm{nm}$. Several interestings effects can be observed in this measurement, which are discussed in the following.
Most trivially, the common SQUID oscillation pattern in B_z is preserved at $B_x = 0$, corresponding to a regular 2π-periodic modulation of the $2 \times 2\,\mu\mathrm{m}^2$ loop area. The CPR of this single sweep is found again in fig. 9.14 (orange curve), preserving the triangular character of previously discussed kinetic effects.
Also, a drift of the oscillation pattern in the (B_z, B_x) plane is observed, which is, at least predominantly, a result of imperfect alignment of the sample[1] and hence perpendicular contributions in $B_z^\mathrm{eff} = B_z + \alpha B_x$ with $\alpha = \mathrm{const} \neq 0$. Flux focussing is expected to contribute similarly. As a result, the pattern is linearly shifted, which is corrected in this plot for clarity.
Already at moderate fields within the zero-order maximum there are evidently additional effects present, creating a contortion of the evolution with respect to the pattern at zero in-plane field. This evolution, if identified as φ_0-behaviour, would represent a phase shift of the still non-degenerate ground state. There is, however, not enough evidence to savely attribute this shift to electronic contributions and not an uncontrolled distortion of the measurement.
Interestingly, hints of a modulation with large period is observed also in direction of B_x, with dips of I_c appearing for $\approx 160 - 210\,\mathrm{mT}$, as can be more clearly seen in fig. 9.17c, the extracted data $I_\mathrm{c}\,(B_z = 0, B_x)$. These dips occur without tilt into the (B_x,B_z)-plane so the question is raised whether this pattern stems from flux penetrating the facet of the SnTe oriented towards B_x, which is denoted as A_x in fig. 9.17a. From the width of the major maximum we derive $\Delta B_x^\mathrm{large} \approx 170\,\mathrm{mT}$, which would correspond to an effectively exposed area $\Delta A_x = \Phi_0/\Delta B_x^\mathrm{large} \approx 0.012\,\mu\mathrm{m}^2$. In contrast, the raw

1 A second measurement of the same sample several months later reproduced the same periodic pattern with a different evolution of this drift.

SEM-derived dimensions of the sample yield $\Delta A_x \approx 0.03\,\mu\mathrm{m}^2$ for the entire flake, or correspondingly an expected modulation of $\Delta B_x^{\mathrm{large}} \approx 68\,\mathrm{mT}$, which differs considerably. On the other hand, screening effects are to be expected in these thin film devices. If one assumes expulsion of fields at the entire SnTe portion screened by the Ta, the flux should mainly penetrate the excess SnTe outside of the junction area, giving rise to an area $\Delta A_x \approx 0.018\,\mu\mathrm{m}^2$ or $\Delta B_x^{\mathrm{large}} \approx 90\,\mathrm{mT}$, which is still much smaller then the observed periodicity.

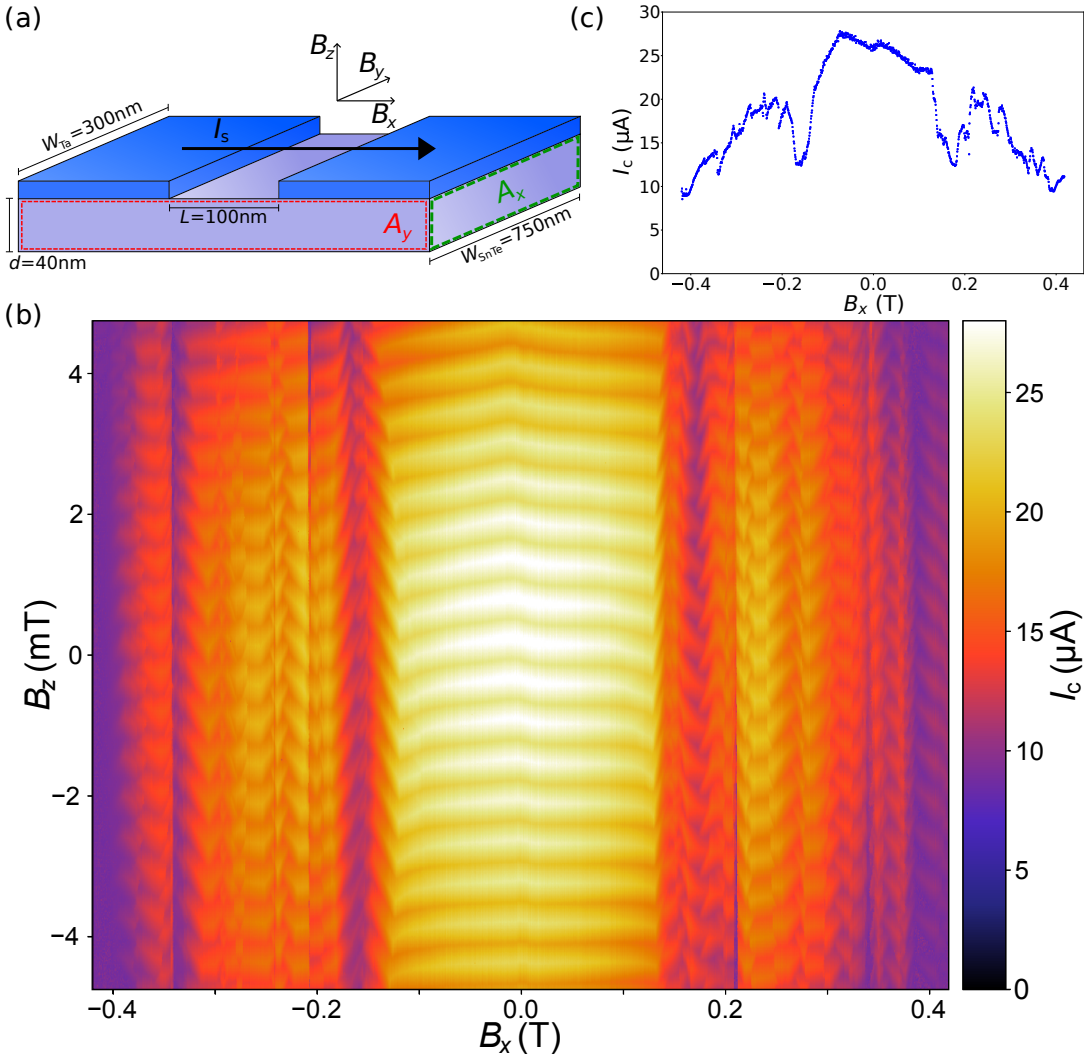

Figure 9.17: a) Schematic of the device, including relevant spatial dimensions and field alignment. The surface area subject to the in-plane field is denoted with $A_{x,y}$. The predominant direction of supercurrent flow I_s aligns with B_x. b) $I_\mathrm{c}\,(B_z, B_x)$ measured in the *Sionludi* cryostat at $T = 500\,\mathrm{mK}$. Non-linear deviations from the common SQUID oscillation pattern at $B_x = 0$ are observed for finite in-plane fields. At larger fields of $B_x \gtrapprox 160\,\mathrm{mT}$, several $0-\pi$-phase shifts are measured. c) $I_\mathrm{c}\,(B_z = 0, B_x)$ along the line of $B_z = 0$. A large modulation of I_c with $\approx 170 - 200\,\mathrm{mT}$ periodicity occurs.

It is further noted, that no significant higher-order Fraunhofer contributions were measured in B_z direction (see fig. 9.9 for the same sample). Consequently, the occurrence of in-plane Fraunhofer modulation due to penetrating flux is thus improbable, which is further supported by angle-dependent measurements which will be discussed in sec. 9.3.2 in the context of a changed transport regime induced by the in-plane field. To anticipate this discussion already, no angle-dependence of this field is observed, which does not meet the expectations of a structure with highly unequal facets A_x and A_y.
Finally, several transitions of the phase are visible, realized as soon as the applied in-plane field exceeds a threshold value of the previously discussed $B_x \approx 155\,\mathrm{mT}$. These transitions persist over a large range in B_x, subordinate to the slow decline of superconductivity for increasing fields. Beyond $B_x = \pm 0.4\,\mathrm{T}$, the critical field of the superconducting state is quickly approached, by this decreasing I_c and triggering the limits of the electronics' detection mechanism.

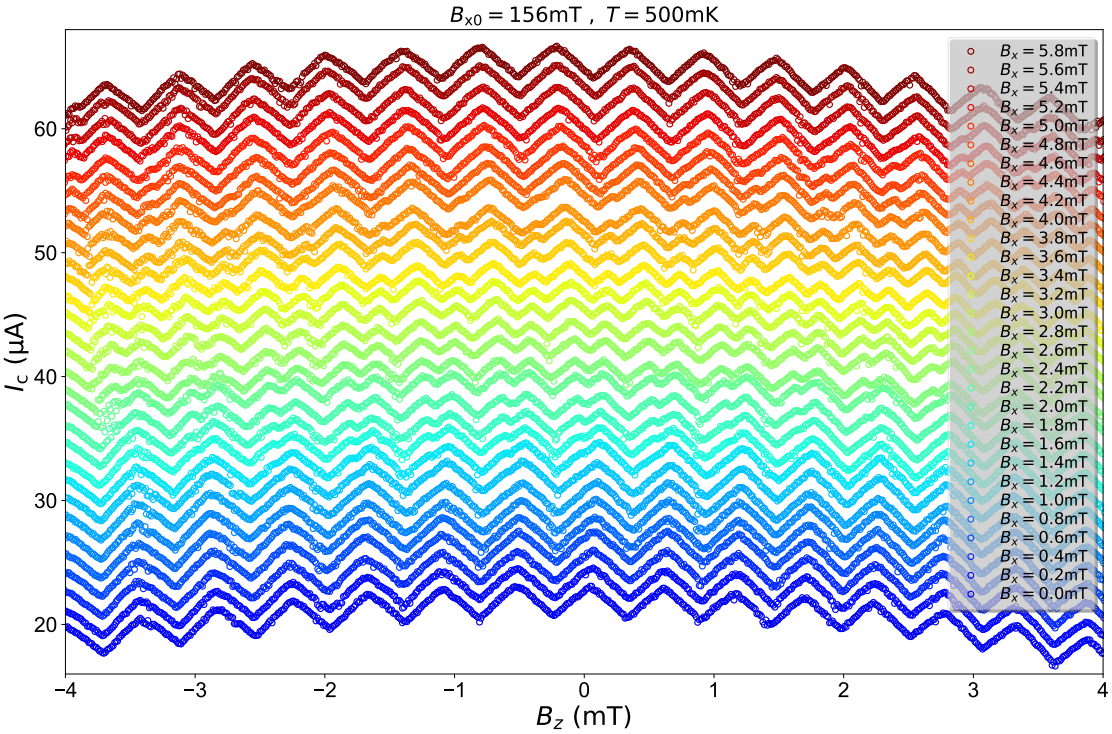

Figure 9.18: $I_\mathrm{c}\,(B_z)$ data for different in-plane fields B_x around the transition at $B_x \approx 220\,\mathrm{mT}$, measured at $T = 500\,\mathrm{mK}$. The curves have a constant offset in I_c for clarity. The assisting in-plane fields induces a continuous $0-\pi$-transition of the CPR.

In fig. 9.18 the second of these transitions, visible at $B_x \approx 220\,\mathrm{mT}$, is shown in more detail. Here, a change of the B_x induces a transition of the phase relation from the linearly shifted and φ_0-modulated CPR at lower fields to a π-shifted state. Interestingly, this transition is not abrupt, but develops in a finite range of in-plane field of approximately $4\,\mathrm{mT}$. This continuous behaviour stands in sharp contrast to effects measured for instance by Murani et al.[278] for a Bi topological nanowire, as it was presented in sec. 4.2.5.

In their setup, they also measured the appearance of φ_0-SQUID behaviour and $0-\pi$-transitions, with the latter abruptly induced at certain in-plane field values.
In fig. 9.19 a close-up of this data is given, showing three characteristic single sweeps of the transition from the 0-state (blue curve) to the π-state (red curve). Particularly, the occurrence of a distinct half integer flux quantum state is stressed (green curve), which is expected at such transitions.
Despite the relatively large fields, the CPR at this transition maintains its triangular shape, indicating a switching behaviour that is at least impacted by the Ta ring and the strong kinetic inductance effects discussed in sec. 9.2. It is, however, pointed out that there is no reason to assume the $0-\pi$-effect itself to originate from the Ta, as this material constitutes a conventional (type-1) s-wave superconductor for which no uncommon shifts of the phase relation can be expected or logically explained. Here, the triangular CPR should hence be seen as a secondary effect, created by the unusually strong proximity coupling observed in our Ta/SnTe hybrid systems.

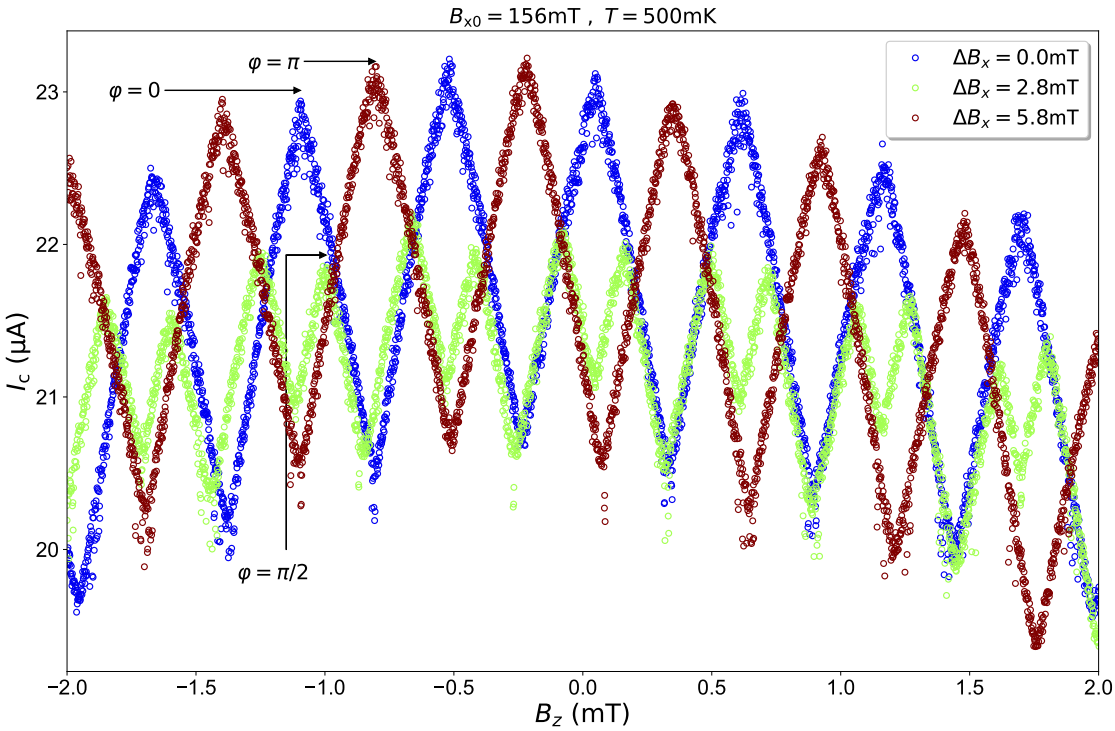

Figure 9.19: Close-up of the $I_c\,(B_z)$ data for the three in-plane field values B_x which realize the standard relation $\varphi = 0$ (blue), the half-integer flux state $\varphi = \Phi_0/2$ (green) and the π-state $\varphi = \pi$(red) at the transition $B_x \approx 220\,\mathrm{mT}$

As can be seen in fig. 9.17, there are actually several such transitions in a relatively short succession upon further increase of B_x. The SQUID geometry of our samples has to be recalled here, which means that a (0,0) configuration switches to (0,π) or (π,0) to realize the observed pattern at the first transition. A transition back to the initial CPR is then possible for either (π,π) or (0,0), which means that either one junctions switches back

and forth or both do with a shifted triggering field. It is further noted, that the number of these observed SQUID transitions $N \geq 3$ inevitably implies a modulation $0-\pi-0(...)$ of (at least one of) the junctions and not a single irreversible change.
Taking unavoidable asymmetry due to the fabrication process into account, including the patterning process and hence slightly different spatial dimensions of the junctions, but also the granularity of the grown SnTe, which is expected to microscopically differ, it is reasonable to assume that one of the junctions experiences a more beneficial coupling to the in-plane field. We hence attribute the observed pattern to both junctions switching at slightly shifted fields.

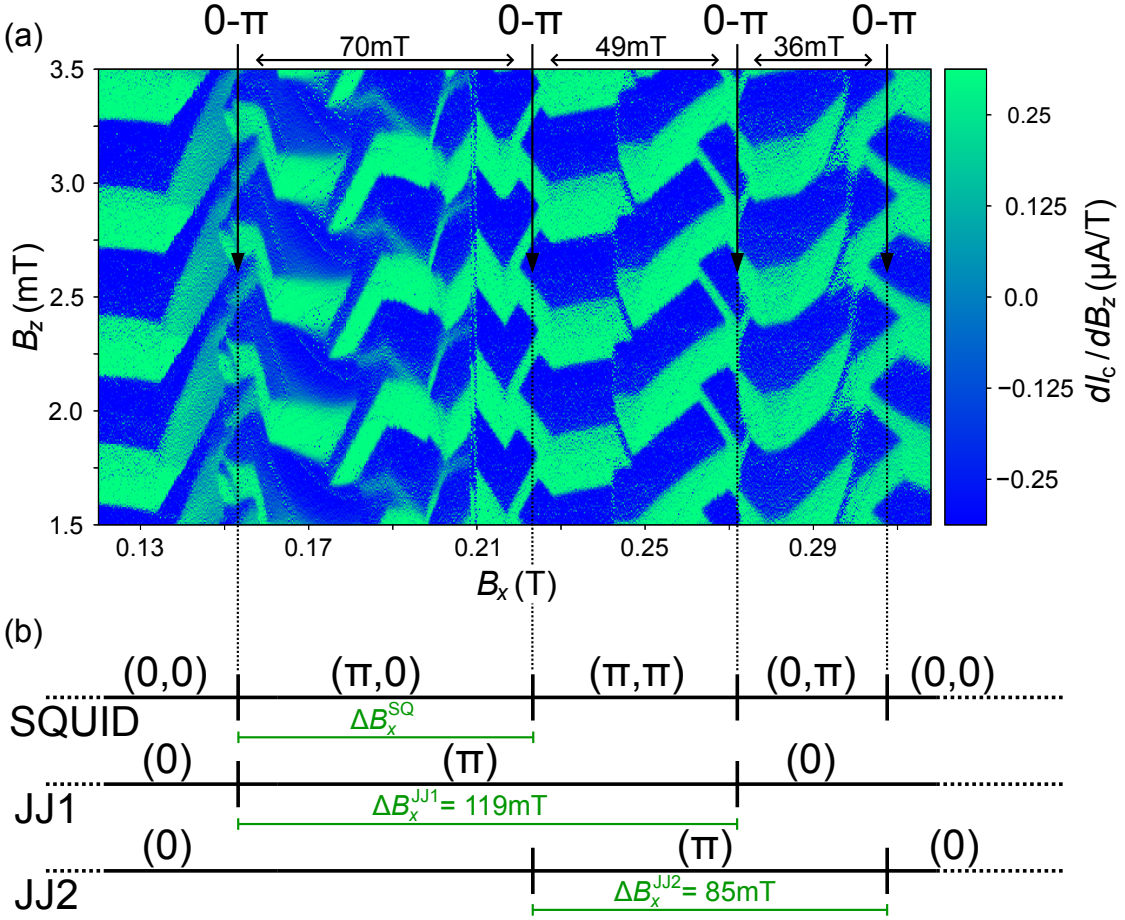

Figure 9.20: a) Derivative of $I_c\,(B_x, B_z)$ at 540 mK showing a set of four transitions, activated for in-plane fields $B_x \gtrapprox 153\,\mathrm{mT}$. The $0-\pi$-transitions appear at quite regularly decreasing in-plane fields. b) Logic of the $0-\pi$-transitions oberserved in the SQUID geometry. A Zeeman field, shifted for the individual junctions due to asymmetry, activates the transitional regime of the individual junctions. The SQUID switches when one of the junctions has a transition.

To shed light on this regime of $0-\pi$-modulation, a close-up of $I_c\,(B_z, B_x)$ is provided in fig. 9.20a, plotted as derivative dI_c/dB_z to enhance the contrast. Here, the green and blue zones correspond to the positive and negative slopes of the triangular SQUID CPR. A

schematic illustration of the switching mechanism is given in fig. 9.20b. Within this range of still moderate B_x values, four clear and distinct $0-\pi$-transition are observed, situated at $B_x = \{153\,\mathrm{mT}, 220\,\mathrm{mT}, 272\,\mathrm{mT}, 308\,\mathrm{mT}\}$. Following the line of thought motivated above, we derive onset Zeeman fields of $B_x^{\mathrm{on,JJ1}} = 153\,\mathrm{mT}$ and $B_x^{\mathrm{on,JJ2}} = 220\,\mathrm{mT}$ necessary to trigger the phase offset in junction 1 and 2, which implies the same physics to be the cause of switching in both junctions.

9.3.2 Discussion of the Transport and Coupling Scenario

Due to the diversity of the observed patterns with assisting in-plane fields it is not straight forward to find a suitable explanation within a narrow and isolated field of physical phenomena. This difficulty is linked with the complexity of the measured system and the fact that both the implications of topological matter as well as the SnTe material itself are still largely unexplored, leading to a continuous shifting of accepted knowledge. In order to evaluate the underlying physics and motivate a possible explanation in this context, different phenomena are therefore discussed in this section. It has to be pointed out that the picture towards a coherent description is still incomplete at this point and will require further examination.

SQUID Asymmetry, Thin Film Properties and SnTe Grain Boundaries

While providing a fast and reliable access to the phase relation of the junctions under investigation, it is clear that the presence of two such interfering junctions in the SQUID geometry inevitably gives rise to the interlacement of primary effects, reliant on the coupling scenario at hand, and secondary effect, which are caused by asymmetries of the system. This is particularly true here for the case of several measurement parameters at once. Asymmetry is not only probed by the current over two non-identical junctions with different I_c (see sec. 4.1.6), but manifests itself in alterations of the modulation pattern in the magnetic field, which can be further complicated due to the non-matched coordination of the sample with the this field $\mathbf{B} = (B_x,B_y,B_z)$ and thus overlapping field contributions.
In this sense, already the different spatial dimensions of the SnTe flakes, their alignment with the superconducting electrodes on top as well as deviating widths of these electrodes are expected to vary flux distributions and/or screening and hence contribute towards some of the effects previously discussed, for instance the linear drift in-plane or the deformation of the major Fraunhofer peak. Likewise, the regular $\Delta B_x^{\mathrm{SQ}} \approx 20\,\mathrm{mT}$ modulation of the observed $0-\pi$-transitions does not hold precisely for higher in-plane fields. We attribute this to the increasing influence of such superimposing asymmetry effects with larger $\mathbf{B}$. Such contributions are neglected for subsequent reasoning, as they do not provide an explanation for the occurring $0-\pi$-shifts but rather cloud the underlying principles.
A related effect that has been only marginally discussed up to now is the granularity of the SnTe layers. Structural analysis (see sec. 6.1.1) revealed monocrystalline growth in the direction corresponding to the out-of-plane field B_z and polycrystalline growth with

an average grain size of $\approx 25-30\,\mathrm{nm}$ in-plane, which governs the transport channels. These crystallites are mostly aligned correctly, with $45\,^\circ$ rotated grains constituting the biggest source of disorder. A phase coherence length of $l_\Phi \approx 120\,\mathrm{nm}$ was derived from WAL measurements at $T = 2\,\mathrm{K}$, much longer than one crystallite, hence indicating coherent transport channels over the entire junction length, possibly related to surface transport. Also, a multitude of diffusively scattered transport channels is expected, as sketched in fig. 9.21 for a single junction.

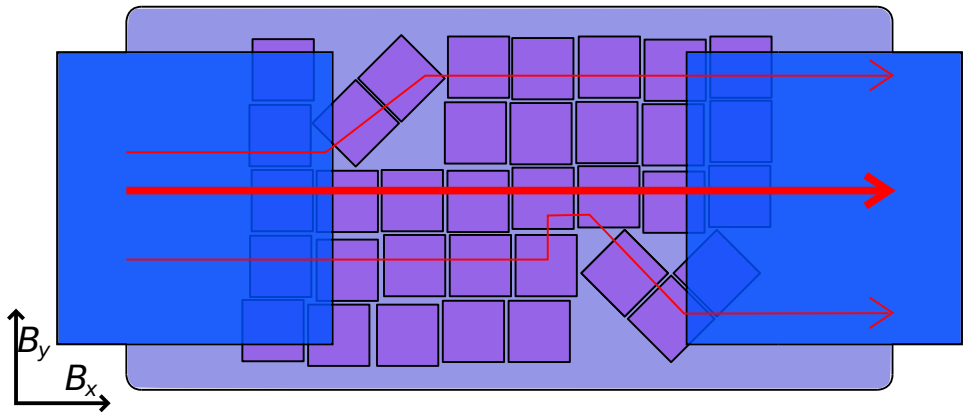

Figure 9.21: Sketch of the transport in the granular SnTe junction, where the crystallites are mostly well-aligned, granting continuous transport channels. Crystallographic discontinuities cause scattering of carriers.

In any case, the exact nanoscopic composition of the junctions in terms of granularity is expected to further contribute to asymmetric influences. On the other hand, one may ask whether the presence of grain boundaries can already give rise to field-induced phase shifts and explain the observed effects.
Indeed, $0-\pi$-transitions were realized in high-T_c cuprate junctions with d-wave pairing symmetry [244], where the π-shift arises naturally at grain boundaries due to the anisotropic order parameter. However, the implementation in π-SQUIDs is usually achieved by controlled growth of boundary facets [331] and do not require the application of in-plane fields, while our layers are expected to have arbitrary boundaries with respect to the field, and yet show a regular pattern in-plane, which vanishes for small B_x. Due to the low congruence of expected pairing symmetry, microscopic composition and triggering of the effect, this possibility is hence discarded.
π-transitions and half-integer flux quantization were also reported [243] for the iron picnitide material group with sign-changing $s_\pm$ gap symmetry. But similarly to the abovementioned cuprates, the granular layers intrinsically gives rise to such shifts without dependence on assisting magnetic fields, which is not the case in our samples. We hence dismiss the granularity of the SnTe as primary cause for the observed shift.
Furthermore, the patterns are not explainable by possible trapping of flux, as no magnetic hysteresis is observed. Repeated measurements of the in-plane behaviour reproduces the modulation pattern at the same field values. This was even confirmed several months later with a second cooldown of this sample.

Topological Surface States and Orbital Flux Modulation

While neither DC nor Shapiro measurements, discussed in sec. 9.1, could provide evidence for the presence of topological surface states in our devices, it should be pointed out that there is a certain experimental agreement that topological surface states can dominate transport characteristics even in bulk-shunted systems [328] [332] [277]. As it was introduced in sec. 4.2.5, particularly the concept of Zeeman fields has recently proven to be useful to evoke characteristics which are believed to originate from topological transport in experiments [276] [278] [277] and theoretical propositions [272].
In particular, and as recently reported by Chen et al. [277], there is good evidence of the realization of Cooper pairing with finite momentum in 3D TI systems, which is a logic follow-up of the work of Hart et al. [276] on 2D QSHI. Both works were briefly introduced in sec. 4.2.5. In the former work, an anomalous Fraunhofer pattern was found, shifted with increasing in-plane fields towards outher nodes.
The surface Dirac spectrum of eq. 4.41, valid for 3D TI and one cone of a TCI, is hence recalled. If the application of a Zeeman field $B_{\mathrm{ip}} = (B_x, 0)$ shifts this surface spectrum by $q = \frac{g_x \mu_\mathrm{B} B_x}{\hbar v_\mathrm{F}}$, a finite center of mass momentum (COMM) of $2q$ is induced to Cooper pairs forming on these shifted contours, which modulates the gap with $\Delta = \Delta_0 \exp(2iqy)$ in y-direction.
Chen et al. argued for the presence of such a Zeeman-induced shift in their system, but noted predominant effects of orbital type, more precisely an Aharonov-Bohm phase modulation encircling the surface, giving rise to a spatial modulation $\Delta = \Delta_0 \exp\left(\frac{\pi B_y d}{\Phi_0} y\right)$. This modulation is dependent on the flake thickness d and found to (almost) entirely dominate for thicker flakes, when more flux is enclosed.
Generally, a Zeeman field is expected to modify the Andreev spectra and hence create φ_0-shifts, but also possibly induce crossings of the levels and thus stimulate CPR sign changes and by this $0-\pi$-transitions. Such effects were predicted for 3D TIs [333], 2DEGs in a topological regime [272] or even semiconducting nanowires with strong spin-orbit coupling [334] and also recently observed in topological Bi nanowires [278]. Common denominator of such systems is spin-momentum locking leading to a predominant spin polarity of transport carriers, either evoced by bulk topology and topological surface states or by spin-orbit fields and a quasi-1D geometry.
Such physics would therefore enforce very selective directionality of the observed effect. To return to the case of surface states in a 3D T(C)I, biasing the transport along k_x, corresponding to the straight red arrow in fig. 9.21, thus leads to the spin pointing in y-direction. Therefore, if Zeeman induced finite COMM was the case, one would expect a strongly suppressed effect for field direction B_y instead of B_x.
In fig. 9.22 measurements with shifted in-plane field are shown, applied with 45 ° angle and along B_y. The observed features generally strongly ressemble the case of B_x, and explicitely no strong suppression of the $0-\pi$-modulation is observed despite this rotation of field. As a result, finite momentum induced to Cooper pairs on surface states should be dismissed as dominant mechanism responsible for the measured phase modulation, although we also cannot entirely rule out such effects. Chen et al. [277] reported these

effects to be small to negligible, depending on system parameters, and dominated by flux-induced modulation.

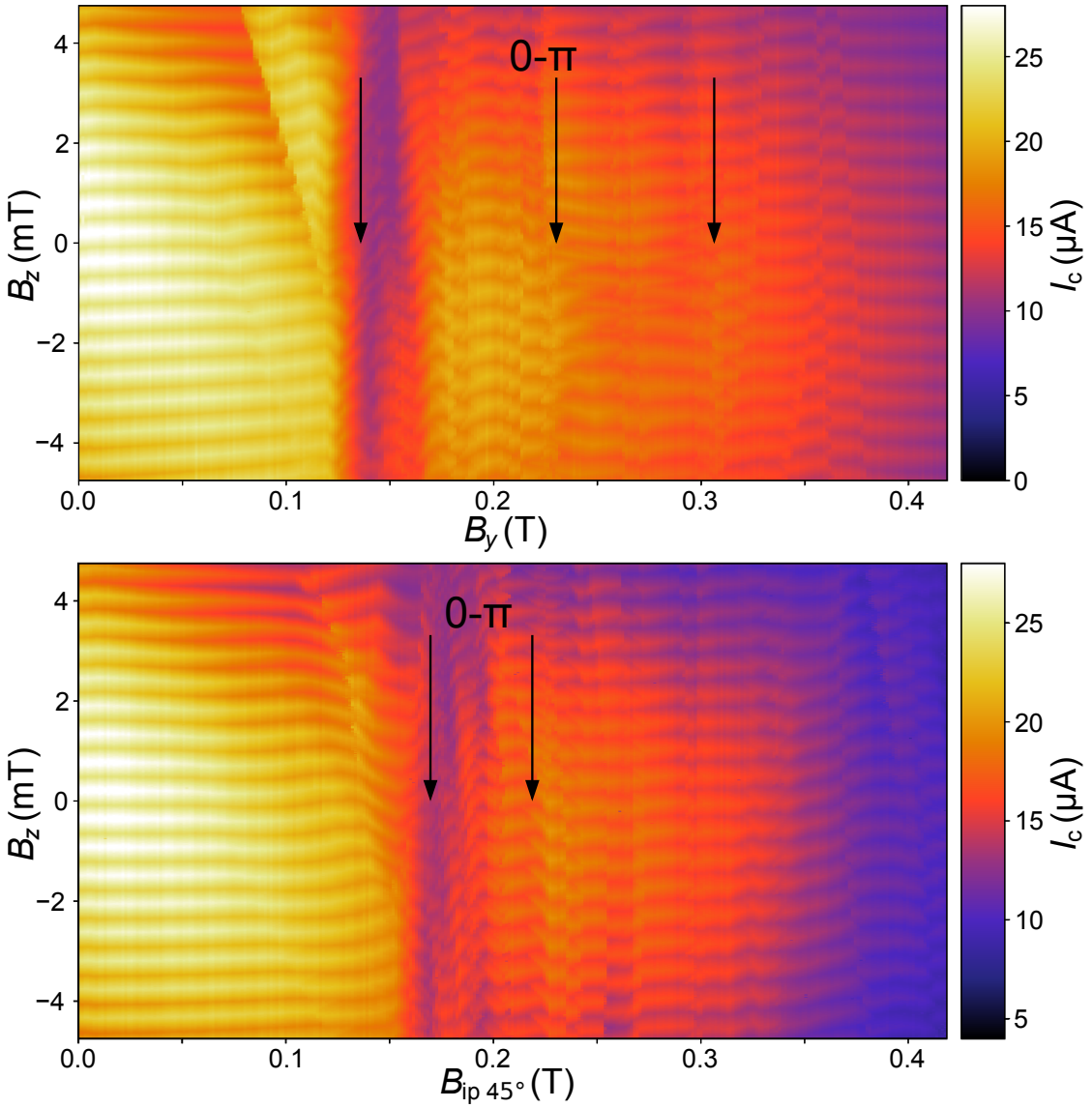

Figure 9.22: In-plane field measurements $I_c\,(B_z, B_{ip})$ at $T = 500\,\mathrm{mK}$ for two differing field directions in the $B_{ip} = (B_x, B_y)$ plane. The arrows serve as guide for the eye for the first $0-\pi$-transitions, placed by means of the derivative (not shown). Again, onset fields close to the case of $B_{ip} = (B_x, 0)$ are observed, here at $B_y \approx 140\,\mathrm{mT}$ and $170\,\mathrm{mT}$ for an angle of $45\,°$.

On the other hand, we only find a very weak dependence of the onset field $\Delta B^{\mathrm{Zee,SQ}}$ on the in-plane angle. The value of $\Delta B_x^{\mathrm{Zee,SQ}} \approx 160\,\mathrm{mT}$ remains basically the same for $45\,°$, slightly increasing if anything, and then slightly decreases to $\Delta B_y^{\mathrm{Zee,SQ}} \approx 140\,\mathrm{mT}$. Also, particularly in B_y-direction no second dip in I_c is observed up to $0.4\,\mathrm{T}$. As mentioned

before in the context of possible in-plane flux penetration, this stands in contrast to the spatial dimensions of the weak link.
Taking the entire flake into account, one would get a ratio $\Delta A_y/\Delta A_x \approx 3.5$, while a restriction only to the uncovered junction area woud give $\Delta A_y/\Delta A_x \approx 0.2$. The scenario at hand is difficult to determine, as the proximity coupling in our system had shown to be very strong and considerable flux expulsion in the SnTe flake should be expected, giving strong deviation of derived spatial dimensions. Nevertheless, a in-plane flux arbitrarily modulated with almost the same areas ΔA_x,ΔA_y seems unlikely. We therefore argue the impact of the field to be of mainly Zeeman character, coupling to the bulk spin distribution rather than to topological surface states.

Rashba Spin Splitting

As SnTe is known to exhibit strong Rashba-type spin-orbit fields[222], their presence should be considered as possible explanation for the measured effects. According to the scheme of fig. 4.16, Rashba SOC gives rise to spin-momentum locking which is then subject to a Zeeman field to create spatial modulation of the gap function Δ.
In contrast to the restricted case of topological surface states, no limitation to mostly k_x-oriented transport channels is imposed. If one considers diffusive bulk channels as dominant contribution, an assumption which is conform with the presented results of this chapter, then a wide distribution of transport channels in the (k_x,k_y)-plane can be expected, schematically represented by the thin read arrows in fig. 9.21. Such a transport mechanism should give rise to evenly distributed spin-orbit fields and hence could explain the similar patterns for different in-plane angles. It is further noted, that the Rashba effect derives from structural inversion asymmetry related to interfaces. Due to the polycrystalline composure in in-plane direction, the missmatch at grain boundaries should contribute to such effects.
In this case, $0-\pi$-transitions are expected when the Zeeman energy $E_\mathrm{Z} = g_\mathrm{eff}\mu_\mathrm{B}B$ equals the Thouless energy E_th[278]. With the deduced modulation of a single junction of the SQUID, $\Delta B^\mathrm{JJ} \approx 35-70\,\mathrm{mT}$, and $E_\mathrm{th} \approx 70\,\mu\mathrm{eV}$ from the $I_\mathrm{c}(T)$ evolution in sec. 9.1.2, one can estimate the effective g-factor of the system as $g_\mathrm{SnTe} = E_\mathrm{th}/\mu_\mathrm{B}\Delta B^\mathrm{JJ} \approx 17-34$. This high g-factor is in line with observations on comparable systems. For instance, Murani et al.[278] derived $g_\mathrm{eff} \approx 30-100$ for Bi, Szombati et al.[247] found $g_\mathrm{eff} \approx 51$ in-plane for InSb. Calculations of g_eff for rock salt SnTe by multi-band **kp**-theory[335] yield $g_\mathrm{eff} \approx 58$ in (111)-direction and $g_\mathrm{eff} \approx 15$ perpendicular to this axis.
An electronic rather than geometrical origin is supported by similar in-plane measurements, shown in fig. 9.23, of the SQUID sample from fig. 6.6. For this sample, the SnTe is entirely constricted to the area between the superconducting Ta electrodes. Again, transitions and half-integer flux effects are observed, but now these effects manifest themselves in a diamond-shaped pattern in the (B_x, B_z)-plane.
This behaviour was confirmed for several equivalent devices on the same substrate, which are patterned from 30 nm layers, in contrast to the 40 nm of the previously presented device. We attribute this to less clearly defined in-plane facets of the SnTe for these samples, resulting from etching of the excess material and the reduced layer thickness.

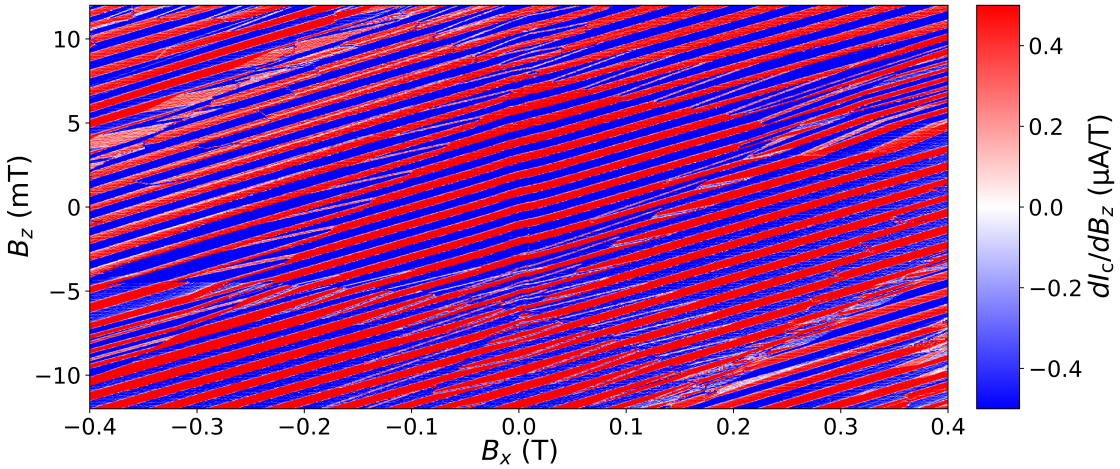

Figure 9.23: $dI_c/dB_z\,(B_z = 0, B_x)$ at $100\,\mathrm{mK}$ for the SQUID from fig. 6.6, patterned from $30\,\mathrm{nm}$ SnTe layers, which are narrowly constricted to the junction area. Here, the measurement is conducted at $T = 100\,\mathrm{mK}$. The transitions, accompanied by half-integer flux effects, shift within the (B_x, B_z)-plane and shape a diamond pattern.

On this account, missalignment and field screening effects should gain more influence and push the transitions into the 3D space of the magnetic field, which hence modulates the bulk spin distribution by Zeeman coupling. However, more studies and possibly a theoretical model are required to support this description.

10 Conclusion and Outlook

In this last chapter, a recapitulation of the presented work of this manuscript is provided, embedded into the respective context. Also, an outlook on the development of the field is given, including medium-term possibilities and requirements of the particular systems discussed in this manuscript and more long-term prospects of the general field.

Two different systems for the implementation of spin-based quantum physics have been studied during this PhD project, supramolecular carbon nanotube systems and tin telluride topological crystalline insulator. Both are fundamentally interesting as platform for the realization of novel spintronics concepts and both will remain fundamental concepts for the time being.
More closely, the status quo of both systems and also the requirements towards application are, however, quite different. In simple terms, one can consider this contrast in analogy to the well-known view of bottom-up versus top-down approaches. One one hand, the properties which govern the characeristic physics of a spin on the molecular scale are well-controlled and engineerable, which is the result of the efficient environmental decoupling and great reproducibility. Here, the difficulty is hence how to connect to these tiny molecules to realize actual devices.
On the other hand, the common and most pressing issue of topological matter is how to remove the (trivial) bulk influence to access the features arising from topological implications, while the technical methods for implementation at this stage are closer to already established ones. This contrast is perfectly reflected in the struggles and achievements presented in the scope of this work.

In order to provide a naturally suited carrier for the localization, detection and manipulation of molecular spin systems, the first goal of this project was the development of reliable carbon nanotube devices, equipped with several small local gate electrodes in order to allow for the abovementioned functionality. As it was introduced in sec. 5.1, known and established approaches for the fabrication of such devices are all highly complex and require close consideration of requirements. This is why carbon nanotubes, albeit being proclaimed as possible mass market application in the earlier stages of the carbon nanophysics upswing, have more recently been used for ultra-clean and low-yield systems to study fundamental aspects of quantum transport.
In this context, two fabrication techniques were investigated in the scope of this PhD project, the first one being the continuation of a formerly initiated two-chip stamping approach, which has been omitted in this manuscript, and the extensively presented second one of a classical one-chip approach. For the latter, the most crucial aspect is the avoidance of leakage, which is likely to occur due to the impact of demanding CVD

growth conditions on delicate nanocircuits. Naturally, such an approach is limited in terms of conceptualdesign, including material choice or spatial dimensions among other parameters.
In the course of this work, a reliable fabrication pattern for closely spaced gate electrodes of $\approx 50\,\mathrm{nm}$ was developed, which show high efficiency and no leakage in the realistically useful voltage range. Nanotubes were grown under optimized conditions to form clean and (so far) at least partially suspended devices. Further upscaling of the 5 incorporated gates or implementation of fully suspended nanotubes should be feasible without significant intricacies.
With these devices we demonstrated the functionality of a locally controllable carrier by means of a double quantum dot configuration, tunable from p- to n-type characteristics. We can realize different coupling scenarios, from one strongly coupled large dot over weakly coupled double dots to almost total pinch-off, by inducing pn-barriers via the local gates. The segments created in this way can be stabily controlled over the entire device length and should hence provide a suitable backbone to study molecular physics. At the end of this project, all details of this fabrication procedure were figured out such that we can reliably produce clean CNT devices controlled by 5 local gates. It is, however, clear that this procedure requires stable conditions, which was not always a given. This is, apart from inherently complex circuit fabrication, amplified by the fact that nanotubes tend to degrade and can thus not easily be stocked, but also by the ramifications of a stochastic growth process: even for flawlessly pre-patterned substrates, the yield of connecting nanotubes of required electronic properties is usually $\approx 5\,\%$.

While the realization of a supramolecular device, based on multi-gated nanotubes and single-molecule magnets, is still lacking, it is emphasized that such systems are still highly desirable. As it has been shown by the NanoSpin group in the past and for different contacting techniques, single-molecule magnets constitute an extremely enticing building block for future spintronics applications. Particularly the use of clean and controllable nanotube carriers should then give way to possible investigation of coupling effects of these hybdrid systems and ultimately be able to contribute to the exploration of possible upscaling.
However, it has to be pointed out that the combination of relatively low-yield carrier fabrication and very low-yield molecular functionalization at this point sets a realistic limit to the concept at hand. The urgent requirement of improvements on this side is thus emphasized. One possible way to overcome these limitations of the second bottleneck would be in situ deposition of molecules, which will presumably be realized with the continuation of this project at the KIT in the medium term.
While such improvements should help to answer pressing questions on the side of fundamental molecular physics in order to provide the purpose, in the long run the most potential of this field is grounded in chemistry. This is because synthesis opens up the possibility of perfect reproducibility and tailoring of properties, which will need to be expanded towards more complex structures eventually.

In the second project, SnTe, a narrow-gap semiconductor of cubic crystal symmetry, whose inverted band structure can give rise to the presence of topological surface states, was investigated. In the context of topological matter, this material remains a still largely unexplored system. Here, SnTe was implemented in the form of thin films, deposited by co-sputtering techniques. Such an approach is useful to gauge possible trends towards more commercial scales, as it represents a fast and relatively simple procedure which stands in contrast to many other 3D topological materials. Also, the thin film geometry offers a naturally convenient platform for implemenation in microelectronics. In this context, the moderate growth conditions $T \leq 150\,^{\circ}\mathrm{C}$ are also pointed out.
Structural characterization studies of the deposited films reveal low surface roughness and mostly regular orientation of the individual crystallites, which grow with strong (001) texture, verifying a good quality of the layers. Electrical characterization of Hall bar samples show predominantly metallic behaviour, a commonly known drawback of the material class, which is amplified by the particular growth procedure. SnTe tends to be very sensitive to stoichiometric imbalance, which creates large p-doping and charge carrier densities. As a result, no gate effect could be observed, which prevents the means to electrostatically tune the SnTe into a topologically non-trivial regime. To limit these bulk influences, SnTe is often grown with molecular beam epitaxy and very carefully adjusted conditions, which, on the other hand, sets a boundary to applications on a larger scale. To our knowledge, no electrostatic tunability has been reported so far in those systems, pointing out the importance of further improvements on the material physics side.
Despite the significant bulk contribution, weak antilocalization measurements, an accepted tool to probe the presence of topological surface states, indicate phase-coherent transport features over length scales much larger than the crystallite size and thus the existence of surface channels. This can be seen as one of several manifestations which encourage the experimental consensus, that topology can impact the transport properties in the limit of a not depleted bulk. It is, however, clear that the elicitation of such effects and even more the potential incorporation in actual devices is extremely difficult.

One of the particularly enticing concepts in this context is the combination of topological properties and (proximity-induced) superconducting pairing, which should give rise to unconventional coupling scenarios. To provide a platform for the investigation of such physics, hybrid systems of topological matter and *s*-wave superconductors need to be established and characterized. Within the scope of this project, we realized fully operational Josephson junctions and SQUIDs out of SnTe/Nb and SnTe/Ta hybrid film systems. Sample geometries, temperature and magnetic field response were further investigated to probe superconducting transport and hunt for effects possibly related to the topological nature of the material. Especially for the Ta-based devices, we found surprisingly strong proximity coupling, giving rise to large critical currents. Here, transport is dominated by strong kinetic effects for a large parameter range, as indicated by the appearance of triangular-shaped current-phase relations. Such effects render the transport mechanism as effectively purely conventional for both DC and rf measurements.

Strikingly, in-plane magnetic field measurements gave rise to the manifestation of φ_0-SQUIDs with tunable $0 - \pi$-transitions. We discuss these features in the context of thin film characteristics, topology and spin-orbit physics. While additional investigation and explanation of the coupling mechanisms at hand are required in order to conclude this particular project, the observed modulations provide first evidence for possible transitions from trivial superconductivity to unconventional coupling regimes in SnTe, which identifies the material class as a promising candidate for further research in the (highly interconnected) fields of topological superconductivity and spin-orbit physics. Here, the observed phenomena are attributed to Zeeman splitting rather than to topology, which can be seen as a consequence of bulk material parameters.

The field of topological matter offers a tremendously promising long term outlook, with the Majorana-based topological quantum computation as the most outstanding example. While significant progress in this still new field can be stated, it is clear that the undoubtful proof of feasibility is still lacking and that the realization of prototype devices or even large-scale application is nowhere near and will require massive improvements, especially in terms of material properties and fabrication. On the other hand, the field is already very wide-spread and continues to diversify at such a speed, that new material systems or possible effects come to the fore on a frequent basis.
In this sense, a gradual improvement of material properties and continued progress in interconnecting the implications of topology and spin in realistic systems will very likely soon produce novel applications in a branch of electronics and spintronics which is less elusive than the mentioned concept of topological quantum computing. To underline this, the recent report [336] on magnetic tunnel junctions based on 3D topoligical insulator is mentioned here as one particular example.
Also, the very rich spectrum of phases in SnTe is pointed out, which are not restricted to the discussed scope of topology, but also provide an opportunity to exploit ferroelectric effects [222] based on (bulk) spin-orbit couplings and even physics that may arise from this interplay and that is not yet identified. On the other hand, as pointed out in this work, there are still ways to go in order to purely access the topological properties of this material. In this sense, further collaborations between Bielefeld, Karlsruhe and Dresden are currently discussed, which would involve a transition towards more controlled (Bi_2Se_3) nanowire systems in order to investigate such physics.

To conclude, I hope that the presented work can make a valuable contribution to further fuel this promising field of research.

Bibliography

[1] M. Julliere. Tunneling between ferromagnetic films. *Phys. Lett. A*, 54(3):225–226, 1975. doi: 10.1016/0375-9601(75)90174-7.

[2] Baibich et al. Giant Magnetoresistance of (001)Fe/(001)Cr Magnetic Superlattices. *Phys. Rev. Lett.*, 61(21):2472–2475, 1988. doi: 10.1103/PhysRevLett.61.2472.

[3] J. Barnas, A. Fuss, R. E. Camley, P. Grunberg, and W. Zinn. Novel magnetoresistance effect in layered magnetic structures: Theory and experiment. *Phys. Rev. B*, 42(13):8110–8120, 1990. doi: 10.1103/PhysRevB.42.8110.

[4] S. Datta and B. Das. Electronic analog of the electro-optic modulator. *Appl. Phys. Lett.*, 56(7): 665–667, 1990. doi: 10.1063/1.102730.

[5] D. C. Ralph and M. D. Stiles. Spin transfer torques. *J. Magn. Magn. Mater.*, 320(7):1190–1216, 2008. doi: 10.1016/j.jmmm.2007.12.019.

[6] A. Brataas and K. M. D. Hals. Spin-orbit torques in action. *Nat. Nanotechnol.*, 9(2):86–88, 2014. doi: 10.1038/nnano.2014.8.

[7] G. Szulczewski, S. Sanvito, and M. Coey. A spin of their own. *Nat. Mater.*, 8(9):693–695, 2009. doi: 10.1038/nmat2518.

[8] L. Bogani and W. Wernsdorfer. Molecular spintronics using single-molecule magnets. *Nat. Mater.*, 7(3):179–186, 2008. doi: 10.1038/nmat2133.

[9] W. Wernsdorfer. Molecular nanomagnets: towards molecular spintronics. *Int. J. Nanotechnol.*, 7 (4/5/6/7/8):497, 2010. ISSN 5. doi: 10.1504/IJNT.2010.031732.

[10] T. Lis. Preparation, structure, and magnetic properties of a dodecanuclear mixed-valence manganese carboxylate. *Acta Crystallogr. Sect. B Struct. Crystallogr. Cryst. Chem.*, 36(9):2042–2046, 1980. doi: 10.1107/S0567740880007893.

[11] J. R. Friedman, M. P. Sarachik, J. Tejada, J. Maciejewski, and R. Ziolo. Steps in the hysteresis loops of a high-spin molecule. *J. Appl. Phys.*, 79(8):6031–6033, 1996. doi: 10.1063/1.361837.

[12] J. Bartolomé, F. Luis, and J. F. Fernández. *Molecular Magnets*. NanoScience and Technology. Springer Berlin Heidelberg, 2014. ISBN 978-3-642-40608-9. doi: 10.1007/978-3-642-40609-6.

[13] Ardavan et al. Will spin-relaxation times in molecular magnets permit quantum information processing? *Phys. Rev. Lett.*, 98(February):1–4, 2007. doi: 10.1103/PhysRevLett.98.057201.

[14] R. Sessoli, D. Gatteschi, A. Caneschi, and M. A. Novak. Magnetic bistability in a metal-ion cluster. *Nature*, 365(6442):141–143, 1993. doi: 10.1038/365141a0.

[15] Sessoli et al. High-spin molecules: [Mn12O12(O2CR)16(H2O)4]. *J. Am. Chem. Soc.*, 115(5): 1804–1816, 1993. doi: 10.1021/ja00058a027.

[16] G. Christou, D. Gatteschi, D. N. Hendrickson, and R. Sessoli. Single-Molecule Magnets. *MRS Bull.*, 25(11):66–71, 2000. doi: 10.1557/mrs2000.226.

[17] X.-G. Li, J. N. Fry, and H.-P. Cheng. Single-molecule magnet Mn12 on graphene. *Phys. Rev. B*, 90 (12):125447, 2014. doi: 10.1103/PhysRevB.90.125447.

[18] J. M. Clemente-Juan, E. Coronado, and A. Gaita-Ariño. Magnetic polyoxometalates: from molecular magnetism to molecular spintronics and quantum computing. *Chem. Soc. Rev.*, 41(22):7464, 2012. doi: 10.1039/c2cs35205b.

[19] Hampe et al. Mass spectrometric characterization of a dinuclear terbium phthalocyaninato complex. *Int. J. Mass Spectrom.*, 325-327:183–188, 2012. doi: 10.1016/j.ijms.2012.06.011.

[20] N. Ishikawa, M. Sugita, T. Ishikawa, S. Koshihara, and Y. Kaizu. Mononuclear Lanthanide Complexes with a Long Magnetization Relaxation Time at High Temperatures: A New Category of Magnets at the Single-Molecular Level. *J. Phys. Chem. B*, 108(31):11265–11271, 2004. doi: 10.1021/jp0376065.

[21] N. Ishikawa, M. Sugita, and W. Wernsdorfer. Quantum Tunneling of Magnetization in Lanthanide Single-Molecule Magnets: Bis(phthalocyaninato)terbium and Bis(phthalocyaninato)dysprosium Anions. *Angew. Chemie Int. Ed.*, 44(19):2931–2935, 2005. doi: 10.1002/anie.200462638.

[22] W. Wernsdorfer, M. Murugesu, and G. Christou. Resonant Tunneling in Truly Axial Symmetry Mn12 Single-Molecule Magnets: Sharp Crossover between Thermally Assisted and Pure Quantum Tunneling. *Phys. Rev. Lett.*, 96(5):057208, 2006. doi: 10.1103/PhysRevLett.96.057208.

[23] Hernández et al. Field tuning of thermally activated magnetic quantum tunnelling in Mn 12 - Ac molecules. *Europhys. Lett.*, 35(4):301–306, 1996. doi: 10.1209/epl/i1996-00570-7.

[24] Thomas et al. Macroscopic quantum tunnelling of magnetization in a single crystal of nanomagnets. *Nature*, 383(6596):145–147, 1996. doi: 10.1038/383145a0.

[25] C. Zener. Non-Adiabatic Crossing of Energy Levels. *Proc. R. Soc. A Math. Phys. Eng. Sci.*, 137 (833):696–702, 1932. doi: 10.1098/rspa.1932.0165.

[26] A. Garg. Dissipation by nuclear spins in macroscopic magnetization tunneling. *Phys. Rev. Lett.*, 70 (10):1541–1544, 1993. doi: 10.1103/PhysRevLett.70.1541.

[27] W. Wernsdorfer, R. Sessoli, and D. Gatteschi. Nuclear-spin-driven resonant tunnelling of magnetisation in Mn 12 acetate. *Europhys. Lett.*, 47(2):254–259, 1999. doi: 10.1209/epl/i1999-00380-5.

[28] Morello et al. Magnetic dipolar ordering and relaxation in the high-spin molecular cluster compound Mn6. *Phys. Rev. B*, 73(13):134406, 2006. doi: 10.1103/PhysRevB.73.134406.

[29] E. M. Chudnovsky and D. A. Garanin. First- and second-order transitions between quantum and classical regimes for the escape rate of a spin system. *Phys. Rev. Lett.*, 79(22):4469–4472, 1997. doi: 10.1103/PhysRevLett.79.4469.

[30] A. Abragam and B. Bleaney. *Electron Paramagnetic Resonance of Transition Ions*. Oxford University Press, 1970. ISBN 978-0199651528.

[31] R. Orbach. Spin-Lattice Relaxation in Rare-Earth Salts. *Proc. R. Soc. A Math. Phys. Eng. Sci.*, 264(1319):458–484, 1961. doi: 10.1098/rspa.1961.0211.

[32] R. Orbach. On the Theory of Spin-Lattice Relaxation in Paramagnetic Salts. *Proc. Phys. Soc.*, 77 (4):821–826, 1961. doi: 10.1088/0370-1328/77/4/301.

[33] A Einstein and W. J. de Haas. Experimental proof of the existence of Ampere's molecular currents. *K. Akad. van Wet. te Amsterdam, Proc.*, 18(September):696–711, 1915.

[34] M. F. O'Keeffe, E. M. Chudnovsky, and D. A. Garanin. Quantum tunneling of the magnetic moment in a free nanoparticle. *J. Magn. Magn. Mater.*, 324(18):2871–2878, 2012. doi: 10.1016/j.jmmm.2012.04.032.

[35] R. Jaafar, E. M. Chudnovsky, and D. A. Garanin. Single magnetic molecule between conducting leads: Effect of mechanical rotations. *EPL (Europhysics Lett.*, 89(2):27001, 2010. doi: 10.1209/0295-5075/89/27001.

[36] R. Jaafar and E. M. Chudnovsky. Magnetic Molecule on a Microcantilever: Quantum Magnetomechanical Oscillations. *Phys. Rev. Lett.*, 102(22):227202, 2009. doi: 10.1103/PhysRevLett.102.227202.

[37] D. A. Garanin and E. M. Chudnovsky. Quantum Entanglement of a Tunneling Spin with Mechanical Modes of a Torsional Resonator. *Phys. Rev. X*, 1(1):011005, 2011. doi: 10.1103/PhysRevX.1.011005.

[38] A. A. Kovalev, L. X. Hayden, G. E. W. Bauer, and Y. Tserkovnyak. Macrospin Tunneling and Magnetopolaritons with Nanomechanical Interference. *Phys. Rev. Lett.*, 106(14):147203, 2011. doi: 10.1103/PhysRevLett.106.147203.

[39] Kyatskaya et al. Anchoring of Rare-Earth-Based Single-Molecule Magnets on Single-Walled Carbon Nanotubes. *J. Am. Chem. Soc.*, 131(42):15143–15151, 2009. doi: 10.1021/ja906165e.

[40] G. S. Ofelt. Structure of the f6 Configuration with Application to Rare-Earth Ions. *J. Chem. Phys.*, 38(9):2171, 1963. doi: 10.1063/1.1733947.

[41] K. S. Thomas, S. Singh, and G. H. Dieke. Energy Levels of Tb3+ in LaCl3 and Other Chlorides. *J. Chem. Phys.*, 38(9):2180, 1963. doi: 10.1063/1.1733948.

[42] A. Abragam and M. H. L. Pryce. Theory of the Nuclear Hyperfine Structure of Paramagnetic Resonance Spectra in Crystals. *Proc. R. Soc. A Math. Phys. Eng. Sci.*, 205(1080):135–153, 1951. doi: 10.1098/rspa.1951.0022.

[43] K. W. H. Stevens. Matrix Elements and Operator Equivalents Connected with the Magnetic Properties of Rare Earth Ions. *Proc. Phys. Soc. Sect. A*, 65(3):209–215, 1952. doi: 10.1088/0370-1298/65/3/308.

[44] H. A. Buckmaster. TABLES OF MATRIX ELEMENTS FOR THE OPERATORS , , ,. *Can. J. Phys.*, 40(11):1670–1677, 1962. doi: 10.1139/p62-171.

[45] D. Smith and J. H. M. Thornley. The use of 'operator equivalents'. *Proc. Phys. Soc.*, 89(4):779–781, 1966. doi: 10.1088/0370-1328/89/4/301.

[46] Ishikawa et al. Determination of Ligand-Field Parameters and f-Electronic Structures of Double-Decker Bis(phthalocyaninato)lanthanide Complexes. *Inorg. Chem.*, 42(7):2440–2446, 2003. doi: 10.1021/ic026295u.

[47] J. M. Baker, J. R. Chadwick, G. Garton, and J. P. Hurrell. E.p.r. and Endor of TbFormula in Thoria. *Proc. R. Soc. A Math. Phys. Eng. Sci.*, 286(1406):352–365, 1965. doi: 10.1098/rspa.1965.0149.

[48] M. Ganzhorn. *Coupling Magnetism and Mechanics at a molecular scale*. PhD thesis, 2012.

[49] R. Vincent, S. Klyatskaya, M. Ruben, W. Wernsdorfer, and F. Balestro. Electronic read-out of a single nuclear spin using a molecular spin transistor. *Nature*, 488(7411):357–360, 2012. doi: 10.1038/nature11341.

[50] S. Iijima. Helical microtubules of graphitic carbon. *Nature*, 354(6348):56–58, 1991. doi: 10.1038/354056a0.

[51] N. Hamada, S. Sawada, and A. Oshiyama. New one-dimensional conductors: Graphitic microtubules. *Phys. Rev. Lett.*, 68(10):1579–1581, 1992. doi: 10.1103/PhysRevLett.68.1579.

[52] S. Iijima and T. Ichihashi. Single-shell carbon nanotubes of 1-nm diameter. *Nature*, 363(6430):603–605, 1993. doi: 10.1038/363603a0.

[53] Bethune et al. Cobalt-catalysed growth of carbon nanotubes with single-atomic-layer walls. *Nature*, 363(6430):605–607, 1993. doi: 10.1038/363605a0.

[54] Tans et al. Individual single-wall carbon nanotubes as quantum wires. *Nature*, 386(6624):474–477, apr 1997. ISSN 0028-0836. doi: 10.1038/386474a0.

[55] M. Bockrath. Single-Electron Transport in Ropes of Carbon Nanotubes. *Science (80-.).*, 275 (5308):1922–1925, 1997. doi: 10.1126/science.275.5308.1922.

[56] R. Martel, T. Schmidt, H. R. Shea, T. Hertel, and P. Avouris. Single- and multi-wall carbon nanotube field-effect transistors. *Appl. Phys. Lett.*, 73(17):2447–2449, 1998. doi: 10.1063/1.122477.

[57] M. S. Fuhrer, B. M. Kim, T. Dürkop, and T. Brintlinger. High-Mobility Nanotube Transistor Memory. *Nano Lett.*, 2(7):755–759, 2002. doi: 10.1021/nl025577o.

[58] J.-P. Cleuziou, W. Wernsdorfer, V. Bouchiat, T. Ondarçuhu, and M. Monthioux. Carbon nanotube superconducting quantum interference device. *Nat. Nanotechnol.*, 1(1):53–59, 2006. doi: 10.1038/nnano.2006.54.

[59] Qin et al. Superconductivity in a chiral nanotube. *Nat. Commun.*, 8:14465, 2017. doi: 10.1038/ncomms14465.

[60] F. Pei, E. A. Laird, G. A. Steele, and L. P. Kouwenhoven. Valley-spin blockade and spin resonance in carbon nanotubes. *Nat. Nanotechnol.*, 7(10):630–634, 2012. doi: 10.1038/nnano.2012.160.

[61] A. Benyamini, A. Hamo, S. V. Kusminskiy, F. von Oppen, and S. Ilani. Real-space tailoring of the electron-phonon coupling in ultraclean nanotube mechanical resonators. *Nat. Phys.*, 10(2):151–156, 2014. doi: 10.1038/nphys2842.

[62] L. Bogani and W. Wernsdorfer. A perspective on combining molecular nanomagnets and carbon nanotube electronics. *Inorganica Chim. Acta*, 361(14-15):3807–3819, 2008. doi: 10.1016/j.ica.2008.03.074.

[63] M. Urdampilleta, S. Klyatskaya, J.-P. Cleuziou, M. Ruben, and W. Wernsdorfer. Supramolecular spin valves. *Nat. Mater.*, 10(7):502–506, 2011. doi: 10.1038/nmat3050.

[64] M. Ganzhorn, S. Klyatskaya, M. Ruben, and W. Wernsdorfer. Strong spin-phonon coupling between a single-molecule magnet and a carbon nanotube nanoelectromechanical system. *Nat. Nanotechnol.*, 8(3):165–9, 2013. doi: 10.1038/nnano.2012.258.

[65] Zheng et al. Ultralong single-wall carbon nanotubes. *Nat. Mater.*, 3(10):673–676, 2004. doi: 10.1038/nmat1216.

[66] A. H. Castro Neto, N. M. R. Peres, K. S. Novoselov, and A. K. Geim. The electronic properties of graphene. *Rev. Mod. Phys.*, 81(1):109–162, 2009. doi: 10.1103/RevModPhys.81.109.
[67] S. Reich, J. Maultzsch, C. Thomsen, and P. Ordejón. Tight-binding description of graphene. *Phys. Rev. B*, 66(3):035412, 2002. doi: 10.1103/PhysRevB.66.035412.
[68] Hwang et al. Fermi velocity engineering in graphene by substrate modification. *Sci. Rep.*, 2(1):590, 2012. doi: 10.1038/srep00590.
[69] R. Saito, M. Fujita, G. Dresselhaus, and M. S. Dresselhaus. Electronic structure of chiral graphene tubules. *Appl. Phys. Lett.*, 60(18):2204, 1992. doi: 10.1063/1.107080.
[70] E. Minot. *Tuning the bandstructure of carbon nanotubes*. PhD thesis, 2004.
[71] C. L. Kane and E. J. Mele. Size, Shape, and Low Energy Electronic Structure of Carbon Nanotubes. *Phys. Rev. Lett.*, 78(10):1932–1935, 1997. doi: 10.1103/PhysRevLett.78.1932.
[72] I. Cabria, J. W. Mintmire, and C. T. White. Metallic and semiconducting narrow carbon nanotubes. *Phys. Rev. B*, 67(12):121406, 2003. doi: 10.1103/PhysRevB.67.121406.
[73] X. Blase, L. X. Benedict, E. L. Shirley, and S. G. Louie. Hybridization effects and metallicity in small radius carbon nanotubes. *Phys. Rev. Lett.*, 72(12):1878–1881, 1994. doi: 10.1103/PhysRevLett.72.1878.
[74] Minot et al. Tuning Carbon Nanotube Band Gaps with Strain. *Phys. Rev. Lett.*, 90(15):156401, 2003. doi: 10.1103/PhysRevLett.90.156401.
[75] Huang et al. Direct Measurement of Strain-Induced Changes in the Band Structure of Carbon Nanotubes. *Phys. Rev. Lett.*, 100(13):136803, 2008. doi: 10.1103/PhysRevLett.100.136803.
[76] M. I. Katsnelson, K. S. Novoselov, and A. K. Geim. Chiral tunnelling and the Klein paradox in graphene. *Nat. Phys.*, 2(9):620–625, 2006. doi: 10.1038/nphys384.
[77] A. F. Young and P. Kim. Quantum interference and Klein tunnelling in graphene heterojunctions. *Nat. Phys.*, 5(3):222–226, 2009. doi: 10.1038/nphys1198.
[78] R. Landauer. Electrical resistance of disordered one-dimensional lattices. *Philos. Mag.*, 21(172):863–867, 1970. doi: 10.1080/14786437008238472.
[79] M. Büttiker, Y. Imry, R. Landauer, and S. Pinhas. Generalized many-channel conductance formula with application to small rings. *Phys. Rev. B*, 31(10):6207–6215, 1985. doi: 10.1103/PhysRevB.31.6207.
[80] Kong et al. Quantum Interference and Ballistic Transmission in Nanotube Electron Waveguides. *Phys. Rev. Lett.*, 87(10):106801, 2001. doi: 10.1103/PhysRevLett.87.106801.
[81] P. L. McEuen and J. Park. Electron Transport in Single-Walled Carbon Nanotubes. *MRS Bull.*, 29(04):272–275, 2011. doi: 10.1557/mrs2004.79.
[82] Kreupl et al. Carbon nanotubes in interconnect applications. *Microelectron. Eng.*, 64(1-4):399–408, 2002. doi: 10.1016/S0167-9317(02)00814-6.
[83] T. Durkop, S. A. Getty, E. Cobas, and M. S. Fuhrer. Extraordinary Mobility in Semiconducting Carbon Nanotubes. *Nano Lett.*, 4(1):35–39, 2004. doi: 10.1021/nl034841q.
[84] C. Dekker, S. J. Tans, and A. R. M. Verschueren. Room-temperature transistor based on a single carbon nanotube. *Nature*, 393(6680):49–52, 1998. doi: 10.1038/29954.
[85] C. Zhou, J. Kong, and H. Dai. Electrical measurements of individual semiconducting single-walled carbon nanotubes of various diameters. *Appl. Phys. Lett.*, 76(12):1597, 2000. doi: 10.1063/1.126107.
[86] A. Javey, J. Guo, Q. Wang, M. Lundstrom, and H. Dai. Ballistic carbon nanotube field-effect transistors. *Nature*, 424(6949):654–657, 2003. doi: 10.1038/nature01797.
[87] F. Léonard and J. Tersoff. Novel Length Scales in Nanotube Devices. *Phys. Rev. Lett.*, 83(24):5174–5177, 1999. doi: 10.1103/PhysRevLett.83.5174.
[88] F. Léonard and J. Tersoff. Role of Fermi-Level Pinning in Nanotube Schottky Diodes. *Phys. Rev. Lett.*, 84(20):4693–4696, 2000. doi: 10.1103/PhysRevLett.84.4693.
[89] Heinze et al. Carbon Nanotubes as Schottky Barrier Transistors. *Phys. Rev. Lett.*, 89(10):106801, 2002. doi: 10.1103/PhysRevLett.89.106801.
[90] Martel et al. Ambipolar Electrical Transport in Semiconducting Single-Wall Carbon Nanotubes. *Phys. Rev. Lett.*, 87(25):256805, 2001. doi: 10.1103/PhysRevLett.87.256805.
[91] Franklin et al. Integration of suspended carbon nanotube arrays into electronic devices and electromechanical systems. *Appl. Phys. Lett.*, 81(5):913, 2002. doi: 10.1063/1.1497710.

[92] J. Cao, Q. Wang, and H. Dai. Electron transport in very clean, as-grown suspended carbon nanotubes. *Nat. Mater.*, 4(10):745–749, 2005. doi: 10.1038/nmat1478.

[93] J. Park and P. L. McEuen. Formation of a p-type quantum dot at the end of an n-type carbon nanotube. *Appl. Phys. Lett.*, 79(9):1363, 2001. doi: 10.1063/1.1396318.

[94] J. U. Lee, P. P. Gipp, and C. M. Heller. Carbon nanotube p-n junction diodes. *Appl. Phys. Lett.*, 85(1):145, 2004. doi: 10.1063/1.1769595.

[95] J. Nygard and D. H. Cobden. Quantum dots in suspended single-wall carbon nanotubes. *Appl. Phys. Lett.*, 79(25):4216, 2001. doi: 10.1063/1.1428117.

[96] Waissman et al. Realization of pristine and locally tunable one-dimensional electron systems in carbon nanotubes. *Nat. Nanotechnol.*, 8(8):569–574, 2013. doi: 10.1038/nnano.2013.143.

[97] E. McCann and V. I. Fal'ko. Symmetry of boundary conditions of the Dirac equation for electrons in carbon nanotubes. *J. Phys. Condens. Matter*, 16(13):2371–2379, 2004. doi: 10.1088/0953-8984/16/13/016.

[98] F. Kuemmeth, S. Ilani, D. C. Ralph, and P. L. McEuen. Coupling of spin and orbital motion of electrons in carbon nanotubes. *Nature*, 452(7186):448–452, 2008. doi: 10.1038/nature06822.

[99] I. Giaever and H. R. Zeller. Superconductivity of Small Tin Particles Measured by Tunneling. *Phys. Rev. Lett.*, 20(26):1504–1507, 1968. doi: 10.1103/PhysRevLett.20.1504.

[100] T. Fulton and G. Dolan. Observation of single-electron charging effects in small tunnel junctions. *Phys. Rev. Lett.*, 59(1):109–112, 1987. doi: 10.1103/PhysRevLett.59.109.

[101] K. Grove-Rasmussen, H.I. Jorgensen, and P.E. Lindelof. Fabry Perot interference, Kondo effect and Coulomb blockade in carbon nanotubes. *Phys. E Low-dimensional Syst. Nanostructures*, 40(1):92–98, 2007. doi: 10.1016/j.physe.2007.05.015.

[102] J. M. Thijssen and H. S. J. van der Zant. Charge transport and single-electron effects in nanoscale systems. *Phys. status solidi*, 245(8):1455–1470, 2008. doi: 10.1002/pssb.200743470.

[103] Leturcq et al. Franck-Condon blockade in suspended carbon nanotube quantum dots. *Nat. Phys.*, 5(5):327–331, 2009. doi: 10.1038/nphys1234.

[104] S. Sapmaz, P. Jarillo-Herrero, L. P. Kouwenhoven, and H. S. J. van der Zant. Quantum dots in carbon nanotubes. *Semicond. Sci. Technol.*, 21(11):S52–S63, 2006. doi: 10.1088/0268-1242/21/11/S08.

[105] C. Dekker, S. J. Tans, M. H. Devoret, and R. J. A. Groeneveld. Electron-electron correlations in carbon nanotubes. *Nature*, 394(6695):761–764, 1998. doi: 10.1038/29494.

[106] Sapmaz et al. Electronic excitation spectrum of metallic carbon nanotubes. *Phys. Rev. B*, 71(15):153402, 2005. doi: 10.1103/PhysRevB.71.153402.

[107] Y. Oreg, K. Byczuk, and B. I. Halperin. Spin Configurations of a Carbon Nanotube in a Nonuniform External Potential. *Phys. Rev. Lett.*, 85(2):365–368, 2000. doi: 10.1103/PhysRevLett.85.365.

[108] D. V. Averin and K. K. Likharev. Coulomb blockade of single-electron tunneling, and coherent oscillations in small tunnel junctions. *J. Low Temp. Phys.*, 62(3-4):345–373, 1986. doi: 10.1007/BF00683469.

[109] G.-L. Ingold and Y. V. Nazarov. Charge Tunneling Rates in Ultrasmall Junctions. 294:87, 2005. doi: 10.1007/978-1-4757-2166-9_2.

[110] D. V. Averin and A. N. Korotkov. Correlated single-electron tunneling via mesoscopic metal particles: Effects of the energy quantization. *J. Low Temp. Phys.*, 80(3-4):173–185, 1990. doi: 10.1007/BF00683484.

[111] D. Averin, A. Korotkov, and K. Likharev. Theory of single-electron charging of quantum wells and dots. *Phys. Rev. B*, 44(12):6199–6211, 1991. doi: 10.1103/PhysRevB.44.6199.

[112] Kueng et al. Corrigendum: Quantum dot occupation and electron dwell time in the cotunneling regime. *New J. Phys.*, 14(10):109501, 2012. doi: 10.1088/1367-2630/14/10/109501.

[113] J. R. Hauptmann, J. Paaske, and P. E. Lindelof. Electric-field-controlled spin reversal in a quantum dot with ferromagnetic contacts. *Nat. Phys.*, 4(5):373–376, 2008. doi: 10.1038/nphys931.

[114] J. Kondo. Resistance Minimum in Dilute Magnetic Alloys. *Prog. Theor. Phys.*, 32(1):37–49, 1964. doi: 10.1143/PTP.32.37.

[115] D. H. Cobden, J. Nygard, and P. E. Lindelof. Kondo physics in carbon nanotubes. *Nature*, 408(6810):342–346, 2000. doi: 10.1038/35042545.

[116] Jarillo-Herrero et al. Orbital Kondo effect in carbon nanotubes. *Nature*, 434(7032):484–488, 2005. doi: 10.1038/nature03422.

[117] A. Makarovski, A. Zhukov, J. Liu, and G. Finkelstein. SU(2) and SU(4) Kondo effects in carbon nanotube quantum dots. *Phys. Rev. B*, 75(24):241407, 2007. doi: 10.1103/PhysRevB.75.241407.

[118] Liang et al. Fabry-Perot interference in a carbon nanotube electron waveguide. *Nature*, 411(6838): 665–669, 2001. doi: 10.1038/35079517.

[119] H. Ajiki and T. Ando. Electronic States of Carbon Nanotubes. *J. Phys. Soc. Japan*, 62(4):1255–1266, apr 1993. doi: 10.1143/JPSJ.62.1255.

[120] J. P. Lu. Novel Magnetic Properties of Carbon Nanotubes. *Phys. Rev. Lett.*, 74(7):1123–1126, 1995. doi: 10.1103/PhysRevLett.74.1123.

[121] T. Ando. Spin-Orbit Interaction in Carbon Nanotubes. *J. Phys. Soc. Japan*, 69(6):1757–1763, 2000. doi: 10.1143/JPSJ.69.1757.

[122] E. D. Minot, Y. Yaish, V. Sazonova, and P. L. McEuen. Determination of electron orbital magnetic moments in carbon nanotubes. *Nature*, 428(6982):536–539, 2004. doi: 10.1038/nature02425.

[123] Jhang et al. Direct Observation of Band-Gap Closure for a Semiconducting Carbon Nanotube in a Large Parallel Magnetic Field. *Phys. Rev. Lett.*, 106(9):096802, 2011. doi: 10.1103/PhysRevLett.106.096802.

[124] Jarillo-Herrero et al. Electronic Transport Spectroscopy of Carbon Nanotubes in a Magnetic Field. *Phys. Rev. Lett.*, 94(15):156802, 2005. doi: 10.1103/PhysRevLett.94.156802.

[125] Laird et al. Quantum transport in carbon nanotubes. *Rev. Mod. Phys.*, 87(3):703–764, 2015. doi: 10.1103/RevModPhys.87.703.

[126] Jespersen et al. Gate-Dependent Orbital Magnetic Moments in Carbon Nanotubes. *Phys. Rev. Lett.*, 107(18):186802, 2011. doi: 10.1103/PhysRevLett.107.186802.

[127] D. Huertas-Hernando, F. Guinea, and A. Brataas. Spin-orbit coupling in curved graphene, fullerenes, nanotubes, and nanotube caps. *Phys. Rev. B*, 74(15):155426, 2006. doi: 10.1103/PhysRevB.74.155426.

[128] W. Izumida, K. Sato, and R. Saito. Spin-Orbit Interaction in Single Wall Carbon Nanotubes: Symmetry Adapted Tight-Binding Calculation and Effective Model Analysis. *J. Phys. Soc. Japan*, 78(7):074707, 2009. doi: 10.1143/JPSJ.78.074707.

[129] Jespersen et al. Gate-dependent spin-orbit coupling in multielectron carbon nanotubes. *Nat. Phys.*, 7(4):348–353, 2011. doi: 10.1038/nphys1880.

[130] Steele et al. Large spin-orbit coupling in carbon nanotubes. *Nat. Commun.*, 4:1573, 2013. doi: 10.1038/ncomms2584.

[131] J. P. Cleuziou, N. V. N'Guyen, S. Florens, and W. Wernsdorfer. Interplay of the Kondo Effect and Strong Spin-Orbit Coupling in Multihole Ultraclean Carbon Nanotubes. *Phys. Rev. Lett.*, 111(13): 136803, 2013. doi: 10.1103/PhysRevLett.111.136803.

[132] R. Hanson, L. P. Kouwenhoven, J. R. Petta, S. Tarucha, and L. M. K. Vandersypen. Spins in few-electron quantum dots. *Rev. Mod. Phys.*, 79(4):1217–1265, 2007. doi: 10.1103/RevModPhys.79.1217.

[133] van der Wiel et al. Electron transport through double quantum dots. *Rev. Mod. Phys.*, 75(1):1–22, 2002. doi: 10.1103/RevModPhys.75.1.

[134] S. Sapmaz, C. Meyer, P. Beliczynski, P. Jarillo-Herrero, and L. P. Kouwenhoven. Excited State Spectroscopy in Carbon Nanotube Double Quantum Dots. *Nano Lett.*, 6(7):1350–1355, 2006. doi: 10.1021/nl052498e.

[135] G. A. Steele, G. Gotz, and L. P. Kouwenhoven. Tunable few-electron double quantum dots and Klein tunnelling in ultraclean carbon nanotubes. *Nat. Nanotechnol.*, 4(6):363–367, 2009. doi: 10.1038/nnano.2009.71.

[136] L. P. Kouwenhoven, D. G. Austing, and S. Tarucha. Few-electron quantum dots. *Reports Prog. Phys.*, 64(6):701–736, 2001. doi: 10.1088/0034-4885/64/6/201.

[137] K. Ono. Current Rectification by Pauli Exclusion in a Weakly Coupled Double Quantum Dot System. *Science (80-.).*, 297(5585):1313–1317, 2002. doi: 10.1126/science.1070958.

[138] B. Wunsch. Few-electron physics in a nanotube quantum dot with spin-orbit coupling. *Phys. Rev. B*, 79(23):235408, 2009. doi: 10.1103/PhysRevB.79.235408.

[139] J. von Stecher, B. Wunsch, M. Lukin, E. Demler, and A. M. Rey. Double quantum dots in carbon nanotubes. *Phys. Rev. B*, 82(12):125437, 2010. doi: 10.1103/PhysRevB.82.125437.

[140] S. Weiss, E. I. Rashba, F. Kuemmeth, H. O. H. Churchill, and K. Flensberg. Spin-orbit effects in carbon-nanotube double quantum dots. *Phys. Rev. B*, 82(16):165427, 2010. doi: 10.1103/PhysRevB.82.165427.

[141] A. A. Reynoso and K. Flensberg. Dephasing and hyperfine interaction in carbon nanotube double quantum dots: The clean limit. *Phys. Rev. B*, 84(20):205449, 2011. doi: 10.1103/PhysRevB.84.205449.

[142] A. A. Reynoso and K. Flensberg. Dephasing and hyperfine interaction in carbon nanotubes double quantum dots: Disordered case. *Phys. Rev. B*, 85(19):195441, 2012. doi: 10.1103/PhysRevB.85.195441.

[143] Thiele et al. Electrical Readout of Individual Nuclear Spin Trajectories in a Single-Molecule Magnet Spin Transistor. *Phys. Rev. Lett.*, 111(3):037203, 2013. doi: 10.1103/PhysRevLett.111.037203.

[144] Lumetti et al. Single-molecule devices with graphene electrodes. *Dalt. Trans.*, 45(42):16570–16574, 2016. doi: 10.1039/C6DT02445A.

[145] Lopes et al. Surface-Enhanced Raman Signal for Terbium Single-Molecule Magnets Grafted on Graphene. *ACS Nano*, 4(12):7531–7537, 2010. doi: 10.1021/nn1018363.

[146] Schnee et al. Quantum transport in carbon nanotubes covalently functionalized with magnetic molecules. *Phys. status solidi*, 253(12):2424–2427, 2016. doi: 10.1002/pssb.201600292.

[147] Choi et al. Single-Molecule Lysozyme Dynamics Monitored by an Electronic Circuit. *Science (80-.).*, 335(6066):319–324, 2012. doi: 10.1126/science.1214824.

[148] Zbydniewska et al. Charge Blinking Statistics of Semiconductor Nanocrystals Revealed by Carbon Nanotube Single Charge Sensors. *Nano Lett.*, 15(10):6349–6356, 2015. doi: 10.1021/acs.nanolett.5b01338.

[149] M. Urdampilleta, S. Klyatskaya, M. Ruben, and W. Wernsdorfer. Landau-Zener tunneling of a single Tb3 magnetic moment allowing the electronic read-out of a nuclear spin. *Phys. Rev. B*, 87(19):195412, 2013. doi: 10.1103/PhysRevB.87.195412.

[150] Krainov et al. Giant Magnetoresistance in Carbon Nanotubes with Single-Molecule Magnets TbPc 2. *ACS Nano*, 11(7):6868–6880, 2017. doi: 10.1021/acsnano.7b02014.

[151] M. Ganzhorn, S. Klyatskaya, M. Ruben, and W. Wernsdorfer. Carbon Nanotube Nanoelectromechanical Systems as Magnetometers for Single-Molecule Magnets. *ACS Nano*, 7(7):6225–6236, 2013. doi: 10.1021/nn402968k.

[152] M. Ganzhorn, S. Klyatskaya, M. Ruben, and W. Wernsdorfer. Quantum Einstein-de Haas effect. *Nat. Commun.*, 7:11443, apr 2016. doi: 10.1038/ncomms11443.

[153] L. Landau. The Theory of Phase Transitions. *Nature*, 138(3498):840–841, 1936. doi: 10.1038/138840a0.

[154] Landau Ginzburg. ON THE THEORY OF SUPERCONDUCTIVITY. In *Collect. Pap. L.D. Landau*, pages 546–568. Elsevier, 1965. doi: 10.1016/B978-0-08-010586-4.50078-X.

[155] J. Bardeen, L. Cooper, and J. Schrieffer. Microscopic Theory of Superconductivity. *Phys. Rev.*, 106(1):162–164, apr 1957. doi: 10.1103/PhysRev.106.162.

[156] T. H. Hansson, V. Oganesyan, and S. L. Sondhi. Superconductors are topologically ordered. *Ann. Phys. (N. Y).*, 313(2):497–538, 2004. doi: 10.1016/j.aop.2004.05.006.

[157] K. V. Klitzing, G. Dorda, and M. Pepper. New Method for High-Accuracy Determination of the Fine-Structure Constant Based on Quantized Hall Resistance. *Phys. Rev. Lett.*, 45(6):494–497, 1980. doi: 10.1103/PhysRevLett.45.494.

[158] D. C. Tsui, H. L. Stormer, and A. C. Gossard. Two-Dimensional Magnetotransport in the Extreme Quantum Limit. *Phys. Rev. Lett.*, 48(22):1559–1562, 1982. doi: 10.1103/PhysRevLett.48.1559.

[159] M. Z. Hasan and C. L. Kane. Colloquium : Topological insulators. *Rev. Mod. Phys.*, 82(4):3045–3067, 2010. doi: 10.1103/RevModPhys.82.3045.

[160] D. J. Thouless, M. Kohmoto, M. P. Nightingale, and M. den Nijs. Quantized Hall Conductance in a Two-Dimensional Periodic Potential. *Phys. Rev. Lett.*, 49(6):405–408, 1982. doi: 10.1103/PhysRevLett.49.405.

[161] X.-L. Qi, Y.-S. Wu, and S.-C. Zhang. General theorem relating the bulk topological number to edge states in two-dimensional insulators. *Phys. Rev. B*, 74(4):045125, 2006. doi: 10.1103/PhysRevB.74.045125.

[162] Koenig et al. Quantum Spin Hall Insulator State in HgTe Quantum Wells. *Science (80-.).*, 318 (5851):766–770, 2007. doi: 10.1126/science.1148047.

[163] J. Maciejko, T. L. Hughes, and S.-C. Zhang. The Quantum Spin Hall Effect. *Annu. Rev. Condens. Matter Phys.*, 2(1):31–53, 2011. doi: 10.1146/annurev-conmatphys-062910-140538.

[164] F. D. M. Haldane. Model for a Quantum Hall Effect without Landau Levels: Condensed-Matter Realization of the "Parity Anomaly". *Phys. Rev. Lett.*, 61(18):2015–2018, 1988. doi: 10.1103/PhysRevLett.61.2015.

[165] S. M. Girvin and A. H. MacDonald. Off-diagonal long-range order, oblique confinement, and the fractional quantum Hall effect. *Phys. Rev. Lett.*, 58(12):1252–1255, mar 1987. doi: 10.1103/PhysRevLett.58.1252.

[166] E. Witten. Quantum field theory and the Jones polynomial. *Commun. Math. Phys.*, 121(3):351–399, 1989. doi: 10.1007/BF01217730.

[167] S. C. Zhang. THE CHERN-SIMONS-LANDAU-GINZBURG THEORY OF THE FRACTIONAL QUANTUM HALL EFFECT. *Int. J. Mod. Phys. B*, 06(01):25–58, 1992. doi: 10.1142/S0217979292000037.

[168] X.-G. Wen. Topological orders and edge excitations in fractional quantum Hall states. *Adv. Phys.*, 44(5):405–473, 1995. doi: 10.1080/00018739500101566.

[169] X. Chen, Z. C. Gu, and X. G. Wen. Local unitary transformation, long-range quantum entanglement, wave function renormalization, and topological order. *Phys. Rev. B - Condens. Matter Mater. Phys.*, 82(15):1–29, 2010. doi: 10.1103/PhysRevB.82.155138.

[170] X.-G. Wen. Zoo of quantum-topological phases of matter. *Phys. Rev. X*, 6(1):011016, 2016.

[171] A. Y. Kitaev. Fault-tolerant quantum computation by anyons. *Ann. Phys. (N. Y).*, 303(1):2–30, 2003. doi: 10.1016/S0003-4916(02)00018-0.

[172] G. Moore and N. Read. Nonabelions in the fractional quantum hall effect. *Nucl. Phys. B*, 360(2-3):362–396, 1991. doi: 10.1016/0550-3213(91)90407-O.

[173] A. Stern. Non-Abelian states of matter. *Nature*, 464(7286):187–193, 2010. doi: 10.1038/nature08915.

[174] A. Y. Kitaev. Unpaired Majorana fermions in quantum wires. *Physics-Uspekhi*, 44(10S):131–136, 2001. doi: 10.1070/1063-7869/44/10S/S29.

[175] L. Fu and C. L. Kane. Superconducting proximity effect and majorana fermions at the surface of a topological insulator. *Phys. Rev. Lett.*, 100(9):1–4, 2008. doi: 10.1103/PhysRevLett.100.096407.

[176] Mourik et al. Signatures of Majorana Fermions in Hybrid Superconductor-Semiconductor Nanowire Devices. *Science (80-.).*, 336(6084):1003–1007, 2012. doi: 10.1126/science.1222360.

[177] C. L. Kane and E. J. Mele. Quantum Spin Hall Effect in Graphene. *Phys. Rev. Lett.*, 95(22):226801, 2005. doi: 10.1103/PhysRevLett.95.226801.

[178] C. L. Kane and E. J. Mele. Z2 topological order and the quantum spin hall effect. *Phys. Rev. Lett.*, 95(14):3–6, 2005. doi: 10.1103/PhysRevLett.95.146802.

[179] L. Fu and C. L. Kane. Topological insulators with inversion symmetry. *Phys. Rev. B*, 76(4):045302, 2007. doi: 10.1103/PhysRevB.76.045302.

[180] Min et al. Intrinsic and Rashba spin-orbit interactions in graphene sheets. *Phys. Rev. B - Condens. Matter Mater. Phys.*, 74(16):1–5, 2006. doi: 10.1103/PhysRevB.74.165310.

[181] B. A. Bernevig, T. L. Hughes, and S.-C. Zhang. Quantum Spin Hall Effect and Topological Phase Transition in HgTe Quantum Wells. *Science (80-.).*, 314(5806):1757–1761, 2006. doi: 10.1126/science.1133734.

[182] Brüne et al. Spin polarization of the quantum spin Hall edge states. *Nat. Phys.*, 8(6):485–490, 2012. doi: 10.1038/nphys2322.

[183] L. Fu, C. L. Kane, and E. J. Mele. Topological Insulators in Three Dimensions. *Phys. Rev. Lett.*, 98(10):106803, 2007. doi: 10.1103/PhysRevLett.98.106803.

[184] J. E. Moore and L. Balents. Topological invariants of time-reversal-invariant band structures. *Phys. Rev. B*, 75(12):121306, 2007. doi: 10.1103/PhysRevB.75.121306.

[185] I. C. Fulga, B. van Heck, J. M. Edge, and A. R. Akhmerov. Statistical topological insulators. *Phys. Rev. B*, 89(15):155424, 2014. doi: 10.1103/PhysRevB.89.155424.

[186] F. Ortmann, S. Roche, and S. O. Valenzuela. *Topological Insulators*. Wiley-VCH Verlag GmbH & Co. KGaA, 2015. doi: 10.1002/9783527681594.

[187] X. L. Qi, T. L. Hughes, and S. C. Zhang. Topological field theory of time-reversal invariant insulators. *Phys. Rev. B - Condens. Matter Mater. Phys.*, 78(19):1–43, 2008. doi: 10.1103/PhysRevB.78.195424.

[188] X. Qi and S. Zhang. The quantum spin Hall effect and topological insulators. *Phys. Today*, 63(1): 33, 2010. doi: 10.1063/1.3293411.

[189] E. Rotenberg. Topological insulators: The dirt on topology. *Nat. Phys.*, 7(1):8–10, 2011. doi: 10.1038/nphys1869.

[190] J. C. Y. Teo, L. Fu, and C. L. Kane. Surface states and topological invariants in three-dimensional topological insulators. *Phys. Rev. B*, 78(4):045426, 2008. doi: 10.1103/PhysRevB.78.045426.

[191] Hsieh et al. A tunable topological insulator in the spin helical Dirac transport regime. *Nature*, 460 (7259):1101–1105, 2009. doi: 10.1038/nature08234.

[192] Hsieh et al. Observation of Unconventional Quantum Spin Textures in Topological Insulators. *Science (80-.).*, 323(5916):919–922, 2009. doi: 10.1126/science.1167733.

[193] Roushan et al. Topological surface states protected from backscattering by chiral spin texture. *Nature*, 460(7259):1106–1109, 2009. doi: 10.1038/nature08308.

[194] Hor et al. p-type Bi2Se3 for topological insulator and low-temperature thermoelectric applications. *Phys. Rev. B*, 79(19):195208, 2009. doi: 10.1103/PhysRevB.79.195208.

[195] Xia et al. Observation of a large-gap topological-insulator class with a single Dirac cone on the surface. *Nat. Phys.*, 5(6):398–402, 2009. doi: 10.1038/nphys1274.

[196] Chen et al. Experimental Realization of a Three-Dimensional Topological Insulator, Bi2Te3. *Science (80-.).*, 325(5937):178–181, 2009. doi: 10.1126/science.1173034.

[197] Hsieh et al. Observation of time-reversal-protected single-dirac-cone topological-insulator states in Bi2Te3 and Sb2Te3. *Phys. Rev. Lett.*, 103(14):2–5, 2009. doi: 10.1103/PhysRevLett.103.146401.

[198] J. Black, E.M. Conwell, L. Seigle, and C.W. Spencer. Electrical and optical properties of some M2v-bN3vi-b semiconductors. *J. Phys. Chem. Solids*, 2(3):240–251, 1957. doi: 10.1016/0022-3697(57)90090-2.

[199] Zhang et al. Band structure engineering in (Bi1-xSbx)2Te3 ternary topological insulators. *Nat. Commun.*, 2:574, 2011. doi: 10.1038/ncomms1588.

[200] Arakane et al. Tunable Dirac cone in the topological insulator Bi2-xSbxTe3-ySey. *Nat. Commun.*, 3, 2012. doi: 10.1038/ncomms1639.

[201] L. Fu. Topological Crystalline Insulators. *Phys. Rev. Lett.*, 106(10):106802, 2011. doi: 10.1103/PhysRevLett.106.106802.

[202] Y. Ando and L. Fu. Topological Crystalline Insulators and Topological Superconductors: From Concepts to Materials. *Annu. Rev. Condens. Matter Phys.*, 6(1):361–381, 2015. doi: 10.1146/annurev-conmatphys-031214-014501.

[203] Hsieh et al. Topological crystalline insulators in the SnTe material class. *Nat. Commun.*, 3(1):982, jan 2012. ISSN 2041-1723. doi: 10.1038/ncomms1969.

[204] M. Serbyn and L. Fu. Symmetry breaking and Landau quantization in topological crystalline insulators. *Phys. Rev. B - Condens. Matter Mater. Phys.*, 90(3):1–10, 2014. doi: 10.1103/PhysRevB.90.035402.

[205] C. Fang, M. J. Gilbert, and B. A. Bernevig. Large-Chern-Number Quantum Anomalous Hall Effect in Thin-Film Topological Crystalline Insulators. *Phys. Rev. Lett.*, 112(4):046801, 2014. doi: 10.1103/PhysRevLett.112.046801.

[206] F. Assaad. Interface superconductivity: Get it strained. *Nat. Phys.*, 10(12):905–905, 2014. doi: 10.1038/nphys3161.

[207] Liu et al. Spin-filtered edge states with an electrically tunable gap in a two-dimensional topological crystalline insulator. *Nat. Mater.*, 13(2):178–183, 2013. doi: 10.1038/nmat3828.

[208] J. Linder, T. Yokoyama, and A. Sudbo. Anomalous finite size effects on surface states in the topological insulator Bi2Se3. *Phys. Rev. B*, 80(20):205401, nov 2009. doi: 10.1103/PhysRevB.80.205401.

[209] H.-Z. Lu, W.-Y. Shan, W. Yao, Q. Niu, and S.-Q. Shen. Massive Dirac fermions and spin physics in an ultrathin film of topological insulator. *Phys. Rev. B*, 81(11):115407, mar 2010. doi: 10.1103/PhysRevB.81.115407.

[210] J. O. Dimmock, I. Melngailis, and A. J. Strauss. Band Structure and Laser Action in PbSnTe. *Phys. Rev. Lett.*, 16(26):1193–1196, 1966. doi: 10.1103/PhysRevLett.16.1193.

[211] B. A. Volkov and O. A. Pankratov. Two-dimensional massless electrons in an inverted contact, 1985. ISSN 0021-3640.

[212] Y. W. Tung and M. L. Cohen. Relativistic Band Structure and Electronic Properties of SnTe, GeTe, and PbTe. *Phys. Rev.*, 180(3):823–826, 1969. doi: 10.1103/PhysRev.180.823.

[213] E. Rogacheva. Nonstoichiometry and Properties of SnTe Semiconductor Phase of Variable Composition. In *Stoichiom. Mater. Sci. - When Numbers Matter*. InTech, 2012. ISBN 978-953-51-0512-1.

[214] J. Shen, J. M. Woods, Y. Xie, M. D. Morales-Acosta, and J. J. Cha. Structural Phase Transition and Carrier Density Tuning in SnSe x Te 1- x Nanoplates. *Adv. Electron. Mater.*, 2(9):1600144, 2016. doi: 10.1002/aelm.201600144.

[215] Tanaka et al. Experimental realization of a topological crystalline insulator in SnTe. *Nat. Phys.*, 8 (11):800–803, 2012. doi: 10.1038/nphys2442.

[216] J. Liu, W. Duan, and L. Fu. Two types of surface states in topological crystalline insulators. *Phys. Rev. B*, 88(24):241303, 2013. doi: 10.1103/PhysRevB.88.241303.

[217] Tanaka et al. Two types of Dirac-cone surface states on the (111) surface of the topological crystalline insulator SnTe. *Phys. Rev. B*, 88(23):235126, 2013. doi: 10.1103/PhysRevB.88.235126.

[218] S. Hikami, A. I. Larkin, and Y. Nagaoka. Spin-Orbit Interaction and Magnetoresistance in the Two Dimensional Random System. *Prog. Theor. Phys.*, 63(2):707–710, 1980. doi: 10.1143/PTP.63.707.

[219] Li et al. Experimental evidence and control of the bulk-mediated intersurface coupling in topological insulator Bi2Te2Se nanoribbons. *Phys. Rev. B*, 91(4):041401, 2015. doi: 10.1103/PhysRevB.91.041401.

[220] Assaf et al. Quantum coherent transport in SnTe topological crystalline insulator thin films. *Appl. Phys. Lett.*, 105(10):102108, 2014. doi: 10.1063/1.4895456.

[221] M. Iizumi, Y. Hamaguchi, K. F. Komatsubara, and Y. Kato. Phase Transition in SnTe with Low Carrier Concentration. *J. Phys. Soc. Japan*, 38(2):443–449, 1975. doi: 10.1143/JPSJ.38.443.

[222] E. Plekhanov, P. Barone, D. Di Sante, and S. Picozzi. Engineering relativistic effects in ferroelectric SnTe. *Phys. Rev. B*, 90(16):161108, 2014. doi: 10.1103/PhysRevB.90.161108.

[223] W. Meissner and R. Ochsenfeld. Ein neuer Effekt bei Eintritt der Supraleitfaehigkeit. *Naturwissenschaften*, 21(44):787–788, 1933. doi: 10.1007/BF01504252.

[224] E. Maxwell. Isotope Effect in the Superconductivity of Mercury. *Phys. Rev.*, 78(4):477–477, 1950. doi: 10.1103/PhysRev.78.477.

[225] F. London and H. London. The Electromagnetic Equations of the Supraconductor. *Proc. R. Soc. A Math. Phys. Eng. Sci.*, 149(866):71–88, 1935. doi: 10.1098/rspa.1935.0048.

[226] B. D. Josephson. Possible new effects in superconductive tunnelling. *Phys. Lett.*, 1(7):251–253, 1962. doi: 10.1016/0031-9163(62)91369-0.

[227] A. Andreev. The Thermal Conductivity of the Intermediate State in Superconductors. *JETP*, 19 (5):1228, 1964. doi: 10.1070/PU1976v019n02ABEH005133.

[228] I. O. Kulik. Macroscopic Quantization and the Proximity Effect in S-N-S Junctions. *Zh. Eksp. Teor. Fiz*, 30(57):1745–1759, 1970. ISSN 1063-7761.

[229] G. E. Blonder, M. Tinkham, and T. M. Klapwijk. Transition from metallic to tunneling regimes in superconducting microconstrictions: Excess current, charge imbalance, and supercurrent conversion. *Phys. Rev. B*, 25(7):4515–4532, 1982. doi: 10.1103/PhysRevB.25.4515.

[230] I. Giaever. Energy Gap in Superconductors Measured by Electron Tunneling. *Phys. Rev. Lett.*, 5 (4):147–148, 1960. doi: 10.1103/PhysRevLett.5.147.

[231] I. Giaever. Electron Tunneling Between Two Superconductors. *Phys. Rev. Lett.*, 5(10):464–466, 1960. doi: 10.1103/PhysRevLett.5.464.

[232] R. Feynman, R. Leighton, and M. Sands. The Schrödinger Equation in a Classical Context: A Seminar on Superconductivity. In *Feynman Lect. Physics, Vol. III*. 1965. ISBN 978-0201021189.

[233] S. Shapiro. Josephson Currents in Superconducting Tunneling: The Effect of Microwaves and Other Observations. *Phys. Rev. Lett.*, 11(2):80–82, 1963. doi: 10.1103/PhysRevLett.11.80.

[234] R. C. Jaklevic, J. Lambe, A. H. Silver, and J. E. Mercereau. Quantum Interference Effects in Josephson Tunneling. *Phys. Rev. Lett.*, 12(7):159–160, 1964. doi: 10.1103/PhysRevLett.12.159.

[235] Della Rocca et al. Measurement of the current-phase relation of superconducting atomic contacts. *Phys. Rev. Lett.*, 99(12), 2007. doi: 10.1103/PhysRevLett.99.127005.

[236] Faucher et al. Niobium and niobium nitride SQUIDs based on anodized nanobridges made with an atomic force microscope. *Phys. C Supercond. its Appl.*, 368(1-4):211–217, 2002. doi: 10.1016/S0921-4534(01)01168-6.

[237] G.-H. Lee, S. Kim, S.-H. Jhi, and H.-J. Lee. Ultimately short ballistic vertical graphene Josephson junctions. *Nat. Commun.*, 6(1):6181, 2015. doi: 10.1038/ncomms7181.

[238] J. Bardeen and J. Johnson. Josephson Current Flow in Pure Superconducting-Normal-Superconducting Junctions. *Phys. Rev. B*, 5(1):72–78, 1972. doi: 10.1103/PhysRevB.5.72.

[239] A. Barone and G. Paternò. *Physics and Applications of the Josephson Effect*. Wiley-VCH Verlag GmbH & Co. KGaA, 1982. doi: 10.1002/352760278X.

[240] K. Hasselbach, D. Mailly, and J. R. Kirtley. Micro-superconducting quantum interference device characteristics. *J. Appl. Phys.*, 91(7):4432–4437, 2002. doi: 10.1063/1.1448864.

[241] K. K. Likharev. Superconducting weak links. *Rev. Mod. Phys.*, 51(1):101–159, 1979. doi: 10.1103/RevModPhys.51.101.

[242] A. I. Buzdin. Proximity effects in superconductor-ferromagnet heterostructures. *Rev. Mod. Phys.*, 77(3):935–976, 2005. doi: 10.1103/RevModPhys.77.935.

[243] C.-T. Chen, C. C. Tsuei, M. B. Ketchen, Z.-A. Ren, and Z. X. Zhao. Integer and half-integer flux-quantum transitions in a niobium-iron pnictide loop. *Nat. Phys.*, 6(4):260–264, apr 2010. doi: 10.1038/nphys1531.

[244] C. C. Tsuei and J. R. Kirtley. Pairing symmetry in cuprate superconductors. *Rev. Mod. Phys.*, 72 (4):969–1016, oct 2000. doi: 10.1103/RevModPhys.72.969.

[245] J. J. A. Baselmans, B. J. van Wees, and T. M. Klapwijk. Direct demonstration of circulating currents in a controllable π-SQUID generated by a 0 to π transition of the weak links. *Phys. Rev. B*, 65(22):224513, jun 2002. doi: 10.1103/PhysRevB.65.224513.

[246] Sickinger et al. Experimental Evidence of a <math display="inline"> <mi>ϕ</mi> </math> Josephson Junction. *Phys. Rev. Lett.*, 109(10):107002, 2012. doi: 10.1103/PhysRevLett.109.107002.

[247] Szombati et al. Josephson varphi-junction in nanowire quantum dots. *Nat. Phys.*, 12(6):568–572, 2016. ISSN 1745-2473. doi: 10.1038/nphys3742.

[248] H. Meissner. Superconductivity of Contacts with Interposed Barriers. *Phys. Rev.*, 117(3):672–680, 1960. doi: 10.1103/PhysRev.117.672.

[249] C.-R. Hu. Midgap surface states as a novel signature for d-wave Superconductivity. *Phys. Rev. Lett.*, 72(10):1526–1529, 1994. doi: 10.1103/PhysRevLett.72.1526.

[250] C. Kallin and J. Berlinsky. Chiral superconductors. *Reports Prog. Phys.*, 79(5):054502, 2016. doi: 10.1088/0034-4885/79/5/054502.

[251] A. P. Mackenzie and Y. Maeno. p-wave superconductivity. *Phys. B Condens. Matter*, 280(1-4): 148–153, 2000. doi: 10.1016/S0921-4526(99)01546-X.

[252] A. Schofield. There and back again: from magnets to superconductors. *Physics (College. Park. Md).*, 2:93, 2009. doi: 10.1103/Physics.2.93.

[253] M. Sato and Y. Ando. Topological superconductors: a review. *Reports Prog. Phys.*, 80(7):076501, 2017. doi: 10.1088/1361-6633/aa6ac7.

[254] M. Leijnse and K. Flensberg. Introduction to topological superconductivity and Majorana fermions. 1:1–21, 2012. doi: 10.1088/0268-1242/27/12/124003.

[255] N. Read and D. Green. Paired states of fermions in two dimensions with breaking of parity and time-reversal symmetries and the fractional quantum Hall effect. *Phys. Rev. B*, 61(15):10267–10297, 2000. doi: 10.1103/PhysRevB.61.10267.

[256] D. A. Ivanov. Non-Abelian Statistics of Half-Quantum Vortices in p-Wave Superconductors. *Phys. Rev. Lett.*, 86(2):268–271, 2001. doi: 10.1103/PhysRevLett.86.268.

[257] H.-J. Kwon, K. Sengupta, and V. M. Yakovenko. Fractional ac Josephson effect in p- and d-wave superconductors. *Eur. Phys. J. B - Condens. Matter*, 37(3):349–361, 2003. doi: 10.1140/epjb/e2004-00066-4.

[258] Das et al. Zero-bias peaks and splitting in an Al-InAs nanowire topological superconductor as a signature of Majorana fermions. *Nat. Phys.*, 8(12):887–895, 2012. doi: 10.1038/nphys2479.

[259] Deng et al. Majorana bound state in a coupled quantum-dot hybrid-nanowire system. *Science (80-.).*, 354(6319):1557–1562, 2016. doi: 10.1126/science.aaf3961.

[260] C.-K. Chiu, J. D. Sau, and S. Das Sarma. Conductance of a superconducting Coulomb-blockaded Majorana nanowire. *Phys. Rev. B*, 96(5):054504, 2017. doi: 10.1103/PhysRevB.96.054504.

[261] E. B. Hansen, J. Danon, and K. Flensberg. Probing electron-hole components of subgap states in Coulomb blockaded Majorana islands. 041411:1–5, 2017. doi: arXiv:1712.07972v2.

[262] M. Snelder, M. Veldhorst, A. A. Golubov, and A. Brinkman. Andreev bound states and current-phase relations in three-dimensional topological insulators. *Phys. Rev. B*, 87(10):104507, 2013. doi: 10.1103/PhysRevB.87.104507.

[263] M. Veldhorst, C. G. Molenaar, C. J. M. Verwijs, H. Hilgenkamp, and A. Brinkman. Optimizing the Majorana character of SQUIDs with topologically nontrivial barriers. *Phys. Rev. B*, 86(2):024509, 2012. doi: 10.1103/PhysRevB.86.024509.

[264] Sochnikov et al. Nonsinusoidal Current-Phase Relationship in Josephson Junctions from the 3D Topological Insulator HgTe. *Phys. Rev. Lett.*, 114(6):066801, 2015. doi: 10.1103/PhysRevLett.114.066801.

[265] C. Kurter, A. D. K. Finck, Y. S. Hor, and D. J. Van Harlingen. Evidence for an anomalous current-phase relation in topological insulator Josephson junctions. *Nat. Commun.*, 6(1):7130, 2015.

[266] Wiedenmann et al. 4π-periodic Josephson supercurrent in HgTe-based topological Josephson junctions. *Nat. Commun.*, 7:10303, 2016. doi: 10.1038/ncomms10303.

[267] Bocquillon et al. Gapless Andreev bound states in the quantum spin Hall insulator HgTe. *Nat. Nanotechnol.*, 12(2):137–143, 2016. doi: 10.1038/nnano.2016.159.

[268] C. Fang, M. J. Gilbert, and B. A. Bernevig. New Class of Topological Superconductors Protected by Magnetic Group Symmetries. *Phys. Rev. Lett.*, 112(10):106401, 2014. doi: 10.1103/PhysRevLett.112.106401.

[269] Snyder et al. Josephson Junctions with Weak Links of Topological Crystalline Insulators. pages 1–5, 2017.

[270] A. Manchon, H. C. Koo, J. Nitta, S. M. Frolov, and R. A. Duine. New perspectives for Rashba spin-orbit coupling. *Nat. Mater.*, 14(9):871–882, sep 2015. doi: 10.1038/nmat4360.

[271] C. R. Reeg and D. L. Maslov. Proximity-induced triplet superconductivity in Rashba materials. *Phys. Rev. B*, 92(13):134512, oct 2015. doi: 10.1103/PhysRevB.92.134512.

[272] Pientka et al. Topological Superconductivity in a Planar Josephson Junction. *Phys. Rev. X*, 7(2):021032, may 2017. doi: 10.1103/PhysRevX.7.021032.

[273] P. Fulde and R. A. Ferrell. Superconductivity in a Strong Spin-Exchange Field. *Phys. Rev.*, 135 (3A):A550–A563, 1964. ISSN 0031-899X. doi: 10.1103/PhysRev.135.A550.

[274] A. I. Larkin and Y. N. Ovchinnikov. Nonuniform state of superconductors. *Sov. Phys. JETP*, 20 (762), 1965.

[275] Qu et al. Topological superfluids with finite-momentum pairing and Majorana fermions. *Nat. Commun.*, 4:1–7, oct 2013. doi: 10.1038/ncomms3710.

[276] Hart et al. Controlled finite momentum pairing and spatially varying order parameter in proximitized HgTe quantum wells. *Nat. Phys.*, 13(1):87–93, sep 2016. ISSN 1745-2473. doi: 10.1038/nphys3877.

[277] Chen et al. Finite momentum Cooper pairing in 3D topological insulator Josephson junctions. *arXiv Mesoscale Nanoscale Phys.*, pages 1–22. doi: arXiv:1801.08504v1.

[278] Murani et al. Ballistic edge states in Bismuth nanowires revealed by SQUID interferometry. *Nat. Commun.*, 8(May):15941, jul 2017. doi: 10.1038/ncomms15941.

[279] C. D. Scott, S. Arepalli, P. Nikolaev, and R. E. Smalley. Erratum to: Growth mechanisms for single-wall carbon nanotubes in a laser ablation process. *Appl. Phys. A*, 74(1):11–11, 2002. doi: 10.1007/s003390101005.

[280] J. P. Gore and A. Sane. Flame Synthesis of Carbon Nanotubes. In *Carbon Nanotub. - Synth. Charact. Appl.* InTech, 2011. doi: 10.5772/21012.

[281] A. Holmen, O. A. Rokstad, and A. Solbakken. High-Temperature Pyrolysis of Hydrocarbons. 1. Methane to Acetylene. *Ind. Eng. Chem. Process Des. Dev.*, 15(3):439–444, 1976. doi: 10.1021/i260059a017.

[282] Nathan R. Franklin, Yiming Li, Robert J. Chen, Ali Javey, and Hongjie Dai. Patterned growth of single-walled carbon nanotubes on full 4-inch wafers. *Appl. Phys. Lett.*, 79(27):4571, 2001. doi: 10.1063/1.1429294.

[283] M. Kumar and Y. Ando. Chemical Vapor Deposition of Carbon Nanotubes: A Review on Growth Mechanism and Mass Production. *J. Nanosci. Nanotechnol.*, 10(6):3739–3758, 2010. doi: 10.1166/jnn.2010.2939.

[284] J. Furer. *Growth of Single-Wall Carbon Nanotubes by Chemical Vapor Deposition for Electrical Devices*. PhD thesis, 2006.

[285] V. N. N'Guyen. *Synthèse et transport électronique dans des nanotubes de carbone ultra- propres*. PhD thesis, 2012.

[286] Hines et al. Nanotransfer printing of organic and carbon nanotube thin-film transistors on plastic substrates. *Appl. Phys. Lett.*, 86(16):163101, 2005. doi: 10.1063/1.1901809.

[287] V. K. Sangwan, V. W. Ballarotto, M. S. Fuhrer, and E. D. Williams. Facile fabrication of suspended as-grown carbon nanotube devices. *Appl. Phys. Lett.*, 93(11):113112, 2008. doi: 10.1063/1.2987457.

[288] C. C. Wu, C. H. Liu, and Z. Zhong. One-Step Direct Transfer of Pristine Single-Walled Carbon Nanotubes for Functional Nanoelectronics. *Nano Lett.*, 10(3):1032–1036, 2010. doi: 10.1021/nl904260k.

[289] J. Gramich, A. Baumgartner, M. Muoth, C. Hierold, and C. Schönenberger. Fork stamping of pristine carbon nanotubes onto ferromagnetic contacts for spin-valve devices. *Phys. status solidi*, 252(11):2496–2502, 2015. doi: 10.1002/pssb.201552213.

[290] Jung et al. Ultraclean Single, Double, and Triple Carbon Nanotube Quantum Dots with Recessed Re Bottom Gates. *Nano Lett.*, 13(9):4522–4526, 2013. doi: 10.1021/nl402455n.

[291] Jorio et al. Characterizing carbon nanotube samples with resonance Raman scattering. *New J. Phys.*, 5(1):139–139, 2003. doi: 10.1088/1367-2630/5/1/139.

[292] Jorio et al. Structural (n,m) Determination of Isolated Single-Wall Carbon Nanotubes by Resonant Raman Scattering. *Phys. Rev. Lett.*, 86(6):1118–1121, 2001. doi: 10.1103/PhysRevLett.86.1118.

[293] M. Milnera, R. Rouse, and R. Rouse. Periodic resonance excitation and intertube interaction from quasicontinuous distributed helicities in single-wall carbon nanotubes. *Phys. Rev. Lett.*, 84(6):1324–1327, 2000. doi: 10.1103/PhysRevLett.84.1324.

[294] Ishikawa et al. Upward temperature shift of the intrinsic phase lag of the magnetization of bis(phthalocyaninato)terbium by ligand oxidation creating an S = 1/2 spin. *Inorg. Chem.*, 43(18):5498–5500, 2004. doi: 10.1021/ic049348b.

[295] Gómez-Segura et al. 2-D Self-assembly of the bis(phthalocyaninato)terbium single-molecule magnet studied by scanning tunnelling microscopy. *Chem. Commun.*, (27):2866–2868, 2006. doi: 10.1039/B606276H.

[296] Zhang et al. High thermoelectric performance by resonant dopant indium in nanostructured SnTe. *Proc. Natl. Acad. Sci.*, 110(33):13261–13266, 2013. doi: 10.1073/pnas.1305735110.

[297] I. Garate and L. Glazman. Weak localization and antilocalization in topological insulator thin films with coherent bulk-surface coupling. *Phys. Rev. B*, 86(3):035422, 2012. doi: 10.1103/PhysRevB.86.035422.

[298] R. Akiyama, K. Fujisawa, T. Yamaguchi, R. Ishikawa, and S. Kuroda. Two-dimensional quantum transport of multivalley (111) surface state in topological crystalline insulator SnTe thin films. *Nano Res.*, 9(2):490–498, 2016. doi: 10.1007/s12274-015-0930-8.

[299] C. Enss and S. Hunklinger. *Low-temperature physics*. Springer Berlin Heidelberg, 2005. ISBN 9783540231646.

[300] D. Gerstenberg and P. M. Hall. Superconducting Thin Films of Niobium, Tantalum, Tantalum Nitride, Tantalum Carbide, and Niobium Nitride. *J. Electrochem. Soc.*, 111(8):936, 1964. doi: 10.1149/1.2426296.

[301] J. R. Rairden and C. A. Neugebauer. Critical temperature of niobium and tantalum films. *Proc. IEEE*, 52(10):1234–1238, 1964. doi: 10.1109/PROC.1964.3311.

[302] H. R. S. Moura and L. de Moura. Melting And Purification Of Niobium. In *AIP Conf. Proc.*, volume 927, pages 165–178, 2007. doi: 10.1063/1.2770689.

[303] Stefan Thiele. *Read-Out and Coherent Manipulation of an Isolated Nuclear Spin*. Springer Theses. Springer International Publishing, 2016. doi: 10.1007/978-3-319-24058-9.

[304] Iwaya et al. Full-gap superconductivity in spin-polarised surface states of topological semimetal β-PdBi2. *Nat. Commun.*, 8(1):976, 2017. doi: 10.1038/s41467-017-01209-9.

[305] V. Ambegaokar and A. Baratoff. Tunneling Between Superconductors. *Phys. Rev. Lett.*, 11(2): 104–104, jul 1963. doi: 10.1103/PhysRevLett.11.104.

[306] H. Courtois, M. Meschke, J. T. Peltonen, and J. P. Pekola. Origin of Hysteresis in a Proximity Josephson Junction. *Phys. Rev. Lett.*, 101(6):067002, 2008. doi: 10.1103/PhysRevLett.101.067002.

[307] T. Hashimoto, K. Yada, M. Sato, and Y. Tanaka. Surface electronic state of superconducting topological crystalline insulator. *Phys. Rev. B*, 92(17):174527, 2015. doi: 10.1103/PhysRevB.92.174527.

[308] Maier et al. Phase-sensitive SQUIDs based on the 3D topological insulator HgTe. *Phys. Scr.*, T164: 014002, 2015. doi: 10.1088/0031-8949/2015/T164/014002.

[309] Qu et al. Strong Superconducting Proximity Effect in Pb-Bi2Te3 Hybrid Structures. *Sci. Rep.*, 2 (1):339, 2012. doi: 10.1038/srep00339.

[310] C. W. J. Beenakker. Universal limit of critical-current fluctuations in mesoscopic Josephson junctions. *Phys. Rev. Lett.*, 67(27):3836–3839, 1991. doi: 10.1103/PhysRevLett.67.3836.

[311] M. Levy and I. Rudnick. Ultrasonic Determination of the Superconducting Energy Gap in Tantalum. *Phys. Rev.*, 132(3):1073–1080, 1963. doi: 10.1103/PhysRev.132.1073.

[312] Tiira et al. Magnetically-driven colossal supercurrent enhancement in InAs nanowire Josephson junctions. *Nat. Commun.*, 8:14984, 2017. doi: 10.1038/ncomms14984.

[313] M. Y. Kuprianov and V. F. Lukichev. Influence of boundary transparency on the critical current of 'dirty' SS'S structures. *Sov. Phys. JETP*, 67(1163), 1988.

[314] A. A. Golubov, M. Y. Kupriyanov, and E. Il'ichev. The current-phase relation in Josephson junctions. *Rev. Mod. Phys.*, 76(2):411–469, apr 2004. doi: 10.1103/RevModPhys.76.411.

[315] Dubos et al. Josephson critical current in a long mesoscopic S-N-S junction. *Phys. Rev. B - Condens. Matter Mater. Phys.*, 63(6):1–5, 2001. doi: 10.1103/PhysRevB.63.064502.

[316] A. Altland, Y. Gefen, and G. Montambaux. What is the Thouless Energy for Ballistic Systems? *Phys. Rev. Lett.*, 76(7):1130–1133, 1996. doi: 10.1103/PhysRevLett.76.1130.

[317] V. Z. Kresin. Josephson current in low-dimensional proximity systems and the field effect. *Phys. Rev. B*, 34(11):7587–7595, 1986. doi: 10.1103/PhysRevB.34.7587.

[318] Galletti et al. Influence of topological edge states on the properties of AlBi2Se3Al hybrid Josephson devices. *Phys. Rev. B*, 89(13):134512, 2014. doi: 10.1103/PhysRevB.89.134512.

[319] A. Johnson, C. Lobb, and M. Tinkham. Effect of leads and energy gap upon the retrapping current of Josephson junctions. *Phys. Rev. Lett.*, 65(10):1263–1266, 1990. doi: 10.1103/PhysRevLett.65.1263.

[320] Angers et al. Proximity dc squids in the long-junction limit. *Phys. Rev. B*, 77(16):165408, apr 2008. doi: 10.1103/PhysRevB.77.165408.

[321] Williams et al. Unconventional Josephson Effect in Hybrid Superconductor-Topological Insulator Devices. *Phys. Rev. Lett.*, 109(5):056803, 2012. doi: 10.1103/PhysRevLett.109.056803.

[322] Suominen et al. Anomalous Fraunhofer interference in epitaxial superconductor-semiconductor Josephson junctions. *Phys. Rev. B*, 95(3):1–11, 2017. doi: 10.1103/PhysRevB.95.035307.

[323] F. Domínguez, F. Hassler, and G. Platero. Dynamical detection of Majorana fermions in current-biased nanowires. *Phys. Rev. B*, 86(14):140503, oct 2012. doi: 10.1103/PhysRevB.86.140503.

[324] Sacépé et al. Gate-tuned normal and superconducting transport at the surface of a topological insulator. *Nat. Commun.*, 2(1):575, 2011. doi: 10.1038/ncomms1586.

[325] C. Kurter, A. D. K. Finck, Y. S. Hor, and D. J. Van Harlingen. Evidence for an anomalous current-phase relation of a dc SQUID with tunable topological junctions. 2013.

[326] Assaf et al. Massive and massless Dirac fermions in Pb1-xSnxTe topological crystalline insulator probed by magneto-optical absorption. *Sci. Rep.*, 6(1):20323, 2016. doi: 10.1038/srep20323.

[327] Sist et al. Carrier concentration dependence of structural disorder in thermoelectric Sn 1- x Te. *IUCrJ*, 3(5):377–388, 2016. doi: 10.1107/S2052252516012707.

[328] Veldhorst et al. Josephson supercurrent through a topological insulator surface state. *Nat. Mater.*, 11(5):417–421, may 2012. doi: 10.1038/nmat3255.

[329] A. Barone. *Principles and Applications of Superconducting Quantum Interference Devices*. World Scientific Pub Co Inc, 1992. ISBN 978-9810209117.

[330] T.T. Heikkilä, J. Särkkä, and F. K. Wilhelm. Supercurrent-carrying density of states in diffusive mesoscopic Josephson weak links. *Phys. Rev. B*, 66(18):184513, 2002. doi: 10.1103/PhysRevB.66.184513.

[331] Schulz et al. Design and realization of an all d-wave dc pi-superconducting quantum interference device. *Appl. Phys. Lett.*, 76(7):912–914, feb 2000. doi: 10.1063/1.125627.

[332] Cho et al. Symmetry protected Josephson supercurrents in three-dimensional topological insulators. *Nat. Commun.*, 4:1689, apr 2013. doi: 10.1038/ncomms2701.

[333] Y. Tanaka, T. Yokoyama, and N. Nagaosa. Manipulation of the Majorana Fermion, Andreev Reflection, and Josephson Current on Topological Insulators. *Phys. Rev. Lett.*, 103(10):107002, sep 2009. doi: 10.1103/PhysRevLett.103.107002.

[334] T. Yokoyama, M. Eto, and Y. V. Nazarov. Anomalous Josephson effect induced by spin-orbit interaction and Zeeman effect in semiconductor nanowires. *Phys. Rev. B*, 89(19):195407, may 2014. doi: 10.1103/PhysRevB.89.195407.

[335] H. Hayasaka and Y. Fuseya. Crystalline spin-orbit interaction and the Zeeman splitting in Pb 1- x Sn x Te. *J. Phys. Condens. Matter*, 28(31):31LT01, aug 2016. doi: 10.1088/0953-8984/28/31/31LT01.

[336] Wang et al. Room temperature magnetization switching in topological insulator-ferromagnet heterostructures by spin-orbit torques. *Nat. Commun.*, 8(1):1364, 2017. doi: 10.1038/s41467-017-01583-4.

A Appendix

A.1 CVD Growth Optimization

As it was mentioned in sec. 5.2.3 of the main text, a full revision of the CVD process parameters was done in 2016 due to degraded quality of the CNT yield. Raman analysis at that point indicated a drift towards lower effective temperatures in the chamber, which was attributed to the deterioration of the thermometry components responsible for the feedback control. Those components and all quartz parts as well as precursor gases were replaced at once for a complete maintenance and the growth parameters subsequently recalibrated by more detailed Raman studies for different temperatures and gas flows, followed by SEM and TEM verification as well as transport measurements. A short summary of the results of the Raman studies is given in the following.

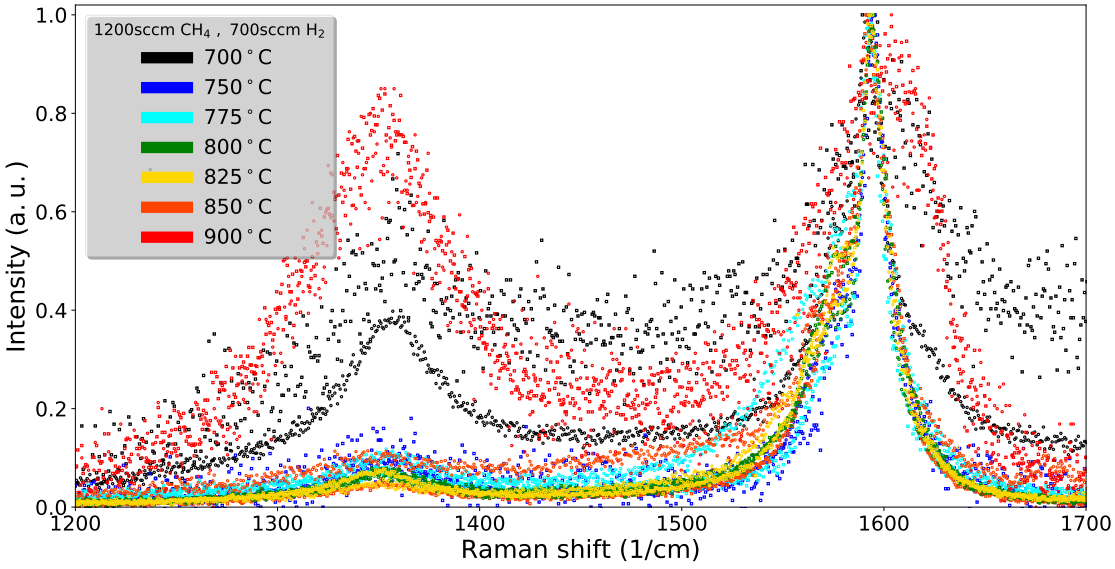

Figure A.1: Temperature series of normalized Raman spectra for CNTs grown on bare Si/SiO_2, measured at random spots. $T = 810\,°C$ is chosen due to lowest defect contributions, represented by the low height ratios of the D-peak (at $\approx 1350\,s^{-1}$) to the G-peak (at $\approx 1600\,s^{-1}$). The choice is based on the evaluation of close-ups of the D-peak, which are not shown.

The growth temperature was found to be the most influential parameter and hence optimized first by keeping the old precursor flow rates of 1200 sccm CH_4 and 700 sccm H_2. To do so the D-peak to G-peak ratios of Raman spectra, with a representative selection shown in fig. A.1, were analyzed. These measurements show low defect contributions for $775 - 850\,°C$, while lower or higher temperatures quickly worsen the result. The new

growth temperature was hence carefully chosen in the middle of this range at $T = 810\,°\mathrm{C}$. Subsequently, the H_2 flow was optimized for this new temperature, while keeping the old 1200 sccm CH_4 flow. The best result was obtained for 800 sccm of H_2, with still strong degradation for flow rates ≥ 1000 sccm and ≤ 500 sccm, as shown in fig. A.2.

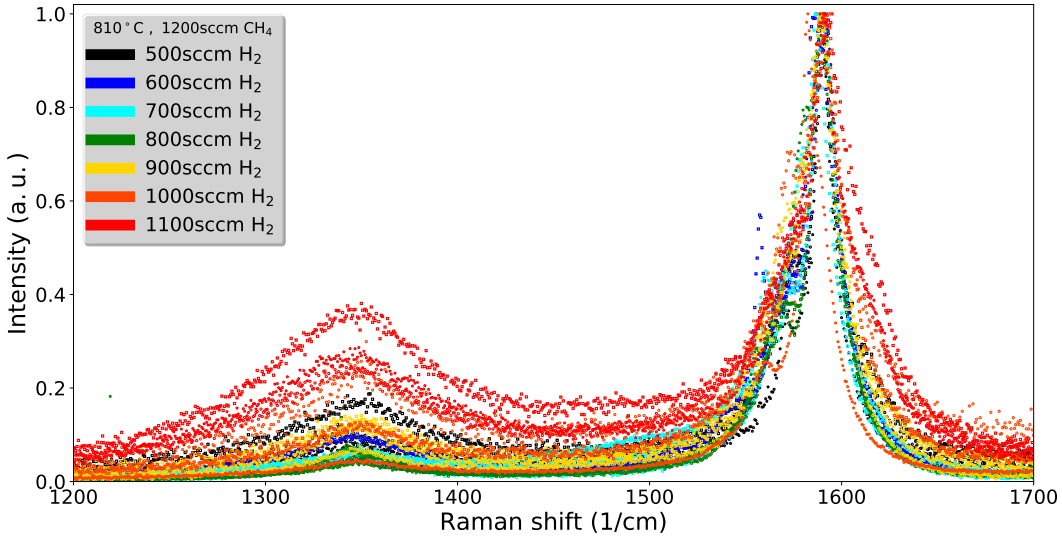

Figure A.2: H_2 series of normalized Raman spectra. Analogously to fig. A.1, a H_2 flow of 800 sccm is chosen from evaluation of the D-peak close-ups.

Finally, the CH_4 flow for established temperature and H_2 flow is optimized. Its influence is found to be small in this parameter range, indicating growth with saturated CH_4 background, where the excess precursor is purged away. A flow of 1000 sccm is chosen.

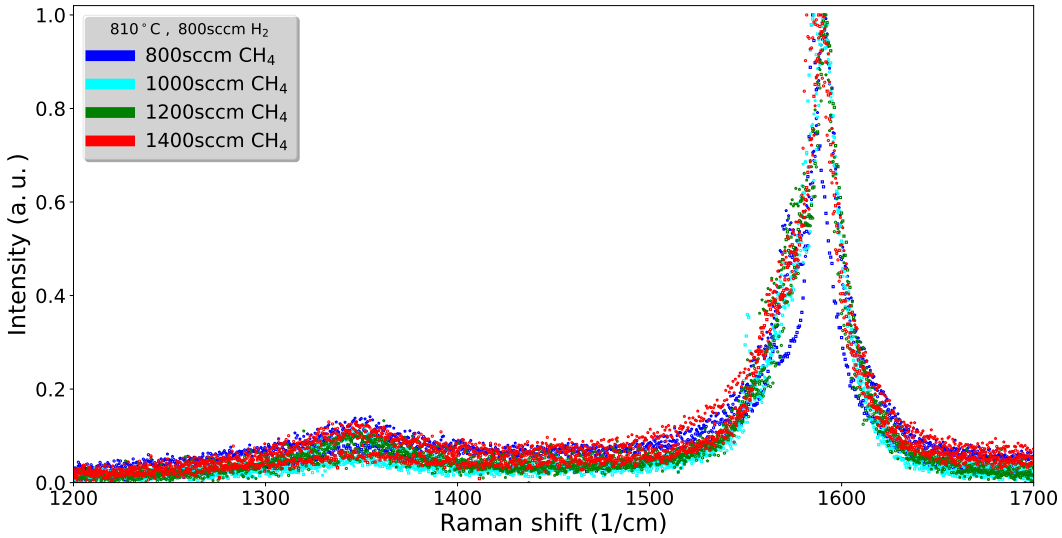

Figure A.3: CH_4 series of normalized Raman spectra. Analogously to fig. A.1, a CH_4 flow of 1000 sccm is chosen from evaluation of the D-peak close-ups.

B Publications

NANO LETTERS
Cite This: Nano Lett. XXXX, XXX, XXX−XXX
Letter
pubs.acs.org/NanoLett

Proximity-Induced Superconductivity and Quantum Interference in Topological Crystalline Insulator SnTe Thin-Film Devices

Robin Klett,*[,†] Joachim Schönle,[‡] Andreas Becker,[†] Denis Dyck,[†] Kiril Borisov,[∥] Karsten Rott,[†] Daniela Ramermann,[†] Björn Büker,[†] Jan Haskenhoff,[†] Jan Krieft,[†] Torsten Hübner,[†] Oliver Reimer,[†] Chandra Shekhar,[§] Jan-Michael Schmalhorst,[†] Andreas Hütten,[†] Claudia Felser,[§] Wolfgang Wernsdorfer,[‡,∥] and Günter Reiss*[,†]

[†]Center for Spinelectronic Materials & Devices, Physics Department, Bielefeld University, Universitätsstraße 25, 33615 Bielefeld, Germany

[‡]CNRS, Institut NEEL and Université Grenoble Alpes, 38000 Grenoble, France

[§]Max Planck Institute for Chemical Physics of Solids, 01187 Dresden, Germany

[∥]Physics Department, Karlsruhe Institute of Technology, Wolfgang-Gaede-Straße 1, 76131 Karlsruhe, Germany

Supporting Information

ABSTRACT: Topological crystalline insulators represent a new state of matter, in which the electronic transport is governed by mirror-symmetry protected Dirac surface states. Due to the helical spin-polarization of these surface states, the proximity of topological crystalline matter to a nearby superconductor is predicted to induce unconventional superconductivity and, thus, to host Majorana physics. We report on the preparation and characterization of Nb-based superconducting quantum interference devices patterned on top of topological crystalline insulator SnTe thin films. The SnTe films show weak anti-localization, and the weak links of the superconducting quantum interference devices (SQUID) exhibit fully gapped proximity-induced superconductivity. Both properties give a coinciding coherence length of 120 nm. The SQUID oscillations induced by a magnetic field show 2π periodicity, possibly dominated by the bulk conductivity.

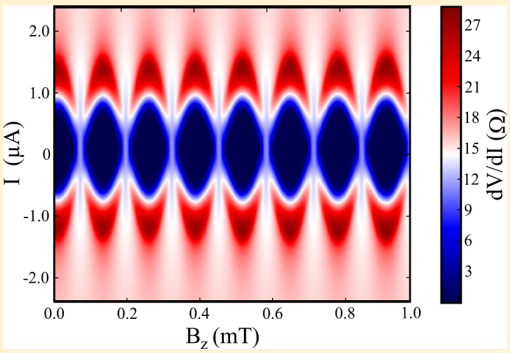

KEYWORDS: *Thin films, topological insulator, superconductivity, mesoscopic devices*

In the past several years, tremendous efforts have been made in investigating new topological states of matter, and it has been widely recognized that the family of topological materials is highly diversified and widespread.[1] One of its species is formed by topological crystalline insulators (TCI), in which topological protection is due to the symmetry of the crystal structures. The first predicted[2] and experimentally verified[3] class of TCI materials was found within the IV−VI semiconductors, with SnTe as a representative model material. SnTe crystallizes in rock-salt structure, and the symmetry responsible for its topological nature is the reflection symmetry with respect to the (110) mirror planes.[2,3] The appearance of unconventional boundary modes in such topologically nontrivial phases has been detected experimentally via several techniques,[4−6] manifesting themselves in linearly dispersing chiral topological surface states (TSS). One of the most-mesmerizing consequences of the TSS and nontrivial topology arises if the material itself undergoes a superconducting phase transition. In this case, theoretical models predict the occurrence of topological (mirror) superconductivity.[7] More specifically, the four Dirac cones in the TCI surface Brillouin zone give rise to host Majorana Fermion quartets.[8] For intrinsic superconducting TCI a couple of smoking gun experiments have been made in In-substituted $Sn_{1-x}In_xTe$,[9,10] which shows a superconducting phase transition at T_c = 3.5−4.7 K while maintaining its nontrivial band structure.[11] However, the issue of extrinsic (proximity-induced) superconductivity in undoped SnTe has not been tackled yet experimentally. In this case, the system can undergo a superconducting phase transition due to its proximity to a nearby conventional s-wave superconductor (SC).[12] Here, we report on the fabrication and characterization of SC−TCI hybrid microstructures. We patterned superconducting quantum interference devices (SQUIDs) made from Nb thin films on co-sputtered SnTe thin films such that bridges from SnTe form weak links between superconducting Nb wires. The resistance of the SnTe shows a weak anti-localization in its magnetic field response and the SnTe weak links become fully superconducting. We additionally studied the SQUID ring behavior in DC magnetic fields. Proximity

Received: November 17, 2017
Revised: January 14, 2018
Published: January 24, 2018

DOI: 10.1021/acs.nanolett.7b04870
Nano Lett. XXXX, XXX, XXX−XXX

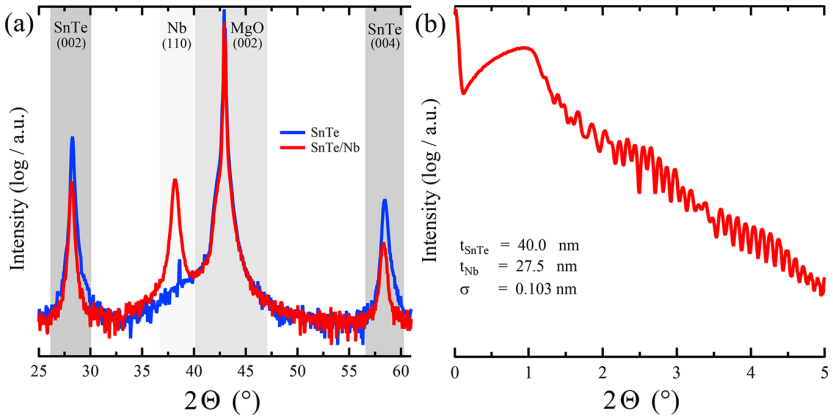

Figure 1. (a) XRD scans taken for a 50 nm and a 40 nm thick SnTe−27.5 nm Nb bilayer grown on a MgO (001) substrate. The SnTe films show a polycrystalline growth with a strong (001) texture. The subsequent Nb layer grows in (110) on top of the SnTe. (b) X-ray reflection measurements of the bilayer structures proof the flatness of the films with a roughness of only 0.1 nm and indicate low strain at the interface of both layers.

induced superconductivity on the TSS by s-wave SC is theoretically predicted to result in an anomalous 4π-periodic characteristic, which is superimposed on the conventional (2π-periodic) SQUID relation:

$$\phi_0 = \frac{h}{2e} = A_S \delta_B \quad (1)$$

where ϕ_0 is the magnetic flux quantum, A_S is the effective area of the SQUID, and δ_B is the oscillation period. A SQUID interference pattern hosting 4π-periodic physics would be an ultimate proof of topological superconductivity[13] and, hence, the presence of Majorana Fermions.

Sample Preparation. In this section, we describe the growth procedure of the TCI−SC hybrids and give a detailed description of the lithography and patterning process. First, thin films of SnTe are grown on MgO substrates at 150 °C via co-sputtering of Sn and Te. We chose insulating MgO (001) substrates due to their cubic crystal structure and their good lattice match to the SnTe lattice constant a_{SnTe} = 0.63 nm ≈ $\sqrt{2}a_{MgO}$.[14] The base pressure of the sputter system is 5×10^{-10} mbar, the Ar-pressure is $p \approx 2.5 \times 10^{-3}$ mbar. As shown in Figure 1a, X-ray diffraction (XRD) in Θ−2Θ geometry clearly produces only the (002) and (004) diffraction peaks. Thus, under these conditions 40 nm SnTe thin films grow polycrystalline (PC) with strong (001) texture. In the next step the TCI thin films are coated with Nb, a well-characterized and established s-wave superconductor. The Nb is deposited without exposing the sample to ambient conditions to prevent TCI surface contamination and to allow a high transparency at the SnTe/Nb interface.[15,16] The nominally deposited 27.5 nm Nb films grow in (110) texture with low strain on top of the SnTe rock-salt lattice, which is confirmed with the XRD peak at 38.3° in Figure 1a. The X-ray reflection data presented in Figure 1b verify smooth film growth with a fitted roughness of $\sigma \approx 0.1$ nm. A low surface roughness has recently been identified as a crucial precondition for the presence of TSS in TCI films.[17,18] Further structural and surface analysis can be found in the Supporting Information. In particular, we performed high-resolution transmission electron microscopy imaging of cross-sections made by focused ion beam milling to further elucidate the microstructure of the MgO/SnTe/Nb film system. The results shown in the Figure S4 show a clean interface between the SnTe and the Nb and a well textured (001) columnar growth of the SnTe with a mean grain size of around 30 nm. Because Nb is known to be a chemically very active metal, the film quality (and the superconducting properties) often suffer from lithographic and etching processes during device patterning. We counter this issue by capping the TCI/SC hybrid with 2.5 nm of Ta and 5 nm of Ru as protection for subsequent fabrication steps. The SQUIDs are patterned with conventional e-beam lithography. After resist development, the film stacks are patterned by Ar-ion dry etching. Controlled via secondary ion mass spectroscopy, we stop the sample etching once the exposed Nb area is removed. In this way, patterned Nb defines the superconducting loop while the bottom SnTe film is intact. The patterned SQUIDs (exemplarily shown in Figure 2) have an effective area A = 16 μm^2 and the Nb lines have a width of w = 200 nm. The length L of the two Josephson junctions is varied between L = 50−200 nm. The samples are characterized electrically both by direct current measurements of the film resistance as well as by a current-biased lock-in technique for differential resistance dV/dI scans.

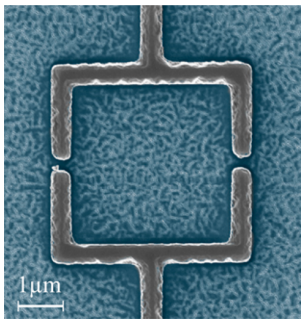

Figure 2. False-color SEM image of one of the fabricated SQUID samples. The Nb lines are highlighted in gray scale, while the SnTe film is pictured in dark blue. The nominally patterned inner area of the device is A = 16 μm^2, and the length of the weak links is L_J = 120 nm.

Results. *SnTe Thin-Film Magnetoresistance.* Before starting the characterization of the proximity induced superconductivity and the SQUID data, we investigate the transport properties of bare SnTe thin films using patterned Hall bar microstructures as schematically shown in the inset of Figure 3a. The determination of the Hall coefficient with Hall

DOI: 10.1021/acs.nanolett.7b04870
Nano Lett. XXXX, XXX, XXX−XXX

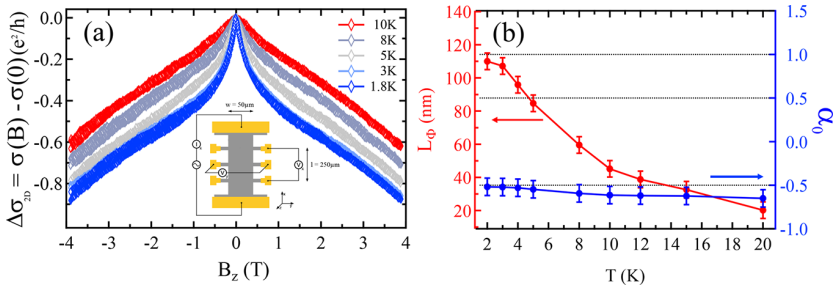

Figure 3. (a) Magneto-conductivity for several temperatures as a function of out-of-plane magnetic field B_z. The image in the inset shows the dimension of the micropatterned Hallbar devices. The data indicate weak anti-localization and, thus, give evidence for two-dimensional electronic transport. (b) Temperature dependence of the phase-coherence length L_Φ and the transport parameter α after fitting the low magnetic field ($B_z < 0.5$ T) conductivity within the HLN formalism.

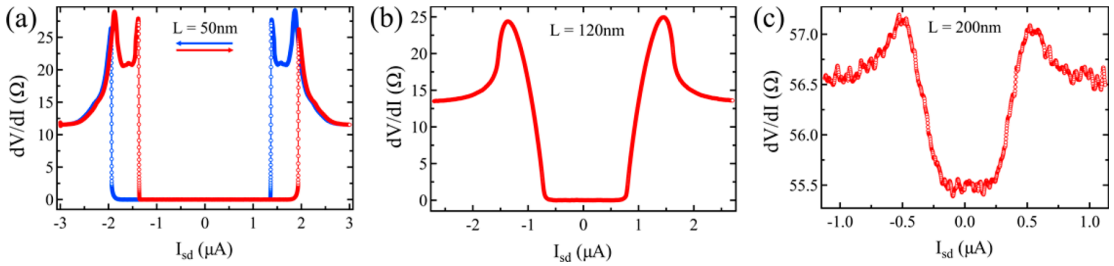

Figure 4. Current-biased dV/dI sweeps for different length of the weak links as a function of the bias current I_{sd}. (a) For a weak link with $L < L_\Phi$ pronouced peaks in the differential resistance at the flanks of the induced superconducting gaps (dV/dI = 0 Ω) are observed. The red and blue arrows indicate the sweep direction of the current. (b) For $L \approx L_\Phi$, the superconductivity is still fully gapped, but no flanking peaks occur, and the superconducting gap is not sharp. (c) For $L > L_\Phi$, the proximity superconductivity does not cover the entire weak link, and the junctions remains resistive.

measurements at 2 K (not presented) shows that the charge-carrier type is strongly hole-like and the carrier density is about $n \approx 4.5 \times 10^{20}$ cm^{-3}. Because SnTe is known to tend intrinsically to high carrier concentrations due to Sn vacancies (and, hence, to p-type behavior), this is consistent with current reports of other researchers.[19] An established all-electrical method of testing the presence of surface state transport are measurements of the longitudinal magnetoresistance (MR), in which a weak anti-localization (WAL) is expected due to surface states.[20] The MR data shown in Figure 3a are plotted as relative change in magneto-conductivity (MC) $\Delta\sigma_{2D} = \sigma(B) - \sigma(0)$ and show sharp cusp-like MR, which can indeed be attributed to WAL and evaluated with the Hikami-Larkin-Nagaoka (HLN) formalism:

$$\Delta\sigma_{2D} = \alpha\frac{e^2}{2\pi^2\hbar}\left(\ln\left(\frac{\hbar}{4eBL_\phi^2}\right) - \psi\left(\frac{1}{2} + \frac{\hbar}{4eBL_\phi^2}\right)\right) \quad (2)$$

where e is the electron charge, $\hbar$ is the Planck's constant, L_Φ is the phase-coherence length of a charge carrier in a given surface channel, $\psi(x)$ is the digamma function, B is the out-of-plane applied magnetic field, and α_0 is a dimensionless transport parameter.[20,21] Data fitting yields information about L_Φ and α_0, which are both plotted as a function of temperature T in Figure 3b. L_Φ is increasing steadily with decreasing T from $L_\Phi \approx 20$ nm at 20 K to $L_\Phi \approx 120$ nm at 2 K, which is the same order of magnitude as stated for other topological materials.[21−23] The coherence length, we obtained from the WAL data is much larger than the mean grain size of the bulk SnTe. Thus, it is well justified to attribute the value of 120 nm to the surface conduction channels. The theoretical prediction of the latter is supposed to yield $\alpha_0 = -0.5$ for one TSS contributing to transport.[20] As shown in Figure 3b, the fit of our data results in $\alpha \approx -0.5$ over the entire temperature range demonstrating topological protected transport. A total of four TSS exist on the surface Brillouin zone (SBZ) of a TCI, each entering with an additional $\alpha_0 = -0.5$ contribution. If one considers that TSS occur at the top and bottom interface, one would end up with a sum of $|\alpha| = 4$.[24] A plausible explanation of one single TSS per surface is most likely due to the valley degeneracy of the SnTe SBZ, giving rise to two different coupling scenarios: intra- and intersurface valley coupling. The first effect can be observed when a carrier is able to scatter coherently between Dirac valleys located on the same surface. Accordingly, a long coherence length results in strong intravalley coupling and, thus, a smaller α; similar behavior is typically observed for other 2D Dirac valley materials such as graphene.[25] The second scatter mechanism is intersurface valley coupling between top and bottom surface valleys. In this coupling regime, charge carriers can scatter coherently between the top and bottom SBZ Dirac valleys via bulk. This scenario has been observed by several other groups[24,26,27] and was attributed to the high bulk carrier concentration. Because WAL, however, is predominantly a 2D phenomenon, the bulk bands are unlikely to be the origin of the WAL.[21,24,28] While WAL has been observed as well in Rashba-split semiconductors,[29−31] such an explanation is ruled out here due to the high carrier concentration of our films.[26] Thus, the WAL features seen in Figure 3a can be considered as consequence of spin-momentum locking of the TCI TSS, but the bulk bands have strong influence on the WAL due to coupling to TSS transport channels.

SnTe/Nb SQUID Proximity-Induced Superconductivity. In the Figure 4a−c, results of the differential resistance (dV/dI) as

DOI: 10.1021/acs.nanolett.7b04870
Nano Lett. XXXX, XXX, XXX−XXX

a function of the bias current I_{sd} for Josephson junction lengths (L_J) of 50, 120, and 200 nm are presented, respectively. If not further stated, all measurements are taken at 85 mK. The lengths of the weak links cover the range of the phase-coherence length L_Φ of the surface state electrons evaluated from the WAL data by HLN analysis. Hence, if surface state properties are contributing to the transport, the features resulting from proximity of the TSS to the Nb should be most prominent for L_J = 50 nm in the dV/dI data (Figure 4a). The individual sweeps can be separated into two sections: first, when I_{sd} is lower than the critical current I_c = 1.89 μA, a dissipationless supercurrent can flow through the system, and the device exhibits a clear zero-resistant state. No spectroscopic features are observed in the gap, so that we can exclude, e.g., quasiparticle hybridization effects, which are known to appear in topological materials. Second, for a bias current larger than I_c, the SQUID can be characterized by its normal state resistance $R_n \approx 12\ \Omega$. Small hysteretic behavior of the switching between both regions is present. While sweeping back (forth) from high positive (negative) bias currents, one can identify small retrapping currents of I_R = 1.39 μA. A plausible explanation for the hysteretic behavior are self-heating effects.[32] The most-prominent features in this dV/dI data are the strong peaks appearing at the outer-gap sides while sweeping forth (back) from the resistive state into the superconducting gap at $I = \pm$ 1.91 μA. Interestingly, when sweeping forth (back) from the inner nonresistive gap-region, the system jumps at the same current back into the resistive state, where the back (forth) biased current reveals the most prominent peak. We attribute the peaks to the contribution of the TSS carrying supercurrents. In this picture, surface Andreev bound states (SABS) generated in analogy to the mirror-protected Dirac points on the (001) surface of the SnTe crystal can host Cooper pairs, which are more robust and manifest themselves as additional peaks outside the bulk-superconducting gap. Hashimoto et al.[33] predicted such mirror-protected SABS hosted in superconducting TCI on the (001) surface if an odd-parity potential is realized. In Figure 4b, the length of the weak link corresponds to the estimated coherence length of the surface channels (L_J = 120 nm $\approx L_\Phi$), and hence, features due to SABS are expected to be weakened but still be present. The induced superconductivity still shows a zero-resistive behavior in the gap, but the observed gap-flanking SABS peaks vanished. Interestingly, the superconducting gap flanks are not showing a sharp jump as in Figure 4a but appear to be tilted outward, which suggests that pure s-wave type is unlikely. If superconductivity is partially carried by TSS, it is theoretically predicted that a mixture of s- and p-wave pairing is present.[34] In Figure 4c, the differential resistance sweeps of a device with a weak link of L_J = 200 nm ($>L_\Phi$) is shown. For this length, an induced superconducting gap is still observable, but it does no longer exhibit a zero-resistance state, keeping a finite in-gap resistance of $R \approx 55\ \Omega$. Results for other samples suggest that a zero resistance states exists for L_J < 175 nm. This result supports the suggestion that the phase-coherence length of the surface currents and the coherence length of the Cooper pairs are correlated and have crucial influence on the proximity-induced superconductivity in our films.

SnTe/Nb SQUID Oscillations. The response of the differential resistance dV/dI to an out-of-plane magnetic field B_z reveals clear oscillations in I_c shown in the color-code plot in Figure 5 for a length L_J = 120 nm and a field range from 0 to 1.1 mT (note that the oscillations persist up to B_z > 10 mT).

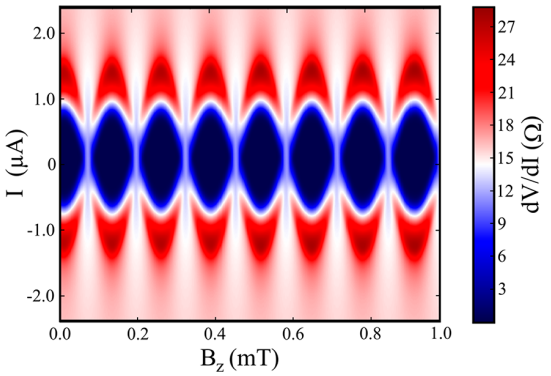

Figure 5. dV/dI color-plot showing the SQUID response (dV/dI as a function of B_z and I) to an external out-of-plane magnetic field B_z and bias current I. Clear oscillations are observable. The critical current I_c oscillates with the period δ_B = 122 μT that corresponds to an effective SQUID area of A_S = 16.9 μm^2, obeying the conventional ϕ_0-relation. The measurement has been offset to $I_c(0)$ = max.

The blue regions correspond to a SQUID resistance R = 0 Ω, while white and red areas represent finite resistance states. This mapping allows the evaluation of the critical current response for each value of the magnetic field B_z. The oscillations are periodic for δ_B = 122 μT. If one takes a closer look at eq 1, this corresponds to an effective area of A_S = 16.9 μm^2, which is in reasonable agreement with the dimensions of the SQUID rings characterized in our experiment if one considers the London penetration length of Nb λ_{Nb} = 350 nm[35] on all sides of the square. Thus, we conclude that the data shows only conventional critical current response through the surface supercurrents, and hence, no 4π-periodic modulation is observed. Our finding agrees with the results of similar experiments performed by other groups on other topological materials, such as strained HgTe or Bi_2Te_3 and Bi_2Se_3 compounds.[35−37] The reason for the absence of 4π-periodicity may be a 2π-signal poisoning arising from the dominating amounts of supercurrents carried by bulk channels, which dominate the transport. This 2π channels coexist with a contribution of $k_y \neq 0$ (k_y is the wave vector-component transversal to the moving direction k_x). Under these circumstances the predicted zero-energy Andreev bound excitations (Majorana Fermions) are gapped out.[38] The small influence of the unique 4π-periodic topological modes would than elusively vanish within this parasitic background. Here, we emphasize that doping-dependent and (locally) gated measurements,[39] as well as RF-transport analysis[40] are necessary next steps to address this problem and access the new field of Majorana physics in TCI thin film systems.

Conclusions. In conclusion, we have demonstrated WAL in the TCI SnTe and the first experimental evidence of fully gapped superconductivity in SnTe/Nb heterostructures at T = 85 mK and a length of Josephson junction weak links below L_J < 175 nm. The phase-coherence length of the TCI extracted from these two properties show reasonable agreement. We additionally investigated the response of Nb-SQUIDs patterned on top of the SnTe to a perpendicular magnetic field. The measured SQUID oscillations follow the relation describing a conventional SQUID interference pattern. Here, our results form a foundation for future investigations of proximity-induced topological superconductivity in the class of topological crystalline matter.

DOI: 10.1021/acs.nanolett.7b04870
Nano Lett. XXXX, XXX, XXX−XXX

■ ASSOCIATED CONTENT

Supporting Information

The Supporting Information is available free of charge on the ACS Publications website at DOI: 10.1021/acs.nanolett.7b04870.

A detailed description of the SnTe thin films growth and film characterization with XRD, AFM, TEM, and texture measurements. (PDF)

■ AUTHOR INFORMATION

Corresponding Authors

*E-mail: rklett@physik.uni-bielefeld.de.
*E-mail: reiss@physik.uni-bielefeld.de.

ORCID

Robin Klett: 0000-0002-6348-495X

Notes

The authors declare no competing financial interest.

■ ACKNOWLEDGMENTS

The financial support by the Deutsche Forschungsgemeinschaft (DFG, German Research Foundation) within the priority program SPP 1666 "Topological Insulators" is gratefully acknowledged.

■ REFERENCES

(1) Ando, Y.; Fu, L. *Annu. Rev. Condens. Matter Phys.* **2015**, *6*, 361−381.
(2) Hsieh, T.; Lin, H.; Liu, J.; Duan, W.; Bansil, A.; Fu, L. *Nat. Commun.* **2012**, *3*, 982.
(3) Tanaka, Y.; Ren, Z.; Sato, T.; Nakayama, K.; Souma, S.; Takahashi, T.; Segawa, K.; Ando, Y. *Nat. Phys.* **2012**, *8*, 800−803.
(4) Tanaka, Y.; Shoman, T.; Nakayama, K.; Souma, S.; Sato, T.; Takahashi, T.; Novak, M.; Segawa, K.; Ando, Y. *Phys. Rev. B: Condens. Matter Mater. Phys.* **2013**, *88*, 235126.
(5) Okada, Y.; Serbyn, M.; Lin, H.; Walkup, D.; Zhou, W.; Dhital, C.; Neupane, M.; Xu, S.; Wang, Y. J.; Sankar, R.; Chou, F.; Bansil, A.; Hasan, M. Z.; Wilson, S. D.; Fu, L.; Madhavan, V. *Science* **2013**, *341* (6153), 1496−1499.
(6) Sessi, P.; Di Sante, D.; Szczerbakow, A.; Glott, F.; Wilfert, S.; Schmidt, H.; Bathon, T.; Dziawa, P.; Greiter, M.; Neupert, T.; Sangiovanni, G.; Story, T.; Thomale, R.; Bode, M. *Science* **2016**, *354* (6317), 1269−1273.
(7) Zhang, F.; Kane, C. L.; Mele, E. J. *Phys. Rev. Lett.* **2013**, *111*, 056403.
(8) Shiozaki, K.; Sato, M. *Phys. Rev. B: Condens. Matter Mater. Phys.* **2014**, *90*, 165114.
(9) Sasaki, S.; Ando, Y. *Cryst. Growth Des.* **2015**, *15* (6), 2748−2752.
(10) Balakrishnan, G.; Bawden, L.; Cavendish, S.; Lees, M. R. *Phys. Rev. B: Condens. Matter Mater. Phys.* **2013**, *87*, 140507.
(11) Sato, T.; Tanaka, Y.; Nakayama, K.; Souma, S.; Takahashi, T.; Sasaki, S.; Ren, Z.; Taskin, A. A.; Segawa, K.; Ando, Y. *Phys. Rev. Lett.* **2013**, *110*, 206804.
(12) Stanescu, T. D.; Sau, J. D.; Lutchyn, R. M.; Das Sarma, S. *Phys. Rev. B: Condens. Matter Mater. Phys.* **2010**, *81* (24), 094522.
(13) Chung, S. B.; Horowitz, J.; Qi, X. *Phys. Rev. B: Condens. Matter Mater. Phys.* **2013**, *88*, 214514.
(14) Tung, Y. W.; Cohen, M. L. *Phys. Rev. B* **1970**, *2*, 1216.
(15) Blonder, G. E.; Tinkham, M.; Klapwijk, T. M. *Phys. Rev. B: Condens. Matter Mater. Phys.* **1982**, *25* (7), 4515−4532.
(16) Strijkers, G. J.; Ji, Y.; Yang, F. Y.; Chien, C. L.; Byers, J. M. *Phys. Rev. B: Condens. Matter Mater. Phys.* **2001**, *63*, 104510.
(17) Zeljkovic, I.; Walkup, D.; Assaf, B. A.; Scipioni, K. L.; Sankar, R.; Chou, F.; Madhavan, V. *Nat. Nanotechnol.* **2015**, *10* (10), 849−853.
(18) Yan, C.; Guo, H.; Wen, J.; Zhang, Z.; Wang, L.; He, K.; Ma, X.; Ji, S.; Chen, X.; Xue, Q. *Surf. Sci.* **2014**, *621*, 104−108.
(19) Mengui, U. A.; Abramof, E.; Rappl, P. H. O.; Ueta, A. Y. *Braz. J. Phys.* **2006**, *36* (2A), 324−327.
(20) Hikami, S.; Larkin, A. I.; Nagaoka, Y. *Prog. Theor. Phys.* **1980**, *63* (2), 707−710.
(21) He, H. H.; Wang, G.; Zhang, T.; Sou, I.-K.; Wong, G. K. L.; Wang, J.-N.; Lu, H.-Z.; Shen, S. Q.; Zhang, F.-C. *Phys. Rev. Lett.* **2011**, *106* (16), 166805.
(22) Shekhar, C.; Kampert, E.; Foerster, T.; Yan, B.; Nayak, A.; Nicklas, M.; Felser, C. Large linear magnetoresistance and weak anti-localization in Y(Lu)PtBi topological insulators. 2015, *arXiv:1502.00604*. arXiv.org e-Print archive. https://arxiv.org/abs/1502.00604 (accessed on November 14, 2017).
(23) Zhao, B.; Cheng, P.; Pan, H.; Zhang, S.; Wang, B.; Wang, G.; Xiu, F.; Song, F. *Sci. Rep.* **2016**, *6*, 22377.
(24) Akiyama, R.; Fujisawa, K.; Yamaguchi, T.; Ishikawa, R.; Kuroda, S. *Nano Res.* **2016**, *9* (2), 490−498.
(25) Wu, X.; Li, X.; Song, Z.; Berger, C.; de Heer, W. A. *Phys. Rev. Lett.* **2007**, *98*, 136801.
(26) Assaf, B. A.; Katmis, F.; Wei, P.; Satpati, B.; Zhang, Z.; Bennett, S. P.; Harris, V. G.; Moodera, J. S.; Heiman, D. *Appl. Phys. Lett.* **2014**, *105*, 102108.
(27) Shen, J.; Xie, Y.; Cha, J. J. *Nano Lett.* **2015**, *15* (6), 3827−3832.
(28) Bao, L.; He, L.; Meyer, N.; Kou, X.; Zhang, P.; Chen, Z.; Fedorov, A.; Zou, J.; Riedemann, T. M.; Lograsso, T. A.; Wang, K. L.; Tuttle, G.; Xiu, F. *Sci. Rep.* **2012**, *2*, 726.
(29) Bergmann, G. *Phys. Rep.* **1984**, *107*, 1.
(30) Kallaher, R. L.; Heremans, J. J. *Phys. Rev. B: Condens. Matter Mater. Phys.* **2009**, *79*, 075322.
(31) Roulleau, P.; Choi, T.; Riedi, S.; Heinzel, T.; Shorubalko, I.; Ihn, T.; Ensslin, K. *Phys. Rev. B: Condens. Matter Mater. Phys.* **2010**, *81*, 155449.
(32) Courtois, H.; Meschke, M.; Peltonen, J. T.; Pekola, J. P. *Phys. Rev. Lett.* **2008**, *101*, 067002.
(33) Hashimoto, T.; Yada, K.; Sato, M.; Tanaka, Y. *Phys. Rev. B: Condens. Matter Mater. Phys.* **2015**, *92*, 174527.
(34) Fu, L.; Kane, C. L. *Phys. Rev. Lett.* **2008**, *100*, 096407.
(35) Maier, L.; Bocquillon, E.; Grimm, M.; Oostinga, J. B.; Ames, C.; Gould, C.; Brüne, C.; Buhmann, H.; Molenkamp, L. W. *Phys. Scr.* **2015**, *T164*, 014002.
(36) Veldhorst, M.; Molenaar, C. G.; Wang, X. L.; Hilgenkamp, H.; Brinkman, A. *Appl. Phys. Lett.* **2012**, *100*, 072602.
(37) Kurter, C.; Finck, A. D. K.; Hor, Y. S.; Van Harlingen, D. J. *Nat. Commun.* **2015**, *6*, 7130.
(38) Oostinga, J. B.; Maier, L.; Schüffelgen, P.; Knott, D.; Ames, C.; Brüne, C.; Tkachov, G.; Buhmann, H.; Molenkamp, L. W. *Phys. Rev. X* **2013**, *3*, 021007.
(39) Bocquillon, E.; Deacon, R. S.; Wiedenmann, J.; Leubner, P. L.; Klapwijk, T. M.; Brüne, C.; Ishibashi, K.; Buhmann, H.; Molenkamp, L. W. *Nat. Nanotechnol.* **2016**, *12*, 137−143.
(40) Wiedenmann, J.; Bocquillon, E.; Deacon, R. S.; Hartinger, S.; Herrmann, O.; Klapwijk, T. W.; Maier, L.; Ames, C.; Brüne, C.; Gould, C.; Oiwa, A.; Tarucha, S.; Buhmann, H.; Molenkamp, L. W.; Ishibashi, K. *Nat. Commun.* **2016**, *7*, 10303.

DOI: 10.1021/acs.nanolett.7b04870
Nano Lett. XXXX, XXX, XXX−XXX

Supporting Information

-

Proximity induced superconductivity and quantum interference in topological crystalline insulator SnTe thin film devices

Robin Klett[1*], Joachim Schönle[2], Andreas Becker[1], Denis Dyck[1], Kiril Borisov[4], Karsten Rott[1], Daniela Ramermann[1], Björn Büker[1], Jan Haskenhoff[1], Jan Krieft[1], Torsten Hübner[1], Oliver Reimer[1], Chandra Shekhar[3], Jan-Michael Schmalhorst[1], Andreas Hütten[1], Claudia Felser[3], Wolfgang Wernsdorfer[2,4] & Günter Reiss[1]

[1]*Center for Spinelectronic Materials & Devices, Physics Department, Bielefeld University, Universitätsstraße 25, 33615 Bielefeld, Germany*

[2]*CNRS, Institut NEEL and Université Grenoble Alpes, 38000 Grenoble, France*

[3]*Max Planck Institute for Chemical Physics of Solids, 01187 Dresden, Germany*

[4]*Karlsruhe Institute of Technology, Physics Department, Wolfgang-Gaede-Straße 1,*

76131 Karlsruhe, Germany

**corresponding author: rklett@physik.uni-bielefeld.de*

In this supplementary section, we further discuss the characterization of the co-sputtered SnTe thin films. In Figure S1 XRD measurements for 40nm thick SnTe films grown on (001) MgO are presented. The SnTe follows the [001] orientation of the substrate showing clear peaks at (002) and (004). The best crystallinity and film quality is obtained for a deposition temperature T_D = 150°C as indicated by the temperature series. For temperatures T > 200°C a decrease in crystallinity, higher surface roughness and optical defects are observed from microscopic images and XRD data. We attribute this to degassing of Te at higher temperatures. However, for T_D = 150°C the films grow smoothly as AFM measurements show in Figure S2 giving an averaged roughness of RMS = 0.48nm. In Figure S2(b) the line scan taken across the red marked path of the AFM map shows a surface height variation of less than 1nm over a width of 3µm, further supported by the height distribution illustrated in

(c). We further characterized the SnTe thin films with texture measurements along the (002), (202) and (222) crystal plane, which are shown in Figure S3. The (002) measurement gives only a pronounced peak at Ψ=0°, stemming from the strong [001] texture already discussed by the XRD scans in S1. Interestingly the (202) and (222) scans show ring-like patterns, which mean that the films are formed by [001] textured polycrystals. The fourfold symmetric (φ =45°, φ =135°, φ =225° and φ =315°) peaks lying on the Ψ =45°ring show that the predominant part of the crystals is growing along the [110] direction of the MgO as explained in the main text. This is further supported via the (222) scan. Again, one can identify the ring-shape pattern with fourfold degenerated peaks at φ =0°, φ =90°, φ =190° and φ =270°. Slight contributions from crystals, which grow 45° tilted to the [110] MgO direction, can be identified by smaller intensity peaks. To further support these data, we cut lamellas from a MgO/SnTe/Nb/Ta/Ru thin film system along the [100] direction of the MgO substrate and performed TEM investigations. In Figure S4 (a) a TEM overview image of one multilayer system is given, which clearly resolves the single layers of the system. As expected from the texture measurements in Figure S3 the SnTe grows in strongly [001] textured crystal grains on top of the MgO. The average grain size in in-plane growth direction is d_{ip} = 27nm (averaged over several crystallites from different images). In growth direction the crystallites match the film thickness and show single-crystalline growth. (b) shows a close-up image of a grain boundary between two high textured SnTe grains. The single-crystallites are tilted by an angle $\alpha \approx 7.5°$ to each other. In (c) a close up of a SnTe single-crystallite is shown. The FFT-TEM image, created from the data within the white box, shows highly ordered and symmetric peaks, and thus provides further evidence of the crystal quality of the individual SnTe grains.

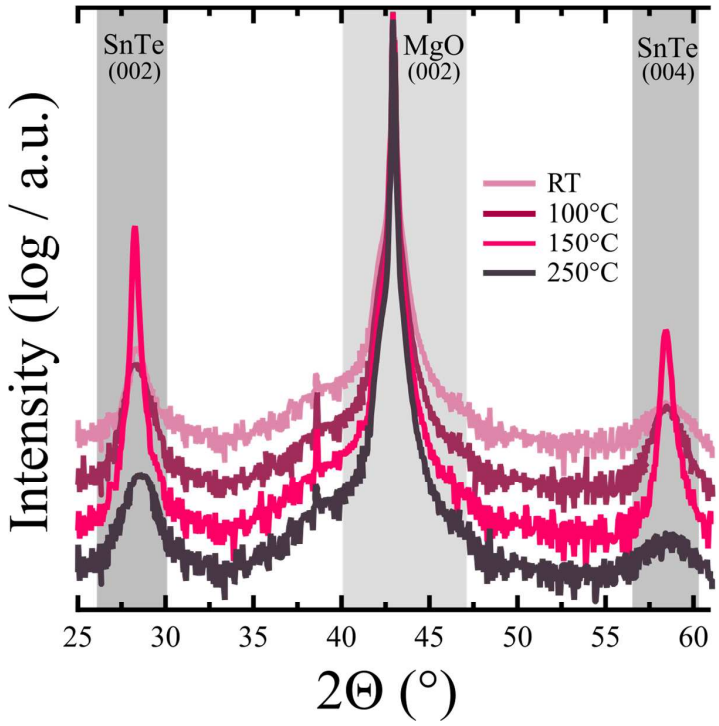

Figure S1 X-ray diffraction measurements of 40nm SnTe thin films grown on (001) MgO substrate for several deposition temperatures. The measurements show that the SnTe thin films grow with strong [001] orientation on top of the MgO without forming any undesired sub-phases. The best film quality is obtained for a deposition temperature T_D = 150°C.

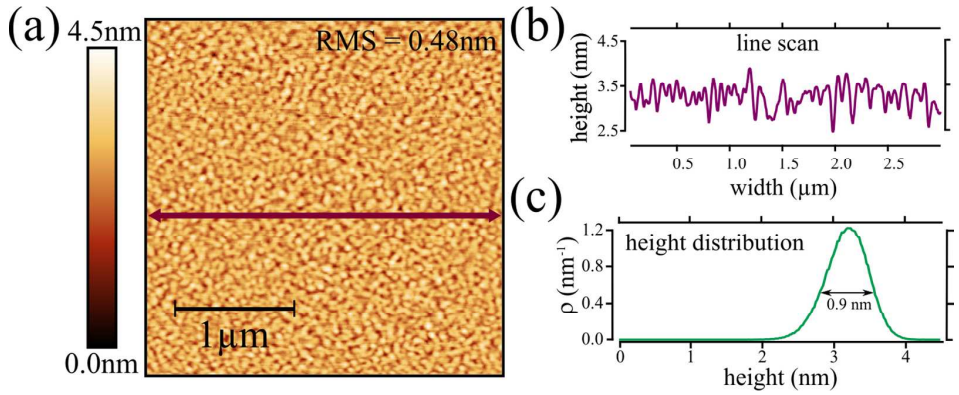

Figure S2 (a) AFM mapping of the surface of a SnTe thin film deposited at T=150°C on MgO substrate. The film grows smoothly with an average roughness RMS = 0.48nm. The red arrow indicates the line scan presented in (b), showing only slight variation in height. (c) shows the height distribution of the AFM measurement.

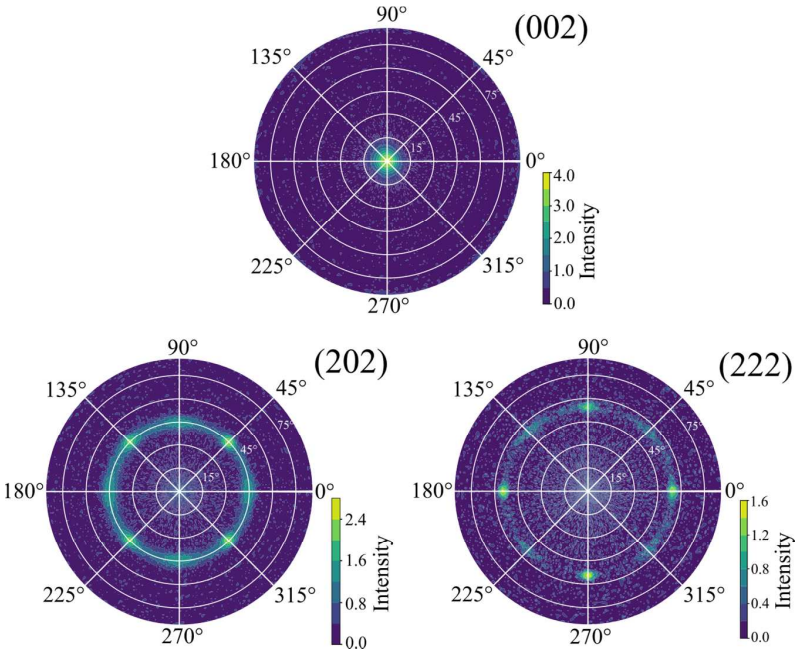

Figure S3 Euler plots in logarithmic color scale along the (002), (202) and (222) SnTe crystal planes. The (002) measurement shows that the SnTe crystals are strongly [001] textured. The (202) plot shows a ring-shaped structure at 45° indicating that the [001] textured SnTe crystallites are misaligned in film-plane to each other. The fourfold symmetric peaks every 45° show that most crystals grow along the $\sqrt{2}$ MgO surface diagonal. This is further supported by the (222) plane scan showing again the ring-shaped pattern with fourfold symmetric peaks.

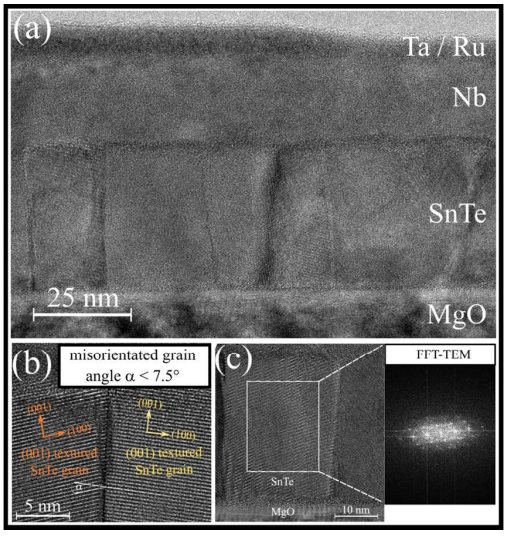

Figure S4 (a) TEM profile image of a MgO/SnTe/Nb/Ta/Ru thin film system lamella showing the (001) textured growth of SnTe polycrystals with an average in-plane grain size of 27nm and a homogenous formation in growth direction. (b) close-up image of a grain boundary between two SnTe grains. The grains are misaligned by a small angle α<7.5°. (c) shows another SnTe crystal and the adjacent FFT□TEM image. The highly symmetric peaks mark the good crystal quality of the SnTe grains.